

Numerical simulation of two-phase flows with complex interfaces

Von der Fakultät für Mathematik, Informatik und Naturwissenschaften der RWTH Aachen University zur Erlangung des akademischen Grades eines Doktors der Naturwissenschaften genehmigte Dissertation

vorgelegt von

M.Sc.

Yuanjun Zhang

aus Dandong, China

Berichter: Universitätsprofessor Dr.rer.nat. Arnold Reusken
apl. Professor Dr.rer.nat. Siegfried Müller

Tag der mündlichen Prüfung: 01.09.2015

Diese Dissertation ist auf den Internetseiten der Universitätsbibliothek online verfügbar.

Acknowledgements

First and foremost I want to express my deep gratitude to my advisor Prof. Arnold Reusken. He made it possible for me to work at the Chair for Numerical Mathematics at the RWTH Aachen University. He introduced me to the research field of two-phase flows and advance topics in numerical mathematics. He was always ready to answer my questions and discuss new problems. He has taught me, consciously or unconsciously, how good science is done through his critical and analytical thinking.

I also thank my co-advisor, Prof. Siegfried Müller, for the fruitful discussions about this thesis and his revision requests. I thank Prof. Martin Grepl and Prof. Roger Andrew Sauer for being examiners in my doctoral defense, and Prof. Christof Erich Melcher for chairing the defense.

I would like to express my hearty thanks to my colleagues at the IGPM (Institut für Geometrie und Praktische Mathematik) at the RWTH Aachen University, who provide an encouraging working environment. Special thanks go to the development team of DROPS. I would like to thank Jens Berger for being my officemate and for providing his solid knowledge in mathematics. His positive attitudes towards life and his cheerful nature greatly impress me. I thank Christoph Lehrenfeld, Patrick Esser, Jörg Grande, Sven Groß, Liang Zhang, Igor Voulis, Eva Loch and Xianmin Xu for countless discussions about software implementations and mathematical delicacies. I would like to specially mention the supports from Christoph Lehrenfeld for the netgen package and from Jörg Grande for the space-time implementation of surface PDEs, which contribute to this thesis.

Last but not least I would like to thank my friends and my family for their warm support. Special thanks go to my wife Hua for her accompany and encouragement. Her love and patience brighten my life everyday.

Abstract

In this thesis numerical simulations of two-phase flows with complex interfaces are presented. Three classes of complex interfaces are considered, namely flows with Marangoni effects, flows with viscous interfaces and flows with insoluble surface active agents (surfactants). We restrict to immiscible incompressible two-phase flow systems. A sharp interface model, which consists of two-phase Navier-Stokes equations and interfacial conditions, is used to describe the flow. At the fluid-fluid interface the surface stress tensor is defined, which models surface forces. Three types of surface stress tensors are considered, namely the constant surface tension force, the variable surface tension force and the viscous interface according to the Boussinesq-Scriven law. The surfactant transport is modeled by a convection-diffusion equation on the interface. Constitutive relations, e.g. the linear relation or the Langmuir model, relate the surfactant concentration to the surface tension coefficient.

The DROPS package, which is developed at the Chair for Numerical Mathematics at RWTH Aachen University, is used to perform numerical simulations of three dimensional two-phase flow problems. The package provides a framework for such problems, and includes a level set method for capturing the unknown interface, a pair of P2-XFEM finite elements for discretizing the two-phase Navier-Stokes equations, a trace finite element method for the surfactant transport equation, a Gauss-Seidel type decoupling scheme for handling the coupled systems, fast iterative solvers *etc.*

The main contributions of this thesis are the following. Numerical methods are developed to treat two-phase flows with complex interfaces. These methods can be categorized into two groups: the numerical treatment of surface stress tensors and the numerical treatment of the nonlinear coupling between fluid dynamics and interface dynamics. By introducing the surface stress tensor and applying the partial integration of the surface force functional, different classes of complex interfaces can be treated with a unified approach. The direct calculation of the mean curvature of the interface, which involves second derivatives, is avoided. Instead we concentrate on the discretization of the projection operator at the interface. The viscous surface force terms, which depend on the velocity unknowns, are discretized and treated implicitly in the momentum equation. The two-phase Navier-Stokes equations and the surfactant equation, coupled through the surface tension coefficient, are solved with a Gauss-Seidel type decoupling scheme. The aforementioned numerical methods are implemented in the DROPS package.

A systematic methodology is applied to validate the numerical solver for the three classes of flows with complex interfaces. We construct benchmark problems, in which theoretical predictions exist and can be considered valid, and perform numerical experiments of these model problems. Numerical results are compared with theoretical predictions. Very good agreements have been achieved. We also discuss certain properties of the numerical

methods, e.g. the convergence rate of the decoupling schemes and the linear algebra aspects of the trace finite element method *etc.* At last, a more complex problem, namely the breakup of droplet in a simple shear flow, is numerically investigated. Theoretical analysis is not known for this problem. We compare numerical results with a recent numerical simulation study.

Zusammenfassung

In der vorliegenden Arbeit werden numerische Simulationen von Zweiphasenströmungen mit komplexen Phasengrenzen vorgestellt. Dabei sind drei Klassen von komplexen Phasengrenzen vorhanden, nämlich die Strömungen mit Marangoni-Effekt, die Strömungen mit viskosen Phasengrenzen und die Strömungen mit unlöslichem Surfactant (Tensid). Die Arbeit beschränkt sich auf das Strömungsverhalten zweier nicht-mischbarer, inkompressibler Fluide. Die Strömung wird durch ein scharfes Grenzschichtmodell, das aus Zweiphasen-Navier-Stokes-Gleichungen und Grenzflächenbedingungen besteht, beschrieben. Der Oberflächenspannungstensor, durch den die Oberflächenkräfte modelliert wird, wird auf der Fluid-Fluid Phasengrenze definiert. Dabei werden drei verschiedene Typen betrachtet, nämlich die konstante Oberflächenspannung, die variable Oberflächenspannung und die viskose Phasengrenze nach dem Boussinesq-Scriven-Ansatz. Der Transport von Surfactants an der Phasengrenze wird durch eine Konvektions-Diffusions-Gleichung modelliert. Die Konzentration des Surfactants hängt über das Materialgesetz mit dem Oberflächenspannungskoeffizient zusammen.

Die numerischen Simulationen der drei-dimensionalen Zweiphasenströmungen wurden mit dem Softwarepaket DROPS durchgeführt. DROPS, das am Lehrstuhl für Numerische Mathematik der RWTH Aachen entwickelt wird, beinhaltet eine Level-Set-Methode zur Bestimmung der unbekanntenen Phasengrenze, ein P2-XFEM Finite-Elemente Ansatzpaar zur Diskretisierung der Zweiphasen-Navier-Stokes-Gleichungen, eine Spur-Finite-Elemente-Methode zur Diskretisierung der Surfactant-Transportgleichung, ein Gauß-Seidel Typ Entkopplungsschema zur Behandlung der gekoppelten Systeme, schnelle iterative Lösungsverfahren usw.

In der Arbeit liegt der Schwerpunkt auf der Entwicklung der numerischen Methoden, um die Zweiphasenströmungen mit komplexen Phasengrenzen zu behandeln. Diese Methoden werden grundsätzlich in zwei Kategorien eingeteilt, nämlich die numerische Behandlung von Oberflächenspannungstensenoren und die numerische Methode zur Lösung der nichtlinearen Kopplung zwischen Fluidodynamik und Phasengrenzendynamik. Durch Einführung des Oberflächenspannungstensors und die partielle Integration der schwachen Form des Oberflächenspannungsfunktional, können die drei oben beschriebenen Klassen der komplexen Phasengrenzen mit einem einheitlichen Ansatz behandelt werden. Die direkte Berechnung der zweiten Ableitungen enthaltenden mittleren Krümmung wird vermieden, stattdessen wird der Projektionsoperator auf den Phasengrenzen numerisch diskretisiert. Die viskosen Oberflächenkräfte, die von dem Geschwindigkeitsfeld abhängen, werden implizit in der Impulserhaltungsgleichung behandelt. Die nichtlineare Kopplung zwischen den Zweiphasen-Navier-Stokes-Gleichungen und der Surfactant-Gleichung durch den Oberflächenspannungskoeffizient wird mit einem Gauß-Seidel Schema entkoppelt. Die obigen Methoden wurden in das DROPS-Paket implementiert.

Die numerischen Methoden zur Lösung der obigen drei Klassen von komplexen Phasengrenzen werden durch eine systematische Methodik validiert. Basierend auf bereits vorhandenen theoretischen Analysen werden zugehörige, sinnvolle numerische Benchmark-Probleme konstruiert. Die Resultate der numerischen Experimente stimmen mit den theoretischen Analysen sehr gut überein. Außerdem werden bestimmte Eigenschaften der numerischen Methoden, wie zum Beispiel die Konvergenzordnung des Entkopplungsschemas und die Eigenschaften der sich aus den Spur-Finite-Elementen ergebenden linearen Systemen, in der Arbeit untersucht. Zum Schluss der Arbeit wird das Problem der Tropfenseparation unter einfacher Scherströmung numerisch untersucht. Da keine theoretische Analyse vorliegt, wird es mit einer kürzlich veröffentlichten Studie verglichen.

Contents

1. Introduction	1
1.1. Outline of the thesis	5
2. A sharp interface model for two-phase flows	7
2.1. Motion of a material body	7
2.2. Fluid interface models	10
2.3. Sharp interface model	10
2.3.1. Interface initialization	11
2.3.2. Interface motion	13
2.4. Mass and momentum conservation for a two-phase body	15
2.5. Surfactant transport on the interface	18
2.6. Constitutive relations	19
2.6.1. Bulk stress tensor	19
2.6.2. Interface stress tensor	19
2.6.3. Variable surface tension coefficient	20
2.7. Summary of equations	21
2.8. One fluid formulation	22
3. Components of the DROPS solver	25
3.1. Introduction	25
3.2. Level set method	27
3.2.1. Discretization of the level set equation	29
3.3. Discretization of Navier-Stokes equations	30
3.3.1. Time discretization	31
3.3.2. Reconstruction of the interface	32
3.3.3. Spatial discretization	33
3.3.4. Discretization of the surface force functional	37
3.4. Fully discrete problem	38
3.5. Decoupling and linearization strategy	39
3.5.1. Decoupling of fluid dynamics and the level set equation	40
3.5.2. Linearization of the Navier-Stokes equation	41
3.6. Numerical treatment of surfactant transport on the interface	42
3.6.1. Weak formulations	42
3.6.2. Space-time finite element method	44
4. Numerical treatment of surface stress tensor	47
4.1. Approximations of surface normals	48
4.2. Convergence acceleration	49
4.2.1. Numerical experiments	52
4.3. Treatment of viscous terms	53

4.4. Coupling between fluid dynamics and surfactant	57
5. Simulation of Marangoni effects	59
5.1. Introduction	59
5.2. Mathematical models	60
5.2.1. A sharp interface model for thermocapillary effects	60
5.2.2. A stationary Stokes model for thermocapillary effects	62
5.2.3. Instationary Navier-Stokes problem with Marangoni effects	66
5.3. Benchmark problem and numerical experiments	68
5.3.1. Properties of numerical methods	70
5.3.2. Physical effects	75
5.3.3. Summary	79
6. Simulation of flows with a viscous interface	81
6.1. Introduction	81
6.2. Mathematical models	82
6.2.1. A sharp interface model for flows with a viscous interface	82
6.2.2. A stationary Stokes Model	84
6.2.3. The stationary Stokes model as approximation for the general two- phase Navier-Stokes model	86
6.3. Benchmark problem and numerical experiments	89
7. Simulation of flows with surfactants	97
7.1. Introduction	97
7.2. Mathematical models	98
7.2.1. A sharp interface model for a droplet with insoluble surfactants	98
7.2.2. A stationary Stokes model	99
7.2.3. A quasi-static Stokes approximation	103
7.3. Numerical experiments	107
7.3.1. Clean interface	108
7.3.2. Interface with an insoluble surfactant	111
7.4. Droplet breakup in shear flow	118
7.4.1. Critical capillary number	119
7.4.2. Influence of surfactants	119
8. Discussion and outlook	125
Appendices	133
A. Appendix	133
A.1. Partial integration rules for a surface	133

List of Figures

2.1.	Three-dimensional region model and sharp interface model for fluid interfaces.	10
2.2.	A two-phase control volume with an interface.	11
2.3.	The value of ρ^F depends on the position of the sharp interface Γ	12
2.4.	A two-phase control volume $\omega(t)$ containing a sharp interface $\gamma(t)$	16
3.1.	Components of DROPS package.	26
3.2.	An example of a level set function with contour lines.	28
3.3.	Reconstruction of an approximate interface.	33
3.4.	Additional discontinuous basis functions for one-dimensional case.	35
3.5.	An example of a space-time interface for a two-dimensional domain.	45
4.1.	Illustration of surface normals $\bar{\mathbf{n}}_h$ on Γ_h	48
4.2.	Schematic of the Gauss-Seidel type decoupling scheme.	50
4.3.	Illustration of the approximated interface $\hat{\Gamma}_h$	51
4.4.	Plot of the side lengths of the bounding box.	53
4.5.	Plot of the side lengths of the bounding box.	56
4.6.	Number of Gauss-Seidel iterations for different values of μ_Γ and $\lambda_\Gamma = \mu_\Gamma$	56
4.7.	Schematic of the solution process of the surfactant equation.	58
5.1.	Sketch of the model problem.	65
5.2.	Comparison of theoretical migration velocity and numerical results for various values of $\partial\tau/\partial z$	68
5.3.	A snapshot of a numerical simulation.	69
5.4.	Time dependent numerical migration velocity $U_{mig}^{num}(t)$	71
5.5.	Relative errors in $(U_z^{num}(0))'$ for different Δt and density ratios.	73
5.6.	Absolute value of the initial acceleration $(U_{mig}^{num}(0))'$	74
5.7.	A comparison of time integration schemes at initial phase.	75
5.8.	A comparison of time integration schemes after a reparametrization.	76
5.9.	Initial phase of the numerical migration velocity $U_{mig}^{num}(t)$	77
5.10.	Evolution of diameters in $x/y/z$ -directions for $\tau_0 = 1$ and $\frac{\partial\tau}{\partial z} = 25$	78
6.1.	Cross section of the domain, inflow profile and initial droplet position in Navier-Stokes model.	84
6.2.	Comparison of theoretical migration velocity and numerical results.	88
6.3.	Mesh with level 3 refinement and numerically computed velocities field.	90
6.4.	Droplet shapes for $t = 0, 3, 6$ s.	92
6.5.	Time-dependent numerical migration velocity $U_{mig}^{num}(t)$ for several refinement levels.	93
6.6.	Time-dependent numerical migration velocity $U_{mig}^{num}(t)$ for different Bo^d	93
6.7.	Numerical migration velocity U_{mig}^{num} for different Bo^d	94

List of Figures

7.1. Visualization of numerical results for a droplet in an axi-symmetric extensional flow.	100
7.2. Numerical deformation parameter $D^{num}(t)$ for different domain sizes.	109
7.3. Numerical results $d_z(t)$ and $d_y(t)$ on different refinement levels for a clean droplet.	110
7.4. Numerical deformation parameter \bar{D}^{num} for a clean droplet with various capillary numbers.	111
7.5. Numerical results $d_z(t)$ and $d_y(t)$ for a droplet with surfactant.	112
7.6. Numerical results $d_z(t)$ and $d_y(t)$ for a droplet with surfactant.	113
7.7. Schematics of the definition of r and how the surface quantities r and S/S^* are plotted.	114
7.8. The shape of droplets at $t = 20$ s on different refinement levels.	114
7.9. The shape of droplets at $t = 20$ s on different refinement levels.	115
7.10. Normalized surfactant concentration S/S^* on the deformed droplet.	115
7.11. Numerical deformation parameter \bar{D}^{num} for a droplet with surfactant.	117
7.12. Numerical deformation parameter \bar{D}^{num} with varying α (D_Γ) for a droplet with surfactant.	118
7.13. Evolution of a clean droplet for $Ca = 0.4$ and $Ca = 0.42$	120
7.14. Evolution of a droplet with surfactants for $Ca = 0.42$ and $Re = 0.4$	122
7.16. Comparison between a surfactant covered droplet and a clean droplet.	124

List of Tables

3.1.	L^2 -norm of the approximation error for Q_h and convergence order in one dimensional case.	36
4.1.	Number of Gauss-Seidel iterations.	54
4.2.	Number of Gauss-Seidel iterations for different λ_Γ and μ_Γ	57
5.1.	The numerical migration velocity U_{mig}^{num} on different grid refinements. . . .	71
5.2.	Comparison between the decoupling scheme with a fixed point iteration and a time-lagging scheme.	74
5.3.	Numerical migration velocity U_{mig}^{num} with different $\frac{\partial \tau}{\partial z}$ values.	76
5.4.	Relaxation time for different viscosities.	78
6.1.	Numerical migration velocity U_{mig}^{num} on different grid refinements.	91
6.2.	Numerical migration velocity U_{mig}^{num} in different experiments.	94
7.1.	Definitions of parameters.	105
7.2.	Time averaged results \bar{D}^{num} for different domain sizes.	109
7.3.	Time averaged results \bar{d}_z and \bar{d}_y on different refinement levels.	110
7.4.	Time averaged results of $d_z(t)$ and $d_y(t)$	113
7.5.	Number of unknowns, Gauss Seidel iterations and GMRES iterations. . . .	116
7.6.	Gauss-Seidel iterations and GMRES iterations for different time step sizes. .	116
7.7.	Breakup time of a clean droplet and the surfactant contaminated droplet. .	121

1. Introduction

Fluid interfaces are of fundamental importance in many natural processes and industrial applications. Different physical or chemical phenomena take place at the fluid interfaces, e.g. transfer of mass and heat. In some processes, fluid interfaces are the dominant factor, e.g. liquid-liquid extraction and microfluidics applications. We concentrate on fluid interfaces in the form of droplets or bubbles. Both theoretical and experimental studies have been carried out to investigate the dynamical properties of droplets. The classical theoretical studies assume a (quasi-) *stationary* droplet under *creeping flow conditions* and are based on spherical harmonics and perturbation analysis. We list some of them here. Rybczynski and Hadamard both studied the problem of a spherical droplet moving in an external Stokes flow and derived the terminal velocity of the droplet, cf. [22]. At the interface, they assumed a uniform surface tension force. Young et al. [91] investigated the motion of a spherical droplet in a vertical temperature gradient and calculated the so called “YGB” terminal velocity. Due to the temperature gradient, there exists a gradient of the surface tension coefficient at the interface. Phenomena related to surface tension gradients are called Marangoni effects. Schwalbe et al. [77] investigated the motion of a spherical droplet with a viscous interface. The Boussinesq-Scriven law is used to describe the viscous response of the interface. Stone and Leal [82] studied the deformation and breakup of a droplet under the influence of surface active agents (surfactants) on the interface. The existence of surfactants alters the surface tension coefficient. All the above mentioned theoretical results have the shortcomings that they are only valid if the strict theoretical assumptions are satisfied, i.e. *spherical shape*, *small deformation* and *creeping flow conditions*.

In the last decades, numerical simulations have been applied to study the dynamics of droplets when it is not possible to perform theoretical analysis. Only recently numerical studies of two phase flows with complex interfaces have appeared. Different models and numerical methods have been applied, e.g. the finite difference/front tracking method [57], the volume of fluid method (VOF method)[42, 53], the phase field method [2, 84, 85], the level set method [72] and the boundary integral method [10, 9]. We briefly comment important pros and cons of the aforementioned numerical methods, and refer to [39] for a detailed discussion of the topic. The numerical simulations are based on different fluid interface models, namely a sharp interface model or a diffusive interface model, cf. section 2.2. For a sharp interface model, there are different techniques to represent the fluid interface. The finite difference/front tracking method is an interface *tracking* method, i.e. markers are put on the fluid interfaces and transported by the flow. The position of the interface is then tracked by these markers. The main disadvantage of the front tracking method is that the markers have to be redistributed on the interface during the simulations in order to maintain an accurate resolution of the interface. It is also rather difficult to treat topological changes of the droplets, e.g. break-up or collision processes. VOF and

1. Introduction

the level set method are interface *capturing* method, in which instead of the interface an indicator function is tracked. In VOF this is the discontinuous characteristic function and in the level set method this is a continuous approximate signed distance function. The fluid interface is then reconstructed/recaptured from the indicator function. In general, VOF methods have very good mass-conservation properties. However, the VOF method is restricted to finite volume discretizations. It is also rather tedious to obtain an accurate approximation of the interface with VOF, e.g. the curvature, which is critical in the numerical treatment of interface forces. In the level set method, a continuous function is defined in the whole domain and transported by the flow. The zero level of this function represents the interface, and can be numerically determined. The main disadvantages of the level set method are a relative poor mass-conservation property and the need to maintain the approximate signed distance property. For the latter so-called reparametrization techniques have been developed [39]. In diffusive interface models one assumes a thin three dimensional region for the interface. A mixing energy density is introduced and different models are proposed in the literature, e.g. the Cahn-Hilliard model [18]. Compared to the sharp interface model, in diffusive interface models it is more difficult to incorporate different physical effects, e.g. the mass transport between phases across the interface and surfactants. Finally we mention numerical simulation techniques based on the boundary integral method [9]. In these methods, which apply only in a limited number of flow problems, one needs a discretization only of the boundary and the interface. The bulk fluids are not discretized. In this thesis we only consider sharp interface models and we use the level set interface capturing method.

In this thesis we restrict to *incompressible* two-phase flow systems. Two-phase flows pose very demanding numerical challenges. We mention a few of them:

Unknown interface. In two-phase flow problems, the position of the fluid interface is a-priori *unknown*. Fluid interfaces are transported by the flow field, and local forces act at the interfaces. An accurate numerical method to track the evolution of the interface is essential for the simulation of two-phase flow problems.

Treatment of surface forces. Surface tension force, which depends on the mean curvature of the interfaces, is the dominating force acting on the fluid interfaces. In order to avoid spurious velocities, special numerical techniques are required to approximate the surface tension force. We also need to treat surface tension gradients, surface viscous forces and variable surface tension coefficients due to surfactants.

Nonlinear couplings. The nonlinear incompressible Navier-Stokes equations describe the fluid dynamics. The coupling between the fluid dynamics and the surface forces are highly nonlinear. Hence we need carefully chosen decoupling schemes.

Surfactant transport. Surfactants are surface active chemicals, which adhere to the fluid interfaces and are transported on the interfaces. The interface is a two-dimensional surface embedded in three dimensional space, and it is changing over time. The modeling and numerical treatment of surfactant transport is a very challenging task.

Other topics are also worth mentioning, e.g. the changing material properties across the interfaces, mass and heat transport across the interfaces etc.

We use the DROPS package [1] to perform numerical simulations of three dimensional two-phase flow problems. The DROPS package provides a framework for such problems, and it includes mesh generation and adaptive local refinement/coarsening, a level set method for interface representation, finite element discretization methods for two-phase flow problems, a trace finite element method for surfactant transport equation, decoupling techniques for handling the coupled systems and fast iterative solvers. The package is written in C++ language with high-level template programming and parallelization techniques.

The main new contributions of this thesis are the following. We develop numerical methods to treat two-phase flows with complex interfaces and implement these methods in DROPS; in order to validate these methods, we adopt a systematic methodology by comparing numerical results with theoretical predictions. These numerical methods can be categorized into the following two groups:

Treatment of surface stress tensors. We use a sharp interface model for two-phase flows. At the fluid-fluid interface, the jump of bulk stresses $[\boldsymbol{\sigma}\mathbf{n}]_{\Gamma}$ is balanced by surface forces. Similar to the Cauchy stress tensor $\boldsymbol{\sigma}$ for bulk phases, a surface stress tensor $\boldsymbol{\sigma}_{\Gamma}$ is defined at the interface to model the surface forces. We consider two models for $\boldsymbol{\sigma}_{\Gamma}$: the surface tension model $\boldsymbol{\sigma}_{\Gamma} = \tau\mathbf{P}$, and the viscous interface model according to the Boussinesq-Scriven law. In the former model, the surface tension coefficient τ can be either constant or variable. We use this model for Marangoni effects or for modeling the effect of surfactants on the surface tension force. The latter viscous interface model extends the surface tension model by adding surface viscous stress.

For a successful simulation of two-phase flows with complex interfaces an appropriate treatment of the corresponding surface stress tensors $\boldsymbol{\sigma}_{\Gamma}$ is necessary. In the weak formulation of two-phase flows, the surface force takes the form of a functional in the momentum equation. We need to discretize this force functional on the (approximate) interface, which is composed of planar segments. One important issue here is the approximation of the projection operator \mathbf{P} , which depends on the surface normals. Instead of taking piecewise constant surface normals from the discrete planar interface, we approximate the surface normals using information from the discrete level set function, which is a continuous piecewise quadratic function.

Nonlinear coupling between fluid dynamics and interface dynamics. The fluid-fluid interface is transported by the flow field, surface forces act at the interface and alter the surrounding flow. We use the two-phase Navier-Stokes equations with surface forces to describe the flow field, and a level set equation to capture the evolution of the interface. The coupling between the two sets of equations is highly nonlinear. We apply a Gauss-Seidel type iteration to decouple these two sets of equations. The level set function and the flow variables are updated successively in one iteration. Without further modification, the convergence behavior of this decoupling iteration deteriorates strongly with increasing time step sizes. One idea of convergence acceleration is based on predicting the surface tension force with the help of the updated level set function. We also apply a quasi-Newton method (Broyden's method) to accelerate the convergence of the two sets of equations. Numerical experiments show that the combination of the surface force prediction and Broyden's method results in a much better convergence behavior. For the

1. Introduction

viscous interface case, the surface viscous forces depend on the velocity. In the decoupling scheme, we treat the viscous forces implicitly, i.e. by moving the corresponding viscous force terms into the stiffness matrix. The influence of this procedure on the convergence behavior is investigated. For the surfactant dependent surface force case, we include the surfactant equation into the Gauss-Seidel iteration, i.e. the surfactant concentration is updated each time the level set function and the flow variables are updated. Hence the surfactant transport is coupled strongly with the two-phase flow dynamics.

The methods mentioned above are applied to three classes of two-phase flows with complex interfaces, namely flows with *thermal Marangoni effects*, with *viscous interfaces* and with insoluble *surfactants*. We apply a systematic methodology to validate the numerical solver for these classes of applications. We construct benchmark problems, in which the theoretical predictions can be considered valid, i.e. theoretical assumptions are (approximately) satisfied. In such model problems, theoretical solutions can be considered as good approximations of the solution of two-phase Navier-Stokes equations. We perform numerical experiments of these model problems and compare numerical results with theoretical predictions to validate the accuracy of the solver. The validated numerical methods can then be utilized to investigate more complex problems.

We take the viscous interface case as an example to explain this validation approach. The standard sharp interface model for a viscous interface is the two-phase Navier-Stokes equations with a surface stress tensor $\boldsymbol{\sigma}_\Gamma$ according to the Boussinesq-Scriven law. At the interface, we require that the velocity is continuous, the bulk stress is balanced by the surface stress, and the normal velocity of the interface matches the normal velocity of the surrounding flow. Schwalbe *et al.* [77] studied this problem theoretically. They considered a spherical droplet with a viscous interface in a Poiseuille flow. They made the following assumptions: the domain containing the droplet occupies the whole \mathbb{R}^3 , the moving droplet maintains the spherical shape, and the flow satisfies the creeping flow conditions, i.e. Stokes equations are used to describe the flow. They applied spherical harmonics to obtain the velocity field and derived a prediction of the migration velocity of the droplet. We construct a benchmark problem to compare numerical results with this theoretical migration velocity. To construct such benchmark problem, the following considerations are made: we choose a large enough domain, such that boundary effects can be neglected; the material properties are chosen such that the relevant dimensionless flow numbers (Reynolds number Re , the capillary number Ca and Weber number We) are small, i.e. the Stokes equation can be considered a good approximation of the two-phase Navier-Stokes equations, and the surface tension force is large enough to maintain the initial spherical shape of the droplet. Numerical experiments are then performed for the benchmark problem with the two-phase Navier-Stokes model. The quantity of interest is the mean numerical migration velocity of the droplet, which can be compared with the theoretical migration velocity. Grid convergence tests are performed to study the convergence behavior of the numerical methods. We perform parameter studies to compare the numerical results with theoretical predictions.

1.1. Outline of the thesis

The thesis is organized in the following chapters.

In **Chapter 2**, we introduce a sharp interface model for two-phase flows. The derivation of this model is presented by considering mass and momentum conservation for a two-phase body. We also introduce a surfactant transport model on the sharp interface. The “one fluid formulation” is used in the numerical simulations.

In **Chapter 3** and **Chapter 4** we introduce the numerical methods needed to solve the two-phase flow problems. In **Chapter 3**, we briefly describe the DROPS package, which provides the framework for the numerical simulations of two-phase flow problems with complex interfaces. In **Chapter 4**, we concentrate on the numerical treatment of surface stress tensors. A unified approach for treating complex interfaces is presented.

In **Chapter 5**, **Chapter 6** and **Chapter 7**, numerical simulations of Marangoni effects, viscous interfaces and flows with surfactants are presented. In each chapter, we describe the corresponding sharp interface models, and introduce the theoretical simplified models, which are *stationary* Stokes models. We discuss the conditions needed for the theoretical model to be good approximations of the standard two-phase Navier-Stokes models. Results from instationary numerical experiments are compared to the theoretical predictions.

In **Chapter 8**, we summarize the results and discuss open questions and outlooks.

2. A sharp interface model for two-phase flows

We list here the calculus operators we use in the thesis and their component-wise form in a Cartesian coordinate system. We use \mathbf{e}_i to denote the standard basis and \otimes to denote the outer (or dyadic) product, i.e. $\mathbf{v} \otimes \mathbf{w} := \mathbf{vw}^T$. We consider functions $f : \mathbb{R}^d \rightarrow \mathbb{R}$, $\mathbf{u} : \mathbb{R}^d \rightarrow \mathbb{R}^d$, $\mathbf{f} : \mathbb{R}^d \rightarrow \mathbb{R}^d$ and $\mathbf{F} : \mathbb{R}^d \rightarrow \mathbb{R}^{d \times d}$. We use $F_i \in \mathbb{R}^{1 \times d}$ to denote the i -th row of \mathbf{F} . We use comma to separate components of a vector, i.e. $\mathbf{u} = (u_1, u_2, \dots, u_d)^T$, and we use semicolon to separate rows of a matrix, i.e. $\mathbf{F} = (F_1; F_2; \dots; F_d)$.

notation	component-wise form
∇f	$\sum_{i=1}^d \frac{\partial f}{\partial x_i} \mathbf{e}_i = \left(\frac{\partial f}{\partial x_1}, \frac{\partial f}{\partial x_2}, \dots, \frac{\partial f}{\partial x_d} \right)^T$
$\Delta f := \operatorname{div} \nabla f$	$\sum_{i=1}^d \frac{\partial^2 f}{\partial x_i^2} = \frac{\partial^2 f}{\partial x_1^2} + \frac{\partial^2 f}{\partial x_2^2} + \dots + \frac{\partial^2 f}{\partial x_d^2}$
$\nabla \mathbf{f}$	$\sum_{i=1}^d \sum_{j=1}^d \frac{\partial f_i}{\partial x_j} \mathbf{e}_i \otimes \mathbf{e}_j = \left((\nabla f_1)^T; (\nabla f_2)^T; \dots; (\nabla f_d)^T \right)$
$\operatorname{div} \mathbf{f} := \operatorname{tr}(\nabla \mathbf{f})$	$\sum_{i=1}^d \frac{\partial f_i}{\partial x_i} = \frac{\partial f_1}{\partial x_1} + \frac{\partial f_2}{\partial x_2} + \dots + \frac{\partial f_d}{\partial x_d}$
$(\mathbf{u} \cdot \nabla) \mathbf{f} = \nabla \mathbf{f} \cdot \mathbf{u}$	$\sum_{i=1}^d \sum_{j=1}^d \left(u_j \frac{\partial}{\partial x_j} f_i \right) \mathbf{e}_i$
$\operatorname{div} \mathbf{F}$	$\sum_{i=1}^d \sum_{j=1}^d \frac{\partial F_{ij}}{\partial x_j} \mathbf{e}_i = (\operatorname{div} F_1, \operatorname{div} F_2, \dots, \operatorname{div} F_d)^T$
$\Delta \mathbf{f} := \operatorname{div} \nabla \mathbf{f}$	$\sum_{i=1}^d \sum_{j=1}^d \frac{\partial^2 f_i}{\partial x_j^2} \mathbf{e}_i = (\Delta f_1, \Delta f_2, \dots, \Delta f_d)^T$

We study the motion of a moving and deforming droplet (phase 1) within a bulk fluid (phase 2). There is momentum transfer between the two phases. Mass and energy transfer are not considered. At the fluid-fluid interface, various physical phenomena might occur, which include Marangoni effects, viscous interface and surfactant transport. In this chapter, we introduce a sharp interface model for two-phase flows. The model is based on continuum mechanics principles.

2.1. Motion of a material body

We refer to the fluid mechanics textbook [21] for the content in this section.

We consider a material body, which is a connected continuum of material particles. The one-to-one continuous mapping of the body onto a domain $\Omega \in \mathbb{R}^3$ is denoted by:

$$\mathbf{x} = \mathbf{X}(\sigma),$$

2. A sharp interface model for two-phase flows

where σ is a material particle of the body and $\mathbf{x} = (x_1, x_2, x_3)^T \in \Omega$ is the *Eulerian* coordinate of a point in Ω . We assume that Ω is an open bounded domain. The fluid dynamics is studied in a fixed time interval $[0, T]$.

To study the fluid motion, we need to trace a material particle. Consider a material particle σ that occupies the position \mathbf{x}_0 at $t = t_0 \in (0, T)$. For a small time interval $(t_0 - \epsilon, t_0 + \epsilon)$ with a sufficiently small $\epsilon > 0$, we define the trajectory of the particle σ as

$$\mathbf{X}_\sigma : (t_0 - \epsilon, t_0 + \epsilon) \rightarrow \mathbb{R}^3, \quad (2.1)$$

with $\mathbf{X}_\sigma(t_0) = \mathbf{x}_0$. The mapping \mathbf{X}_σ is assumed to be a C^1 -diffeomorphism. We use $\mathbf{u}_\sigma(t) := \frac{d}{dt}\mathbf{X}_\sigma(t)$ to denote the time rate of change of position of a material particle. The material particles are transported by a velocity field $\mathbf{u} = \mathbf{u}(\mathbf{x}, t) \in \mathbb{R}^3$. Hence

$$\mathbf{u}_\sigma(t) = \mathbf{u}(\mathbf{X}_\sigma(t), t).$$

The *material derivative* of a (sufficiently smooth) function $\mathbf{f}(\mathbf{x}, t)$ following the trajectory of a particle σ is defined as

$$\dot{\mathbf{f}}(\mathbf{X}_\sigma(t), t) := \frac{d}{dt}\mathbf{f}(\mathbf{X}_\sigma(t), t).$$

Applying the chain rule and note that $\frac{d}{dt}\mathbf{X}_\sigma(t) = \mathbf{u}(\mathbf{X}_\sigma(t), t)$, we obtain

$$\dot{\mathbf{f}} = \frac{\partial \mathbf{f}}{\partial t} + (\mathbf{u} \cdot \nabla)\mathbf{f}. \quad (2.2)$$

Reynolds transport theorem. We now consider the transport theorem for a *material control volume* denoted by ω_0 , which is a connected and bounded subset of Ω at $t = 0$. The control volume is transported by the (sufficiently smooth) velocity field \mathbf{u} . No material enters or leaves the volume, thus the control volume at time t is denoted by

$$\omega(t) := \{\mathbf{X}_\sigma(t) : \mathbf{X}_\sigma(0) = \mathbf{x}_0 \in \omega_0\}.$$

We consider a (sufficiently smooth) function $\mathbf{f} := \mathbf{f}(\mathbf{x}, t)$, which is either a scalar or a vector. The *Reynolds transport theorem* holds for \mathbf{f} [73, 49, 21]:

$$\frac{d}{dt} \int_{\omega(t)} \mathbf{f} dx = \int_{\omega(t)} \dot{\mathbf{f}} + \mathbf{f} \operatorname{div} \mathbf{u} dx, \quad (2.3)$$

where $\dot{\mathbf{f}}$ is the material derivative defined in (2.2).

Applying the identity $\operatorname{div}(\mathbf{v} \otimes \mathbf{w}) = (\operatorname{div} \mathbf{w})\mathbf{v} + (\mathbf{w} \cdot \nabla)\mathbf{v}$, we obtain

$$\frac{d}{dt} \int_{\omega(t)} \mathbf{f} dx = \int_{\omega(t)} \frac{\partial \mathbf{f}}{\partial t} + \operatorname{div}(\mathbf{f} \otimes \mathbf{u}) dx. \quad (2.4)$$

Conservation of mass. We do not consider reaction processes in the bulk phase, and there are no sources or sinks of mass in the domain. Therefore, the law of mass conservation states that the total mass of a control volume is invariant w.r.t time, which means that

$$\frac{d}{dt} \int_{\omega(t)} \rho dx = 0. \quad (2.5)$$

Applying the Reynolds transport theorem (2.3) to (2.5), we obtain

$$\int_{\omega(t)} \dot{\rho} + \rho \operatorname{div} \mathbf{u} \, dx = 0. \quad (2.6)$$

For a material control volume $\omega(t)$ composed of *incompressible* fluid, the density ρ is assumed to have a *constant* positive value. Hence the material derivative $\dot{\rho}$ equals *zero*. $\omega(t)$ is arbitrary, $\operatorname{div} \mathbf{u}$ is assumed to be continuous, thus we obtain

$$\operatorname{div} \mathbf{u} = 0 \quad \text{in} \quad \Omega(t). \quad (2.7)$$

Conservation of momentum. From Newton's second law of motion, the change of the momentum of a material body equals the sum of the forces acting on the body. In our context, the change of the momentum equals $\frac{d}{dt} \int_{\omega(t)} \rho \mathbf{u} \, dx$. The forces acting on the fluid body come from two sources: body force and contact force.

We consider gravity force as the only body force acting on the fluid body, the sum of which is given by

$$F_g := \int_{\omega(t)} \rho \mathbf{g} \, dx,$$

with \mathbf{g} the gravitational acceleration vector.

For a control volume $\omega(t)$, the contact forces on the boundary of $\omega(t)$ come from the traction of neighboring fluids outside of $\omega(t)$. According to Cauchy stress theorem [79], the sum of the contact forces is

$$F_\gamma := \int_{\partial\omega(t)} \boldsymbol{\sigma} \mathbf{n} \, ds,$$

where $\boldsymbol{\sigma}$ is the Cauchy stress tensor and $\mathbf{n} \in \mathbb{R}^3$ is the outward pointing normals on $\partial\omega(t)$. We consider $\boldsymbol{\sigma}$ as a matrix from $\mathbb{R}^{3 \times 3}$.

With the introduction of F_g and F_γ , the conservation of momentum takes the form:

$$\begin{aligned} \frac{d}{dt} \int_{\omega(t)} \rho \mathbf{u} \, dx &= F_g + F_\gamma \\ &= \int_{\omega(t)} \rho \mathbf{g} \, dx + \int_{\partial\omega(t)} \boldsymbol{\sigma} \mathbf{n} \, ds. \end{aligned} \quad (2.8)$$

Applying the Reynolds transport theorem (2.4) and the divergence theorem, we obtain

$$\int_{\omega(t)} \frac{\partial(\rho \mathbf{u})}{\partial t} + \operatorname{div}(\rho \mathbf{u} \otimes \mathbf{u}) \, dx = \int_{\omega(t)} \rho \mathbf{g} + \operatorname{div} \boldsymbol{\sigma} \, dx.$$

Note that $\frac{\partial \rho}{\partial t} = 0$, $\operatorname{div} \mathbf{u} = 0$ and $\omega(t)$ is arbitrary, the conservation of momentum takes the form

$$\rho \left(\frac{\partial \mathbf{u}}{\partial t} + (\mathbf{u} \cdot \nabla) \mathbf{u} \right) = \rho \mathbf{g} + \operatorname{div} \boldsymbol{\sigma} \quad \text{in} \quad \Omega(t). \quad (2.9)$$

We need a constitutive relation for $\boldsymbol{\sigma}$ which will be explained later.

2.2. Fluid interface models

We treat fluid interfaces which separate two bulk phases with different material properties, e.g. densities, viscosities *etc.* The fluid interface is best regarded as a *three-dimensional region* with a thickness of several molecular diameters or more, cf. [80]. Densities and concentration of the two species vary smoothly within this region.

Continuum models of a fluid interface can be divided into two categories:

- Three-dimensional region model. One of the first models of this type is introduced by Korteweg [45], where he studied the stress-deformation behavior of the interface treated as a spherical shell. Phase field models, which were first introduced by Fix [30] and Langer [47], also belong to this category. In this method, a partial differential equation for the evolution of a smooth function (order parameter), which describes the mixing effects between phases, is used to model the interfacial region.
- Sharp interface model. Due to the small thickness of the fluid interface, it is natural to treat it as a *two-dimensional sharp* interface. Gibbs [31] first proposed this approach. The two phases are considered to be separated by an infinitesimal thin boundary. Densities, viscosities and other material properties are considered to be constant until the sharp interface is reached.

In Figure 2.1, we show schematics of the three-dimensional region model and the sharp interface model. The two bulk phases are denoted by P_1 and P_2 , and the fluid interfaces are denoted by I and Γ . In this thesis, we adopt the sharp interface model.

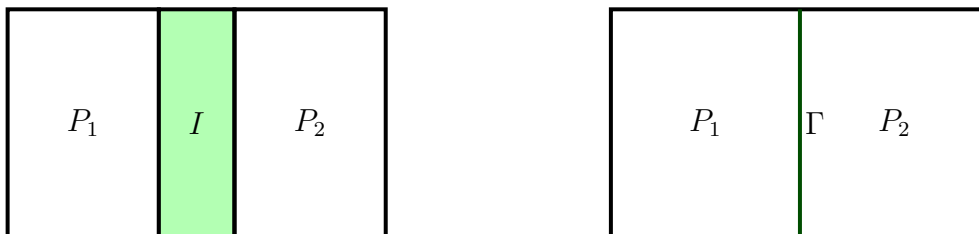
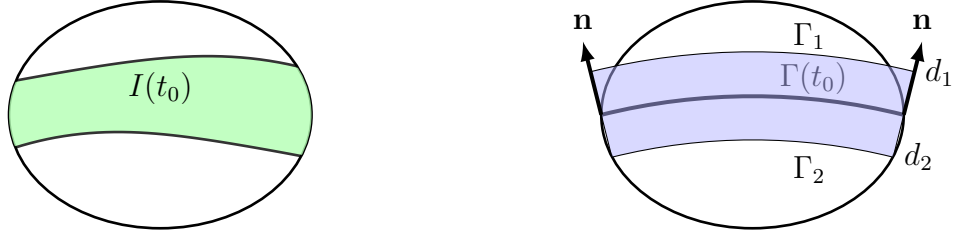


Figure 2.1.: Three-dimensional region model and sharp interface model for fluid interfaces.

2.3. Sharp interface model

Related to the sharp interface model there are several important modeling aspects, e.g. where to put the sharp interface, and how to conserve the mass and momentum of the two-phase material volume, etc. In the following sections we will briefly address these topics. More information can be found in [80].

We consider a material control volume $\omega(t)$ with $t \in [0, T]$. At $t = t_0 \in (0, T)$, the control volume occupies $\omega(t_0)$ and the interface region occupies $I(t_0)$ as illustrated in Figure 2.2.



(a) Material volume with an interface region

(b) Sharp interface model

Figure 2.2.: A two-phase control volume with an interface (2D illustration).

2.3.1. Interface initialization

We first describe how to choose the position of the sharp interface at $t = t_0$. For this purpose, we study the total mass of the two-phase control volume. We assume that the densities are constants outside the interfacial region $I(t_0)$, which are ρ_1 and ρ_2 (top and bottom phases in Figure 2.2). The density in $I(t_0)$ is assumed to be a smooth function of the position and denoted by $\rho^I = \rho^I(\mathbf{x})$ for $\mathbf{x} \in I(t_0)$. For simplicity, we define a piece-wise constant density function ρ , which equals ρ_i with $i = 1, 2$ in the corresponding bulk phases. The total mass of the two-phase control volume equals

$$\mathcal{M}_I := \int_{\omega(t_0) \setminus I(t_0)} \rho \, dx + \int_{I(t_0)} \rho^I \, dx. \quad (2.10)$$

We now introduce an *ideal* sharp dividing interface $\Gamma(t_0)$, which is located in the interfacial region $I(t_0)$. In Figure 2.2, the material volume $\omega(t_0)$ is then divided into $\omega_1(t_0)$ (up) and $\omega_2(t_0)$ (bottom). In the sharp interface model, the densities are assumed to be *constant* in both domains, i.e. $\rho = \rho_i$ for $\mathbf{x} \in \omega_i(t)$ with $i = 1, 2$. With this assumption, the total mass depends on the position of $\Gamma(t_0)$ as depicted in Figure 2.3 for the one dimensional case. In order to conserve the total mass, we introduce an **interfacial excess mass density** $\rho^\Gamma(\mathbf{x})$ for $\mathbf{x} \in \Gamma(t_0)$. The total mass of the two-phase control volume with a sharp interface then equals

$$\mathcal{M}_\Gamma := \int_{\omega(t_0)} \rho \, dx + \int_{\Gamma(t_0)} \rho^\Gamma \, ds. \quad (2.11)$$

Clearly, \mathcal{M}_I from (2.10) should equal \mathcal{M}_Γ from (2.11). Note that $\rho_\Gamma(\mathbf{x})$ for $\mathbf{x} \in \Gamma(t_0)$ in (2.11) depends on the position of $\Gamma(t_0)$.

Remark 2.3.1. *The value of ρ^Γ depends on the position of the sharp interface $\Gamma(t_0)$, it can be either positive or negative, or even zero. As an example we take a simple one dimensional two-phase system. In Figure 2.3, we show a fictive density profile of the two-phase system. At time t_0 , the system occupies $[0, \omega]$. One phase has a density ρ_1 and the other phase has a density ρ_2 . In the interface region $x \in [I_1, I_2]$, the density changes smoothly from ρ_1 to ρ_2 , and is denoted by $\rho^I(x)$ for $x \in [I_1, I_2]$. The total mass of the two-phase system at time t_0 can be calculated as*

$$\mathcal{M}_I := \int_0^{I_1} \rho_1 \, dx + \int_{I_1}^{I_2} \rho^I \, dx + \int_{I_2}^\omega \rho_2 \, dx.$$

2. A sharp interface model for two-phase flows

We introduce a sharp interface Γ in $[I_1, I_2]$. In the sharp interface model, densities of the bulk phases are considered to be constant left and right of Γ . In this degenerate case, the mass assigned to the interface (the surface integral) equals ρ^Γ , which is a variable value depending on the position of Γ . The total mass of the sharp interface model equals

$$\mathcal{M}_\Gamma := \int_0^\Gamma \rho_1 dx + \int_\Gamma^\omega \rho_2 dx + \rho^\Gamma.$$

\mathcal{M}_Γ should have the same value as \mathcal{M}_I . By changing the position of Γ , we can alter the value of ρ^Γ . Three different cases are shown in Figure 2.3. In the figure, we mark the difference between the quantity $\int_0^\Gamma \rho_1 dx + \int_\Gamma^\omega \rho_2 dx$ and the total mass with **red** (extra mass) and **blue** (loss mass). There exists one position of the sharp interface, such that the extra mass equals the loss mass and the interfacial excess mass density ρ^Γ is zero.

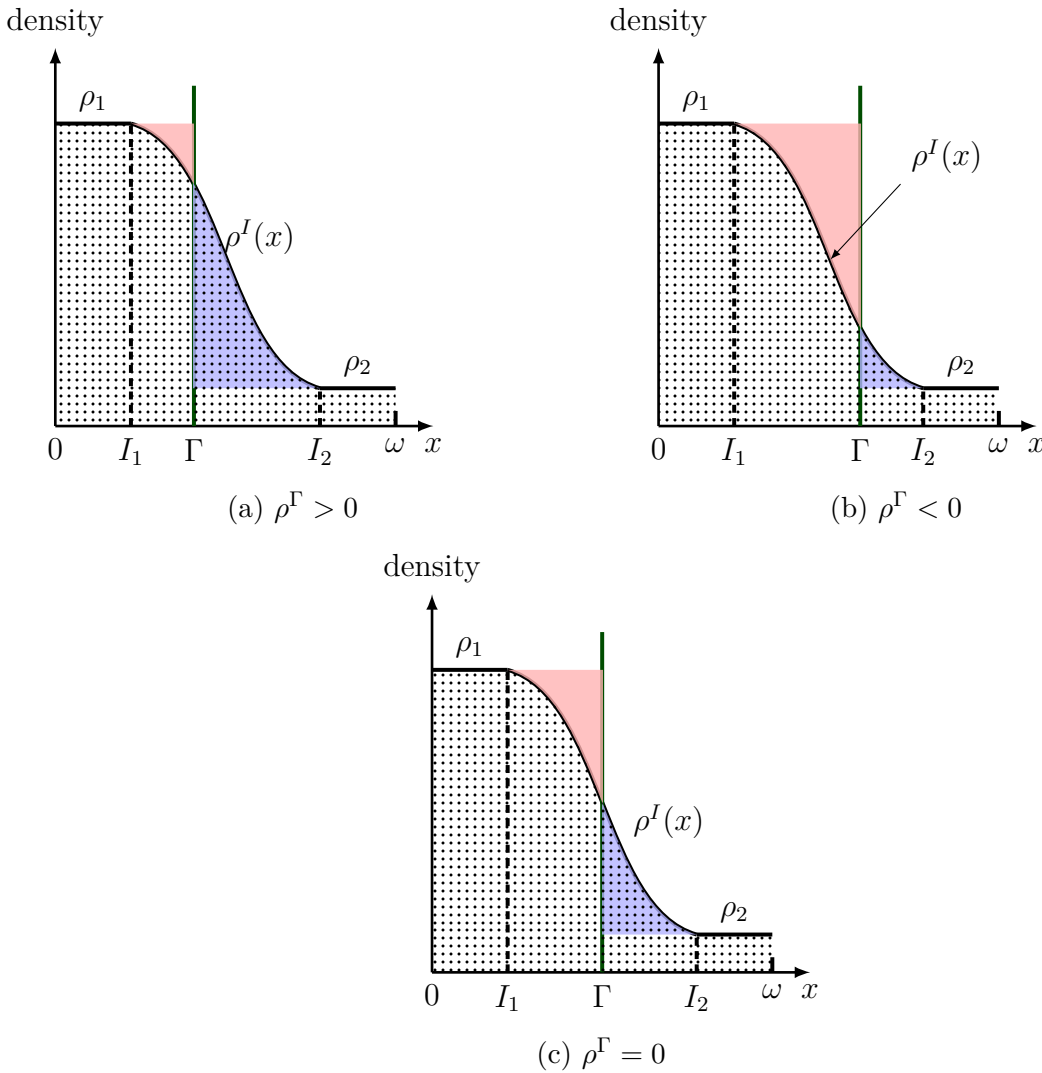


Figure 2.3.: The value of ρ^Γ depends on the position of the sharp interface Γ .

The position of $\Gamma(t_0)$. We follow the usual practice to take the position of $\Gamma(t_0)$ such that $\rho^\Gamma(\mathbf{x}) = 0$ for $\mathbf{x} \in \Gamma(t_0)$.

In the three dimensional case, the sharp interface is treated as a two dimensional surface, the exact definition of which will be introduced afterwards. We only make a remark here

about the nature of ρ^Γ . We rewrite the expression of total mass \mathcal{M}_I in equation (2.10) with $\rho = \rho_i$ for $\mathbf{x} \in \omega_i(t_0)$ with $i = 1, 2$:

$$\mathcal{M}_I = \int_{\omega(t_0)} \rho \, dx + \int_{I(t_0)} (\rho^I - \rho) \, dx, \quad (2.12)$$

where $(\rho^I - \rho)$ is the difference shown in Figure 2.3. Comparing equation (2.12) with equation (2.11) and note that $\mathcal{M}_I = \mathcal{M}_\Gamma$, we conclude that

$$\int_{\Gamma(t_0)} \rho^\Gamma \, ds = \int_{I(t_0)} (\rho^I - \rho) \, dx. \quad (2.13)$$

We derive a point-wise evaluation of $\rho^\Gamma(\mathbf{x})$ from equation (2.13). For this purpose, we assume that the sharp interface $\Gamma(t_0)$ is smooth, and we introduce two surfaces Γ_1 and Γ_2 , which are “parallel” to $\Gamma(t_0)$, i.e. the points on Γ_1 and Γ_2 have constant distances $|d_1|$ and $|d_2|$ respectively along the normal directions $\mathbf{n}(\mathbf{x})$ for $\mathbf{x} \in \Gamma(t_0)$, cf. Figure 2.2. We use $I^*(t_0)$ to denote the volume bounded by Γ_1 and Γ_2 . The signed distances d_1 and d_2 are chosen such that the interfacial region $I(t_0)$ is contained in $I^*(t_0)$. We approximate the volume integral in equation (2.13) by

$$\int_{I(t_0)} (\rho^I - \rho) \, dx \approx \int_{I^*(t_0)} (\rho^I - \rho) \, dx, \quad (2.14)$$

where we set $\rho^I = \rho$ when $\mathbf{x} \notin I(t_0)$. For the volume integral over $I^*(t_0)$ the following holds [80] (p.57)

$$\int_{I^*(t_0)} (\rho^I - \rho) \, dx = \int_{\Gamma(t_0)} \int_{d_2}^{d_1} (\rho^I - \rho)(1 - \kappa_1 d)(1 - \kappa_2 d) \, d\lambda ds, \quad (2.15)$$

where d is the signed distance along the normal $\mathbf{n}(\mathbf{x})$ of $\mathbf{x} \in \Gamma(t_0)$, κ_1 and κ_2 are the principal curvatures of $\Gamma(t_0)$. d_1 and d_2 can be assumed to be very small, thus $|\kappa_i d| \ll 1$ for $d \in [d_2, d_1]$. Considering equation (2.13), (2.14) and (2.15), we approximate $\rho^\Gamma(\mathbf{x})$ by

$$\rho^\Gamma(\mathbf{x}) \approx \int_{d_2}^{d_1} (\rho^I - \rho) \, d\lambda,$$

which can be interpreted as an excess quantity in the normal direction of $\Gamma(t_0)$, cf. one dimensional case in Remark 2.3.1. As in 1D case we can take a sharp interface position such that $\int_{d_2}^{d_1} (\rho^I - \rho) \, d\lambda = 0$. Hence we obtain the initial position $\Gamma(t_0)$.

2.3.2. Interface motion

Before introducing the motion of $\Gamma(t)$, we describe the properties of $\Gamma(t)$. We assume that $\Gamma(t)$ is the boundary of an open bounded subset $\Omega_1(t) \subset \mathbb{R}^d$, $\Gamma(t)$ is connected and compact. At time t , we assume that $\Gamma(t) \subset \mathbb{R}^d$ is an oriented C^2 -hypersurface. The definition of a C^2 -hypersurface is as follows: for each point $\mathbf{x}_0 \in \Gamma(t)$, there is an open subset $W \subset \mathbb{R}^d$ containing \mathbf{x}_0 and a C^2 -function $f : W \rightarrow \mathbb{R}$ such that

- (1) $\Gamma(t) \cap W = \{\mathbf{x} \in W \mid f(\mathbf{x}) = 0\}$;
- (2) $\nabla f(\mathbf{x}) \neq 0$ for all $\mathbf{x} \in W \cap \Gamma(t)$.

2. A sharp interface model for two-phase flows

At $\mathbf{x}_0 \in \Gamma(t)$, the tangent space $T_{\mathbf{x}_0}\Gamma(t)$ is the vector subspace of \mathbb{R}^d with the dimension $d-1$ and is orthogonal to $\nabla f(\mathbf{x}_0)$. An oriented surface is a surface together with a smooth choice of unit normals \mathbf{n} at each point, i.e., a continuous vector function $\mathbf{n}: \Gamma(t) \rightarrow \mathbb{R}^d$ such that, for any point $\mathbf{x}_0 \in \Gamma(t)$, $\mathbf{n}(\mathbf{x}_0)$ is a unit vector orthogonal to $T_{\mathbf{x}_0}\Gamma(t)$.

We define the *tangential gradient* of a C^1 -function $f: W \rightarrow \mathbb{R}$ by

$$\nabla_{\Gamma} f(\mathbf{x}) := (\mathbf{I} - \mathbf{n}(\mathbf{x})\mathbf{n}(\mathbf{x})^T)\nabla f(\mathbf{x}) =: \mathbf{P}(\mathbf{x})\nabla f(\mathbf{x}), \quad \mathbf{x} \in \Gamma(t), \quad (2.16)$$

where $\mathbf{P}(\mathbf{x}) := \mathbf{I} - \mathbf{n}(\mathbf{x})\mathbf{n}(\mathbf{x})^T$ is the orthogonal projection from \mathbb{R}^d onto $T_{\mathbf{x}_0}\Gamma(t)$.

For $t \in [t_0, T]$, we assume that the evolution of $\Gamma(t)$ is sufficiently smooth, in the sense that for each point $(\mathbf{x}_0, t) \in \Gamma(t)$, there exists an open subset $W \subset \mathbb{R}^d$ containing \mathbf{x}_0 , $\epsilon > 0$ and a $C^{2,1}$ -function $f: W \times (t - \epsilon, t + \epsilon) \rightarrow \mathbb{R}$ (C^2 in space and C^1 in time) such that:

- (1) $\Gamma(t) \cap W = \{\mathbf{x} \in W \mid f(\mathbf{x}, t) = 0\}$;
- (2) $\nabla f(\mathbf{x}, t) \neq 0$ for all $\mathbf{x} \in W \cap \Gamma(t)$.

$\Gamma(t)$ is transported by a C^1 velocity field $\mathbf{u}_{\Gamma}(\mathbf{x}, t)$. The evolution of $\Gamma(t)$ that fulfills the above conditions is denoted by

$$\Gamma_T := \bigcup_{t_0 < t < T} \Gamma(t) \times \{t\}. \quad (2.17)$$

Velocity field \mathbf{u}_{Γ} for immiscible two-phase flow problems. For $\mathbf{x} \in \Gamma(t)$, we decompose the velocity field $\mathbf{u}_{\Gamma}(\mathbf{x}, t)$ as $\mathbf{u}_{\Gamma} = (\mathbf{u}_{\Gamma} \cdot \mathbf{n})\mathbf{n} + \mathbf{P}\mathbf{u}_{\Gamma}$. From now on, we use $V_{\Gamma} := \mathbf{u}_{\Gamma} \cdot \mathbf{n}$ to denote the normal velocity of $\Gamma(t)$. For a two-phase flow problem, the velocity field that transports the bulk fluid is denoted by \mathbf{u} . The *immiscibility* assumption of a two-phase flow problem requires that

$$V_{\Gamma} = \mathbf{u} \cdot \mathbf{n}, \quad (2.18)$$

which means that the interface $\Gamma(t)$ is transported with the same velocity as the bulk fluids, and *no* phase change occurs at $\Gamma(t)$. Due to the viscosities of the fluids, it is generally accepted that the jump of the tangential velocity across the sharp interface is *zero*. We use brackets to denote the jump across the interface. The condition on the tangential velocity of \mathbf{u} is $[\mathbf{P}\mathbf{u}]_{\Gamma} = 0$.

Thus we obtain

$$\mathbf{P}\mathbf{u}_{\Gamma}(\mathbf{x}) = \mathbf{P}\mathbf{u}(\mathbf{x}) \quad \text{for } \mathbf{x} \in \Gamma(t). \quad (2.19)$$

From conditions (2.18) and (2.19), we conclude that $\mathbf{u}_{\Gamma}(\mathbf{x}) = \mathbf{u}(\mathbf{x})$ for $\mathbf{x} \in \Gamma(t)$ holds for immiscible two-phase flow problems.

The position of $\Gamma(t)$. At time $t = t_0$, the choice of the position of $\Gamma(t_0)$ is explained in the previous section. For $t > t_0$, the interface is then transported by the velocity field \mathbf{u} , i.e. for a material particle σ that occupies $\mathbf{x}_0 \in \Gamma(t_0)$, $\mathbf{X}_{\sigma}(t) \in \Gamma(t)$ and $\frac{d}{dt}\mathbf{X}_{\sigma}(t) = \mathbf{u}(\mathbf{X}_{\sigma}(t), t)$ hold for all $t \in [t_0, T]$. We use the level set equation (3.2) to track the position of $\Gamma(t)$.

2.4. Mass and momentum conservation for a two-phase body

We adopt the sharp interface model for a two-phase material body. Hence, in each phase we assume that the mass conservation condition (2.6) and the momentum conservation condition (2.8) hold. For the effect of the sharp interface, we derive conditions on the interface, i.e. for the interfacial excess quantities.

First we introduce the *Reynolds transport theorem* for an evolving *sharp interface*.

Reynolds transport theorem for a moving interface. We consider a sharp interface $\Gamma(t)$ satisfying the conditions from the previous section and a function $\mathbf{f} := \mathbf{f}(\mathbf{x}, t)$, which is a $C^{1,1}$ -function (C^1 in both \mathbf{x} and t) in a neighborhood of Γ_T (cf. definition (2.17)). The Reynolds transport theorem holds for \mathbf{f} :

$$\frac{d}{dt} \int_{\Gamma(t)} \mathbf{f} \, ds = \int_{\Gamma(t)} \dot{\mathbf{f}} + \mathbf{f} \operatorname{div}_{\Gamma} \mathbf{u} \, ds, \quad (2.20)$$

where $\dot{\mathbf{f}}$ is the material derivative defined in (2.2), $\operatorname{div}_{\Gamma} \mathbf{u}$ is the *tangential divergence* of \mathbf{u} and is defined as $\operatorname{div}_{\Gamma} \mathbf{u} := \operatorname{tr}(\nabla_{\Gamma} \mathbf{u}) = \operatorname{tr}(\mathbf{P} \nabla \mathbf{u})$. A proof of (2.20) can be found in [14, 25].

The Reynolds transport theorem (2.20) also holds for an open subset $\gamma(t) \subset \Gamma(t)$ with a boundary $\partial\gamma(t)$, and *no additional* boundary terms occur, cf. [14, 25] and Figure 2.4.

Conservation of mass for a two-phase body. Without reaction processes in the bulk phases or at the interface, the law of mass conservation states that the total mass of the control volume $\omega(t)$ should be invariant w.r.t time, which means $\frac{d}{dt} \mathcal{M}_{\Gamma} = 0$. From equation (2.11), we obtain

$$\frac{d}{dt} \mathcal{M}_{\Gamma} = \frac{d}{dt} \left(\int_{\omega(t)} \rho \, dx + \int_{\gamma(t)} \rho^{\Gamma} \, ds \right) = 0. \quad (2.21)$$

Applying Reynolds transport theorem (2.3) and (2.20) to equation (2.21), we obtain

$$\sum_{i=1}^2 \int_{\omega_i(t)} (\dot{\rho} + \rho \operatorname{div} \mathbf{u}) \, dx + \int_{\gamma(t)} (\dot{\rho}^{\Gamma} + \rho^{\Gamma} \operatorname{div}_{\Gamma} \mathbf{u}) \, ds = 0. \quad (2.22)$$

Applying the mass conservation property (2.6) in both bulk phases, we can eliminate the volume integral terms and the remaining term is

$$\int_{\gamma(t)} (\dot{\rho}^{\Gamma} + \rho^{\Gamma} \operatorname{div}_{\Gamma} \mathbf{u}) \, ds = 0. \quad (2.23)$$

$\gamma(t)$ is arbitrary. Hence the following holds for the excess mass density ρ^{Γ} ,

$$\dot{\rho}^{\Gamma} + \rho^{\Gamma} \operatorname{div}_{\Gamma} \mathbf{u} = 0 \quad \text{on} \quad \Gamma(t), \quad (2.24)$$

with initial conditions $\rho^{\Gamma}(\mathbf{x}, t_0) = 0$ for $\mathbf{x} \in \Gamma(t_0)$. This is a linear ordinary differential equation on the trajectory of a material particle σ , which starts at $\mathbf{x}_0 \in \Gamma(t_0)$. Assuming that $\operatorname{div}_{\Gamma} \mathbf{u}$ is bounded, the solution of (2.24) is $\rho^{\Gamma}(\mathbf{x}, t) \equiv 0$ for $\mathbf{x} \in \Gamma(t)$.

2. A sharp interface model for two-phase flows

Remark 2.4.1. For incompressible flows, the condition $\operatorname{div} \mathbf{u} = 0$ holds. However, the term $\operatorname{div}_\Gamma \mathbf{u}$ is generally not zero, and accounts for the compressibility of the interface, e.g., different material bodies with the same volume can have different total surface areas.

Conservation of momentum for a two-phase body. We illustrate the two-phase control volume in Figure 2.4. We define the normal field on $\Gamma(t)$ pointing from $\Omega_1(t)$ to $\Omega_2(t)$ as \mathbf{n} . The control volume $\omega(t)$ contains an open subset $\gamma(t) \subset \Gamma(t)$, the boundary of which is denoted by $\partial\gamma(t)$. In three dimensional case, $\partial\gamma(t)$ is a closed curve on $\Gamma(t)$. For each point $\mathbf{x} \in \partial\gamma(t)$, we define the normal vector $\boldsymbol{\xi}(\mathbf{x})$, which is normal to $\partial\gamma(t)$ and belongs to the tangent plane $T_{\mathbf{x}}\Gamma(t)$, i.e., $\boldsymbol{\xi}$ is orthogonal to the surface normal \mathbf{n} .

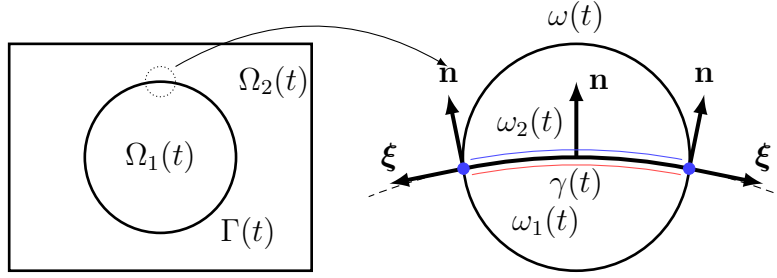


Figure 2.4.: A two-phase control volume $\omega(t)$ containing a sharp interface $\gamma(t)$.

Besides the volume force $(F_g)_i$ and the contact force $(F_\gamma)_i$ in the bulk phases $\omega_i(t)$, $i = 1, 2$, there exists an interface force on $\gamma(t)$, which accounts for the different molecular cohesive forces from both sides of $\gamma(t)$. This force is called *surface tension*, and the physical unit is N/m . The force vector is on the tangent plane of $\Gamma(t)$. The sum of this surface forces on the control volume is then

$$F_{\partial\gamma} := \int_{\partial\gamma(t)} \mathbf{t} \, dl,$$

with \mathbf{t} the surface force vector (unit: N/m). $\mathbf{t}(\mathbf{x})$ for $\mathbf{x} \in \Gamma(t)$ is in the tangent plane $\mathbf{t} \in T_{\mathbf{x}}\Gamma(t)$, thus it has to satisfy the following two conditions:

- (1) $\mathbf{t}^T \mathbf{n} = 0$,
- (2) $\mathbf{P} \mathbf{t} = \mathbf{t}$.

Similar to the Cauchy stress tensor $\boldsymbol{\sigma}$ in bulk phases, we can define a *surface stress tensor* $\boldsymbol{\sigma}_\Gamma : T_{\mathbf{x}}\Gamma(t) \rightarrow T_{\mathbf{x}}\Gamma(t)$ such that $\mathbf{t} = \boldsymbol{\sigma}_\Gamma \boldsymbol{\xi}$. The following holds for $\boldsymbol{\sigma}_\Gamma$

$$\boldsymbol{\sigma}_\Gamma = \mathbf{P} \boldsymbol{\sigma}_\Gamma \mathbf{P}. \quad (2.25)$$

Note that \mathbf{P} is symmetric, the condition (1) is easily shown to be valid since $\mathbf{t}^T \mathbf{n} = (\boldsymbol{\sigma}_\Gamma \boldsymbol{\xi})^T \mathbf{n} = (\mathbf{P} \boldsymbol{\sigma}_\Gamma \mathbf{P} \boldsymbol{\xi})^T \mathbf{n} = (\boldsymbol{\sigma}_\Gamma \boldsymbol{\xi})^T (\mathbf{P} \mathbf{n}) = 0$. Condition (2) is also valid since $\mathbf{P} \mathbf{t} = \mathbf{P} \boldsymbol{\sigma}_\Gamma \boldsymbol{\xi} = \mathbf{P} \boldsymbol{\sigma}_\Gamma \mathbf{P} \boldsymbol{\xi} = \boldsymbol{\sigma}_\Gamma \boldsymbol{\xi} = \mathbf{t}$. The kernel of $\boldsymbol{\sigma}_\Gamma$ contains the one dimensional subspace $\{\mathbf{x} : \mathbf{x} = \alpha \mathbf{n}, \alpha \in \mathbb{R}\}$. Hence the rank of $\boldsymbol{\sigma}_\Gamma$ is less than or equals to 2.

With the introduction of the surface stress tensor $\boldsymbol{\sigma}_\Gamma$, we can formulate the conservation of momentum according to Newton's second law of motion for a two-phase body with a sharp interface:

$$\frac{d}{dt} \left(\int_{\omega(t)} \rho \mathbf{u} \, dx + \int_{\gamma(t)} \rho^\Gamma \mathbf{u} \, ds \right) = \sum_{i=1}^2 ((F_g)_i + (\hat{F}_\gamma)_i) + F_{\partial\gamma},$$

2.4. Mass and momentum conservation for a two-phase body

where $(F_g)_i := \int_{\omega_i(t)} \rho \mathbf{g} dx$, and $(\hat{F}_\gamma)_i := \int_{\partial\omega_i(t) \cap \partial\omega(t)} \boldsymbol{\sigma} \mathbf{n}_{\partial\omega_i} ds$, which is the sum of contact forces from *outside* acting on $\partial\omega(t)$. $\mathbf{n}_{\partial\omega_i}$ denotes the outward pointing normals on $\partial\omega_i(t)$. The surface normal \mathbf{n} on $\gamma(t)$ is pointing from $\omega_1(t)$ to $\omega_2(t)$, thus we obtain $\mathbf{n}_{\partial\omega_1}(\mathbf{x}) = -\mathbf{n}_{\partial\omega_2}(\mathbf{x}) = \mathbf{n}(\mathbf{x})$ for $\mathbf{x} \in \gamma(t)$.

Due to $\rho^\Gamma \equiv 0$, the second term on the left hand equals zero. Hence we obtain

$$\sum_{i=1}^2 \frac{d}{dt} \int_{\omega_i(t)} \rho \mathbf{u} dx = \sum_{i=1}^2 \left(\int_{\omega_i(t)} \rho \mathbf{g} dx + \int_{\partial\omega_i(t)} \boldsymbol{\sigma} \mathbf{n} ds \right) - \int_{\gamma(t)} [\boldsymbol{\sigma} \mathbf{n}]_\Gamma ds + \int_{\partial\gamma(t)} \boldsymbol{\sigma}_\Gamma \boldsymbol{\xi} dl. \quad (2.26)$$

The jump term $\int_{\gamma(t)} [\boldsymbol{\sigma} \mathbf{n}]_\Gamma ds$ is due to the missing boundaries between $\partial\omega_i(t)$ and $\partial\omega_i(t) \cap \partial\omega(t)$, cf. blue and red lines in Figure 2.4. For both bulk phases, the momentum conservation relation (2.8) holds. Hence the remaining terms are

$$\int_{\gamma(t)} [\boldsymbol{\sigma} \mathbf{n}]_\Gamma ds = \int_{\partial\gamma(t)} \boldsymbol{\sigma}_\Gamma \boldsymbol{\xi} dl. \quad (2.27)$$

We apply the surface divergence theorem (A.7) to the right hand side:

$$\int_{\partial\gamma(t)} \boldsymbol{\sigma}_\Gamma \boldsymbol{\xi} dl = \int_{\gamma(t)} \operatorname{div}_\Gamma \boldsymbol{\sigma}_\Gamma ds - \int_{\gamma(t)} \kappa \boldsymbol{\sigma}_\Gamma \mathbf{n} ds.$$

\mathbf{n} is in the kernel of $\boldsymbol{\sigma}_\Gamma$, therefore the second term on the right hand side equals zero. We obtain the momentum balance condition for a sharp interface model:

$$[\boldsymbol{\sigma} \mathbf{n}]_\Gamma = \operatorname{div}_\Gamma \boldsymbol{\sigma}_\Gamma \quad \text{on} \quad \Gamma(t). \quad (2.28)$$

Remark 2.4.2. *By choosing different constitutive equations for $\boldsymbol{\sigma}_\Gamma$, various fluidic interfacial phenomena can be modeled, cf. section 2.6. We take a simple example here, which is the static capillary pressure of a droplet governed by the Young-Laplace equation. For the surface stress tensor $\boldsymbol{\sigma}_\Gamma$, we take the clean interface model $\boldsymbol{\sigma}_\Gamma = \tau \mathbf{P}$, cf. equation (2.34). We consider a static droplet floating in a bulk fluid. Figure 2.4 illustrates the two-phase system and a control volume $\omega(t)$. For simplicity, we drop the time dependence and write ω and γ . For the bulk phase Cauchy stress tensor, we take (2.32) for incompressible Newtonian fluids. The two-phase system is at rest, thus $\mathbf{u} = 0$ and $\mathbf{D}(\mathbf{u}) = 0$ (definition in section 2.6). The jump term $[\boldsymbol{\sigma} \mathbf{n}]_\Gamma$ is then given by*

$$[\boldsymbol{\sigma} \mathbf{n}]_\Gamma = \boldsymbol{\sigma}_1 \mathbf{n} - \boldsymbol{\sigma}_2 \mathbf{n} = (-p_1 \mathbf{n}) - (-p_2 \mathbf{n}) = -(p_1 - p_2) \mathbf{n}.$$

From equation (2.35), the term $\operatorname{div}_\Gamma \boldsymbol{\sigma}_\Gamma = \operatorname{div}_\Gamma(\tau \mathbf{P})$ is given by

$$\operatorname{div}_\Gamma(\tau \mathbf{P}) = \tau \operatorname{div}_\Gamma \mathbf{P} = -\tau \kappa \mathbf{n},$$

where κ is the mean curvature. Hence equation (2.28) leads to

$$-(p_1 - p_2) \mathbf{n} = -\tau \kappa \mathbf{n} \iff p_1 - p_2 = \tau \kappa,$$

which is the Young-Laplace equation for the static capillary pressure. For the control volume ω in Figure 2.4, the mean curvature κ is positive, thus $p_1 > p_2$.

2. A sharp interface model for two-phase flows

From the force balance point of view, on γ the surface force balances the pressure difference for a static droplet, i.e.

$$\int_{\gamma} (-\tau \kappa \mathbf{n}) ds + \int_{\gamma} (p_1 - p_2) \mathbf{n} ds = - \int_{\gamma} (p_1 - p_2) \mathbf{n} ds + \int_{\gamma} (p_1 - p_2) \mathbf{n} ds = 0.$$

For other complex surface force models, the same principle holds: the surface force acts on γ to balance the momentum. In section 2.8 we introduce our “one fluid” model for two-phase flows, in which the surface force enters into the momentum equation.

2.5. Surfactant transport on the interface

In this thesis, we also treat a surface transport problem, namely the *surfactant* transport problem. Surfactant is the abbreviation of *surface active agents*, which are chemicals that adsorbed at the fluid-fluid interface and *lower* the surface tension coefficient τ . Surfactants are widely used in industry and daily life as detergents, foaming agents and emulsifiers [74].

The dynamics of surfactants in fluids includes the adsorption process from the bulk fluids to the interface, the transport of surfactant on the fluid interface and the desorption process from the interface to the bulk fluids. In this thesis, we only treat *the transport of surfactant on the fluid interface* and neglect adsorption and desorption processes, i.e., the surfactants are assumed to exist **only** on $\Gamma(t)$ and **stay** there.

To model the surfactant transport problem, we consider the conservation of a concentration field $S(\mathbf{x}, t)$ for $\mathbf{x} \in \Gamma(t)$. At the initial time $t = t_0$, $S(\mathbf{x}, t_0)$ is given. We consider a connected bounded subset of $\Gamma(t_0)$, which is denoted by γ_0 , and apply the conservation of mass principle on $\gamma(t) := \{\mathbf{X}_{\sigma}(t) : \mathbf{X}_{\sigma}(0) = \mathbf{x}_0 \in \gamma_0\} \subset \Gamma(t)$ for the quantity S with $t \in (t_0 - \epsilon, t_0 + \epsilon)$ and $\epsilon > 0$ sufficiently small:

$$\frac{d}{dt} \int_{\gamma(t)} S ds + \int_{\partial\gamma(t)} \mathbf{J} \cdot \boldsymbol{\xi} dl = 0, \quad (2.29)$$

where \mathbf{J} denotes the flux of S on the boundary of $\gamma(t)$, and $\boldsymbol{\xi}$ is the outward pointing normal to $\partial\gamma(t)$ on $T_{\mathbf{x}}\Gamma(t)$, c.f. Figure 2.4.

We restrict ourselves to the *diffusive flux* on $\partial\gamma(t)$ modeled by Fick’s law, i.e. $\mathbf{J} = -D_{\Gamma} \nabla_{\Gamma} S$ with a surface diffusion coefficient D_{Γ} . Applying the surface divergence theorem (A.7) to the flux term and note that $\mathbf{Jn} = 0$, we obtain $\int_{\partial\gamma(t)} \mathbf{J} \cdot \boldsymbol{\xi} dl = \int_{\gamma(t)} \operatorname{div}_{\Gamma} \mathbf{J} ds$. Inserting this into equation (2.29) and applying the surface Reynolds transport theorem, equation (2.29) becomes

$$\int_{\gamma(t)} \dot{S} + S \operatorname{div}_{\Gamma} \mathbf{u} + \operatorname{div}_{\Gamma} (-D_{\Gamma} \nabla_{\Gamma} S) ds = 0. \quad (2.30)$$

We assume that D_{Γ} has a constant value on $\Gamma(t)$, and define $\Delta_{\Gamma} S := \operatorname{div}_{\Gamma} \nabla_{\Gamma} S$. Since $\gamma(t)$ is arbitrary, we obtain the following model for surfactant transport problem:

$$\frac{\partial S}{\partial t} + (\mathbf{u} \cdot \nabla) S + S \operatorname{div}_{\Gamma} \mathbf{u} = D_{\Gamma} \Delta_{\Gamma} S \quad \text{on } \Gamma(t). \quad (2.31)$$

2.6. Constitutive relations

After introducing the momentum balance for bulk phases in (2.9) and for interfaces in (2.28), we now introduce proper models for $\boldsymbol{\sigma}$ and $\boldsymbol{\sigma}_\Gamma$, which are called *constitutive relations*.

As we have mentioned in the previous section, surfactant on $\Gamma(t)$ *lower* the surface tension coefficient τ . Hence we will also introduce constitutive relations between S and τ .

2.6.1. Bulk stress tensor

For an *incompressible Newtonian* fluid, the Cauchy stress tensor takes the form

$$\boldsymbol{\sigma} = -p\mathbf{I} + \mu\mathbf{D}(\mathbf{u}), \quad (2.32)$$

where p is the pressure, \mathbf{I} is the identity operator in \mathbb{R}^3 , μ is the dynamic viscosity and $\mathbf{D}(\mathbf{u}) = \nabla\mathbf{u} + (\nabla\mathbf{u})^T$ is the rate of strain tensor. Inserting $\boldsymbol{\sigma}$ into (2.9), we obtain

$$\rho \left(\frac{\partial\mathbf{u}}{\partial t} + (\mathbf{u} \cdot \nabla)\mathbf{u} \right) = -\nabla p + \operatorname{div}(\mu\mathbf{D}(\mathbf{u})) + \rho\mathbf{g} \quad \text{in } \Omega(t). \quad (2.33)$$

We further assume that μ is constant within the bulk phase. Together with the incompressible condition $\operatorname{div}\mathbf{u} = 0$, we obtain

$$\rho \left(\frac{\partial\mathbf{u}}{\partial t} + (\mathbf{u} \cdot \nabla)\mathbf{u} \right) = -\nabla p + \mu\Delta\mathbf{u} + \rho\mathbf{g} \quad \text{in } \Omega(t).$$

Equation (2.33) together with equation (2.7) are called the *Navier-Stokes* equations for incompressible Newtonian flows.

Remark 2.6.1. *In this thesis, we use the formulation in (2.33) for incompressible two-phase flows with constant viscosities. This formulation is needed for incorporating interface force in the momentum equation of our “one fluid” model for two-phase flows, which will be introduced in section 2.8.*

2.6.2. Interface stress tensor

We discuss here three models for $\boldsymbol{\sigma}_\Gamma$: the clean interface model, the variable surface tension model and the viscous interface model. The first two models consider only surface tension effects, and the last one also incorporates surface viscous effects.

In the **clean interface** model and **variable surface tension** model the surface stress tensor $\boldsymbol{\sigma}_\Gamma$ takes the form:

$$\boldsymbol{\sigma}_\Gamma = \tau\mathbf{P}. \quad (2.34)$$

The difference between the above mentioned models is whether the surface tension coefficient τ has a constant value. For the clean interface model, τ is constant on $\Gamma(t)$; for the variable surface tension model, τ depends on other quantities, e.g. temperature or

2. A sharp interface model for two-phase flows

chemical compositions on $\Gamma(t)$. For the **clean interface** model, the momentum balance condition (2.28) becomes

$$[\boldsymbol{\sigma}\mathbf{n}]_{\Gamma} = \operatorname{div}_{\Gamma}(\tau\mathbf{P}) = \tau \operatorname{div}_{\Gamma} \mathbf{P} = -\tau\kappa\mathbf{n} \quad \text{on } \Gamma(t), \quad (2.35)$$

where κ is the mean curvature, cf. (A.4).

For the **variable surface tension** model, we have one more term:

$$[\boldsymbol{\sigma}\mathbf{n}]_{\Gamma} = \operatorname{div}_{\Gamma}(\tau\mathbf{P}) = -\tau\kappa\mathbf{n} + \nabla_{\Gamma}\tau \quad \text{on } \Gamma(t), \quad (2.36)$$

where $\nabla_{\Gamma}\tau \in T_{\mathbf{x}}\Gamma(t)$ is an additional stress term due to surface tension gradient and is responsible for the so-called *Marangoni effects*, cf. (A.4).

Remark 2.6.2. *The constitutive relation (2.34) for $\boldsymbol{\sigma}_{\Gamma}$ resembles the pressure part of $\boldsymbol{\sigma}$ in (2.32). \mathbf{P} is the identity operator on $\Gamma(t)$, i.e. $\mathbf{P}\mathbf{x} = \mathbf{x}$ for $\mathbf{x} \in \Gamma(t)$.*

The **viscous interface** model also incorporates surface viscous effect. We use the *Boussinesq-Scriven* constitutive law. The surface stress tensor then takes the form [80]:

$$\boldsymbol{\sigma}_{\Gamma} = [\tau + (\lambda_{\Gamma} - \mu_{\Gamma}) \operatorname{div}_{\Gamma} \mathbf{u}] \mathbf{P} + \mu_{\Gamma} \mathbf{D}_{\Gamma}(\mathbf{u}), \quad (2.37)$$

where λ_{Γ} is the surface dilatational viscosity coefficient, μ_{Γ} is the surface shear viscosity coefficient, and $\mathbf{D}_{\Gamma}(\mathbf{u}) := \mathbf{P} \left(\nabla_{\Gamma} \mathbf{u} + (\nabla_{\Gamma} \mathbf{u})^T \right) \mathbf{P}$ is the surface rate of strain tensor. λ_{Γ} and μ_{Γ} have to satisfy the condition: $\lambda_{\Gamma} \geq \mu_{\Gamma} \geq 0$.

Remark 2.6.3. *$\boldsymbol{\sigma}_{\Gamma}$ from the viscous interface model resembles the bulk phase stress tensor $\boldsymbol{\sigma}$. For a general Newtonian fluid, the stress tensor $\boldsymbol{\sigma}$ takes the form [8]:*

$$\boldsymbol{\sigma} = -[p + \left(\frac{2}{3}\mu - \lambda\right) \operatorname{div} \mathbf{u}] \mathbf{I} + \mu \mathbf{D}(\mathbf{u})$$

The negative sign in front of p is due to the consideration that the (hydrostatic) pressure is acting towards the control volume, and the positive sign in front of τ comes from the fact that the surface tension is a line tension that expands the surface area.

2.6.3. Variable surface tension coefficient

The existence of surfactants on $\Gamma(t)$ or variations of temperature changes the surface tension coefficient τ [22]. Constitutive relations are used to relate τ and S or T .

For the existence of surfactants, the simplest one is the **linear** relation, which takes the form

$$\tau = \tau(S) = \tau_0 - SRT, \quad (2.38)$$

where τ_0 is the surface tension coefficient corresponding to a surfactant free interface (clean interface), R is the gas constant, and T is the absolute temperature. For dilute surfactant concentrations and small perturbations around equilibrium, such a linear relation is a good approximation of the nonlinear dependence of τ on S and often used in theoretical analysis due to its simplicity [82], [89].

Another very popular relation is the **Langmuir** adsorption model. We consider a version of this model, which is derived in [39]:

$$\tau(S) = \tau_0 + RTS_\infty \ln\left(1 - \frac{S}{S_\infty}\right), \quad (2.39)$$

where S_∞ is the maximal surface concentration. Note that this relation is nonlinear in S .

For the variation of temperature, we only mention one simple linear relation between τ and T , which takes the form [53, 41, 91]

$$\tau(T) = \tau_0 + \sigma_T(T - T_0), \quad (2.40)$$

where τ_0 corresponds to the surface tension coefficient at a reference temperature T_0 , and σ_T is the thermal surface tension coefficient. σ_T is determined by

$$\sigma_T = \frac{d\tau}{dT}.$$

For most fluids σ_T is a *negative* constant.

2.7. Summary of equations

We summarize the equations of the sharp interface model for two-phase flow problems. We consider a fixed domain $\Omega \subset \mathbb{R}^3$ containing two different immiscible incompressible phases. The two subdomains containing the two phases are denoted by $\Omega_1(t)$ and $\Omega_2(t)$ with $\bar{\Omega} = \bar{\Omega}_1(t) \cup \bar{\Omega}_2(t)$ and $\Omega_1(t) \cap \Omega_2(t) = \emptyset$. $\Omega_1(t)$ represents the droplet phase, and $\Omega_2(t)$ represents the continuous phase. Both of them are considered to be connected, and the droplet will not touch the outer boundary, i.e. $\partial\Omega_1(t) \cap \partial\Omega = \emptyset$. The interface between them is denoted by $\Gamma(t) := \bar{\Omega}_1(t) \cap \bar{\Omega}_2(t)$. An illustration of the domains is given in Figure 2.4. The time interval is $[t_0, T]$.

For incompressible Newtonian fluids with a sharp interface, the standard two-phase model takes the form:

$$\rho_i \left(\frac{\partial \mathbf{u}}{\partial t} + (\mathbf{u} \cdot \nabla) \mathbf{u} \right) = -\nabla p + \operatorname{div}(\mu_i \mathbf{D}(\mathbf{u})) + \rho \mathbf{g} \quad \text{in } \Omega_i(t), \quad (2.41a)$$

$$\operatorname{div} \mathbf{u} = 0 \quad \text{in } \Omega_i(t), \quad (2.41b)$$

$$[\mathbf{u}]_\Gamma = 0 \quad \text{on } \Gamma(t), \quad (2.41c)$$

$$V_\Gamma = \mathbf{u} \cdot \mathbf{n} \quad \text{on } \Gamma(t), \quad (2.41d)$$

$$[\boldsymbol{\sigma} \mathbf{n}]_\Gamma = \operatorname{div}_\Gamma \boldsymbol{\sigma}_\Gamma \quad \text{on } \Gamma(t). \quad (2.41e)$$

To make the problem well-posed, we still need proper initial and (outer-)boundary conditions, which will be introduced later.

Remark 2.7.1. *The standard two-phase flows model (2.41) is posed for two bulk fluids in two separate domains $\Omega_1(t)$ and $\Omega_2(t)$. The information, i.e. the velocity \mathbf{u} and the pressure p in $\Omega_i(t)$, is exchanged across the interface by imposing interfacial conditions*

2. A sharp interface model for two-phase flows

(2.41c) and (2.41d). In section 2.8 we introduce a “one fluid” formulation for two-phase flows, in which the problem is posed for one fluid with variable physical properties in Ω . The continuity condition for velocity (2.41c) is built into the trial space, and the interfacial force balance condition (2.41e) is incorporated in the momentum equation.

The Cauchy stress tensor $\boldsymbol{\sigma}$ of an incompressible Newtonian fluid is given by

$$\boldsymbol{\sigma} = -p\mathbf{I} + \mu\mathbf{D}(\mathbf{u}).$$

The surface stress tensor $\boldsymbol{\sigma}_\Gamma$ of a clean interface or an interface with variable surface tension is given by

$$\boldsymbol{\sigma}_\Gamma = \tau\mathbf{P}.$$

For a viscous interface, the surface stress tensor according to the Boussinesq-Scriven law is given by

$$\boldsymbol{\sigma}_\Gamma = [\tau + (\lambda_\Gamma - \mu_\Gamma) \operatorname{div}_\Gamma \mathbf{u}]\mathbf{P} + \mu_\Gamma \mathbf{D}_\Gamma(\mathbf{u}).$$

For surfactants transported on $\Gamma(t)$ with a constant diffusion coefficient, the model is

$$\frac{\partial S}{\partial t} + (\mathbf{u} \cdot \nabla)S + S \operatorname{div}_\Gamma \mathbf{u} = D_\Gamma \Delta_\Gamma S \quad \text{on } \Gamma(t). \quad (2.42)$$

The simple linear relation between τ and S takes the form

$$\tau = \tau(S) = \tau_0 - SRT.$$

The Langmuir adsorption model between τ and S takes the form

$$\tau = \tau(S) = \tau_0 + RTS_\infty \ln \left(1 - \frac{S}{S_\infty} \right).$$

The linear relation between τ and T takes the form

$$\tau = \tau(T) = \tau_0 + \sigma_T(T - T_0).$$

2.8. One fluid formulation

In this section we introduce a “one fluid” formulation of the two-phase flow problems (2.41) and the weak formulation. Instead of treating two bulk fluids in two separate domains we consider an (artificial) fluid with piecewise constant physical properties, i.e. density and viscosity, and incorporate the interfacial force balance condition (2.41e) in the momentum equation. The trial space for velocity solutions is *continuous* in the whole domain Ω . The “one fluid” formulation is inspired by the continuum surface force model (CSF model) [15]. The difference is that we do not introduce a continuum volume force term in the neighborhood of the interface, but a *local* surface force term, which acts only at the sharp interface.

We define the density and viscosity function of the artificial fluid as:

$$\rho(\mathbf{x}, t) := \begin{cases} \rho_1 & \text{for } \mathbf{x} \in \Omega_1(t) \\ \rho_2 & \text{for } \mathbf{x} \in \Omega_2(t) \end{cases}, \quad \mu(\mathbf{x}, t) := \begin{cases} \mu_1 & \text{for } \mathbf{x} \in \Omega_1(t) \\ \mu_2 & \text{for } \mathbf{x} \in \Omega_2(t) \end{cases}.$$

A local force term is defined by

$$\mathbf{f}_\Gamma := \operatorname{div}_\Gamma \boldsymbol{\sigma}_\Gamma \delta_\Gamma,$$

where δ_Γ is the Dirac distribution $\delta_\Gamma : C_0^\infty(\Omega) \rightarrow \mathbb{R}$ defined by

$$\langle \delta_\Gamma, \phi \rangle := \int_\Omega \delta_\Gamma \phi \, dx = \int_{\Gamma(t)} \phi \, ds. \quad \text{for all } \phi \in C_0^\infty(\Omega).$$

The interfacial force balance condition (2.41e) is included in the momentum equation, cf. remark 2.4.2. The ‘‘one fluid’’ formulation of two-phase flows is given by

$$\rho \left(\frac{\partial \mathbf{u}}{\partial t} + (\mathbf{u} \cdot \nabla) \mathbf{u} \right) = -\nabla p + \operatorname{div}(\mu \mathbf{D}(\mathbf{u})) + \rho \mathbf{g} + \mathbf{f}_\Gamma \quad \text{in } \Omega \times [t_0, T], \quad (2.43a)$$

$$\operatorname{div} \mathbf{u} = 0 \quad \text{in } \Omega \times [t_0, T], \quad (2.43b)$$

$$V_\Gamma = \mathbf{u} \cdot \mathbf{n} \quad \text{on } \Gamma(t). \quad (2.43c)$$

Remark 2.8.1. *Due to the Dirac distribution δ_Γ , equation (2.43a) is not well-defined in the strong form, but in the sense of distributions. The one fluid formulation (2.43) is consistent with the standard two-phase model (2.41). If the solution of the one fluid model (2.43) is smooth, then it also solves the standard model (2.41), and vice versa, cf. the momentum conservation equation for a sharp interface model (2.26).*

We consider the following boundary conditions: on $\partial\Omega_D$, we apply the Dirichlet boundary condition $\mathbf{u} = \mathbf{u}_D$, and on $\partial\Omega \setminus \partial\Omega_D$, we apply homogeneous natural boundary condition $\boldsymbol{\sigma} \mathbf{n} = 0$, i.e. stress free condition, with the outward pointing normal \mathbf{n} . We use the following spaces for the weak formulation of (2.43):

$$\begin{aligned} \mathbf{V} &:= H^1(\Omega)^3, \\ \mathbf{V}_0 &:= \{\mathbf{v} \in \mathbf{V} : \mathbf{v} = 0 \quad \text{on } \partial\Omega_D\}, \\ \mathbf{V}_D &:= \{\mathbf{v} \in \mathbf{V} : \mathbf{v} = \mathbf{u}_D \quad \text{on } \partial\Omega_D\}, \\ Q &:= \{q \in L^2(\Omega) : \int_\Omega q \, dx = 0\}. \end{aligned}$$

We define the bilinear forms:

$$\begin{aligned} m : \mathbf{V} \times \mathbf{V} &\rightarrow \mathbb{R} : \quad m(\mathbf{u}, \mathbf{v}) := \int_\Omega \rho \mathbf{u} \cdot \mathbf{v} \, dx, \\ a : \mathbf{V} \times \mathbf{V} &\rightarrow \mathbb{R} : \quad a(\mathbf{u}, \mathbf{v}) := \frac{1}{2} \int_\Omega \mu \operatorname{tr}(\mathbf{D}(\mathbf{u}) \mathbf{D}(\mathbf{v})) \, dx, \\ b : \mathbf{V} \times Q &\rightarrow \mathbb{R} : \quad b(\mathbf{v}, q) := - \int_\Omega q \operatorname{div} \mathbf{v} \, dx, \end{aligned}$$

and the trilinear form:

$$c : \mathbf{V} \times \mathbf{V} \times \mathbf{V} \rightarrow \mathbb{R} : \quad c(\mathbf{u}; \mathbf{v}, \mathbf{w}) := \int_\Omega \rho (\mathbf{u} \cdot \nabla) \mathbf{v} \cdot \mathbf{w} \, dx.$$

For the surface force term \mathbf{f}_Γ in (2.43), we introduce the linear functional $f_\Gamma : \mathbf{V} \rightarrow \mathbb{R}$,

$$f_\Gamma(\mathbf{v}) := \int_{\Gamma(t)} (\operatorname{div}_\Gamma \boldsymbol{\sigma}_\Gamma) \cdot \mathbf{v} \, ds. \quad (2.44)$$

For now we assume that $\operatorname{div}_\Gamma \boldsymbol{\sigma}_\Gamma$ is bounded on $\Gamma(t)$, thus $f_\Gamma(\mathbf{v})$ is a bounded linear functional on \mathbf{V} , i.e. $f_\Gamma \in \mathbf{V}'$.

2. A sharp interface model for two-phase flows

Remark 2.8.2. We briefly comment on the surface force functional $f_\Gamma(\mathbf{v})$. For the clean interface model and variable surface tension model the surface stress tensor $\boldsymbol{\sigma}_\Gamma$ takes the form $\boldsymbol{\sigma}_\Gamma = \tau \mathbf{P}$ as in equation (2.34). The surface divergence of $\boldsymbol{\sigma}_\Gamma$ is a vector field on $\Gamma(t)$ (cf. (2.35), (2.36)) which depends on the geometry of $\Gamma(t)$, e.g. the curvature κ and the normal field \mathbf{n} . In such cases we understand the force functional $f_\Gamma(\mathbf{v})$ in (2.44) as $f_\Gamma(\mathbf{v}) = f_{\Gamma(t)}(\mathbf{v})$. For the viscous interface model $\boldsymbol{\sigma}_\Gamma$ takes the form (2.37), which depends on the velocity field \mathbf{u} in addition to $\Gamma(t)$, and we understand $f_\Gamma(\mathbf{v})$ as $f_\Gamma(\mathbf{v}) = f_{\Gamma(t)}(\mathbf{u}, \mathbf{v})$.

The weak formulation for the one fluid formulation (2.43) is as follows: Find $(\mathbf{u}, p) \in \mathbf{V}_D \times Q$ such that for $t \in [t_0, T]$ the following equations hold:

$$m\left(\frac{\partial \mathbf{u}}{\partial t}, \mathbf{v}\right) + c(\mathbf{u}; \mathbf{u}, \mathbf{v}) + a(\mathbf{u}, \mathbf{v}) + b(\mathbf{v}, p) = (\rho \mathbf{g}, \mathbf{v})_{L^2(\Omega)} + f_\Gamma(\mathbf{v}), \quad \text{for all } \mathbf{v} \in \mathbf{V}_0, \quad (2.45a)$$

$$b(\mathbf{u}, q) = 0 \quad \text{for all } q \in Q, \quad (2.45b)$$

with proper initial conditions.

In addition we still need the kinematic condition (2.41d) to describe the dynamics of the interface $\Gamma(t)$. There are several techniques to track the movement of $\Gamma(t)$ [39], we use the level set method, which will be introduced in the following chapter.

3. Components of the DROPS solver

3.1. Introduction

We use the DROPS package[1] to perform simulations of the two-phase flow problem introduced in chapter 2. The DROPS package is developed at the Chair for Numerical Mathematics at RWTH Aachen University with the aim of providing reliable, fast and efficient numerical procedures for the aforementioned problem class. It is implemented in C++ with high levels of template programming and parallelization. For solving the two-phase flow problem, we utilize the following components of the DROPS package:

- **Mesh generation and adaptive local refinement/coarsening.** A nested multilevel hierarchy of tetrahedral triangulations is constructed, which allows adaptive local refinement/coarsening according to the position of the interface.
- **Level set method for interface representation.** The moving interface is captured by a level set function. To obtain the position of the interface at a given time, the zero level of the level set function is numerically determined. The level set equation, which determines the level set function, is a linear hyperbolic equation. We use the streamline diffusion method to stabilize the finite element discretization. Reinitialization of the level set function, which is also called reparametrization, is performed to increase the stability of numerical methods. Volume correction by shifting the level set function ensures the conservation of the droplet volume.
- **Discretization methods for two-phase flow problem.** We use simplicial finite elements to discretize the two-phase flow problem. The extended finite element method (XFEM) is used to discretize the discontinuous quantities, e.g. pressure. A special Laplace-Beltrami method is used to discretize the surface force integral. Implicit time discretization methods lead to a strongly coupled system of fluid dynamics and interface dynamics.
- **Trace FEM method for surfactant transport equation.** The surfactant transport equation (2.42) has to be solved on the moving interface. We use the trace space of the volume finite elements to discretize the surfactant equation. A space-time formulation is used to treat the moving interface problem.
- **Iterative methods for solving the coupled system.** A fixed point iteration is used to decouple the solution process of the fluid dynamics and the interface dynamics, i.e. the level set equation. The Navier-Stokes equation, which is a non-linear problem, is linearized by a Richardson type of method. The aforementioned decoupling and linearization strategies create two levels of iteration.

3. Components of the DROPS solver

- **Fast iterative solvers.** We use the GMRES method with a Gauss-Seidel preconditioner to solve the discrete level set equation. For the linearized Navier-Stokes equation, we apply a preconditioned generalized conjugate residual method (GCR). Special block preconditioners are used.
- **Parallelization.** Parallelization techniques are used in the assembling of the linear equation systems as well as in the iterative solvers. Shared memory type and distributed memory type of parallelism are both implemented.

In Figure 3.1, we illustrate the interactions between the two main parts of DROPS, i.e. the two-phase Navier-Stokes equation (fluid dynamics) and the level set equation (interface dynamics). The two-phase Navier-Stokes equation (cf. equation (2.43)) determines the fluid velocity and pressure with a given interface position. The calculated fluid velocity transports the interface. We use the level set method (cf. section 3.2) to track the dynamics of the interface. The surface force term (cf. equation (2.44)) depends on the position of the interface and influences the two-phase Navier-Stokes equation. If surfactant is considered in the model, a convection-diffusion equation for surfactant (cf. equation (2.42)) has to be solved on the interface, and the concentration of the surfactant may influence the surface tension coefficient (cf. section 2.6.3). We also list the important numerical modules in the diagram. The underlined components will not be discussed in this thesis. For further explanations on these topics, we refer to [39].

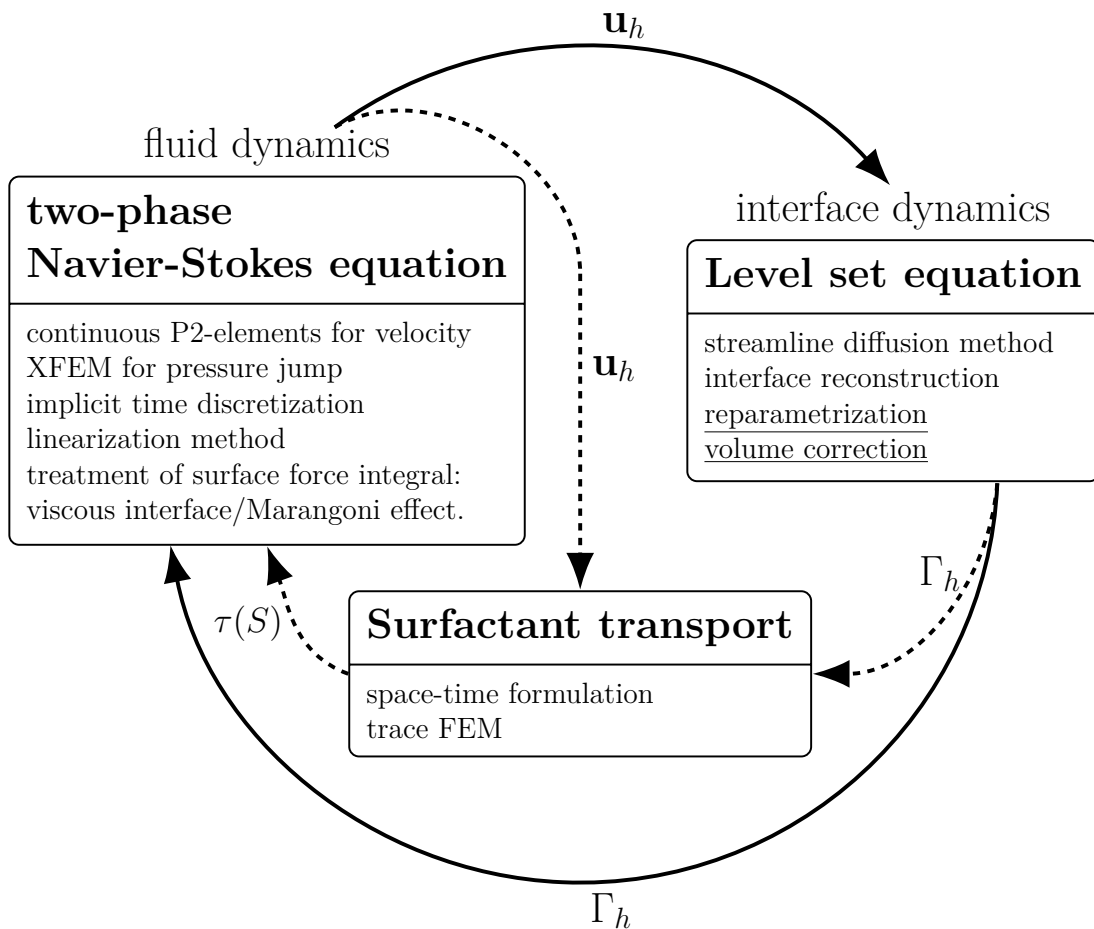


Figure 3.1.: Components of DROPS package.

In the following sections and chapter 4, we briefly describe the listed components of the DROPS solver in the diagram, which are related to the simulation of two-phase flows with complex interfaces. Detailed information of the DROPS solver can be found in [35, 39].

3.2. Level set method

The interface $\Gamma(t)$ is transported by the velocity field \mathbf{u} , and important physical phenomena happen at the interface, e.g. the jump of momentum (2.41e), the transport of surfactants (2.42). Hence we need to know the position of $\Gamma(t)$. There are two categories of numerical methods for this purpose: *interface tracking* method and *interface capturing* method [39]. The difference between these is whether the interface is explicitly or implicitly represented. An *interface tracking* method *explicitly* represents the interface, e.g. by putting markers on $\Gamma(t_0)$ and following the position of the markers. *Interface capturing* method, on the other hand, utilize an *implicit* representation of the interface, generally in the form of a globally defined function in Ω , which either captures one phase of the fluid (e.g. the characteristic function in volume-of-fluid method) or captures the position of the interface (e.g. the zero level of the level set method).

The level set method [19, 65, 78], which is an *interface capturing* method, is used in DROPS. A continuous scalar function $\phi(\mathbf{x}, t_0)$ is defined on Ω . The interface $\Gamma(t_0)$ is *implicitly* represented as the zero level of $\phi(\mathbf{x}, t_0)$, i.e. $\Gamma(t_0) = \{\mathbf{x} \in \Omega : \phi(\mathbf{x}, t_0) = 0\}$. As described in (2.1) from the previous chapter, we use \mathbf{X}_σ to denote the trajectory of a material particle σ . The dynamics of the scalar function ϕ is described by a pure advection, i.e. the value of ϕ is constant along the trajectory \mathbf{X}_σ :

$$\phi(\mathbf{X}_\sigma(t), t) = \phi(\mathbf{X}_\sigma(t_0), t_0) = \phi(\mathbf{x}_0, t_0) \quad \text{for } \mathbf{x}_0 \in \Omega. \quad (3.1)$$

Hence the material derivative of $\phi(\mathbf{x}, t)$ equals zero. From the definition of the material derivative (2.2), we obtain the level set equation as follows

$$\frac{\partial \phi}{\partial t} + (\mathbf{u} \cdot \nabla) \phi = 0 \quad \text{in } \Omega \times [t_0, T]. \quad (3.2)$$

The zero level of ϕ is transported by the velocity field \mathbf{u} , therefore we obtain $\Gamma(t) = \{\mathbf{x} \in \Omega : \phi(\mathbf{x}, t) = 0\}$.

Equation (3.2) is a hyperbolic PDE, which has to be solved in a bounded domain Ω . Hence we need both the initial condition $\phi_0(\mathbf{x}) := \phi(\mathbf{x}, t_0)$ and proper boundary conditions $\phi(\mathbf{x}, t)$ for $\mathbf{x} \in \partial\Omega$.

The initial condition $\phi_0(\mathbf{x})$ should be a continuous scalar function and satisfy the condition that $\Gamma(t_0)$ is the only zero level of $\phi_0(\mathbf{x})$. Hence ϕ_0 should have different signs in the two phases. We usually make the convention: if \mathbf{x} is in the droplet phase $\Omega_1(t_0)$, then $\phi_0(\mathbf{x}) < 0$; if \mathbf{x} is in the surrounding phase $\Omega_2(t_0)$, then $\phi_0(\mathbf{x}) > 0$. A typical choice of ϕ_0 is the *signed distance* function, which obviously satisfies the requirements. An example of a level set function is illustrated in Figure 3.2.

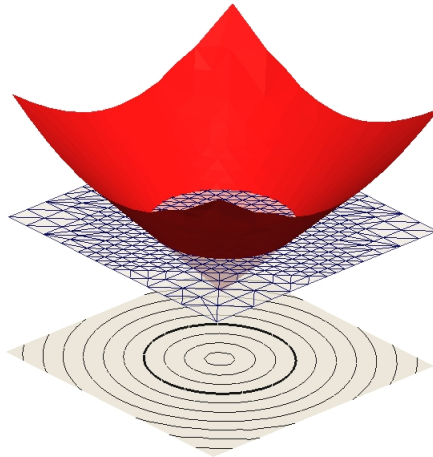


Figure 3.2.: An example of a level set function with contour lines.

Remark 3.2.1. *The two-phase volumes $\Omega_i(t)$ with $i = 1, 2$ and the level set function are both transported by the same velocity field \mathbf{u} , therefore the sign of ϕ in $\Omega_i(t)$ will not change. $\Omega_i(t)$ can then be characterized as*

$$\Omega_1(t) = \{\mathbf{x} \in \Omega : \phi(\mathbf{x}, t) < 0\}, \quad \Omega_2(t) = \{\mathbf{x} \in \Omega : \phi(\mathbf{x}, t) > 0\}.$$

For the boundary conditions of ϕ , on the Dirichlet boundaries of Ω (denoted by $\partial\Omega_D$) we assign constant values for ϕ , i.e. $\phi(\mathbf{x}, t) = \phi(\mathbf{x}, t_0) = \phi_0(\mathbf{x})$ for $\mathbf{x} \in \partial\Omega_D$. For other types of boundary conditions, we refer to [52].

In section 2.3.2, we assume that $\Gamma(t)$ is an oriented C^2 -hypersurface. Hence if $\phi(\mathbf{x}, t)$ is continuously differentiable in a neighborhood of the zero level, then the surface normal $\mathbf{n}(\mathbf{x}, t)$ for $\mathbf{x} \in \Gamma(t)$ is given by

$$\mathbf{n}(\mathbf{x}, t) = \frac{\nabla\phi(\mathbf{x}, t)}{\|\nabla\phi(\mathbf{x}, t)\|_2} \quad \text{for } \mathbf{x} \in \Gamma(t). \quad (3.3)$$

We choose the signed distance function for ϕ_0 , i.e. $\|\nabla\phi_0(\mathbf{x})\|_2 = 1$ for $\mathbf{x} \in \Gamma(t_0)$, which is favorable to the numerical determination of the zero level of ϕ . However, this property is generally lost for $t > t_0$ due to the velocity field \mathbf{u} . Hence we need proper reinitialization techniques (also called reparametrization techniques) for the level set equation, which recovers the signed distance property approximately. We refer to [39] for a discussion of the reinitialization techniques used in DROPS.

With the introduction of the level set function, we can replace the kinematic condition (2.41d) $V_\Gamma = \mathbf{u} \cdot \mathbf{n}$ on $\Gamma(t)$ by the level set equation (3.2). We define density and viscosity functions depending on ϕ :

$$\rho(\phi) := \begin{cases} \rho_1 & : \phi < 0 \\ \rho_2 & : \phi > 0 \end{cases}, \quad \mu(\phi) := \begin{cases} \mu_1 & : \phi < 0 \\ \mu_2 & : \phi > 0 \end{cases}$$

The one fluid formulation of two-phase flows (2.43) can be rewritten as

$$\rho(\phi)\left(\frac{\partial \mathbf{u}}{\partial t} + (\mathbf{u} \cdot \nabla)\mathbf{u}\right) = -\nabla p + \operatorname{div}(\mu(\phi)\mathbf{D}(\mathbf{u})) + \rho(\phi)\mathbf{g} + \mathbf{f}_\Gamma \quad \text{in } \Omega \times [t_0, T], \quad (3.4a)$$

$$\operatorname{div} \mathbf{u} = 0 \quad \text{in } \Omega \times [t_0, T], \quad (3.4b)$$

$$\frac{\partial \phi}{\partial t} + (\mathbf{u} \cdot \nabla)\phi = 0 \quad \text{in } \Omega \times [t_0, T], \quad (3.4c)$$

together with proper initial and boundary conditions for \mathbf{u} and ϕ .

Remark 3.2.2. *The equation system (3.4) is a strongly coupled system between the two-phase Navier-Stokes equations and the level set equation. The fluid velocity field \mathbf{u} transports the level set function ϕ , thus the interface position is moved. The interface force term \mathbf{f}_Γ depends on the position of the interface, and changes the velocity field. In section 3.2.1 and section 3.3 we introduce the methods for discretizing the level set equation and the two-phase Navier-Stokes equations separately. In section 3.5 we introduce the decoupling strategy for solving the equation system (3.4).*

3.2.1. Discretization of the level set equation

In this section and the following sections, we assume Ω to be a polygonal Lipschitz domain.

The level set equation (3.2) is a hyperbolic equation, and it is well known that the standard continuous Galerkin finite element method is not suitable for such equations. Non-physical oscillations will occur [23]. Hence a stabilization method is needed. In DROPS, we use piecewise quadratic finite elements combined with a streamline diffusion stabilization to discretize the level set equation. In this stabilization method a consistent numerical diffusion term is added in the direction of the velocity field \mathbf{u} . We use \mathcal{T}_h to denote a triangulation of the domain Ω , and V_h to denote the space of continuous piecewise quadratic finite elements:

$$V_h := \{v_h \in C(\overline{\Omega}) : v_h|_T \in \mathcal{P}_2 \quad \text{for all } T \in \mathcal{T}_h\}.$$

As described in the previous section, on $\partial\Omega_D$ we need to assign boundary conditions for ϕ , which is denoted by ϕ_D . The spaces $V_{0,h}$ and $V_{D,h}$ are defined by

$$\begin{aligned} V_{0,h} &:= \{v_h \in V_h : v_h = 0 \quad \text{on } \partial\Omega_D\}, \\ V_{D,h} &:= \{v_h \in V_h : v_h = I(\phi_D) \quad \text{on } \partial\Omega_D\}, \end{aligned}$$

where $I(\phi_D)$ is the interpolation of the boundary condition ϕ_D . We approximate the initial condition ϕ_0 by $\phi_{0,h} \in V_h$. The spatial discretization of the level set equation is given by:

Find $\phi_h(t) \in V_{D,h}$ for $t \in [t_0, T]$ with $\phi_h(t_0) = \phi_{0,h}$ such that

$$\sum_{T \in \mathcal{T}_h} \left(\frac{\partial \phi_h}{\partial t} + \mathbf{u} \cdot \nabla \phi_h, v_h + \zeta_T \mathbf{u} \cdot \nabla v_h \right)_{L^2(T)} = 0 \quad \text{for all } v_h \in V_{0,h}, \quad (3.5)$$

3. Components of the DROPS solver

where $\zeta_T \in [0, 1]$ is a stabilization parameter, which can be chosen for each tetrahedron. We refer to [39] for the details of this method.

We use $\{\xi_i\}_{i \in \{1, 2, \dots, N\}}$ to denote the standard nodal basis functions in $V_{0,h}$, where $N := \dim(V_{0,h})$. We use $(\partial V_h)_D$ to denote the set of degree of freedoms on $\partial\Omega_D$, and the corresponding nodal basis functions are denoted by $\{\eta_j\}_{j \in \{1, 2, \dots, \dim(V_h) - N\}}$. A function $\phi_h(t) \in V_{D,h}$ is given by

$$\phi_h(t) = \sum_{i=1}^N \varphi_i(t) \xi_i + \sum_{j=1}^{\dim(V_h) - N} \phi_D(\mathbf{x}_j, t) \eta_j =: \sum_{i=1}^N \varphi_i(t) \xi_i + \phi_{D,h}(t), \quad (3.6)$$

where $\{\varphi_i(t)\}_{i \in \{1, 2, \dots, N\}}$ are the coefficients. We gather these coefficients in a vector $\vec{\phi}(t) \in \mathbb{R}^N$, the i -th component of which equals $\varphi_i(t)$. We can insert (3.6) into (3.5) and define the matrices $\mathbf{M}_\phi = \mathbf{M}_\phi(\mathbf{u}) \in \mathbb{R}^{N \times N}$ and $\mathbf{N}_\phi = \mathbf{N}_\phi(\mathbf{u}) \in \mathbb{R}^{N \times N}$ with elements:

$$\begin{aligned} (\mathbf{M}_\phi)_{i,j} &:= \sum_{T \in \mathcal{T}_h} (\xi_j, \xi_i + \zeta_T \mathbf{u} \cdot \nabla \xi_i)_{L^2(T)}, \\ (\mathbf{N}_\phi)_{i,j} &:= \sum_{T \in \mathcal{T}_h} (\mathbf{u} \cdot \nabla \xi_j, \xi_i + \zeta_T \mathbf{u} \cdot \nabla \xi_i)_{L^2(T)}. \end{aligned}$$

We also define a vector $\vec{\phi}_D \in \mathbb{R}^N$ with elements:

$$(\vec{\phi}_D)_i := \sum_{T \in \mathcal{T}_h} \left(\frac{\partial \phi_{D,h}}{\partial t} + \mathbf{u} \cdot \nabla \phi_{D,h}, \xi_i + \zeta_T \mathbf{u} \cdot \nabla \xi_i \right)_{L^2(T)}.$$

The boundary part of the initial condition $\phi_{0,h}$ has already been taken into account in $\phi_{D,h}$, thus we only define a vector $\vec{\phi}_0 \in \mathbb{R}^N$.

The matrix-vector form of (3.5) is given by:

Find $\vec{\phi}(t) \in \mathbb{R}^N$ with $\vec{\phi}(t_0) = \vec{\phi}_0$ such that the following holds

$$\mathbf{M}_\phi(\mathbf{u}) \frac{d}{dt} \vec{\phi}(t) + \mathbf{N}_\phi(\mathbf{u}) \vec{\phi}(t) = -\vec{\phi}_D(\mathbf{u}) \quad \text{for all } t \in [t_0, T]. \quad (3.7)$$

We assume that the velocity \mathbf{u} is *known* at two time steps n and $n + 1$. A θ -scheme is applied to (3.7), the resulting equation for two time steps n and $n + 1$ is given by

$$\begin{aligned} \frac{\vec{\phi}^{n+1} - \vec{\phi}^n}{\Delta t} &= \theta \mathbf{M}_\phi(\bar{\mathbf{u}}^{n+1})^{-1} \left(-\mathbf{N}_\phi(\bar{\mathbf{u}}^{n+1}) \vec{\phi}^{n+1} - \vec{\phi}_D(\bar{\mathbf{u}}^{n+1}) \right) \\ &\quad + (1 - \theta) \mathbf{M}_\phi(\bar{\mathbf{u}}^n)^{-1} \left(-\mathbf{N}_\phi(\bar{\mathbf{u}}^n) \vec{\phi}^n - \vec{\phi}_D(\bar{\mathbf{u}}^n) \right). \end{aligned} \quad (3.8)$$

3.3. Discretization of Navier-Stokes equations

In this section, we introduce some of the discretization methods used in DROPS for discretizing the two-phase Navier-Stokes equations (3.4a) and (3.4b). Due to the jump of bulk stresses caused by the surface stress at $\Gamma(t)$, cf. (2.41e), the pressure is generally *discontinuous* across $\Gamma(t)$. The standard Taylor-Hood (P2-P1) finite elements, which are

often used for the discretization of velocity and pressure unknowns in one-phase flow problems, are not suitable. We need a special treatment of the discontinuous pressure. In DROPS, an extended finite element method (XFEM) is used to discretize the pressure unknowns, in which the standard piecewise continuous P1 finite element space is enriched by additional discontinuous basis functions. For the discretization of the surface force functional (2.44), we reconstruct an approximation of the zero level of the discrete level set function ϕ_h .

Due to the changing pressure XFEM space, cf. section 3.3.3, we adopt a *Rothe* approach for the time discretization, i.e. we first discretize the problem in time, then in space.

Important physical phenomena happen at the interface $\Gamma(t)$, which is moving and deforming in Ω . Hence we need triangulations of the domain in such a way that the resolution close to $\Gamma(t)$ is sufficiently high. In order to decrease the computational effort, it is beneficial to use coarser triangulations far from the interface. The nested multilevel hierarchy of tetrahedral triangulations used in DROPS are constructed in such a way that the resulting grid fulfills these requirements. The grids are constructed in a consistent and stable manner, cf. [39]. Local refinement and coarsening can be applied according to a certain criterion, e.g. the position of $\Gamma(t)$. The nested finite element spaces on the multilevel triangulations are advantageous for using the multigrid method in solving the linear systems.

3.3.1. Time discretization

We apply implicit time discretization schemes for the following reasons:

- There exist strong couplings and nonlinearities in the two-phase model (3.4), i.e. the coupling between fluid dynamics and the level set function is through the nonlinear surface force term $\mathbf{f}_\Gamma(\phi)$.
- It is well-known that after spatial discretization the Navier-Stokes equations result in a very **stiff** ODE system [17].

We use the reduced XFEM space \tilde{Q}_h^X to discretize the pressure unknowns, cf. section 3.3.3. The dimension of \tilde{Q}_h^X depends on the position of Γ_h . Hence at time steps n and $n + 1$, the pressure space might be different. It is not clear how to apply the method of lines in such situation, cf. discussions in [39]. Instead a *Rothe* approach is used to discretize the Navier-Stokes equations, i.e. we first discretize the problem in time, then in space. Recall the weak formulations in (2.45):

Find $(\mathbf{u}, p) \in \mathbf{V}_D \times Q$ such that for $t \in [t_0, T]$ the following equations hold:

$$m\left(\frac{\partial \mathbf{u}}{\partial t}, \mathbf{v}\right) + c(\mathbf{u}; \mathbf{u}, \mathbf{v}) + a(\mathbf{u}, \mathbf{v}) + b(\mathbf{v}, p) = (\rho \mathbf{g}, \mathbf{v})_{L^2(\Omega)} + f_\Gamma(\mathbf{v}), \quad \text{for all } \mathbf{v} \in \mathbf{V}_0,$$

$$b(\mathbf{u}, q) = 0 \quad \text{for all } q \in Q.$$

For simplicity, we only consider the case with homogeneous Dirichlet boundary condition for \mathbf{u} , i.e. the test space is the same as the trial space \mathbf{V}_0 . We introduce the subspace

3. Components of the DROPS solver

$\mathbf{V}_{\text{div}} := \{\mathbf{v} \in \mathbf{V}_0 : \text{div } \mathbf{v} = 0\}$, which is a Hilbert space w.r.t to the $\|\cdot\|_1$ norm. The weak formulation can then be formulated as:

Find $\mathbf{u} \in \mathbf{V}_{\text{div}}$ such that for $t \in [t_0, T]$ the following equation holds:

$$m\left(\frac{\partial \mathbf{u}}{\partial t}, \mathbf{v}\right) = (\rho \mathbf{g}, \mathbf{v})_{L^2(\Omega)} + f_\Gamma(\mathbf{v}) - c(\mathbf{u}; \mathbf{u}, \mathbf{v}) - a(\mathbf{u}, \mathbf{v}) =: \tilde{f}(\mathbf{u}, \mathbf{v}, \Gamma), \quad \text{for all } \mathbf{v} \in \mathbf{V}_{\text{div}}, \quad (3.9)$$

with proper initial condition $\mathbf{u}_0 \in \mathbf{V}_{\text{div}}$. Equation (3.9) can be discretized with the following θ -scheme: for given $\mathbf{u}^n \in \mathbf{V}_{\text{div}}$ ($n \geq 0$), determine $\mathbf{u}^{n+1} \in \mathbf{V}_{\text{div}}$ such that

$$m_{n+\frac{1}{2}}\left(\frac{\mathbf{u}^{n+1} - \mathbf{u}^n}{\Delta t}, \mathbf{v}\right) = \theta \tilde{f}(\mathbf{u}^{n+1}, \mathbf{v}, \Gamma^{n+1}) + (1 - \theta) \tilde{f}(\mathbf{u}^n, \mathbf{v}, \Gamma^n), \quad \text{for all } \mathbf{v} \in \mathbf{V}_{\text{div}},$$

with the bilinear form $m_{n+\frac{1}{2}}(\mathbf{u}, \mathbf{v}) := \int_\Omega \frac{\rho(\phi(t_n)) + \rho(\phi(t_{n+1}))}{2} \mathbf{u} \cdot \mathbf{v} \, dx$. We can now re-introduce the pressure $p \in Q$ as a Lagrange multiplier for the condition $\mathbf{u}^{n+1} \in \mathbf{V}_{\text{div}}$:

Find $(\mathbf{u}^{n+1}, p) \in \mathbf{V}_0 \times Q$, such that for all $\mathbf{v} \in \mathbf{V}_0$ and $q \in Q$ the following equations hold

$$m_{n+\frac{1}{2}}\left(\frac{\mathbf{u}^{n+1} - \mathbf{u}^n}{\Delta t}, \mathbf{v}\right) + b(\mathbf{v}, p) = \theta \tilde{f}(\mathbf{u}^{n+1}, \mathbf{v}, \Gamma^{n+1}) + (1 - \theta) \tilde{f}(\mathbf{u}^n, \mathbf{v}, \Gamma^n), \quad (3.10a)$$

$$b(\mathbf{u}^{n+1}, q) = 0. \quad (3.10b)$$

Before introducing the spatial discretization of the system (3.10), we first describe the method used in DROPS to reconstruct the interface from the discrete level set function ϕ_h .

3.3.2. Reconstruction of the interface

For the discretization of the surface force functional (2.44), we reconstruct an approximate interface Γ_h from the implicitly given zero level of the discrete level set function ϕ_h . As described in section 3.2.1, ϕ_h is from the space of piecewise quadratic finite elements on a tetrahedral triangulation \mathcal{T}_h . In order to circumvent the computationally very demanding task of determining the zero level of quadratic functions, we construct an approximate interface on a regular refinement of \mathcal{T}_h , which is denoted by $\mathcal{T}_{\frac{1}{2}h}$. On $\mathcal{T}_{\frac{1}{2}h}$, we define the continuous piecewise *linear* function $I(\phi_h)$, which interpolates ϕ_h at all vertices of all tetrahedra in $\mathcal{T}_{\frac{1}{2}h}$. The approximate interface is defined by

$$\Gamma_h(t) := \{\mathbf{x} \in \Omega : I(\phi_h(t))(\mathbf{x}) = 0 \quad \text{for } t \in [t_0, T]\}.$$

$\Gamma_h(t)$ is composed of piecewise planar segments, which are either triangles or quadrilaterals. The quadrilaterals can be further divided into two triangles. In general, the planar segments of $\Gamma_h(t)$ are not aligned with the faces of the tetrahedral triangulation \mathcal{T}_h . In Figure 3.3, we illustrate this reconstruction of Γ_h for one tetrahedron. In [39], it is shown that if the level set function ϕ is sufficiently smooth, the following approximation property holds

$$\text{dist}(\Gamma_h, \Gamma) \leq ch_\Gamma^2.$$

where h_Γ is the interface mesh size parameter. h_Γ is defined as the maximal diameter of the interface planar segments.

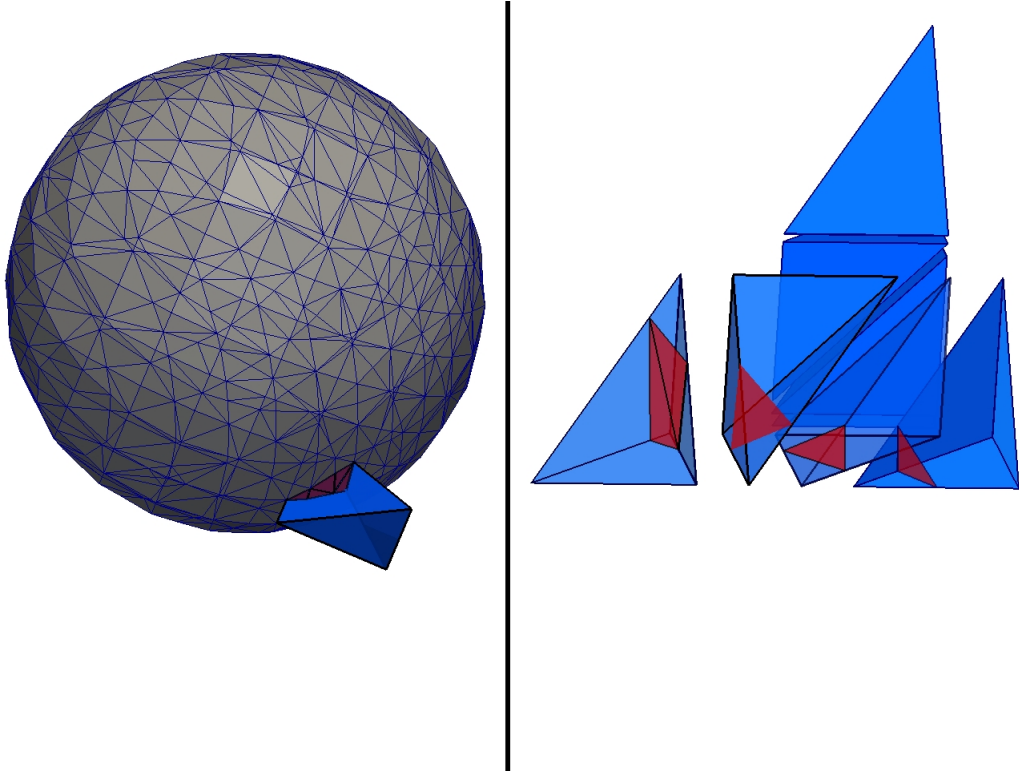


Figure 3.3.: Reconstruction of an approximate interface Γ_h and an example of a tetrahedron (left). This tetrahedron is refined once into eight sub-tetrahedra (right). Γ_h is then determined for each sub-tetrahedron.

3.3.3. Spatial discretization

In this section, we introduce the spatial discretization of the discrete-time equation system (3.10). Taylor-Hood finite elements are often used for discretization of one-phase flow problems. In two-phase flow problems, due to the surface force term (2.44) the pressure is discontinuous across the interface. If we continue using the standard continuous piecewise P_1 finite element space for the discontinuous pressure, the pressure jump at the interface will not be resolved and oscillations of pressure occur, which generate very large undesirable *spurious* velocities at the interface, cf. [39, 35]. In DROPS, the so-called extended finite element method (XFEM) is used to discretize the discontinuous pressure. We explain the main idea of this method. More details are given in [38, 70].

XFEM for discontinuous pressure. We use Q_h to denote the standard continuous piecewise linear finite element space:

$$Q_h := \{q \in C(\bar{\Omega}) : q|_T \in \mathcal{P}_1 \text{ for all } T \in \mathcal{T}_h\}.$$

The dimension of Q_h is denoted by $M = \dim(Q_h)$. The degrees of freedoms of Q_h are indexed by $\mathcal{J} = \{1, 2, \dots, M\}$. The nodal basis functions of Q_h are denoted by $\{\eta_i\}_{i \in \mathcal{J}}$,

3. Components of the DROPS solver

and the corresponding nodal coordinates are denoted by \mathbf{x}_i . Clearly the following property holds for η_i : $\eta_i(\mathbf{x}_j) = 1$ if $i = j \in \mathcal{J}$ and $\eta_i(\mathbf{x}_j) = 0$ for $i \neq j$. In the XFEM method, we enrich Q_h by choosing additional basis functions [56, 11]. We use \mathcal{T}_h^Γ to denote the tetrahedra that are “cut” by the interface, and we use \mathcal{J}^Γ to denote the index of basis functions that are “cut” by the interface:

$$\begin{aligned}\mathcal{T}_h^\Gamma &:= \{T \in \mathcal{T}_h : \text{meas}_2(\Gamma_h \cap T) > 0\}, \\ \mathcal{J}^\Gamma &:= \{j \in \mathcal{J} : \text{meas}_2(\Gamma_h \cap \text{supp } \eta_j) > 0\}.\end{aligned}$$

The space Q_h is enriched by discontinuous basis functions denoted by $\{\eta_j^X\}_{j \in \mathcal{J}^\Gamma}$. They are constructed as follows. Let $d : \Omega \rightarrow \mathbb{R}$ be the signed distance function w.r.t. Γ with negative sign in $\Omega_1(t)$ and positive sign in $\Omega_2(t)$. We define a step function $H_\Gamma : \Omega \rightarrow \mathbb{R}$ in the following way

$$H_\Gamma(\mathbf{x}) := \begin{cases} 1 & \mathbf{x} \in \Omega_2(t), \\ 0 & \mathbf{x} \in \bar{\Omega}_1(t). \end{cases}$$

The enrichment function Φ_j is then defined by $\Phi_j(\mathbf{x}) := H_\Gamma(\mathbf{x}) - H_\Gamma(\mathbf{x}_j)$ and the additional basis functions are defined by $\eta_j^X := \eta_j \Phi_j$ for $j \in \mathcal{J}^\Gamma$. The support of η_j^X is a subset of \mathcal{T}_h^Γ . In Figure 3.4, we illustrate a simple one-dimensional case for the above mentioned functions. In the figure the domains are $\Omega = (0, 1)$, $\Omega_1 = (0, \frac{4}{9})$ and $\Omega_2 = (\frac{4}{9}, 1)$, the interface Γ is at $x = \frac{4}{9}$. Ω is divided uniformly into 3 sub-intervals with $h = \frac{1}{3}$. In this case, the index set is $\mathcal{J} = \{1, 2, 3, 4\}$, \mathcal{J}^Γ is $\{2, 3\}$, and two discontinuous basis functions $\eta_2^X(x)$ and $\eta_3^X(x)$ are added.

The XFEM space that we use is given by

$$Q_h^X := Q_h \oplus \text{span}(\{\eta_j^X : j \in \mathcal{J}^\Gamma\}).$$

Remark 3.3.1. *The space Q_h^X varies if the interface Γ changes. The dimension of Q_h^X is also not fixed.*

Remark 3.3.2. *We take a simple one-dimensional example to explain why we add additional basis functions. Take the same domain and the interface as in Figure 3.4. We define a function $g(x)$ which equals 1 in Ω_1 and 2 in Ω_2 . The domains are $\Omega_1 := (0, 4/9)$ and $\Omega_2 := (4/9, 1)$. The interface Γ is at $x = 4/9$. In Q_h , the best approximation of $g(x)$ is $\tilde{g}(x) = 1 \cdot \eta_1(x) + 1 \cdot \eta_2(x) + 2 \cdot \eta_3(x) + 2 \cdot \eta_4(x)$, which looks like . The L^2 -norm of the approximation errors w.r.t to the grid size h are given in Table 3.1, which behave like $\mathcal{O}(\sqrt{h})$. By adding the two additional basis functions η_2^X and η_3^X , we can represent $g(x)$ exactly in Q_h^X : $g(x) = 1 \cdot \eta_1(x) + 1 \cdot \eta_2(x) + 2 \cdot \eta_3(x) + 2 \cdot \eta_4(x) + 1 \cdot \eta_2^X(x) + 1 \cdot \eta_3^X(x)$.*

In [38, 70] the authors have shown that for two- and three-dimensional problems the approximation errors behave like $\mathcal{O}(\sqrt{h})$ for the standard continuous space Q_h , and $\mathcal{O}(h^2)$ for the extended space Q_h^X . In DROPS, Q_h^X is used to discretize pressure unknowns.

Discretization of the velocity. We use the standard continuous piecewise quadratic finite elements (P_2), which is denoted by \mathbf{V}_h , to discretize the velocity \mathbf{u} . We use $(\partial\mathbf{V}_h)_D$ to denote the degree of freedoms on $\partial\Omega_D$. The spaces are denoted by $\mathbf{V}_{0,h}$ for $\mathbf{v}_h = 0$ on $(\partial\mathbf{V}_h)_D$ and $\mathbf{V}_{D,h}$ for $\mathbf{v}_h = I(\mathbf{u}_D)$ on $(\partial\mathbf{V}_h)_D$, where $I(\mathbf{u}_D)$ is the interpolation of boundary function \mathbf{u}_D .

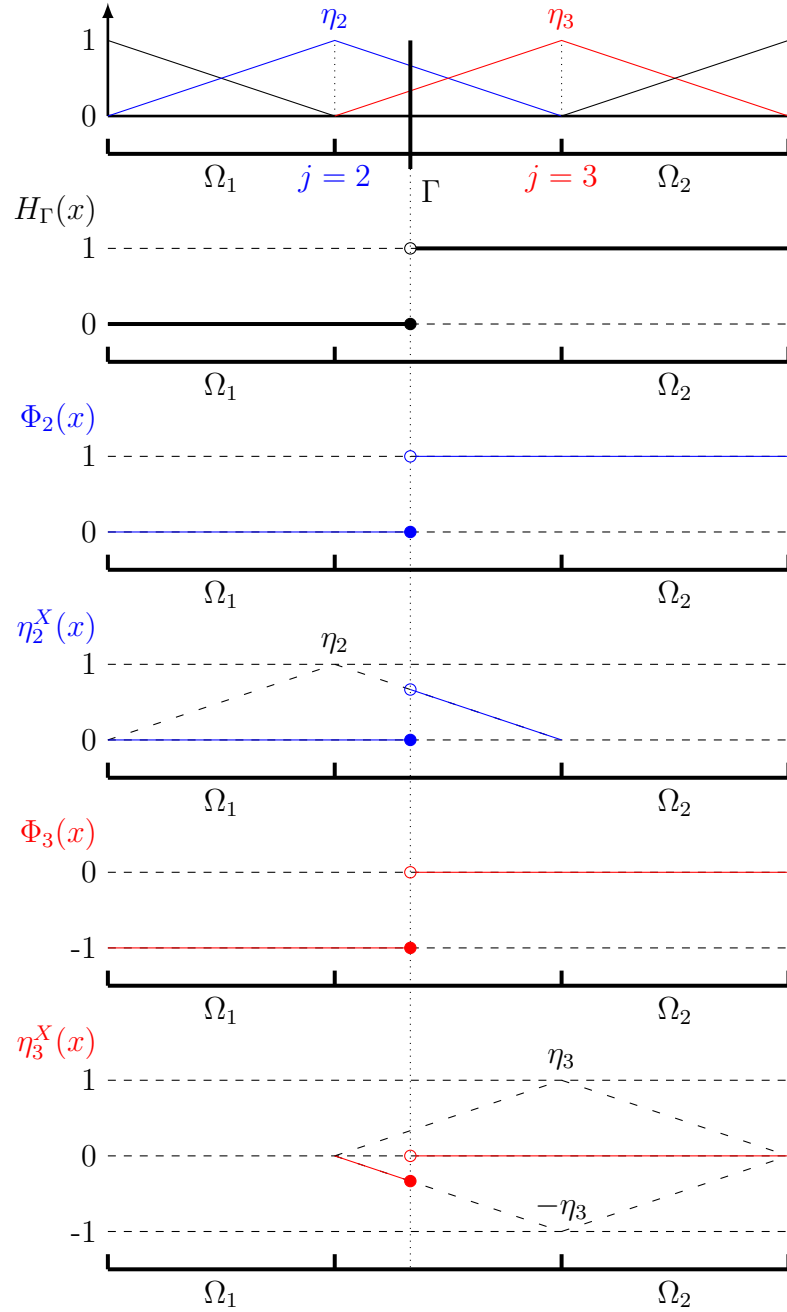


Figure 3.4.: Additional discontinuous basis functions for one-dimensional case.

3. Components of the DROPS solver

h	$\ \tilde{g}(x) - g(x)\ _{L^2(0,1)}$	order
1/3	0.192450	
1/6	0.136083	0.5
1/12	0.0962250	0.5
1/24	0.0680414	0.5

Table 3.1.: L^2 -norm of the approximation error for Q_h and convergence order in one dimensional case.

The Taylor-Hood pair P_2 - P_1 is shown to be LBB stable. The LBB stability of the pair P_2 - Q_h^X however is an open problem.

Remark 3.3.3. *From the numerical experiments shown in [39] Section 7.10.3, the stability of the pair P_2 - Q_h^X deteriorates if the supports of the added discontinuous basis functions η_j^X are “small” in some regions. Hence in the numerical experiments we choose a “cut off” parameter for Q_h^X , i.e. we only take the extended basis functions with relatively large supports. The resulting XFEM space is called the reduced extended finite element space and denoted by \tilde{Q}_h^X .*

Vector forms of \mathbf{u}_h and p_h . We use $\{\xi_i\}_{i \in \{1,2,\dots,N\}}$ to denote the standard nodal scalar basis function of the space $V_{0,h}$. For a vector function $\mathbf{u}_h \in \mathbf{V}_{0,h}$, we use one scalar basis function for each component of \mathbf{u}_h . Hence \mathbf{u}_h can be represented by

$$\mathbf{u}_h = \sum_{i=1}^N \begin{pmatrix} \xi_i & 0 & 0 \\ 0 & \xi_i & 0 \\ 0 & 0 & \xi_i \end{pmatrix} \begin{pmatrix} v_{i,1} \\ v_{i,2} \\ v_{i,3} \end{pmatrix} = \sum_{i=1}^N \xi_i \vec{v}_i, \quad (3.11)$$

where $\vec{v}_i := (v_{i,1}, v_{i,2}, v_{i,3})^T$ is the vector coefficient. We can gather these coefficients into one vector $\vec{\mathbf{u}} \in \mathbb{R}^{3N}$. The ordering is according to the position of the basis function, i.e.

$$\vec{\mathbf{u}} = (v_{1,1}, v_{1,2}, v_{1,3}, v_{2,1}, v_{2,2}, v_{2,3}, \dots, v_{i,j}, \dots, v_{N,1}, v_{N,2}, v_{N,3})^T.$$

Remark 3.3.4. *We can also use the index set $\{1, 2, \dots, 3N\}$ to order the elements of $\vec{\mathbf{u}}$, i.e. $\vec{\mathbf{u}} = (v_1, v_2, \dots, v_k, \dots, v_{3N})^T$. For an element $v_{i,j}$ with $i \in \{1, \dots, N\}$ and $j \in \{1, 2, 3\}$, the corresponding index is $k = 3(i-1) + j$. \mathbf{u}_h can be represented with coefficients v_k and vector nodal basis functions $\{\xi_k\}_{k \in \{1,2,\dots,3N\}}$ in the following way*

$$\mathbf{u}_h = \sum_{i=1}^N \xi_i \vec{v}_i = \sum_{i=1}^N \sum_{j=1}^3 \xi_i v_{i,j} \mathbf{e}_j =: \sum_{k=1}^{3N} \xi_k v_k,$$

where $\xi_k := \xi_i \mathbf{e}_j$. In section 3.4 we use such representation of \mathbf{u}_h for defining matrices.

We use M^X to denote the dimension of \tilde{Q}_h^X (cf. Remark 3.3.3). A function $p_h \in \tilde{Q}_h^X$ can be represented by

$$p_h = \sum_{i=1}^M q_i \eta_i + \sum_{j=1}^{M^X - M} q_j^X \eta_j^X,$$

where $\{q_i\}_{i \in \{1,2,\dots,M\}}$ and $\{q_j^X\}_{j \in \{1,2,\dots,M^X - M\}}$ are coefficients. We gather them into one vector $\vec{p} \in \mathbb{R}^{M^X}$. The first M elements of \vec{p} are q_i and the rest are q_j^X . We can also order

the basis functions as $\{\tilde{\eta}_i\}_{i \in \{1, 2, \dots, M^X\}}$:

$$\tilde{\eta}_i = \begin{cases} \eta_i & i \in \{1, 2, \dots, M\}, \\ \eta_j^X & i \in \{M+1, \dots, M^X\}, j \in \{1, 2, \dots, M^X - M\}, \end{cases}$$

and represent p_h by $p_h = \sum_{i=1}^{M^X} \tilde{q}_i \tilde{\eta}_i$. We can gather the coefficients \tilde{q}_i into a vector in \mathbb{R}^{M^X} , which is the same as \vec{p} .

3.3.4. Discretization of the surface force functional

The Galerkin discretization of the weak formulation (2.45) of the one fluid model leads to the surface functional

$$f_\Gamma(\mathbf{v}_h) = \int_\Gamma (\operatorname{div}_\Gamma \boldsymbol{\sigma}_\Gamma) \cdot \mathbf{v}_h \, ds, \quad \mathbf{v}_h \in \mathbf{V}_{0,h}.$$

Applying the partial integration rule (A.11) (together with (A.12)) and the property $\boldsymbol{\sigma}_\Gamma = \mathbf{P} \boldsymbol{\sigma}_\Gamma \mathbf{P}$ from (2.25), we obtain

$$f_\Gamma(\mathbf{v}_h) = \int_\Gamma (\operatorname{div}_\Gamma \boldsymbol{\sigma}_\Gamma) \cdot \mathbf{v}_h \, ds = - \int_\Gamma \operatorname{tr} \left(\boldsymbol{\sigma}_\Gamma (\nabla_\Gamma \mathbf{v}_h)^T \right) \, ds = - \sum_{i=1}^3 \int_\Gamma (\mathbf{e}_i^T \boldsymbol{\sigma}_\Gamma) \cdot \nabla_\Gamma v_i \, ds, \quad (3.12)$$

where $\mathbf{v}_h = (v_1, v_2, v_3)^T$ is the test function from $\mathbf{V}_{0,h}$.

Remark 3.3.5. *For the clean interface and the variable surface tension model, instead of applying the partial integration rule (A.11) to $f_\Gamma(\mathbf{v}_h)$ as in (3.12), we could also use the equivalent form in (2.36), i.e. $\operatorname{div}_\Gamma(\tau \mathbf{P}) = -\tau \kappa \mathbf{n} + \nabla_\Gamma \tau$ ($\nabla_\Gamma \tau = 0$ for the clean interface model). The surface force functional then takes the form*

$$f_\Gamma(\mathbf{v}_h) = \int_\Gamma (-\tau \kappa \mathbf{n} + \nabla_\Gamma \tau) \cdot \mathbf{v}_h \, ds.$$

Consider the Laplace-Beltrami characterization of the mean curvature, cf. [39],

$$-\Delta_\Gamma \operatorname{id}_\Gamma(x) = \kappa(x) \mathbf{n}(x), \quad x \in \Gamma, \quad (3.13)$$

where id_Γ is the identity function for $x \in \Gamma$. Inserting (3.13) in $f_\Gamma(\mathbf{v}_h)$, we obtain

$$f_\Gamma(\mathbf{v}_h) = \int_\Gamma \tau \Delta_\Gamma \operatorname{id}_\Gamma \cdot \mathbf{v}_h \, ds + \int_\Gamma \nabla_\Gamma \tau \cdot \mathbf{v}_h \, ds. \quad (3.14)$$

Applying the partial integration rule (A.11) and note that $\nabla \operatorname{id}_\Gamma = \mathbf{I}$ and $\nabla_\Gamma \operatorname{id}_\Gamma = \mathbf{P} \nabla \operatorname{id}_\Gamma = \mathbf{P}$, (3.14) takes the form

$$f_\Gamma(\mathbf{v}_h) = - \int_\Gamma \operatorname{tr} \left(\nabla_\Gamma \operatorname{id}_\Gamma (\nabla_\Gamma (\tau \mathbf{v}_h))^T \right) \, ds + \int_\Gamma \nabla_\Gamma \tau \cdot \mathbf{v}_h \, ds.$$

Note that $(\nabla_\Gamma (\tau \mathbf{v}_h))^T = \tau (\nabla_\Gamma \mathbf{v}_h)^T + \nabla_\Gamma \tau \mathbf{v}_h^T$, we obtain

$$\begin{aligned} f_\Gamma(\mathbf{v}_h) &= - \int_\Gamma \tau \operatorname{tr} \left(\nabla_\Gamma \operatorname{id}_\Gamma (\nabla_\Gamma \mathbf{v}_h)^T \right) \, ds - \int_\Gamma \operatorname{tr} (\nabla_\Gamma \operatorname{id}_\Gamma \nabla_\Gamma \tau \mathbf{v}_h^T) \, ds + \int_\Gamma \nabla_\Gamma \tau \cdot \mathbf{v}_h \, ds \\ &= - \int_\Gamma \tau \operatorname{tr} \left(\nabla_\Gamma \operatorname{id}_\Gamma (\nabla_\Gamma \mathbf{v}_h)^T \right) \, ds - \int_\Gamma \operatorname{tr} (\mathbf{P} \nabla_\Gamma \tau \mathbf{v}_h^T) \, ds + \int_\Gamma \nabla_\Gamma \tau \cdot \mathbf{v}_h \, ds \\ &= - \int_\Gamma \tau \operatorname{tr} \left(\nabla_\Gamma \operatorname{id}_\Gamma (\nabla_\Gamma \mathbf{v}_h)^T \right) \, ds = - \sum_{i=1}^3 \int_\Gamma \tau (\mathbf{e}_i^T \mathbf{P}) \cdot \nabla_\Gamma v_i \, ds, \end{aligned}$$

3. Components of the DROPS solver

which is the same as (3.12) with $\boldsymbol{\sigma}_\Gamma = \tau \mathbf{P}$.

We use the aforementioned Γ_h which consists of planar segments to approximate Γ . Hence we obtain an *approximated* force functional

$$f_{\Gamma_h}(\mathbf{v}_h) = - \int_{\Gamma_h} \text{tr} \left(\boldsymbol{\sigma}_\Gamma (\nabla_{\Gamma_h} \mathbf{v}_h)^T \right) ds = - \sum_{i=1}^3 \int_{\Gamma_h} (\mathbf{e}_i^T \boldsymbol{\sigma}_\Gamma) \cdot \nabla_{\Gamma_h} v_i ds, \quad (3.15)$$

which is used in our discretization. We postpone the numerical treatment of the surface stress tensor $\boldsymbol{\sigma}_\Gamma$ in (3.15) to Chapter 4.

We use the Galerkin method to discretize the equation (3.10) to obtain the fully discrete problem, i.e. we use the finite element spaces $(\mathbf{V}_{0,h}, \tilde{Q}_h^X(t_{n+1}))$ for discretizing $(\mathbf{u}^{n+1}, p^{n+1})$. The fully discrete problem is given by:

Given $\mathbf{u}_h^n \in \mathbf{V}_{0,h}$ with $n \geq 0$, determine $\mathbf{u}_h^{n+1} \in \mathbf{V}_{0,h}$ and $p_h^{n+1} \in \tilde{Q}_h^X(t_{n+1})$ such that for all $\mathbf{v}_h \in \mathbf{V}_{0,h}$ and $q_h \in \tilde{Q}_h^X(t_{n+1})$ the following equations hold

$$m_{n+\frac{1}{2}} \left(\frac{\mathbf{u}_h^{n+1} - \mathbf{u}_h^n}{\Delta t}, \mathbf{v}_h \right) + b(\mathbf{v}_h, p_h^{n+1}) = \theta \tilde{f}(\mathbf{u}_h^{n+1}, \mathbf{v}_h, \Gamma_h^{n+1}) + (1 - \theta) \tilde{f}(\mathbf{u}_h^n, \mathbf{v}_h, \Gamma_h^n), \quad (3.16a)$$

$$b(\mathbf{u}_h^{n+1}, q_h) = 0. \quad (3.16b)$$

Remark 3.3.6. In equations (3.16), the space $\tilde{Q}_h^X(t_{n+1})$ and the interface Γ_h^{n+1} are implicitly given by the level set function ϕ^{n+1} , which is unknown and can be solved by the discrete level set equation (3.8). Equation (3.16) and (3.8) together describe a fully coupled problem between the unknown quantities \mathbf{u}_h^{n+1} and ϕ^{n+1} . In DROPS, we use a decoupling scheme to solve the fully coupled system, which will be introduced in section 3.5.

3.4. Fully discrete problem

We summarize the fully discrete two-phase flow problem. We introduce the following matrices:

$$\begin{aligned} \mathbf{M}(\phi_h) &\in \mathbb{R}^{3N \times 3N}, & \mathbf{M}(\phi_h)_{i,j} &= \int_{\Omega} \rho(\phi_h) \boldsymbol{\xi}_i \cdot \boldsymbol{\xi}_j dx, \\ \mathbf{A}(\phi_h) &\in \mathbb{R}^{3N \times 3N}, & \mathbf{A}(\phi_h)_{i,j} &= \frac{1}{2} \int_{\Omega} \mu(\phi_h) \text{tr}(\mathbf{D}(\boldsymbol{\xi}_i) \mathbf{D}(\boldsymbol{\xi}_j)) dx, \\ \mathbf{N}(\mathbf{u}_h, \phi_h) &\in \mathbb{R}^{3N \times 3N}, & \mathbf{N}(\mathbf{u}_h, \phi_h)_{i,j} &= \int_{\Omega} \rho(\phi_h) (\mathbf{u}_h \cdot \nabla) \boldsymbol{\xi}_j \cdot \boldsymbol{\xi}_i dx, \\ \mathbf{B}(\phi_h) &\in \mathbb{R}^{M^X \times 3N}, & \mathbf{B}(\phi_h)_{i,j} &= - \int_{\Omega} \tilde{\eta}_i \text{div} \boldsymbol{\xi}_j dx. \end{aligned}$$

The mean mass matrix between time steps t_{n+1} and t_n is defined by

$$\tilde{\mathbf{M}}(\phi_h^{n+1}, \phi_h^n) := \frac{1}{2} \left(\mathbf{M}(\phi_h^{n+1}) + \mathbf{M}(\phi_h^n) \right).$$

We also introduce the following vectors:

$$\begin{aligned}\vec{\mathbf{g}}(\phi_h) &\in \mathbb{R}^{3N}, \quad \vec{\mathbf{g}}(\phi_h)_i = \int_{\Omega} \rho(\phi_h) \mathbf{g} \cdot \boldsymbol{\xi}_i \, dx, \\ \vec{\mathbf{f}}_{\Gamma_h}(\phi_h) &\in \mathbb{R}^{3N}, \quad \vec{\mathbf{f}}_{\Gamma_h}(\phi_h)_i = - \int_{\Gamma_h} \text{tr} \left(\boldsymbol{\sigma}_{\Gamma}(\nabla_{\Gamma_h} \boldsymbol{\xi}_i)^T \right) \, ds.\end{aligned}$$

Note that the discretization of the surface stress tensor $\boldsymbol{\sigma}_{\Gamma}$ has not been introduced yet. Detail information can be found in chapter 4. In remark 2.8.2 we mentioned that for the viscous interface model the surface force functional $f_{\Gamma}(\mathbf{v})$ also depends on the velocity field \mathbf{u} . Hence in the discrete setting we need to introduce a surface force vector as follows

$$\vec{\mathbf{f}}_{\Gamma_h}(\mathbf{u}_h, \phi_h) \in \mathbb{R}^{3N}, \quad \vec{\mathbf{f}}_{\Gamma_h}(\mathbf{u}_h, \phi_h)_i = - \int_{\Gamma_h} \text{tr} \left(\boldsymbol{\sigma}_{\Gamma}(\mathbf{u}_h)(\nabla_{\Gamma_h} \boldsymbol{\xi}_i)^T \right) \, ds. \quad (3.17)$$

The fully discrete two-phase flow problem is given by:

Given $\vec{\mathbf{u}}^0$ and $\vec{\phi}^0$, for $n \geq 0$ determine $\vec{\mathbf{u}}^{n+1}$, \vec{p}^{n+1} and $\vec{\phi}^{n+1}$ from

$$\begin{aligned}\frac{1}{\Delta t} \tilde{\mathbf{M}}(\vec{\phi}^{n+1}, \vec{\phi}^n) \vec{\mathbf{u}}^{n+1} + \theta \left(\mathbf{A}(\vec{\phi}^{n+1}) + \mathbf{N}(\vec{\mathbf{u}}^{n+1}, \vec{\phi}^{n+1}) \right) \vec{\mathbf{u}}^{n+1} + \mathbf{B}(\vec{\phi}^{n+1})^T \vec{p}^{n+1} \\ = \frac{1}{\Delta t} \tilde{\mathbf{M}}(\vec{\phi}^{n+1}, \vec{\phi}^n) \vec{\mathbf{u}}^n - (1 - \theta) \left(\mathbf{A}(\vec{\phi}^n) + \mathbf{N}(\vec{\mathbf{u}}^n, \vec{\phi}^n) \right) \vec{\mathbf{u}}^n \\ + \theta \left(\vec{\mathbf{g}}(\vec{\phi}^{n+1}) + \vec{\mathbf{f}}_{\Gamma_h}(\vec{\phi}^{n+1}) \right) + (1 - \theta) \left(\vec{\mathbf{g}}(\vec{\phi}^n) + \vec{\mathbf{f}}_{\Gamma_h}(\vec{\phi}^n) \right),\end{aligned} \quad (3.18a)$$

$$\mathbf{B}(\vec{\phi}^{n+1}) \vec{\mathbf{u}}^{n+1} = 0, \quad (3.18b)$$

$$\begin{aligned}\frac{\vec{\phi}^{n+1} - \vec{\phi}^n}{\Delta t} = \theta \mathbf{M}_{\phi}(\vec{\mathbf{u}}^{n+1})^{-1} \left(-\mathbf{N}_{\phi}(\vec{\mathbf{u}}^{n+1}) \vec{\phi}^{n+1} - \vec{\phi}_D(\vec{\mathbf{u}}^{n+1}) \right) \\ + (1 - \theta) \mathbf{M}_{\phi}(\vec{\mathbf{u}}^n)^{-1} \left(-\mathbf{N}_{\phi}(\vec{\mathbf{u}}^n) \vec{\phi}^n - \vec{\phi}_D(\vec{\mathbf{u}}^n) \right)\end{aligned} \quad (3.18c)$$

Remark 3.4.1. In (3.18c) we need to solve two linear systems numerically, which correspond to $\mathbf{M}_{\phi}(\vec{\mathbf{u}}^{n+1})^{-1}$ and $\mathbf{M}_{\phi}(\vec{\mathbf{u}}^n)^{-1}$. By defining a new variable

$$\vec{\mathbf{w}}^n = \mathbf{M}_{\phi}(\vec{\mathbf{u}}^n)^{-1} \left(-\mathbf{N}_{\phi}(\vec{\mathbf{u}}^n) \vec{\phi}^n - \vec{\phi}_D(\vec{\mathbf{u}}^n) \right)$$

and inserting $\vec{\mathbf{w}}^n$ in (3.18c), we can avoid one solution process for linear system and compute $\vec{\phi}^{n+1}$. $\vec{\mathbf{w}}^{n+1}$ is then updated by $\theta \vec{\mathbf{w}}^{n+1} = (\vec{\phi}^{n+1} - \vec{\phi}^n)/\Delta t - (1 - \theta) \vec{\mathbf{w}}^n$. We refer to [39] for details.

3.5. Decoupling and linearization strategy

The equation system (3.18) has a strong coupling between the fluid quantities and the level set function. We need a proper *decoupling* strategy to solve this system. In this section, we introduce the decoupling strategy used in DROPS. For simplicity, the implicit Euler scheme ($\theta = 1$) is considered, which is also the common scheme used in the numerical experiments presented in the following chapters. The same strategy can also be used in other time integration schemes.

3. Components of the DROPS solver

Clean interface model and variable surface tension model. In such models the surface force functional f_{Γ_h} depends on Γ_h but not on \mathbf{u}_h , cf. (2.34) and (3.15). The discrete system of the implicit Euler scheme is given by:

Given $\bar{\mathbf{u}}^0$ and $\bar{\phi}^0$, for $n \geq 0$ determine $\bar{\mathbf{u}}^{n+1}$, \bar{p}^{n+1} and $\bar{\phi}^{n+1}$ from

$$\begin{aligned} \frac{1}{\Delta t} \tilde{\mathbf{M}}(\bar{\phi}^{n+1}, \bar{\phi}^n) \bar{\mathbf{u}}^{n+1} + \left(\mathbf{A}(\bar{\phi}^{n+1}) + \mathbf{N}(\bar{\mathbf{u}}^{n+1}, \bar{\phi}^{n+1}) \right) \bar{\mathbf{u}}^{n+1} + \mathbf{B}(\bar{\phi}^{n+1})^T \bar{p}^{n+1} \\ = \frac{1}{\Delta t} \tilde{\mathbf{M}}(\bar{\phi}^{n+1}, \bar{\phi}^n) \bar{\mathbf{u}}^n + \bar{\mathbf{g}}(\bar{\phi}^{n+1}) + \bar{\mathbf{f}}_{\Gamma_h}(\bar{\phi}^{n+1}), \end{aligned} \quad (3.19a)$$

$$\mathbf{B}(\bar{\phi}^{n+1}) \bar{\mathbf{u}}^{n+1} = 0, \quad (3.19b)$$

$$\frac{1}{\Delta t} \mathbf{M}_\phi(\bar{\mathbf{u}}^{n+1}) \bar{\phi}^{n+1} + \mathbf{N}_\phi(\bar{\mathbf{u}}^{n+1}) \bar{\phi}^{n+1} = \frac{1}{\Delta t} \mathbf{M}_\phi(\bar{\mathbf{u}}^{n+1}) \bar{\phi}^n - \bar{\phi}_D(\bar{\mathbf{u}}^{n+1}). \quad (3.19c)$$

To simplify our notations, we introduce the unknown variables: $\bar{\mathbf{x}} = \bar{\mathbf{u}}^{n+1}$, $\bar{\mathbf{y}} = \bar{p}^{n+1}$ and $\bar{\mathbf{z}} = \bar{\phi}^{n+1}$. The mean mass matrix $\tilde{M}(\bar{\phi}^{n+1}, \bar{\phi}^n)$ is denoted by $\tilde{M}(\bar{\mathbf{z}})$ to indicate the dependence on $\bar{\phi}^{n+1}$. The known solutions $\bar{\mathbf{u}}^n$ and $\bar{\phi}^n$ are denoted by $\bar{\mathbf{x}}^0$ and $\bar{\mathbf{z}}^0$ respectively. The coupled system is then given by:

$$\frac{1}{\Delta t} \tilde{\mathbf{M}}(\bar{\mathbf{z}}) \bar{\mathbf{x}} + \left(\mathbf{A}(\bar{\mathbf{z}}) + \mathbf{N}(\bar{\mathbf{x}}, \bar{\mathbf{z}}) \right) \bar{\mathbf{x}} + \mathbf{B}(\bar{\mathbf{z}})^T \bar{\mathbf{y}} = \frac{1}{\Delta t} \tilde{\mathbf{M}}(\bar{\mathbf{z}}) \bar{\mathbf{x}}^0 + \bar{\mathbf{g}}(\bar{\mathbf{z}}) + \bar{\mathbf{f}}_{\Gamma_h}(\bar{\mathbf{z}}), \quad (3.20a)$$

$$\mathbf{B}(\bar{\mathbf{z}}) \bar{\mathbf{x}} = 0, \quad (3.20b)$$

$$\frac{1}{\Delta t} \mathbf{M}_\phi(\bar{\mathbf{x}}) \bar{\mathbf{z}} + \mathbf{N}_\phi(\bar{\mathbf{x}}) \bar{\mathbf{z}} = \frac{1}{\Delta t} \mathbf{M}_\phi(\bar{\mathbf{x}}) \bar{\mathbf{z}}^0 - \bar{\phi}_D(\bar{\mathbf{x}}). \quad (3.20c)$$

Viscous interface model. According to the Boussinesq-Scriven law (2.37) σ_Γ also depends on the velocity field. Hence the surface force vector $\bar{\mathbf{f}}_{\Gamma_h}(\bar{\mathbf{z}})$ in (3.20a) has to be replaced by $\bar{\mathbf{f}}_{\Gamma_h}(\bar{\mathbf{x}}, \bar{\mathbf{z}})$.

3.5.1. Decoupling of fluid dynamics and the level set equation

In DROPS, a Gauss-Seidel type iterative method is used to decouple the solving process of $\bar{\mathbf{u}}^{n+1}$ and $\bar{\phi}^{n+1}$ in (3.19). Given $\bar{\mathbf{x}}^0$ and $\bar{\mathbf{z}}^0$, iterate for $k = 0, 1, 2, \dots$ until convergence or the maximal iteration number is reached:

1. Solve for $\bar{\mathbf{z}}^{k+1}$ from

$$\frac{1}{\Delta t} \mathbf{M}_\phi(\bar{\mathbf{x}}^k) \bar{\mathbf{z}}^{k+1} + \mathbf{N}_\phi(\bar{\mathbf{x}}^k) \bar{\mathbf{z}}^{k+1} = \frac{1}{\Delta t} \mathbf{M}_\phi(\bar{\mathbf{x}}^k) \bar{\mathbf{z}}^0 - \bar{\phi}_D(\bar{\mathbf{x}}^k). \quad (3.21)$$

2. Solve for $\bar{\mathbf{x}}^{k+1}$ and $\bar{\mathbf{y}}^{k+1}$ with the known $\bar{\mathbf{z}}^{k+1}$ from

$$\begin{aligned} \frac{1}{\Delta t} \tilde{\mathbf{M}}(\bar{\mathbf{z}}^{k+1}) \bar{\mathbf{x}}^{k+1} + \left(\mathbf{A}(\bar{\mathbf{z}}^{k+1}) + \mathbf{N}(\bar{\mathbf{x}}^{k+1}, \bar{\mathbf{z}}^{k+1}) \right) \bar{\mathbf{x}}^{k+1} + \mathbf{B}(\bar{\mathbf{z}}^{k+1})^T \bar{\mathbf{y}}^{k+1} \\ = \frac{1}{\Delta t} \tilde{\mathbf{M}}(\bar{\mathbf{z}}^{k+1}) \bar{\mathbf{x}}^0 + \bar{\mathbf{g}}(\bar{\mathbf{z}}^{k+1}) + \bar{\mathbf{f}}_{\Gamma_h}(\bar{\mathbf{z}}^{k+1}), \end{aligned} \quad (3.22a)$$

$$\mathbf{B}(\bar{\mathbf{z}}^{k+1}) \bar{\mathbf{x}}^{k+1} = 0. \quad (3.22b)$$

In (3.22a) $\vec{\mathbf{f}}_{\Gamma_h}(\vec{\mathbf{z}}^{k+1})$ has to be replaced by $\vec{\mathbf{f}}_{\Gamma_h}(\vec{\mathbf{x}}^{k+1}, \vec{\mathbf{z}}^{k+1})$ for viscous interface, which also depends on the unknown velocity $\vec{\mathbf{x}}^{k+1}$. In chapter 4 we explain how to solve (3.22) for a viscous interface with $\vec{\mathbf{f}}_{\Gamma_h}(\vec{\mathbf{x}}^{k+1}, \vec{\mathbf{z}}^{k+1})$.

In step 2, we need to solve a nonlinear saddle point problem due to the convection term $\mathbf{N}(\vec{\mathbf{x}}^{k+1}, \vec{\mathbf{z}}^{k+1})$. In DROPS, a reparametrization method for the level set equation and a volume correction method are also incorporated in the Gauss-Seidel iteration, we refer to [39] for details.

Remark 3.5.1. *Due to the strong coupling between the surface force and the level set function the Gauss-Seidel type of decoupling method introduced above converges slowly, cf. Table 4.1 in section 4.2.1. In chapter 4 we describe a convergence acceleration method.*

Remark 3.5.2. *We mention one important aspect of the decoupling scheme here. In each iteration, $\vec{\mathbf{z}}^{k+1}$, $\vec{\mathbf{x}}^{k+1}$ and $\vec{\mathbf{y}}^{k+1}$ are tentative solutions at time step t_{n+1} , which is easily seen from the structure of the equations (3.21) and (3.22), i.e. the quotient form of the time differentiation.*

The decoupling scheme introduced above can also be treated as a fixed-point iteration. To this end, we define two solution operators \mathbf{S}_1 and \mathbf{S}_2 as follows:

$$\vec{\mathbf{z}}^{k+1} = \mathbf{S}_1(\vec{\mathbf{x}}^k), \quad \vec{\mathbf{x}}^{k+1} = \mathbf{S}_2(\vec{\mathbf{z}}^{k+1}),$$

which corresponds to (3.21) and (3.22) respectively. The decoupling scheme is then given by

$$\vec{\mathbf{x}}^{k+1} = \mathbf{S}_2 \left(\mathbf{S}_1(\vec{\mathbf{x}}^k) \right), \quad (3.23)$$

with the initial data $\vec{\mathbf{x}}^0 = \vec{\mathbf{u}}^n$. A fixed point, denoted by $\vec{\mathbf{x}}^*$, of (3.23) is the solution of the decoupling scheme. In DROPS, a Broyden type of method is used to accelerate the convergence of the fixed-point iteration (3.23). More details can be found in [39].

3.5.2. Linearization of the Navier-Stokes equation

As it is described in the previous section, a nonlinear saddle point problem (3.22) has to be solved in each iteration of the decoupled system. An *adaptive defect correction* method is used in DROPS to linearize the nonlinear problem (3.22), which is a Richardson type of method. We define a matrix $\mathbf{L} = \mathbf{L}(\vec{\mathbf{x}})$:

$$\mathbf{L}(\vec{\mathbf{x}}^{k+1}) := \begin{pmatrix} \frac{1}{\Delta t} \tilde{\mathbf{M}}(\vec{\mathbf{z}}^{k+1}) + \mathbf{A}(\vec{\mathbf{z}}^{k+1}) + \mathbf{N}(\vec{\mathbf{x}}^{k+1}, \vec{\mathbf{z}}^{k+1}) & \mathbf{B}(\vec{\mathbf{z}}^{k+1})^T \\ \mathbf{B}(\vec{\mathbf{z}}^{k+1}) & 0 \end{pmatrix}.$$

For simplicity, we rename the unknowns: $\vec{\mathbf{x}}_* := \vec{\mathbf{x}}^{k+1}$ and $\vec{\mathbf{y}}_* := \vec{\mathbf{y}}^{k+1}$ and define the right hand side of (3.22a) as $\vec{\mathbf{b}} := \frac{1}{\Delta t} \tilde{\mathbf{M}}(\vec{\mathbf{z}}^{k+1}) \vec{\mathbf{x}}^0 + \vec{\mathbf{g}}(\vec{\mathbf{z}}^{k+1}) + \vec{\mathbf{f}}_{\Gamma_h}(\vec{\mathbf{z}}^{k+1})$. The matrix $\mathbf{L}(\vec{\mathbf{x}}_*)$ is invertible. Hence the nonlinear problem (3.22) can be rewritten as

$$\mathbf{L}(\vec{\mathbf{x}}_*) \begin{pmatrix} \vec{\mathbf{x}}_* \\ \vec{\mathbf{y}}_* \end{pmatrix} = \begin{pmatrix} \vec{\mathbf{b}} \\ 0 \end{pmatrix}. \quad (3.24)$$

A Richardson type of method for equation (3.24) is given by:

3. Components of the DROPS solver

Given a proper initial guess $\vec{\mathbf{x}}_*^0$ and $\vec{\mathbf{y}}_*^0$, iterate for $\ell = 0, 1, 2, \dots$ until convergence or the maximal iteration number is reached:

$$\begin{pmatrix} \vec{\mathbf{x}}_*^{\ell+1} \\ \vec{\mathbf{y}}_*^{\ell+1} \end{pmatrix} = \begin{pmatrix} \vec{\mathbf{x}}_*^\ell \\ \vec{\mathbf{y}}_*^\ell \end{pmatrix} - \omega_{\ell+1} \mathbf{L}(\vec{\mathbf{x}}_*^\ell)^{-1} \left(\mathbf{L}(\vec{\mathbf{x}}_*^\ell) \begin{pmatrix} \vec{\mathbf{x}}_*^\ell \\ \vec{\mathbf{y}}_*^\ell \end{pmatrix} - \begin{pmatrix} \vec{\mathbf{b}} \\ 0 \end{pmatrix} \right), \quad (3.25)$$

where $\omega_{\ell+1}$ is a scalar parameter adaptively chosen for each iteration, cf. section 5.1 in [39].

3.6. Numerical treatment of surfactant transport on the interface

In this section, we introduce a space-time trace finite element method for solving the surfactant transport equation (2.42) on the moving interface $\Gamma(t)$. We refer to [63, 60] for the details. Such a trace finite element method was first introduced for a Laplace-Beltrami equation on a stationary interface, cf. [61]. This method has been further extended to an advection-diffusion problem [64]. Other numerical aspects and applications of this method can be found in [59, 62, 71, 36, 32, 34].

3.6.1. Weak formulations

For the presentation of the method we assume that the evolution of $\Gamma(t)$ and the velocity field $\mathbf{u}(\mathbf{x}, t)$ are *known* for $t \in [t_0, T]$. The unknown variable is the surfactant concentration $S(\mathbf{x}, t)$ for $\mathbf{x} \in \Gamma(t)$.

We use a space-time formulation of the problem (2.42). The space-time manifold is denoted by

$$\mathcal{S} = \bigcup_{t \in (t_0, T]} \Gamma(t) \times \{t\},$$

which is a subset of \mathbb{R}^4 . We use $L^2(\mathcal{S})$ to denote the space of square integrable functions on \mathcal{S} . Instead of using the standard inner product on $L^2(\mathcal{S})$, based on the equality

$$\int_{t_0}^T \int_{\Gamma(t)} f(s, t) ds dt = \int_{\mathcal{S}} f(s) (1 + (\mathbf{u} \cdot \mathbf{n}_\Gamma)^2)^{-\frac{1}{2}} ds,$$

we use the inner product

$$(v, w)_{L^2(\mathcal{S})} = \int_{t_0}^T \int_{\Gamma(t)} vw ds dt$$

and the corresponding norm on $L^2(\mathcal{S})$. We define the following function spaces based on $L^2(\mathcal{S})$:

$$H := \{v \in L^2(\mathcal{S}) : \|\nabla_\Gamma v\|_{L^2(\mathcal{S})} < \infty\}, \quad (3.26)$$

with the inner product $(v, w)_H = (v, w)_{L^2(\mathcal{S})} + (\nabla_\Gamma v, \nabla_\Gamma w)_{L^2(\mathcal{S})}$ and the induced norm $\|v\|_H^2 = \int_{t_0}^T \int_{\Gamma(t)} v^2 + \nabla_\Gamma v \cdot \nabla_\Gamma v ds dt$.

3.6. Numerical treatment of surfactant transport on the interface

Define the material derivative of $v \in H$ as the functional $\dot{v} : C_0^1(\mathcal{S}) \rightarrow \mathbb{R}$ (cf. derivation in [63]),

$$\langle \dot{v}, \phi \rangle = - \int_{t_0}^T \int_{\Gamma(t)} v \dot{\phi} + v \phi \operatorname{div}_{\Gamma} \mathbf{u} \, ds dt, \quad \text{for all } \phi \in C_0^1(\mathcal{S}). \quad (3.27)$$

Assume for some $v \in H$, the following norm is *bounded*:

$$\|\dot{v}\|_{H'} = \sup_{\phi \in C_0^1(\mathcal{S}), \phi \neq 0} \frac{\langle \dot{v}, \phi \rangle}{\|\phi\|_H}$$

In [63] Lemma 3.5, the authors have proved that: the space H is a Hilbert space, and the space $C_0^1(\mathcal{S})$ is dense in H , i.e. $H = \overline{C_0^1(\mathcal{S})}^{\|\cdot\|_H}$. Hence \dot{v} can be extended to a linear bounded functional on H , i.e. $\dot{v} \in H'$. We define the space W as

$$W := \{v \in H : \dot{v} \in H'\}, \quad (3.28)$$

with the norm $\|v\|_W^2 := \|v\|_H^2 + \|\dot{v}\|_{H'}^2$. In [63] Theorem 3.6, it is proved that: W is a Hilbert space, $C^1(\mathcal{S})$ is dense in W , and for every $t \in [t_0, T]$ there is a well-defined trace operator $u|_{\Gamma(t)}$ for functions in W , i.e. $u|_{\Gamma(t)} : W \rightarrow L^2(\Gamma(t))$ is a bounded linear operator.

We define a symmetric bilinear form

$$a_s(v, w) := D_{\Gamma}(\nabla_{\Gamma} v, \nabla_{\Gamma} w)_{L^2(\mathcal{S})} + (\operatorname{div}_{\Gamma} \mathbf{u} v, w)_{L^2(\mathcal{S})}, \quad v, w \in H.$$

Assume $\operatorname{div}_{\Gamma} \mathbf{u}$ is bounded and denote $\mu_{\infty} := \|\operatorname{div}_{\Gamma} \mathbf{u}\|_{L^{\infty}(\mathcal{S})}$, the bilinear form $a_s(v, w)$ is then continuous on $H \times H$:

$$a_s(v, w) \leq (D_{\Gamma} + \mu_{\infty}) \|v\|_H \|w\|_H.$$

We choose W as the trial space and H as the test space. One possible weak formulation of (2.42) is given by:

Find $S \in W$ with $S|_{\Gamma(t_0)} = S_0$, such that

$$\langle \dot{S}, v \rangle + a_s(S, v) = 0, \quad \text{for all } v \in H, \quad (3.29)$$

where S_0 is the initial distribution of S at t_0 .

The well-posedness of (3.29) is shown in [63] for a transformed zero initial data problem. The analysis is based on the continuity and inf-sup conditions for the term $\langle \dot{S}, v \rangle + a_s(S, v)$, cf. [17].

From an implementation point of view, we use a time-discontinuous variant of (3.29), such that a time stepping discontinuous Galerkin method can be performed. We partition the time interval $(t_0, T]$ by $t_0 < t_1 < \dots < t_N = T$. A sub-time-interval is denoted by $I_n = (t_{n-1}, t_n]$. The space-time interface corresponding to I_n is denoted by $\mathcal{S}^n := \bigcup_{t \in I_n} \Gamma(t) \times \{t\}$ and $\mathcal{S} = \bigcup_{n \in [1, N]} \mathcal{S}^n$. The following spaces are defined

$$\begin{aligned} H_n &:= \{v \in H : v = 0 \text{ on } \mathcal{S} \setminus \mathcal{S}^n\}, \\ W_n &:= \{v \in H_n : \dot{v} \in H'_n\}, \quad \text{with } \|v\|_{W_n}^2 = \|v\|_H^2 + \|\dot{v}\|_{H'_n}^2, \\ W^b &:= \bigoplus_{n=1}^N W_n, \quad \text{with } \|v\|_{W^b}^2 := \sum_{n=1}^N \|v\|_{W_n}^2. \end{aligned}$$

3. Components of the DROPS solver

For $v \in H$ we define $v_n := v|_{\mathcal{S}^n} \in H_n$. For $v \in W_n$, the following one-sided limits are well defined in $L^2(\Gamma(t_n))$ [63]:

$$v_n^+ = \lim_{\epsilon \rightarrow 0^+} v(\cdot, t_n + \epsilon), \quad v_n^- = \lim_{\epsilon \rightarrow 0^+} v(\cdot, t_n - \epsilon).$$

At t_0 and t_N only v_0^+ and v_N^- are defined respectively. We define a jump operator as follows: for $v \in W^b$, $[v]_n := v_n^+ - v_n^-$ with $n \in \mathbb{N}$, and $v_0^- = v_0$, which is the initial data. The following bilinear forms are defined on $W^b \times W^b$:

$$\begin{aligned} d(v, w) &:= \sum_{n=1}^N ([v]_{n-1}, w_{n-1}^+)_{L^2(\Gamma(t_{n-1}))} \\ \langle \dot{v}, w \rangle_b &:= \sum_{n=1}^N \langle \dot{v}_n, w_n \rangle_{I_n}, \end{aligned}$$

where $\langle \dot{v}_n, \phi \rangle_{I_n}$ is defined by

$$\langle \dot{v}_n, \phi \rangle_{I_n} = - \int_{t_{n-1}}^{t_n} \int_{\Gamma(t)} v_n \dot{\phi} + v_n \phi \operatorname{div}_{\Gamma} \mathbf{u} \, ds dt, \quad \text{for all } \phi \in C_0^1(\mathcal{S}^n).$$

The time-discontinuous variant of (3.29) is given by:

Find $S \in W^b$ such that

$$\langle \dot{S}, v \rangle_b + a_s(S, v) + d(S, v) = 0, \quad \text{for all } v \in W^b. \quad (3.30)$$

The initial condition S_0 is built in $d(S, v)$, i.e. the initial condition is satisfied weakly. The well-posedness of (3.30) and the consistency of (3.29) and (3.30) are shown in [63].

3.6.2. Space-time finite element method

We apply a Galerkin space-time finite element method to the weak formulation (3.30). We choose a subspace $W_h \subset W^b$, and find $S_h \in W_h$ such that

$$\langle \dot{S}_h, v_h \rangle_b + a_s(S_h, v_h) + d(S_h, v_h) = 0, \quad \text{for all } v_h \in W_h. \quad (3.31)$$

The space W_h is constructed as follows. We partition the space-time volume $\mathcal{V} = \Omega \times (t_0, T] \subset \mathbb{R}^4$ into time slabs $\mathcal{V}_n := \Omega \times I_n$ with $I_n = (t_{n-1}, t_n]$ as described above and $1 \leq n \leq N$. The spatial triangulation of Ω in I_n is denoted by \mathcal{T}_n , cf. section 3.3. $\mathcal{P}_n := \mathcal{T}_n \times I_n$ is a triangulation of the space-time slab \mathcal{V}_n into space-time *prismatic* elements. $\mathcal{P}_h := \bigcup_{1 \leq n \leq N} \mathcal{P}_n$ is the triangulation of the space-time volume \mathcal{V} . If adaptive refinement/coarsening is performed, the triangulation \mathcal{T}_n will change with time, and the elements of \mathcal{P}_h might not match at the boundary $t = t_n$. The spatial triangulation \mathcal{T}_n is not fitted to $\Gamma(t_n)$, cf. section 3.3.2, thus the space-time triangulation \mathcal{P}_h is not fitted to \mathcal{S} . In Figure 3.5, we show a space-time volume for a two-dimensional domain. In the figure, the space-time interface cuts through the space-time triangular prismatic elements.

We use Q_n to denote the space of continuous piecewise linear finite element space on the spatial triangulation \mathcal{T}_n , and define the space-time finite element space on \mathcal{P}_n

$$Q_n := \{ q : \mathcal{V}_n \rightarrow \mathbb{R} \mid q(x, t) = v_0(x) + tv_1(x), v_0, v_1 \in Q_n \}.$$

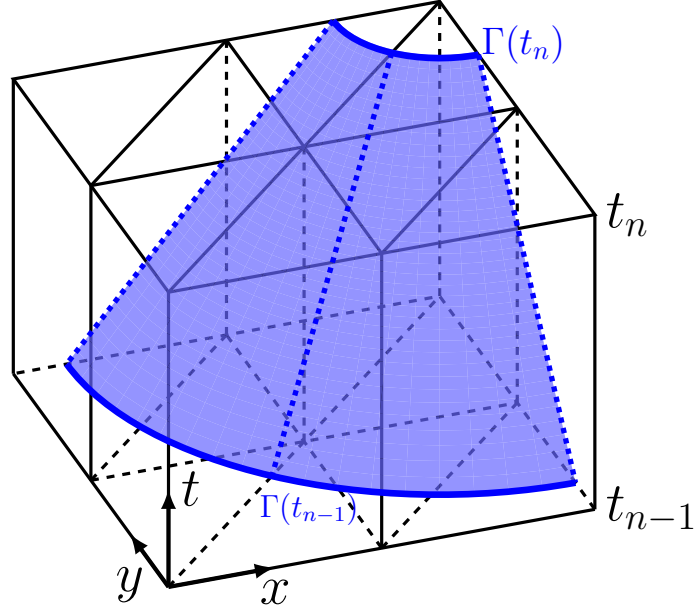


Figure 3.5.: An example of a space-time interface for a two-dimensional domain.

$\mathcal{Q}_h := \{q : \mathcal{V} \rightarrow \mathbb{R} \mid q|_{\mathcal{V}_n} \in \mathcal{Q}_n\}$ is the space of piecewise linear functions on the space-time triangulation \mathcal{P}_h . Functions in \mathcal{Q}_h are continuous in space and discontinuous in time.

We use a *trace* space of \mathcal{Q}_n on the space-time interface \mathcal{S}^n :

$$W_h^n := \{w : \mathcal{S}^n \rightarrow \mathbb{R} \mid w = v|_{\mathcal{S}^n}, v \in \mathcal{Q}_n\}.$$

The test and trial space W_h in (3.31) is defined by

$$W_h := \bigoplus_{n=1}^N W_h^n$$

Since $S_h \in C^1(\mathcal{V}_n)$ for all $n \in [1, N]$, the term $\langle \dot{S}_h, v_h \rangle_b$ in (3.31) can be reformulated as

$$\langle \dot{S}_h, v_h \rangle_b = \sum_{n=1}^N \int_{t_{n-1}}^{t_n} \int_{\Gamma(t)} \left(\frac{\partial S_h}{\partial t} + \mathbf{u} \cdot \nabla S_h \right) v_h \, ds dt.$$

We can solve the problem (3.31) with a time-stepping mechanism by treating one time slab after another.

Remark 3.6.1. *We briefly comment on the major tasks of implementing the space-time trace finite element method. More details are found in [32]. We assume that the velocity field \mathbf{u} and the level set function ϕ are known in a time interval $[t_{n-1}, t_n]$. The coupling problem between fluid dynamics and the surfactant equation is treated in chapter 7. For each time slab \mathcal{V}_n we write an implicit space-time problem for the unknown function $S_h|_{I_n} \in W_h^n$. There are two major numerical tasks, namely approximating the space-time integrals, i.e. $\langle \dot{S}_h, v_h \rangle_b$ and $a_s(S_h, v_h)$, and the representation of functions in W_h^n . For both tasks we need an approximation of the space-time manifold \mathcal{S}^n , which is denoted by \mathcal{S}^h (for simplicity we omit the time interval I_n here, but remember that the approximation is done time-slab-wise). We use the level set function to capture the evolution of $\Gamma(t)$, cf. section 3.2, thus the space time manifold \mathcal{S}^n is the zero level (in \mathbb{R}^4) of the level*

3. Components of the DROPS solver

set function $\phi(\mathbf{x}, t)$ for $t \in I_n$. We use $(h, \Delta t)$ to denote the grid size of a space-time prismatic element $P := T \times I_n \in \mathcal{P}_h$ with $T \in \mathcal{T}_n$. The approximation \mathcal{S}^h is constructed by determining the zero level of $I(\phi_h)$, which is the nodal interpolation function of the discrete level set function ϕ_h on a regular refinement of the space-time prismatic element P , i.e. with grid size $(1/2h, 1/2\Delta t)$. The space-time integrals are then approximated on \mathcal{S}^h with a proper quadrature rule, cf. [32].

The functions in the trace space \tilde{W}_h^n , which corresponds to \mathcal{S}^h , are represented with nodal basis functions from the space-time finite element space \mathcal{Q}_n . We only include nodal basis functions belonging to space-time elements $P \in \mathcal{Q}_n$ with the property $P \cap \mathcal{S}^h \neq \emptyset$, i.e. elements which are “cut” by the space-time interface \mathcal{S}^h . Functions in \tilde{W}_h^n are then represented by a linear combination of the nodal basis functions of the “cut” elements.

There are many open problems related to the resulting linear system of the space-time method (3.31). We do not treat these problems here. In Table 7.5 and Table 7.6, we present some results concerning the linear algebra aspect for a model problem.

4. Numerical treatment of surface stress tensor

In this chapter we introduce the numerical treatment of the surface stress tensor $\boldsymbol{\sigma}_\Gamma$ in the surface force functional $f_{\Gamma_h}(\mathbf{v}_h)$, cf. (3.15). The surface force functional $f_{\Gamma_h}(\mathbf{v}_h) : \mathbf{V}_h \rightarrow \mathbb{R}$ takes the form

$$f_{\Gamma_h}(\mathbf{v}_h) = - \int_{\Gamma_h} \text{tr} \left(\boldsymbol{\sigma}_\Gamma (\nabla_{\Gamma_h} \mathbf{v}_h)^T \right) ds = - \sum_{i=1}^3 \int_{\Gamma_h} (\mathbf{e}_i^T \boldsymbol{\sigma}_\Gamma) \cdot \nabla_{\Gamma_h} v_i ds,$$

and the integration is performed on the piecewise planar interface Γ_h , cf. section 3.3.2.

We consider two types of constitutive relations for $\boldsymbol{\sigma}_\Gamma$, namely the simple one (2.34)

$$\boldsymbol{\sigma}_\Gamma = \tau \mathbf{P},$$

which models the clean interface and the variable surface tension case, and the viscous interface model (2.37)

$$\boldsymbol{\sigma}_\Gamma = \tau \mathbf{P} + (\lambda_\Gamma - \mu_\Gamma) \text{div}_\Gamma \mathbf{u} \mathbf{P} + \mu_\Gamma \mathbf{D}_\Gamma(\mathbf{u}),$$

where $\mathbf{D}_\Gamma(\mathbf{u}) = \mathbf{P}(\nabla_\Gamma \mathbf{u} + (\nabla_\Gamma \mathbf{u})^T) \mathbf{P}$ is the surface rate of strain tensor.

The numerical treatment of the surface stress tensor $\boldsymbol{\sigma}_\Gamma$ is a main new contribution of this thesis. By introducing $\boldsymbol{\sigma}_\Gamma$, the *generalized* interface momentum balance condition is given by (2.28), which is the basis for treating complex interfaces with surface forces that may be more general than surface tension only, c.f. section 2.6.2. The introduction of $\boldsymbol{\sigma}_\Gamma$ allows a special numerical treatment of surface forces. The surface force functional (3.12) is easier to handle in the sense that it does not have an explicit curvature term, c.f. Remark 3.3.5. We consider only a few models for $\boldsymbol{\sigma}_\Gamma$. The development of appropriate continuum models for $\boldsymbol{\sigma}_\Gamma$ in cases with complex interfaces is an active research field in rheology.

A major task in treating $\boldsymbol{\sigma}_\Gamma$ is the discretization of the projection operator \mathbf{P} . Recall that $\mathbf{P} = \mathbf{I} - \mathbf{n}\mathbf{n}^T$. Hence we need to approximate the surface normals $\mathbf{n}(\mathbf{x})$ for $\mathbf{x} \in \Gamma(t)$ on the discrete level, i.e. with the piecewise planar interface Γ_h and the discrete level set function ϕ_h . Another topic in this chapter is the role of $f_{\Gamma_h}(\mathbf{v}_h)$ in the decoupling scheme introduced in section 3.5.1. With numerical experiments we show that the original decoupling scheme converges slowly due to the strong coupling between the fluid dynamics and the level set equation through $f_{\Gamma_h}(\mathbf{v}_h)$. We present a convergence acceleration technique by improving the approximation of the surface force functional in the solution process of Navier-Stokes equations (3.22). The third topic is the numerical treatment of the viscous interface model (2.37).

4.1. Approximations of surface normals

We first consider the simple constitutive relation $\boldsymbol{\sigma}_\Gamma = \tau \mathbf{P}$, which models the clean interface and the variable surface tension, and also exists in the viscous interface model, cf. (2.34). Numerical treatment of the viscous terms are presented in section 4.3.

Recall that $\mathbf{P} = \mathbf{I} - \mathbf{n}\mathbf{n}^T$ and $\nabla_\Gamma f = \mathbf{P}\nabla f$. For the discretization of $f_{\Gamma_h}(\mathbf{v}_h)$ we need a discretized orthogonal projection operator \mathbf{P}_h , which approximates \mathbf{P} . The discretized surface stress tensor is then given by $\boldsymbol{\sigma}_\Gamma = \tau \mathbf{P}_h$. Hence the surface force functional takes the form

$$f_{\Gamma_h}(\mathbf{v}_h) = - \int_{\Gamma_h} \tau \operatorname{tr} \left(\mathbf{P}_h (\nabla_{\Gamma_h} \mathbf{v}_h)^T \right) ds = - \sum_{i=1}^3 \int_{\Gamma_h} \tau (\mathbf{e}_i^T \mathbf{P}_h) \cdot \nabla_{\Gamma_h} v_i ds. \quad (4.1)$$

To properly define \mathbf{P}_h we need an approximation of the surface normals $\mathbf{n}(\mathbf{x})$. We introduce two methods for approximating surface normals:

Surface normals from planar segments. As described in 3.3.2, Γ_h consists of piecewise planar segments, cf. Figure 3.3. We can take the outward pointing surface normals of these planar segments, denoted by $\bar{\mathbf{n}}_h$, to approximate $\mathbf{n}(\mathbf{x})$. Clearly $\bar{\mathbf{n}}_h$ is constant on each planar segment, and possibly discontinuous across the edges of the segments, cf. Figure 4.1.

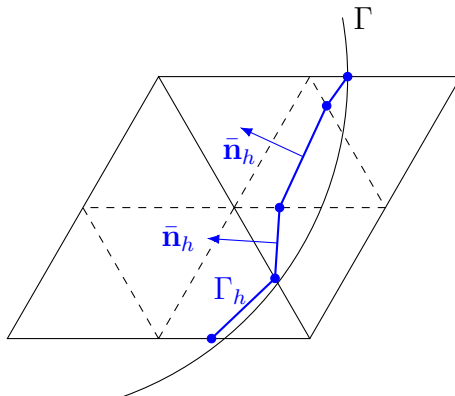


Figure 4.1.: Illustration of surface normals $\bar{\mathbf{n}}_h$ on Γ_h .

In [39] the authors have shown that under suitable conditions on Γ_h and the triangulations, the following approximation error bound holds for \bar{f}_{Γ_h} with $\bar{\mathbf{P}}_h := \mathbf{I} - \bar{\mathbf{n}}_h \bar{\mathbf{n}}_h^T$ and a constant τ :

$$\|f_\Gamma - \bar{f}_{\Gamma_h}\|_{\mathbf{V}'_h} := \sup_{\mathbf{v}_h \in \mathbf{V}_h, \mathbf{v}_h \neq 0} \frac{|f_\Gamma(\mathbf{v}_h) - \bar{f}_{\Gamma_h}(\mathbf{v}_h)|}{\|\mathbf{v}_h\|_{H^1}} \leq \tau c \sqrt{h_\Gamma},$$

where h_Γ is the maximal diameter of triangular segments in Γ_h . Experiments indicate that this bound is sharp, cf. Table 7.8 [39].

Improved approximation from ϕ_h . Recall that the surface normal $\mathbf{n}(\mathbf{x})$ can be characterized by (3.3)

$$\mathbf{n}(\mathbf{x}) = \frac{\nabla \phi(\mathbf{x})}{\|\nabla \phi(\mathbf{x})\|_2} \quad \text{for } \mathbf{x} \in \Gamma(t).$$

Hence we can approximate $\mathbf{n}(\mathbf{x})$ by utilizing the piecewise quadratic function ϕ_h . We define a surface normal field $\hat{\mathbf{n}}_h$:

$$\hat{\mathbf{n}}_h := \frac{\nabla\phi_h(\mathbf{x})}{\|\nabla\phi_h(\mathbf{x})\|_2} \quad \text{for } \mathbf{x} \in \Gamma_h. \quad (4.2)$$

The corresponding discrete surface force functional $\hat{f}_{\Gamma_h}(\mathbf{v}_h)$ takes the form

$$\hat{f}_{\Gamma_h}(\mathbf{v}_h) = - \int_{\Gamma_h} \tau \operatorname{tr} \left(\hat{\mathbf{P}}_h (\hat{\nabla}_{\Gamma_h} \mathbf{v}_h)^T \right) ds = - \sum_{i=1}^3 \int_{\Gamma_h} \tau (\mathbf{e}_i^T \hat{\mathbf{P}}_h) \cdot \hat{\nabla}_{\Gamma_h} v_i ds, \quad (4.3)$$

where $\hat{\mathbf{P}}_h := \mathbf{I} - \hat{\mathbf{n}}_h \hat{\mathbf{n}}_h^T$ and $\hat{\nabla}_{\Gamma_h} = \hat{\mathbf{P}}_h \nabla$.

In [33] it is shown that error bound for \hat{f}_{Γ_h} is given by

$$\|f_{\Gamma} - \hat{f}_{\Gamma_h}\|_{\mathbf{v}'_h} \leq \tau c h_{\Gamma}^{\frac{3}{2}}.$$

Experiments in [33] indicate that this exponent $\frac{3}{2}$ is sharp.

Remark 4.1.1. *From the Strang lemma, cf. Corollary 7.10.5 [39], the approximation error $\|f_{\Gamma} - \hat{f}_{\Gamma_h}\|_{\mathbf{v}'_h}$ is essential in the discretization error analysis of velocity and pressure in two-phase Navier-Stokes model. Hence we use the improved projection operator $\hat{\mathbf{P}}_h$ in this thesis, i.e. $\hat{f}_{\Gamma_h}(\mathbf{v}_h)$.*

4.2. Convergence acceleration

The Gauss-Seidel type decoupling scheme introduced in section 3.5.1 is our starting point for solving the fully discrete system (3.19). A schematic of this decoupling scheme is shown in Figure 4.2. However, as shown in the numerical experiments in section 4.2.1, this decoupling scheme is not robust with respect to variation of time step sizes. The reason is the highly nonlinear coupling between Navier-Stokes equations and the level set equation through the surface force functional f_{Γ_h} .

Recall the second stage of the decoupling scheme (3.22), i.e. the solution process of Navier-Stokes equations

$$\begin{aligned} \frac{1}{\Delta t} \tilde{\mathbf{M}}(\vec{\phi}^{k+1}) \vec{\mathbf{u}}^{k+1} + \left(\mathbf{A}(\vec{\phi}^{k+1}) + \mathbf{N}(\vec{\mathbf{u}}^{k+1}, \vec{\phi}^{k+1}) \right) \vec{\mathbf{u}}^{k+1} + \mathbf{B}(\vec{\phi}^{k+1})^T \vec{p}^{k+1} \\ = \frac{1}{\Delta t} \tilde{\mathbf{M}}(\vec{\phi}^{k+1}) \vec{\mathbf{u}}^0 + \vec{\mathbf{g}}(\vec{\phi}^{k+1}) + \vec{\mathbf{f}}_{\Gamma_h}(\vec{\phi}^{k+1}), \end{aligned} \quad (4.4a)$$

$$\mathbf{B}(\vec{\phi}^{k+1}) \vec{\mathbf{u}}^{k+1} = 0. \quad (4.4b)$$

where $\vec{\phi}^{k+1}$ is known from the first stage (3.21), $\vec{\mathbf{u}}^{k+1}$ and \vec{p}^{k+1} are the unknown velocity and pressure, $\vec{\mathbf{u}}^0$ is the initial data for the decoupling scheme, i.e. the velocity from previous time step. To simplify the presentation, we rename the velocity and the level set

4. Numerical treatment of surface stress tensor

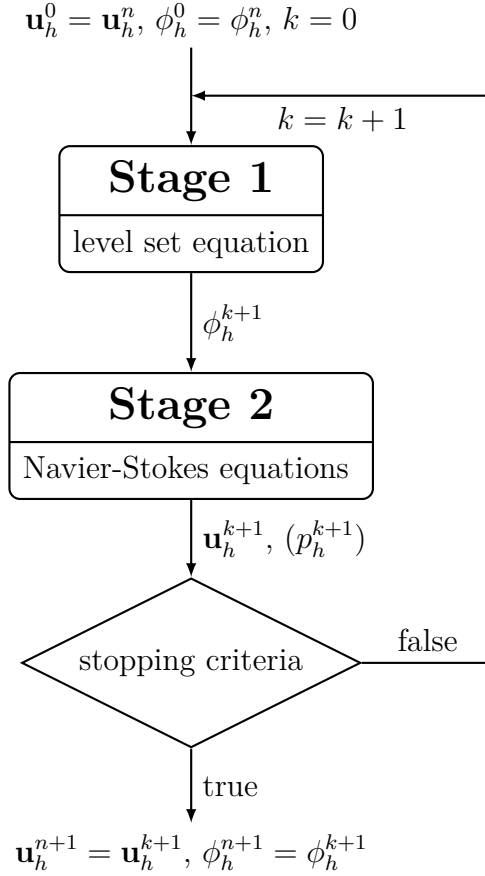


Figure 4.2.: Schematic of the Gauss-Seidel type decoupling scheme from section 3.5.1.

function as follows:

$$\mathbf{u}_h^{new} := \mathbf{u}_h^{k+1} = \sum_{i=1}^{3N} \boldsymbol{\xi}_i \bar{\mathbf{u}}_i^{k+1},$$

$$\mathbf{u}_h^{old} := \mathbf{u}_h^k = \sum_{i=1}^{3N} \boldsymbol{\xi}_i \bar{\mathbf{u}}_i^k,$$

$$\phi_h^{old} := \phi_h^{k+1} = \sum_{j=1}^N \xi_j \bar{\phi}_j^{k+1}.$$

The following matrix and vector are defined

$$\tilde{\mathbf{A}}(\vec{\phi}^{old}, \vec{\mathbf{u}}^{new}) := \frac{1}{\Delta t} \tilde{\mathbf{M}}(\vec{\phi}^{old}) + \mathbf{A}(\vec{\phi}^{old}) + \mathbf{N}(\vec{\mathbf{u}}^{new}, \vec{\phi}^{old}),$$

$$\vec{\mathbf{b}} := \frac{1}{\Delta t} \tilde{\mathbf{M}}(\vec{\phi}^{old}) \vec{\mathbf{u}}^0 + \vec{\mathbf{g}}(\vec{\phi}^{old}),$$

and (4.4) can be reformulated as follows

$$\tilde{\mathbf{A}}(\vec{\phi}^{old}, \vec{\mathbf{u}}^{new}) \vec{\mathbf{u}}^{new} + \mathbf{B}(\vec{\phi}^{old})^T \vec{p}^{new} = \vec{\mathbf{b}} + \vec{\mathbf{f}}_{\Gamma_h}(\vec{\phi}^{old}), \quad (4.5a)$$

$$\mathbf{B}(\vec{\phi}^{old}) \vec{\mathbf{u}}^{new} = 0. \quad (4.5b)$$

We restrict here to the case $\boldsymbol{\sigma}_\Gamma = \tau \mathbf{P}$. An identity function id_{Γ_h} on Γ_h is defined. Note that $\nabla \text{id}_{\Gamma_h} = \mathbf{I}$, and $\nabla_{\Gamma_h} \text{id}_{\Gamma_h} = \mathbf{P}_h \nabla \text{id}_{\Gamma_h} = \mathbf{P}_h$. Hence the discretized surface force functional (4.1) can be reformulated

$$\begin{aligned} f_{\Gamma_h}(\mathbf{v}_h) &= - \sum_{i=1}^3 \int_{\Gamma_h} \tau (\mathbf{e}_i^T \mathbf{P}_h) \cdot \nabla_{\Gamma_h} v_i \, ds = - \int_{\Gamma_h} \tau \, \text{tr} \left(\nabla_{\Gamma_h} \text{id}_{\Gamma_h} (\nabla_{\Gamma_h} \mathbf{v}_h)^T \right) \, ds \\ &= - \int_{\Gamma_h} \tau \nabla_{\Gamma_h} \text{id}_{\Gamma_h} : \nabla_{\Gamma_h} \mathbf{v}_h \, ds, \end{aligned} \quad (4.6)$$

where the Frobenius product is defined by $\nabla_{\Gamma_h} \text{id}_{\Gamma_h} : \nabla_{\Gamma_h} \mathbf{v}_h := \text{tr} \left(\nabla_{\Gamma_h} \text{id}_{\Gamma_h} (\nabla_{\Gamma_h} \mathbf{v}_h)^T \right)$. The surface force functional $\vec{\mathbf{f}}_{\Gamma_h}(\vec{\phi}^{old})$ in (4.5) corresponds to

$$f_{\Gamma_h(\phi_h^{old})}(\mathbf{v}_h) = - \int_{\Gamma_h(\phi_h^{old})} \tau \nabla_{\Gamma_h(\phi_h^{old})} \text{id}_{\Gamma_h(\phi_h^{old})} : \nabla_{\Gamma_h(\phi_h^{old})} \mathbf{v}_h \, ds. \quad (4.7)$$

As mentioned in Remark 3.3.5, (4.7) is the discretization of the weak form of Laplace-Beltrami operator on Γ_h . More details about the treatment of Laplace-Beltrami operator can be found in [39], [24], [6], [37].

We adopt the method of convergence acceleration presented in [39] by improving the approximation of the surface force functional. The idea of this method is using a better, more implicit, approximation of Γ_h for id_{Γ_h} in (4.7), which incorporates the unknown velocity \mathbf{u}_h^{new} . We use $\hat{\Gamma}_h$ to denote this approximated interface, and define $\hat{\Gamma}_h(\mathbf{u}_h^{new}, \mathbf{u}_h^{old})$ as

$$\hat{\Gamma}_h(\mathbf{u}_h^{new}, \mathbf{u}_h^{old}) := \{ \hat{\mathbf{x}} \in \Omega : \hat{\mathbf{x}} = \mathbf{x} + \Delta t \left(\mathbf{u}_h^{new}(\mathbf{x}) - \mathbf{u}_h^{old}(\mathbf{x}) \right), \quad \mathbf{x} \in \Gamma_h(\phi_h^{old}) \}, \quad (4.8)$$

which means that we use the velocity difference $\delta \mathbf{u}_h(\mathbf{x}) := \mathbf{u}_h^{new}(\mathbf{x}) - \mathbf{u}_h^{old}(\mathbf{x})$ to transport the point \mathbf{x} on $\Gamma_h(\phi_h^{old})$ to $\hat{\mathbf{x}}$. In Figure 4.3, we illustrate how to construct $\hat{\Gamma}_h$. Recall that in each iteration, we always use the velocity \mathbf{u}_h^{old} to transport the initial level set function ϕ_h^0 in order to obtain ϕ_h^{old} , cf. (3.21).

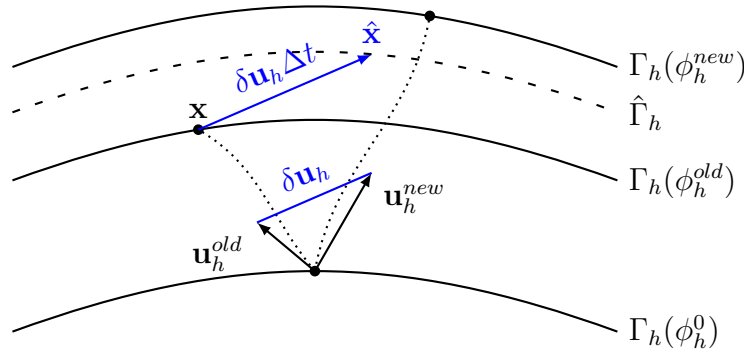


Figure 4.3.: Illustration of the approximated interface $\hat{\Gamma}_h$. The velocity difference $\delta \mathbf{u}_h$ equals $\mathbf{u}_h^{new} - \mathbf{u}_h^{old}$. Note that the positions of the interfaces are implicitly determined by the corresponding level set functions. The velocity fields are used to transport the level set function, not the interfaces.

On $\hat{\Gamma}_h$ the identity operator is given by

$$\text{id}_{\hat{\Gamma}_h} := \text{id}_{\Gamma_h(\phi_h^{old})} + \Delta t \left(\mathbf{u}_h^{new} - \mathbf{u}_h^{old} \right). \quad (4.9)$$

4. Numerical treatment of surface stress tensor

We choose now $\hat{\Gamma}_h$ for the identity operator in (4.7), and obtain a modified surface force functional

$$\begin{aligned} \hat{f}_{\Gamma_h}(\phi_h^{old}, \hat{\Gamma}_h, \mathbf{v}_h) &:= - \int_{\Gamma_h(\phi_h^{old})} \tau \nabla_{\Gamma_h(\phi_h^{old})} \text{id}_{\hat{\Gamma}_h} : \nabla_{\Gamma_h(\phi_h^{old})} \mathbf{v}_h \, ds \\ &= f_{\Gamma_h(\phi_h^{old})}(\mathbf{v}_h) - \Delta t \int_{\Gamma_h(\phi_h^{old})} \tau \nabla_{\Gamma_h(\phi_h^{old})} (\mathbf{u}_h^{new} - \mathbf{u}_h^{old}) : \nabla_{\Gamma_h(\phi_h^{old})} \mathbf{v}_h \, ds, \end{aligned} \quad (4.10)$$

where $f_{\Gamma_h(\phi_h^{old})}(\mathbf{v}_h)$ is defined in (4.7).

We introduce a matrix $\mathbf{L}(\phi_h)$ as follows

$$\mathbf{L}(\phi_h)_{i,j} := \int_{\Gamma_h(\phi_h)} \tau \nabla_{\Gamma_h(\phi_h)} \boldsymbol{\xi}_j : \nabla_{\Gamma_h(\phi_h)} \boldsymbol{\xi}_i \, ds.$$

With the modified surface force functional \hat{f}_{Γ_h} , (4.5) takes the form

$$\left(\tilde{\mathbf{A}}(\vec{\phi}^{old}, \vec{\mathbf{u}}^{new}) + \Delta t \mathbf{L}(\vec{\phi}^{old}) \right) \vec{\mathbf{u}}^{new} + \mathbf{B}(\vec{\phi}^{old})^T \vec{p}^{new} = \vec{\mathbf{b}} + \tilde{\mathbf{f}}_{\Gamma_h}(\vec{\phi}^{old}) + \Delta t \mathbf{L}(\vec{\phi}^{old}) \vec{\mathbf{u}}^{old}, \quad (4.11a)$$

$$\mathbf{B}(\vec{\phi}^{old}) \vec{\mathbf{u}}^{new} = 0. \quad (4.11b)$$

Remark 4.2.1. *The modified system (4.11) is consistent with the two phase model (3.18), i.e. if \mathbf{u}_h^k converges to the solution \mathbf{u}_h^* , then the terms related to \mathbf{L} matrix cancel each other. In [39], the authors proved that for small enough Δt , both (4.4) and (4.11) converge, and the method (4.11) generally has a smaller contraction number. From Theorem 9.1.1 [39], the following holds*

$$\text{Method (4.5): } \|\mathbf{e}^{k+1}\| \leq (L_1 + \Delta t L_2) \|\tilde{\mathbf{A}}^{-1}\| \|\mathbf{e}^k\|, \quad (4.12)$$

$$\text{Method (4.11): } \|\mathbf{e}^{k+1}\| \leq L_1 \|(\tilde{\mathbf{A}} + \Delta t \mathbf{L}^k)^{-1}\| \|\mathbf{e}^k\|, \quad (4.13)$$

where \mathbf{e}^k is the error in \mathbf{u}^k , i.e. $\mathbf{e}^k := \mathbf{u}^* - \mathbf{u}^k$, L_1 is the Lipschitz constant of the linearized surface force functional f_{Γ_h} , cf. the definition (9.13) and (9.15) in [39], and L_2 is the bound of the matrix norm $\|\mathbf{L}\|$.

4.2.1. Numerical experiments

In this section, we present numerical experiments for testing the convergence behavior of both methods, namely the original decoupling scheme with (4.4) and the decoupling scheme with the modified surface force functional (4.11). A similar experiment can be found in section 9.1.1 [39].

We solve Stokes equation for an ellipsoid droplet, which is initially at rest in a domain $\Omega = (0, 2)^3$. The center of the droplet is at the center of the domain. The ellipsoid droplet has a semi-principal axis of length 0.6 in x -direction and 0.4 in y/z -directions. The droplet domain is denoted by Ω_1 , and the surrounding phase is Ω_2 . The material properties of the two phases are: $\rho_1 = 10$, $\rho_2 = 1$, $\mu_1 = 0.1$, $\mu_2 = 0.01$. The interface of the two phase is a clean interface with a constant surface tension coefficient $\tau = 1$. No gravity force is considered, i.e. $\mathbf{g} = 0$.

A uniform tetrahedral mesh is used for discretization. Each side length of Ω is denoted by ℓ . Ω is first divided into cubes of equal size with side lengths $\frac{\ell}{12}$. Each cube is then divided into six tetrahedra.

Due to the surface tension force, the ellipsoid droplet retracts into a sphere, and the retraction process oscillates. We illustrate the side length of the bounding box for the ellipsoid droplet in Figure 4.4.

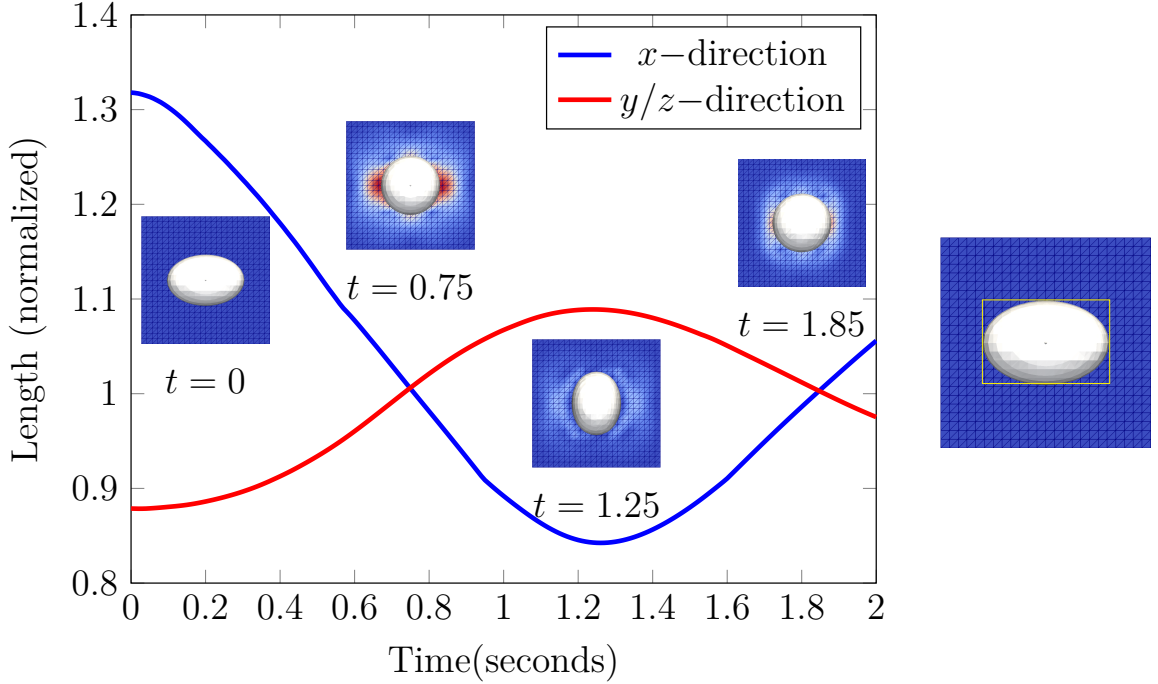


Figure 4.4.: Plot of the side lengths of the bounding box, which contains the ellipsoid droplet (right). The values are normalized by the diameter of the retracted sphere, i.e. $d = 2\sqrt[3]{0.6 \cdot 0.4 \cdot 0.4} \approx 0.9158$.

To study the convergence behavior of the decoupling scheme (4.4) and the improved scheme (4.11), we solve one time step of the coupled system at $t = 1.25$ and compare the number of iterations needed for both methods until the residual of \mathbf{u} is smaller than 10^{-8} . The results are listed in Table 4.1 (columns 2 to 5). Δt is chosen in a wide span from 1.0×10^{-3} to 1.0 to test the robustness of the schemes. From the results, we can conclude that the combination of the Broyden method [39] and the improved surface force functional outperforms other schemes with respect to the speed of convergence. Introducing the improved surface force functional \hat{f}_{Γ_h} greatly accelerates the convergence of the Gauss-Seidel iteration.

4.3. Treatment of viscous terms

Recall the surface stress tensor $\boldsymbol{\sigma}_\Gamma$ for the viscous interface model (2.37)

$$\boldsymbol{\sigma}_\Gamma = [\tau + (\lambda_\Gamma - \mu_\Gamma) \operatorname{div}_\Gamma \mathbf{u}] \mathbf{P} + \mu_\Gamma \mathbf{D}_\Gamma(\mathbf{u}),$$

4. Numerical treatment of surface stress tensor

Δt	no acceleration	only Broyden	only \hat{f}_{Γ_h}	Broyden + \hat{f}_{Γ_h}	$\lambda_\Gamma = 0.2, \mu_\Gamma = 0.1$
1.0×10^{-3}	4(29)	4(29)	4(28)	4(28)	3(25)
2.0×10^{-3}	5(34)	4(33)	4(33)	4(33)	4(28)
5.0×10^{-3}	8(53)	6(47)	7(49)	6(45)	4(35)
1.0×10^{-2}	41(195)	10(70)	13(75)	9(62)	5(42)
2.0×10^{-2}	>250	21(136)	26(138)	15(92)	6(54)
5.0×10^{-2}	>250	>250	74(410)	27(180)	8(94)
1.0×10^{-1}	>250	>250	162(1316)	41(380)	11(172)
2.0×10^{-1}	>250	>250	>250	65(890)	16(323)
5.0×10^{-1}	>250	>250	>250	103(2516)	28(835)
1.0	>250	>250	>250	218(8643)	58(2374)

Table 4.1.: Number of Gauss-Seidel iterations needed to reach the stopping criterion. The total numbers of Stokes solver (GMRES) iterations are given in parenthesis. The data in the last column is from the experiments for a viscous interface with $\lambda_\Gamma = 0.2$ and $\mu_\Gamma = 0.1$. Note that both Broyden method and \hat{f}_{Γ_h} are used for the viscous interface experiments.

with the surface rate of strain tensor $\mathbf{D}_\Gamma(\mathbf{u}) = \mathbf{P} \left(\nabla_\Gamma \mathbf{u} + (\nabla_\Gamma \mathbf{u})^T \right) \mathbf{P}$. We assume that λ_Γ and μ_Γ are constant on Γ and satisfy $\lambda_\Gamma \geq \mu_\Gamma$. Note that $\text{div}_\Gamma \mathbf{u} = \text{tr}(\nabla_\Gamma \mathbf{u})$, we use the discrete velocity $\mathbf{u}_h \in \mathbf{V}_h$ and the improved projection $\hat{\mathbf{P}}_h$ to discretize the viscous surface stress tensor $\boldsymbol{\sigma}_\Gamma$. The discrete surface force functional (3.15) is then given by

$$\begin{aligned}
f_{\Gamma_h}(\mathbf{u}_h, \mathbf{v}_h) &= - \int_{\Gamma_h} \left(\tau + (\lambda_\Gamma - \mu_\Gamma) \text{tr} \left(\hat{\nabla}_{\Gamma_h} \mathbf{u}_h \right) \right) \text{tr} \left(\hat{\mathbf{P}}_h \left(\hat{\nabla}_{\Gamma_h} \mathbf{v}_h \right)^T \right) ds \\
&\quad - \int_{\Gamma_h} \mu_\Gamma \text{tr} \left(\mathbf{D}_{\Gamma_h}(\mathbf{u}_h) \left(\hat{\nabla}_{\Gamma_h} \mathbf{v}_h \right)^T \right) ds \\
&= - \sum_{i=1}^3 \int_{\Gamma_h} \left(\tau + (\lambda_\Gamma - \mu_\Gamma) \text{tr} \left(\hat{\nabla}_{\Gamma_h} \mathbf{u}_h \right) \right) \left(\mathbf{e}_i^T \hat{\mathbf{P}}_h \right) \cdot \hat{\nabla}_{\Gamma_h} v_i ds \\
&\quad - \sum_{i=1}^3 \int_{\Gamma_h} \mu_\Gamma \mathbf{e}_i^T \mathbf{D}_{\Gamma_h}(\mathbf{u}_h) \cdot \hat{\nabla}_{\Gamma_h} v_i ds, \tag{4.14}
\end{aligned}$$

with $\mathbf{D}_{\Gamma_h}(\mathbf{u}_h) := \hat{\mathbf{P}}_h \left(\hat{\nabla}_{\Gamma_h} \mathbf{u}_h + \left(\hat{\nabla}_{\Gamma_h} \mathbf{u}_h \right)^T \right) \hat{\mathbf{P}}_h$.

In order to incorporate the viscous surface force functional $f_{\Gamma_h}(\mathbf{u}_h, \mathbf{v}_h)$ in the second stage of the decoupling scheme (4.4), we split $f_{\Gamma_h}(\mathbf{u}_h, \mathbf{v}_h)$ into three parts $f_{\Gamma_h}(\mathbf{u}_h, \mathbf{v}_h) = f_\tau(\mathbf{v}_h) + f_\lambda(\mathbf{u}_h, \mathbf{v}_h) + f_\mu(\mathbf{u}_h, \mathbf{v}_h)$, which are defined by

$$\begin{aligned}
f_\tau(\mathbf{v}_h) &:= - \int_{\Gamma_h} \tau \text{tr} \left(\hat{\mathbf{P}}_h \left(\hat{\nabla}_{\Gamma_h} \mathbf{v}_h \right)^T \right) ds, \\
f_\lambda(\mathbf{u}_h, \mathbf{v}_h) &:= - \int_{\Gamma_h} (\lambda_\Gamma - \mu_\Gamma) \text{tr} \left(\hat{\nabla}_{\Gamma_h} \mathbf{u}_h \right) \text{tr} \left(\hat{\mathbf{P}}_h \left(\hat{\nabla}_{\Gamma_h} \mathbf{v}_h \right)^T \right) ds, \\
f_\mu(\mathbf{u}_h, \mathbf{v}_h) &:= - \int_{\Gamma_h} \mu_\Gamma \text{tr} \left(\mathbf{D}_{\Gamma_h}(\mathbf{u}_h) \left(\hat{\nabla}_{\Gamma_h} \mathbf{v}_h \right)^T \right) ds,
\end{aligned}$$

where $f_\tau(\mathbf{v}_h)$ corresponds to the surface tension part, $f_\lambda(\mathbf{u}_h, \mathbf{v}_h)$ corresponds to the surface dilatational viscous part, and $f_\mu(\mathbf{u}_h, \mathbf{v}_h)$ corresponds to the surface shear viscous part. From the properties of the matrix trace, it is easy to show that the following equations

hold

$$\begin{aligned} f_\lambda(\mathbf{u}_h, \mathbf{v}_h) &= - \int_{\Gamma_h} (\lambda_\Gamma - \mu_\Gamma) \operatorname{tr} \left(\hat{\nabla}_{\Gamma_h} \mathbf{u}_h \right) \operatorname{tr} \left(\hat{\nabla}_{\Gamma_h} \mathbf{v}_h \right) ds, \\ f_\mu(\mathbf{u}_h, \mathbf{v}_h) &= \frac{-1}{2} \int_{\Gamma_h} \mu_\Gamma \operatorname{tr} \left(\mathbf{D}_{\Gamma_h}(\mathbf{u}_h) \mathbf{D}_{\Gamma_h}(\mathbf{v}_h) \right) ds. \end{aligned}$$

We adopt the improved functional (4.10) for treating $f_\tau(\mathbf{v}_h)$. For f_λ and f_μ , we choose \mathbf{u}_h^{k+1} for the velocity, and introduce the following matrices $\mathbf{V}_\lambda(\phi_h)$ and $\mathbf{V}_\mu(\phi_h)$:

$$\begin{aligned} \mathbf{V}_\lambda(\phi_h)_{i,j} &= \int_{\Gamma_h(\phi_h)} (\lambda_\Gamma - \mu_\Gamma) \operatorname{tr} \left(\hat{\mathbf{P}}_h \nabla \boldsymbol{\xi}_j \right) \operatorname{tr} \left(\hat{\mathbf{P}}_h \nabla \boldsymbol{\xi}_i \right) ds, \\ \mathbf{V}_\mu(\phi_h)_{i,j} &= \frac{1}{2} \int_{\Gamma_h(\phi_h)} \mu_\Gamma \operatorname{tr} \left(\mathbf{D}_{\Gamma_h(\phi_h)}(\boldsymbol{\xi}_j) \mathbf{D}_{\Gamma_h(\phi_h)}(\boldsymbol{\xi}_i) \right) ds. \end{aligned}$$

Given $\lambda_\Gamma > \mu_\Gamma > 0$, $\mathbf{V}_\lambda(\phi_h)$ and $\mathbf{V}_\mu(\phi_h)$ are symmetric positive semi-definite. The second stage of the decoupling scheme for a viscous interface is then given by

$$\begin{aligned} [\tilde{\mathbf{A}}(\vec{\phi}^{k+1}, \vec{\mathbf{u}}^{k+1}) + \Delta t \mathbf{L}(\vec{\phi}^{k+1}) + \mathbf{V}_\lambda(\vec{\phi}^{k+1}) + \mathbf{V}_\mu(\vec{\phi}^{k+1})] \vec{\mathbf{u}}^{k+1} + \mathbf{B}(\vec{\phi}^{k+1})^T \vec{p}^{k+1} \\ = \vec{\mathbf{b}} + \vec{\mathbf{f}}_{\Gamma_h}(\vec{\phi}^{k+1}) + \Delta t \mathbf{L}(\vec{\phi}^{k+1}) \vec{\mathbf{u}}^k, \end{aligned} \quad (4.15a)$$

$$\mathbf{B}(\vec{\phi}^{k+1}) \vec{\mathbf{u}}^{k+1} = 0. \quad (4.15b)$$

The additions of symmetric positive semi-definite matrices \mathbf{V}_λ and \mathbf{V}_μ in (4.15) have positive effects on the convergence behavior of the decoupling scheme. Recall the result of the convergence analysis (4.13), and the following holds

$$\|(\tilde{\mathbf{A}} + \Delta t \mathbf{L}^k + \mathbf{V}_\lambda + \mathbf{V}_\mu)^{-1}\| \leq \|(\tilde{\mathbf{A}} + \Delta t \mathbf{L}^k)^{-1}\|, \quad (4.16)$$

thus we expect a faster convergence when solving the system (4.15).

We solve one time step of the coupled system (4.15) to study the convergence behavior after adding \mathbf{V}_λ and \mathbf{V}_μ . We take the surface dilatational viscosity $\lambda_\Gamma = 0.2$ and the surface shear viscosity $\mu_\Gamma = 0.1$. The other material properties remain the same as in section 4.2.1. Due to the introduction of surface viscosities, the retraction process of the droplet is slightly changed, which is presented in Figure 4.5. The shape shown in Figure 4.4 at time $t = 1.25$ is now at $t = 1.31$. From the physical point of view, the surface viscous effects dissipate energy, thus the droplet retracts slower with smaller amplitudes. We solve one time step at $t = 1.31$ and the results are listed in the sixth column of Table 4.1. A much faster convergence behavior is observed in the table. In order to check the individual effect of \mathbf{V}_λ and \mathbf{V}_μ on the convergence behavior, we choose one $\Delta t = 0.2$ s and vary the values of λ_Γ and μ_Γ . We solve one time step at $t = 1.25$. The initial velocity field is taken from the previous experiment, i.e. $\lambda_\Gamma = 0.2$ and $\mu_\Gamma = 0.1$. Results are listed in Table 4.2. We observe that the number of Gauss-Seidel iteration is only slightly changed with varying λ_Γ . The fast convergence behavior is due to the introduction of μ_Γ , i.e. \mathbf{V}_μ . Even if the surface viscous term \mathbf{V}_μ is only local at the interface, its effect on the convergence behavior of the Gauss-Seidel iteration is very significant, cf. Figure 4.6.

4. Numerical treatment of surface stress tensor

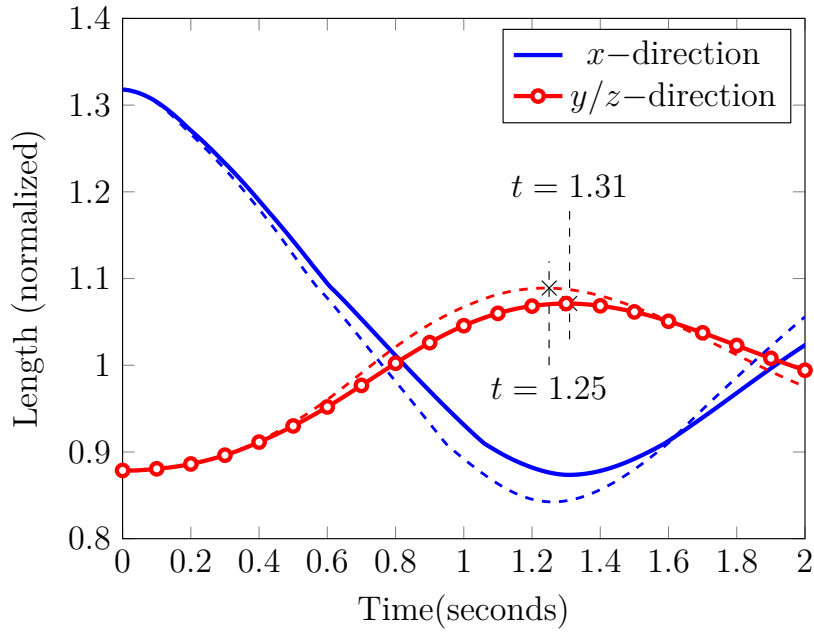


Figure 4.5.: Plot of the side lengths of the bounding box, which contains the ellipsoid droplet with surface viscosities. The values are normalized by the diameter of the retracted sphere, i.e. $d = 2\sqrt[3]{0.6 \cdot 0.4 \cdot 0.4} \approx 0.9158$. The dashed lines are the results from Figure 4.4 without surface viscosities.

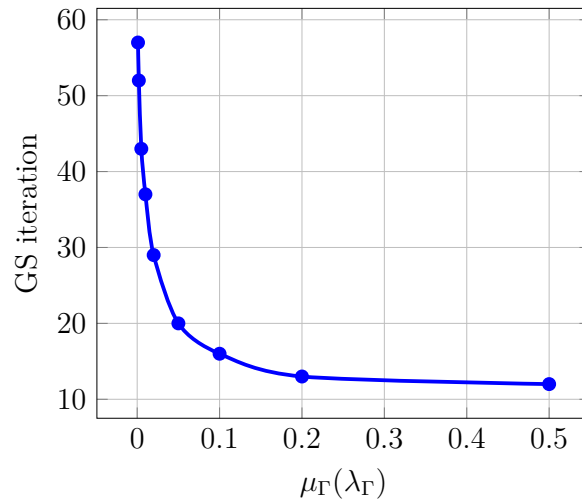


Figure 4.6.: Number of Gauss-Seidel iterations for different values of μ_Γ and $\lambda_\Gamma = \mu_\Gamma$.

λ_Γ	μ_Γ	GS iteration
0	0	62 (899)
0.02	0	59 (793)
0.04	0	56 (757)
0.06	0	58 (752)
0.08	0	51 (729)
0.1	0	55 (729)

λ_Γ	μ_Γ	GS iteration
0.001	0.001	57 (831)
0.002	0.002	52 (763)
0.005	0.005	43 (661)
0.01	0.01	37 (562)
0.02	0.02	29 (457)
0.05	0.05	20 (351)
0.1	0.1	16 (310)
0.2	0.2	13 (312)
0.5	0.5	12 (349)

Table 4.2.: Number of Gauss-Seidel iterations needed to reach the stopping criterion for different values of λ_Γ and μ_Γ . The total numbers of Stokes solver (GMRES) iterations are given in parenthesis. Note that in \mathbf{V}_λ the coefficient is $(\lambda_\Gamma - \mu_\Gamma)$.

4.4. Coupling between fluid dynamics and surfactant

The coupling between the two-phase fluid flow in the bulk phases and the surfactant transport on the interfaces is through the surface tension force. We use the two-phase Navier Stokes equations (3.4) to describe the flow behavior, which in the weak form includes the (local) surface force functional (2.44). The surfactant transport is described by the equation (2.42) posed on the moving interface $\Gamma(t)$. The dependence of the surface tension coefficient τ on the surfactant concentration causes the coupling. We use constitutive relations in the form (2.38) or (2.39). We have introduced the numerical treatments of the two sets of equations separately in chapter 3 and in previous sections of this chapter. In this section, we introduce the scheme to couple them together.

Recall the decoupling scheme for solving the two-phase Navier-Stokes problem, cf. Figure 4.2, in each time interval $[t_n, t_{n+1}]$, the level set function ϕ_h^n and the velocity \mathbf{u}_h^n are known, we solve a fixed point problem to obtain the unknowns \mathbf{u}_h^{n+1} , p_h^{n+1} and ϕ_h^{n+1} , cf. section 3.5. Note that in each iteration, we obtain a pair of tentative solutions ϕ_h^{k+1} and \mathbf{u}_h^{k+1} (p_h^{k+1}) at time step t_{n+1} , cf. Remark 3.5.2. In section 3.6, the space-time finite element method is introduced for solving the surfactant transport equation. In each time slab $\Omega \times [t_n, t_{n+1}]$, both the level set function and the velocity are assumed to be known in the whole time slab. In order to couple the two sets of equations, we propose the following scheme: given $\mathbf{u}_h^0 := \mathbf{u}_h^n$, $\phi_h^0 := \phi_h^n$ and $S_h^0 := S_h^n$, iterate for $k = 0, 1, 2, \dots$ until convergence or the maximal iteration number is reached:

1. Solve for ϕ_h^{k+1} from the discrete level set equation (3.21) with the known solution \mathbf{u}_h^k .
2. Solve for \mathbf{u}_h^{k+1} and p_h^{k+1} from the discrete Navier-Stokes equations (3.22) with the known solution ϕ_h^{k+1} . The surface force functional is determined by considering S_h^k for the constitutive relation $\tau = \tau(S_h^k)$.
3. Solve for S_h^{k+1} from the discrete surfactant equation (3.31). The time slab is $\Omega \times [t_n, t_{n+1}]$. At time step t_n , the known solutions are S_h^n , \mathbf{u}_h^n and ϕ_h^n . At time step

4. Numerical treatment of surface stress tensor

t_{n+1} , we use the tentative solutions \mathbf{u}_h^{k+1} and ϕ_h^{k+1} .

For the stopping criterion, we consider the residual of the velocity solution. We illustrate the last stage of the decoupling scheme in Figure 4.7. In chapter 7, we present numerical results by utilizing the aforementioned decoupling scheme to a model problem.

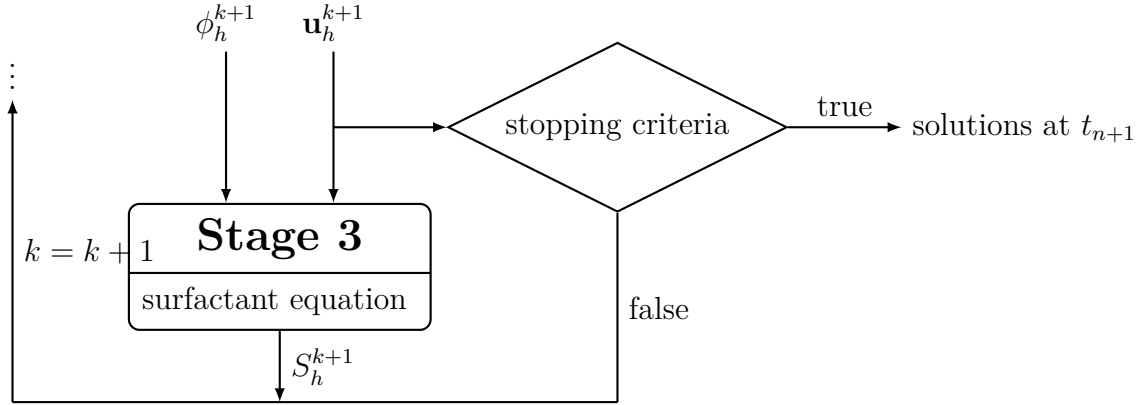


Figure 4.7.: Schematic of the solution process of the surfactant equation.

5. Simulation of Marangoni effects

5.1. Introduction

Marangoni effects are caused by surface tension gradients $\nabla_{\Gamma}\tau$, which create tangential velocity field at the interface. The surface tension gradients can be results of varying interfacial concentrations, temperature or electrical properties [22], i.e. τ is *not* constant on Γ and it is a function of the interfacial concentration $\tau = \tau(S)$ or the temperature $\tau = \tau(T)$. If temperature causes Marangoni effects, this phenomenon is also called thermocapillary motion, which is an important mechanism in experimental and industrial applications under reduced gravity or microfluidics conditions. In recent years a great number of publications on thermocapillary motion has appeared. We refer to [83] for an overview. Young *et al.* [91] first studied thermocapillary motion of droplets both experimentally and theoretically and derived a prediction for the migration velocity of a spherical droplet in a constant temperature-gradient field within an unbounded domain under negligible Reynolds number and Marangoni number conditions, i.e. the convective transports of momentum and energy are neglected. Other authors [4, 40] extended Young's analysis to allow a non-negligible Reynolds number, and studied the influence of shape deformation of the droplet on the migration velocity. Droplet motion in the presence of surfactants coupled with thermocapillary motion has also been investigated theoretically in the case of negligible Reynolds and Marangoni numbers [43, 44, 20]. For a non-negligible Marangoni number, asymptotic analysis has been utilized to predict the migration velocity [86, 5].

Numerical simulations have been used to study thermocapillary motions under (not so small) finite Reynolds and Marangoni number where it is not possible to perform theoretical analysis [16, 41, 28]. In these papers the authors focused on the deformation of a droplet in thermocapillary motion and the coupling of fluid dynamics with the temperature field. Brady *et al.* [16] also looked at the impact of numerical factors (initial conditions and domain geometry) on droplet dynamics.

In this chapter we do not treat modeling issues but concentrate on certain aspects of numerical simulations of Marangoni effects, i.e. time integration and nonlinear coupling between fluid dynamics and interface motion. We study a droplet in thermocapillary motion under negligible Reynolds and Marangoni number conditions. As mentioned in previous chapters, two-phase flow problems have a very high numerical complexity. The unknown interface causes a strong nonlinearity in the system. The surface tension force at the unknown interface has a strong effect on the fluid dynamics. Thermocapillary motion is a good example of this effect, in which the whole dynamics of the system is induced only by surface forces. Discontinuity in physical quantities across the interface need to be properly handled. Finally, the coupling of the fluid dynamics and the interface evolution

requires special attention.

5.2. Mathematical models

In this section we introduce the models that we consider. In section 5.2.1, we introduce a standard instationary sharp interface model for describing the behavior of two-phase incompressible flows with thermocapillary effects. A much simpler model, in which the temperature equation is decoupled from the fluid dynamics, has been analyzed in [91] under the assumption that the Reynolds and the Marangoni number are negligible. We describe this simple model and the theoretical results in section 5.2.2. In section 5.2.3, we introduce the model used in numerical simulations. We are interested in the droplet motion induced by surface tension gradients, hence we assume the temperature field is known and it is decoupled from fluid dynamics, i.e. heat diffusion is much greater than convection, cf. equation (5.1). The corresponding Marangoni number, cf. (5.4) $Ma \sim \frac{1}{\alpha}$, can be negligible.

In this chapter, we assume that only the surface tension coefficient depends on the temperature, densities and viscosities are assumed to be piecewise constants.

5.2.1. A sharp interface model for thermocapillary effects

We consider a droplet inside a continuous phase. The two fluids are immiscible and incompressible. Let $\Omega \subset \mathbb{R}^3$ be a domain containing the two different phases. The time dependent sub-domains containing the two phases are denoted by $\Omega_1(t)$ and $\Omega_2(t)$ with $\bar{\Omega} = \bar{\Omega}_1 \cup \bar{\Omega}_2$ and $\Omega_1 \cap \Omega_2 = \emptyset$. We assume that Ω_1 and Ω_2 are connected and $\partial\Omega_1 \cap \partial\Omega = \emptyset$ (i.e., Ω_1 is completely contained in Ω). Ω_1 denotes the droplet, and Ω_2 denotes the continuous phase. The (sharp) interface is denoted by $\Gamma(t) = \bar{\Omega}_1(t) \cap \bar{\Omega}_2(t)$. The unknown pressure is $p = p(x, t)$, and the unknown velocity is $\mathbf{u} = \mathbf{u}(x, t)$.

Surface tension force acts at the fluid-fluid interface, which is a result of different intermolecular forces in both phases. For a fluid interface with only surface tension effects, the interfacial momentum balance condition is

$$[\boldsymbol{\sigma}\mathbf{n}]_{\Gamma} = \text{div}_{\Gamma}(\tau\mathbf{P}),$$

where τ is the surface tension coefficient, cf. (2.34). When τ is constant on the whole interface, this fluid interface is called a clean interface. When temperature variations or surfactants exist, τ is a function of both time and position. The interface condition takes the form (2.36)

$$[\boldsymbol{\sigma}\mathbf{n}]_{\Gamma} = \text{div}_{\Gamma}(\tau\mathbf{P}) = -\tau\kappa\mathbf{n}_{\Gamma} + \nabla_{\Gamma}\tau,$$

with κ the mean curvature and ∇_{Γ} the surface gradient. Thermocapillary effect is characterized by a non-zero surface gradient term $\nabla_{\Gamma}\tau$.

We consider here the simple linear relation between τ and the temperature (2.40)

$$\tau(T) = \tau_0 + \sigma_T(T - T_0),$$

where τ_0 is the surface tension coefficient at a reference temperature T_0 , and σ_T is the thermal surface tension coefficient,

$$\sigma_T = \frac{d\tau}{dT}.$$

For most fluids σ_T is a negative constant.

Recall the standard sharp interface model for two-phase fluid system (2.41):

$$\begin{aligned} \rho_i \left(\frac{\partial \mathbf{u}}{\partial t} + (\mathbf{u} \cdot \nabla) \mathbf{u} \right) &= -\nabla p + \operatorname{div}(\mu_i \mathbf{D}(\mathbf{u})) + \rho \mathbf{g} \quad \text{in } \Omega_i(t), \\ \operatorname{div} \mathbf{u} &= 0 \quad \text{in } \Omega_i(t), \\ [\mathbf{u}]_\Gamma &= 0 \quad \text{on } \Gamma(t), \\ V_\Gamma &= \mathbf{u} \cdot \mathbf{n} \quad \text{on } \Gamma(t), \\ [\boldsymbol{\sigma} \mathbf{n}]_\Gamma &= \operatorname{div}_\Gamma \boldsymbol{\sigma}_\Gamma = \operatorname{div}_\Gamma(\tau \mathbf{P}) \quad \text{on } \Gamma(t). \end{aligned}$$

We consider the surface tension coefficient τ as a function defined on $\Gamma(t)$ obeying the constitutive equation (2.40). To make this problem well-posed we need a description of the temperature field T , suitable boundary conditions for \mathbf{u} , an initial condition $\mathbf{u}(\mathbf{x}, 0)$ and an initial configuration of the interface $\Gamma(0)$.

The unknown location of the interface $\Gamma(t)$ is coupled to the fluid dynamics via the condition $V_\Gamma = \mathbf{u} \cdot \mathbf{n}$. We use the level set method for capturing the interface, cf. section 3.2. The two Navier-Stokes equations in Ω_i , $i = 1, 2$ together with the interfacial conditions can be reformulated in *one* Navier-Stokes equation on the whole domain Ω with a surface tension force term localized at the interface, cf. section 2.8. Combining this with the level set method leads to the one fluid formulation (3.4). The surface force functional takes the form

$$f_\Gamma(\mathbf{v}) = - \int_\Gamma \operatorname{tr} \left(\boldsymbol{\sigma}_\Gamma (\nabla_\Gamma \mathbf{v})^T \right) ds = - \int_\Gamma \operatorname{tr} \left(\tau \mathbf{P} (\nabla_\Gamma \mathbf{v})^T \right) ds,$$

which can be numerically treated as presented in chapter 4.

The temperature field $T = T(\mathbf{x}, t)$ is determined by a convection-diffusion equation:

$$\frac{\partial T}{\partial t} - \alpha_i \Delta T + (\mathbf{u} \cdot \nabla) T = 0 \quad \text{in } \Omega_i(t), \quad (5.1)$$

where α_i is the thermal diffusivity in each phases. Across the interface $\Gamma(t)$, the temperature and the heat flux are continuous:

$$[T]_\Gamma = 0 \quad \text{on } \Gamma(t), \quad (5.2a)$$

$$[k_i \nabla T \cdot \mathbf{n}]_\Gamma = 0 \quad \text{on } \Gamma(t), \quad (5.2b)$$

where $k_i = \alpha_i \rho_i c_p$ (c_p : the specific heat capacity) is the thermal conductivity and $k_i \nabla T \cdot \mathbf{n}$ is the heat flux. Suitable boundary conditions for T and an initial condition $T(\mathbf{x}, 0)$ are needed for the well-posedness.

The standard sharp interface model (2.41) together with (5.1), (5.2) and the constitutive equation (2.40) determine the two-phase flow problem with thermocapillary effects. The coupling between the fluid dynamics and the temperature field is through \mathbf{u} and $\tau(T)$.

5.2.2. A stationary Stokes model for thermocapillary effects

In this section, we describe a stationary Stokes model for a droplet in thermocapillary motion under negligible Reynolds and Marangoni numbers condition. This simple model is first studied by Young *et al.* [91]. In their paper, a spherical droplet is considered floating in another fluid, which occupies an infinite domain. A temperature field with a constant temperature gradient exists in the whole domain. The authors assumed that the flow satisfies a creeping flow condition (Reynolds number is small, i.e. $Re \ll 1$) and the temperature field is purely diffusive (convective transport of heat is neglected, i.e. $Ma \ll 1$). They obtained a theoretical prediction of the droplet migration velocity \mathbf{U}_{mig}^{theo} , cf. (5.19).

We describe the model used in Young's paper [91]. A spherical droplet with radius R occupies the domain Ω_1 . The center of the droplet is taken as the origin of the coordinate system, and the gravity direction as the polar axis (z -axis). The fluid outside the droplet occupies $\Omega_2 = \mathbb{R}^3 \setminus \Omega_1$. The flow is assumed to be quasi-static, i.e. under the creeping flow assumption ($Re \ll 1$). The droplet velocity is defined as $\mathbf{U}_{\Omega_1} := \frac{1}{|\Omega_1|} \int_{\Omega_1} \mathbf{u}(\mathbf{x}) d\mathbf{x}$ with the *time-independent* velocity field $\mathbf{u}(\mathbf{x})$. Densities, viscosities, thermal diffusivities of the two phases are denoted by ρ_i , μ_i and α_i . For this simple model, the Reynolds number is given by

$$Re = \frac{\rho_2 \|\mathbf{U}_{\Omega_1}\| R}{\mu_2}, \quad (5.3)$$

and the Marangoni number is given by

$$Ma = \frac{\|\mathbf{U}_{\Omega_1}\| R}{\alpha_2}. \quad (5.4)$$

When Reynolds and Marangoni numbers are small, i.e. $Re \ll 1$ and $Ma \ll 1$, we can neglect inertial terms in the fluid dynamics and the convective transport term in determining the temperature field. The authors assumed that the droplet moves at a constant speed, and has a stationary spherical shape. If we choose a moving frame fixed to the center of the droplet, stationary Stokes equations can be used to determine the flow:

$$\begin{cases} -\mu_i \Delta \mathbf{u} + \nabla p = \rho_i \mathbf{g} & \text{in } \Omega_i \\ \operatorname{div} \mathbf{u} = 0 & \text{in } \Omega_i \end{cases} \quad (5.5)$$

On the stationary interface Γ , interfacial conditions are assigned. Continuity of velocities across the interface takes the form:

$$[\mathbf{u}]_{\Gamma} = 0. \quad (5.6)$$

To keep the spherical shape of the droplet, the normal velocity at the interface needs to vanish, which leads to

$$V_{\Gamma} = \mathbf{u} \cdot \mathbf{n} = 0 \quad \text{on } \Gamma. \quad (5.7)$$

Tangential stress balance condition at the interface takes the form

$$[\mathbf{P}\sigma\mathbf{n}]_{\Gamma} = \mathbf{P} \operatorname{div}_{\Gamma}(\tau\mathbf{P}) = \nabla_{\Gamma}\tau. \quad (5.8)$$

The Marangoni force term (thermocapillary effect) $\nabla_{\Gamma}\tau$ is coupled to the temperature field T through the constitutive equation (2.40). At the interface Γ , we have applied both normal (5.7) and tangential (5.8) interface condition. Whether the normal stress balance, i.e. $[(\mathbf{n}^T \boldsymbol{\sigma} \mathbf{n})\mathbf{n}]_{\Gamma} = -\tau \kappa \mathbf{n}$, is satisfied at the interface is not clear. We discuss this issue below, after introducing the temperature equation and the far-field condition.

The temperature field is also assumed to be at steady state. The convective transport of energy can be neglected for a small (zero) Marangoni number. The convection-diffusion equation (5.1) then simplifies to the Laplace's equation

$$\Delta T = 0 \quad \text{in } \mathbb{R}^3. \quad (5.9)$$

The temperature and heat flux continuity conditions (5.2a) and (5.2b) are assigned at the interface. Note that the simplification in (5.9) is consistent with the creeping flow assumption.

Proper far-field conditions have to be assigned. We define the droplet velocity with respect to the fixed frame as the droplet migration velocity $\mathbf{U}_{mig} := \mathbf{U}_{\Omega_1}$. We denote the temperature at the origin ($z = 0$) by T_0 and the constant temperature gradient by $T_c := \frac{\partial T}{\partial z}$. The solutions of the stationary Stokes equation (in the moving frame) (5.5) and the temperature equation (5.9) have to satisfy asymptotic conditions:

$$\mathbf{u}(\mathbf{x}) \rightarrow (0, 0, -\mathbf{U}_{mig} \cdot \mathbf{e}_z), \quad p \rightarrow -\rho_2 \mathbf{g} \cdot \mathbf{e}_z z, \quad T \rightarrow T_0 + T_c z \quad \text{for } \|\mathbf{x}\| \rightarrow \infty. \quad (5.10)$$

The first condition in (5.10) is the far-field condition of velocity in the moving frame, which corresponds to the zero velocity condition in the fixed frame.

This model problem is axi-symmetric and can be simplified to a two-dimensional problem. In plane polar coordinates, the Laplace equation (5.9) can be solved by a separation of variables in the form $T(r, \theta) = F(r)G(\theta)$ with $F(r) = a_n r^n + b_n r^{-n}$ and $G(\theta) = c_n \cos(n\theta) + d_n \sin(n\theta)$, where a_n, b_n, c_n and d_n are unknown coefficients. By utilizing the interface condition (5.2a), (5.2b) and the far-field condition of temperature in (5.10), the unknown constants of the solution can be determined. Thus the temperature field can be solved independently from fluid dynamics. On Γ , we obtain

$$T(z) = T_0 + \frac{3T_c}{2 + k_1/k_2} z. \quad (5.11)$$

From (5.11) and the constitutive equation (2.40), we can then solve for τ :

$$\tau(z) = \tau_0 + \sigma_T \frac{3T_c}{2 + k_1/k_2} z, \quad (5.12)$$

where $\tau_0 := \tau(T_0) = \tau(z = 0)$ is the surface tension coefficient at the equator.

We address the problem of normal stress balance on Γ now. Note that the far-field velocity condition (5.10) contains an *unknown* velocity \mathbf{U}_{mig} . Due to symmetry considerations, \mathbf{U}_{mig} should have only one nonzero component $U_{mig,z} := \mathbf{U}_{mig} \cdot \mathbf{e}_z$. Assuming a given scalar g , we can construct a far-field condition as follows:

$$\mathbf{u}(\mathbf{x}) \rightarrow (0, 0, g), \quad \text{for } \|\mathbf{x}\| \rightarrow \infty, \quad (5.13)$$

5. Simulation of Marangoni effects

which is a generalization of the condition in (5.10). With this far-field condition and interfacial conditions (5.6), (5.7) and (5.8), the Stokes equation (5.5) has a *unique* velocity solution, which is denoted by $\mathbf{u}(\mathbf{x}; g)$. For an arbitrary value of g , the solution $\mathbf{u}(\mathbf{x}; g)$ does *not* satisfy the normal stress balance condition on Γ . Hence, by testing the normal stress balance condition on Γ , i.e.

$$[(\mathbf{n}^T \boldsymbol{\sigma}(\mathbf{x}; g) \mathbf{n}) \mathbf{n}]_{\Gamma} \stackrel{!}{=} -\tau \kappa \mathbf{n}, \quad (5.14)$$

we can obtain the physically correct migration velocity. Note that the condition (5.14) is a *scalar* condition due to symmetry considerations.

Remark 5.2.1 (Comments on normal stress balance (5.14)). *The Stokes equation (5.5) with interfacial conditions (5.6), (5.7) and (5.8) and far-field conditions (5.13) has a unique velocity solution $\mathbf{u}(\mathbf{x}; g)$, but does not have a unique solution for the droplet pressure p_1 , which can be easily shown by adding a constant pressure to p_1 . In other words, the vanishing normal velocity condition (5.7) together with the stationary spherical shape constraint are not sufficient to recover the physics. By reintroducing the normal stress condition (5.14), which is a scalar condition, we can solve for the correct droplet pressure p_1 and the unknown migration velocity. We explain this in more detail.*

We expand the bulk stress tensor $\boldsymbol{\sigma}$ with $\boldsymbol{\sigma} = -p\mathbf{I} + \mu\mathbf{D}(\mathbf{u})$ and $\mathbf{D}(\mathbf{u}) := \nabla\mathbf{u} + (\nabla\mathbf{u})^T$. The left hand side of equation (5.14) becomes

$$[(\mathbf{n}^T \boldsymbol{\sigma} \mathbf{n}) \mathbf{n}]_{\Gamma} = [(-p + 2\mu \mathbf{n}^T \nabla \mathbf{u} \mathbf{n}) \mathbf{n}]_{\Gamma} = [-p \mathbf{n}]_{\Gamma} + [(2\mu \mathbf{n}^T \nabla \mathbf{u} \mathbf{n}) \mathbf{n}]_{\Gamma}. \quad (5.15)$$

We show that due to the spherical and axi-symmetric assumption, the scalar term $(\mathbf{n}^T \nabla \mathbf{u} \mathbf{n})$, which measures the velocity gradient $\nabla \mathbf{u}(\mathbf{x}; g)$ in the normal direction, depends only on the z -direction on Γ . We show this dependency in a polar coordinate system as is done by Young et al. [91]. We assume that the velocity \mathbf{u} does not depend on the azimuthal angle φ , and express \mathbf{u} in a polar coordinate system as is shown in Figure 5.1. In this coordinate system, the velocity \mathbf{u} has two components $\mathbf{u}(r, \theta) = (u_r, u_{\theta})^T$. For an axially symmetric flow around and within a spherical droplet, the solutions have been derived by Rybczynski and Hadamard. We refer to [46] and references therein. For a given far-field condition as in (5.13) and the axi-symmetric configuration, the radial velocities $u_{1,r}$ (inside the droplet) and $u_{2,r}$ (outside the droplet) take the forms [91]

$$\begin{aligned} u_{1,r} &= \frac{A}{\mu_1} (r^2 - R^2) \cos \theta =: c_1(r; g) \cos \theta, \\ u_{2,r} &= \left(\frac{B}{\mu_2} (r^{-1} - R^2 r^{-3}) + g(1 - R^3 r^{-3}) \right) \cos \theta =: c_2(r; g) \cos \theta, \end{aligned}$$

where A and B are unknown variables. The scalar term $(\mathbf{n}^T \nabla \mathbf{u} \mathbf{n})|_{\Omega_i}$ takes the form

$$(\mathbf{n}^T \nabla \mathbf{u} \mathbf{n})|_{\Omega_i} = \frac{\partial u_{i,r}}{\partial r} = \frac{\partial c_i}{\partial r}(r; g) \cos \theta. \quad (5.16)$$

On Γ , which has a constant radius R , we obtain $(\mathbf{n}^T \nabla \mathbf{u} \mathbf{n})|_{\Omega_i} = \frac{\partial c_i}{\partial r}(R; g) \cos \theta =: C_i(g) \cos \theta$. Note that $z = r \cos \theta$, and thus on Γ the term $(\mathbf{n}^T \nabla \mathbf{u} \mathbf{n})|_{\Omega_i}$ can be written as $(\mathbf{n}^T \nabla \mathbf{u} \mathbf{n})|_{\Omega_i} = \frac{C_i(g)}{R} z$. The jump term becomes

$$[(2\mu \mathbf{n}^T \nabla \mathbf{u} \mathbf{n}) \mathbf{n}]_{\Gamma} = [2\mu \frac{C_i(g)}{R} \mathbf{n}]_{\Gamma} z. \quad (5.17)$$

We also expand the right-hand side of the normal stress balance (5.14) with the solution τ on Γ (5.12):

$$-\tau\kappa\mathbf{n} = -\left(\tau_0 + \sigma_T \frac{3T_c}{2 + k_1/k_2} z\right)\kappa\mathbf{n} = -\tau_0\kappa\mathbf{n} - \frac{\partial\tau}{\partial z}\kappa\mathbf{n} \cdot z. \quad (5.18)$$

Comparing (5.15),(5.17) with (5.18), we can conclude that $-\tau_0\kappa$ balances the pressure jump term and determines p_1 , the constant scalar $-\frac{\partial\tau}{\partial z}\kappa$ determines the unknown migration velocity g .

Explicit formulas for \mathbf{U}_{mig} can be derived. The analysis relies on a representation of \mathbf{u} and T in the basis of solutions to the axisymmetric Laplace problem. In the analysis, it is essential that the droplet is *spherical*. The following theoretical result is from [91]:

$$\mathbf{U}_{mig}^{theo} = \left(\frac{2R^2 g(\rho_2 - \rho_1)(\mu_1 + \mu_2)}{3\mu_2(2\mu_2 + 3\mu_1)} - \frac{2R\sigma_T T_c}{(2\mu_2 + 3\mu_1)(2 + k_1/k_2)} \right) \mathbf{e}_z. \quad (5.19)$$

A sketch of the model problem is presented in Figure 5.1. In the sketch, we neglect the gravity force. Note that σ_T is negative, if the temperature gradient is negative, i.e., $\frac{\partial T}{\partial z} < 0$, which means that the bottom of the domain is hotter than the top of the domain, then \mathbf{U}_{mig}^{theo} is negative, the droplet moves towards the hot end.

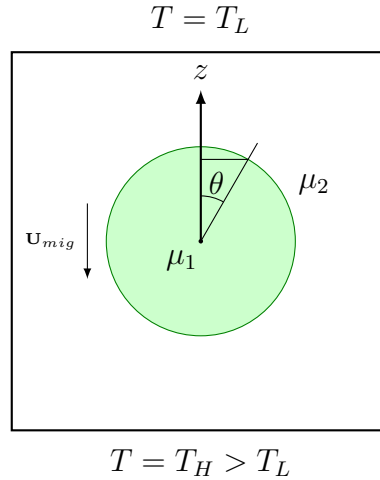


Figure 5.1.: Sketch of the model problem.

Remark 5.2.2 (Special case: $k_1 = k_2$). If thermal conductivities k_1 and k_2 are equal, the continuity condition of the heat flux simplifies to

$$[\nabla T \cdot \mathbf{n}]_{\Gamma} = 0 \quad \text{on } \Gamma.$$

The temperature solution in (5.11) takes the simple form $T = T_0 + T_c z$. The function $\tau(z)$ on Γ is given by

$$\tau(z) = \tau_0 + \sigma_T T_c z = \tau_0 + \frac{\partial\tau}{\partial z} z, \quad (5.20)$$

where $\sigma_T T_c = \frac{\partial\tau}{\partial z}$ is a constant. In the example of Figure 5.1, T_c and σ_T have negative values, thus $\frac{\partial\tau}{\partial z}$ is positive. τ has larger value at the top end of the droplet and smaller

5. Simulation of Marangoni effects

value at the bottom end. Neglecting the gravity force, \mathbf{U}_{mig}^{theo} from (5.19) takes the simple form

$$\mathbf{U}_{mig}^{theo} = -\frac{2R}{3(2\mu_2 + 3\mu_1)} \frac{\partial \tau}{\partial z} \mathbf{e}_z. \quad (5.21)$$

5.2.3. Instationary Navier-Stokes problem with Marangoni effects

In this section, we introduce the model used in the simulations. We only investigate the fluid dynamics of a droplet with Marangoni effects. Hence we assume $\alpha_1 = \alpha_2 = \alpha$ and $k_1 = k_2 = k$. Under the assumption that the Marangoni number is small (zero), the instationary temperature field (5.1) simplifies to

$$\frac{\partial T}{\partial t} - \alpha \Delta T = 0 \quad \text{in } \Omega_i, \quad i = 1, 2, \quad (5.22)$$

with interfacial conditions (5.2). We consider the initial temperature field $T(0)$ with a constant temperature gradient as described in the last section. With suitable boundary conditions, we achieve a stationary solution $T(z) = T_0 + T_c z$ with a constant T_c . This solution does not depend on either the velocity field \mathbf{u} or the instantaneous position of Γ . Hence the solution process of the temperature equation and the fluid dynamics is *decoupled*. From this temperature solution, we derive the surface tension coefficient function $\tau(\mathbf{x}, t)$ on $\Gamma(t)$

$$\tau(\mathbf{x}, t) = \tau_0 + \sigma_T T_c z = \tau_0 + \frac{\partial \tau}{\partial z} z, \quad \mathbf{x} \in \Gamma(t), \quad (5.23)$$

where τ_0 is the surface tension coefficient on $\Gamma(0)$ at the equator, and $\frac{\partial \tau}{\partial z} = \sigma_T T_c$ is a constant. The Marangoni effect is characterized by the function $\tau(\mathbf{x}, t)$ on $\Gamma(t)$. In the numerical simulations, we use the standard sharp interface model of two-phase incompressible flows (2.41) with $\tau(\mathbf{x}, t)$ as in (5.23).

We now specify the domain, boundary and initial conditions for the Navier-Stokes two phase flow problem with Marangoni effects. For Ω we take a cube with a side length L . The interface $\Gamma(0)$ is a sphere at the center of the cube with radius R . $\Omega_1(0)$ is the interior of this sphere. The boundary conditions for \mathbf{u} are *zero* velocity. The values for L and R will be specified further on. A snapshot of the cross section of Ω is given in Figure 5.3.

The theoretical result (5.21) predicts the steady migration velocity of a spherical droplet due to Marangoni effects. The analysis is based on a stationary Stokes model in an infinite domain, and the interface conditions differ from the ones used in the standard model, i.e. the spherical droplet assumption in the theoretical analysis and the normal stress balance condition in the standard model. We expect that this relation yields a good prediction of the droplet velocity in the standard model, when the Reynolds number and the capillary number are negligible. In what follows, we explain under which conditions the latter is a good approximation to the standard model.

From the infinite domain to a bounded domain

We consider the stationary Stokes model described above. We set $\mu_1 = \mu_2 = 1 \text{ kg/ms}$. Instead of an infinite domain we consider this model in a cube Ω with edge length L . In

the bounded domain Ω we consider the stationary Stokes equations as in (5.5). The interface conditions are as in (5.6), (5.7) and (5.8). At all boundaries, we assign the Dirichlet condition $\mathbf{u}(\mathbf{x}) = (0, 0, -\mathbf{U}_{\Omega_1} \cdot \mathbf{e}_z)$ for $\mathbf{x} \in \partial\Omega$. This model is implemented in the flow solver ngsflow [58]. We refer to [50] for details of this package.

Remark 5.2.3 (Several aspects concerning the implementation). *The tetrahedral grids used are aligned to the interface Γ . The interface can be treated as an internal boundary. For the discretization $H(\text{div})$ conforming finite elements are used. The polynomial degree of the elements is varied in the experiments to check the accuracy of the discretization. The shape constraint $\mathbf{u} \cdot \mathbf{n} = 0$ on the interface is easy to implement as a Dirichlet condition on the internal boundary Γ . The tangential interfacial stress condition $[\mathbf{P}\boldsymbol{\sigma}\mathbf{n}]_{\Gamma} = \nabla_{\Gamma}\tau$ is treated as a natural internal boundary condition. As discussed in section 5.2.2, we determine the unknown scalar migration velocity $\mathbf{U}_{\Omega_1} = g\mathbf{e}_z$ by introducing an integral condition of the normal stress balance (5.14), which is given by*

$$h(g) := \mathbf{e}_z \cdot \int_{\Gamma} [(\mathbf{n}^T \boldsymbol{\sigma} \mathbf{n}) \mathbf{n}]_{\Gamma} ds \stackrel{!}{=} \mathbf{e}_z \cdot \int_{\Gamma} (-\tau \kappa \mathbf{n}) ds. \quad (5.24)$$

The right-hand side of the equation (5.24) can be integrated for a spherical droplet with a radius R and a given function $\tau(z)$ from (5.20):

$$h(g) \stackrel{!}{=} -\frac{4}{3}\pi R^3 \kappa \frac{\partial \tau}{\partial z} = -\frac{8}{3}\pi R^2 \frac{\partial \tau}{\partial z}. \quad (5.25)$$

The correct value of g can be numerically determined as follows. We assign $(0, 0, -g\mathbf{e}_z)$ as the boundary condition of the stationary Stokes model on the bounded domain Ω . This Stokes problem can be solved and the resulting velocity field and pressure are used to calculate the scalar quantity $h(g)$. Using a simple root finding algorithm, the solution of (5.25) denoted by g^* , can be determined approximately, which leads to the correct migration velocity $\mathbf{U}_{\Omega_1} = g^*\mathbf{e}_z$.

Using this implementation we performed experiments for the case $\mu_1 = \mu_2 = 1 \text{ kg/ms}$. Based on the results, we choose $L = 0.032 \text{ m}$ and a droplet radius $R = 0.002 \text{ m}$, and obtain at most 1% difference between the numerically computed migration velocity and the theoretical prediction (5.21), which is derived for an unbounded domain. In what follows, we keep the values of L and R fixed.

The theoretical migration velocity depends on the value of $\frac{\partial \tau}{\partial z}$. We perform numerical experiments in ngsflow [58] to test this dependency. The comparison between numerical migration velocities and theoretical predictions are shown in Figure 5.2. We obtain a good agreement, thus boundary effects can be neglected for the chosen configuration, i.e. the choice of L and R .

Restrictions on Reynolds number and capillary number

In the Navier-Stokes model we have to specify ρ_i , μ_i as well as $\frac{\partial \tau}{\partial z}$. The Reynolds number defined in (5.3) relates the size of inertia to that of viscous stresses. With $R = 0.002 \text{ m}$

5. Simulation of Marangoni effects

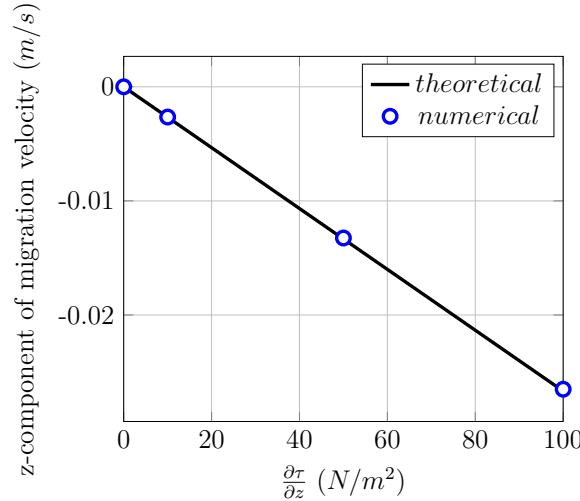


Figure 5.2.: Comparison of theoretical migration velocity and numerical results for various values of $\partial\tau/\partial z$.

and \mathbf{U}_{mig}^{theo} from (5.21), we obtain

$$\begin{aligned} \text{Re} &= \frac{\rho_2 \|\mathbf{U}_{mig}^{theo}\| R}{\mu_2} = \frac{\rho_2 R^2}{\mu_2} \left| \frac{\partial\tau}{\partial z} \right| \frac{2}{3(2\mu_2 + 3\mu_1)} \ll 1, \\ \Rightarrow \left| \frac{\partial\tau}{\partial z} \right| &\frac{\rho_2}{\mu_2(2\mu_2 + 3\mu_1)} \ll 3.75 \times 10^5. \end{aligned}$$

In order to maintain the spherical shape, the capillary number also has to be small. For this model problem, it is defined by

$$\text{Ca} := \frac{\mu_2 \|\mathbf{U}_{mig}^{theo}\|}{\tau_0}.$$

We require that $\text{Ca} \ll 1$, which leads to

$$\begin{aligned} \text{Ca} &= \frac{\mu_2 \|\mathbf{U}_{mig}^{theo}\|}{\tau_0} = \frac{\mu_2 R}{\tau_0} \left| \frac{\partial\tau}{\partial z} \right| \frac{2}{3(2\mu_2 + 3\mu_1)} \ll 1, \\ \Rightarrow \left| \frac{\partial\tau}{\partial z} \right| &\frac{1}{\tau_0(2 + 3\mu_1/\mu_2)} \ll 750. \end{aligned}$$

In this parameter range we expect that the flow behavior, modeled by the incompressible two-phase Navier-Stokes equations, can be good approximated by the stationary Stokes model. In the next section, we present numerical results in comparison with theoretical predictions.

5.3. Benchmark problem and numerical experiments

In this section we present results of our numerical solver applied to the two-phase Navier-Stokes model described in section 5.2.3. In section 5.3.1 we show some properties of our

solver, related to the mesh convergence and the choice of time integration schemes. In section 5.3.2 we study a few physical phenomena related to Marangoni effects, for example, the relaxation time and the sphericity of the droplet.

Based on the analysis in section 5.2.3 we consider a specific benchmark problem that is “close to” the Stokes model studied in [91]. To test our numerical methods, we solve the Navier-Stokes equation within a bounded domain with *zero velocity* at all boundaries. A snapshot of a numerical simulation is shown in Figure 5.3.

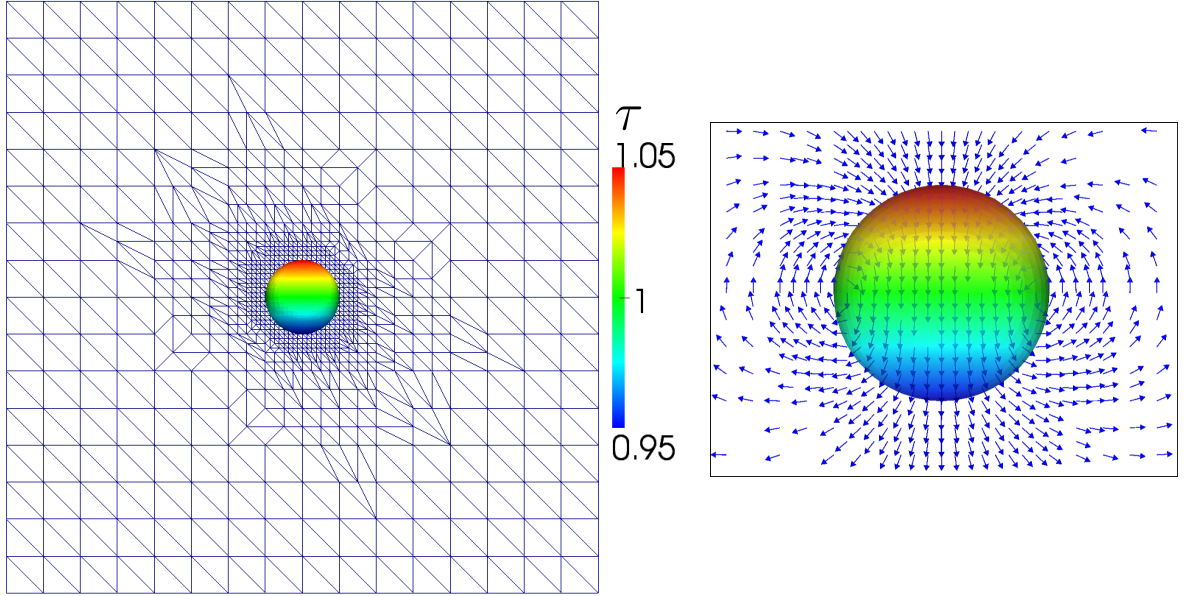


Figure 5.3.: A snapshot of a numerical simulation. The droplet is magnified in the right figure. The arrows shows the circulation pattern of the velocity field.

We choose the total simulation time such that the droplet moves approximately one diameter length. For investigating physical phenomena, we solve a simpler problem by introducing a proper transformation of the velocity which will be described in detail later. In the simulations, we determine the droplet migration velocities numerically and compare the results with theoretical predictions, e.g. (5.21). The z -component of the droplet velocity is denoted by $U_{mig}^{num}(t)$, and defined by

$$U_{mig}^{num}(t) := \frac{1}{|\Omega_{1,h}(t)|} \int_{\Omega_{1,h}(t)} \mathbf{u}_h(\mathbf{x}, t) \cdot \mathbf{e}_z \, d\mathbf{x},$$

where $\Omega_{1,h}(t)$ is determined by $\Gamma_h(t)$, cf. section 3.3.2.

In the experiments, we observe that after a certain time t_* , the velocity $U_{mig}^{num}(t)$ oscillates around a constant value. A time averaged mean value of $U_{mig}^{num}(t)$ for $t \in [t_*, t_{end}]$, which we call the *numerical migration velocity*, is denoted by U_{mig}^{num} and can be compared to the scalar quantity $U_{mig}^{Stokes} := \mathbf{U}_{mig}^{theo} \cdot \mathbf{e}_z$ according to (5.21).

Parameters in the experiments are as follows. The computational domain is given by $\Omega = [-0.032, 0.032] \times [-0.032, 0.032] \times [-0.032, 0.032] \, m^3$. The boundary conditions on $\partial\Omega$ are *zero velocity*. The initial droplet domain $\Omega_1(0)$ is a sphere with a radius

5. Simulation of Marangoni effects

$R = 0.002 m$ located in the center of the cube. The initial velocity $\mathbf{u}(0)$ is zero. The reference surface tension coefficient τ_0 is $1 N/m$.

The initial mesh is a uniform one with 8 cubic elements in each direction. Every cubic element is further divided into six tetrahedra. In a small neighborhood of the interface, the mesh is locally refined. We use backward Euler scheme for the time integration and solve the coupled system (3.19) between the level set equation and the fluid dynamics in each time step. The techniques introduced in chapter 4, i.e. the improved surface normals and the convergence acceleration, are also applied.

5.3.1. Properties of numerical methods

In this section, we discuss a few properties of our numerical solver applied to the aforementioned stationary Navier-Stokes model. The quantity of interest is the migration velocity. We present the convergence behavior of our solver with respect to the mesh refinement. The oscillatory behavior of a specific time integration scheme is relevant to the accuracy of numerical results. With numerical experiments, we compare three time integration schemes with respect to perturbations in the simulations. We also show the necessity of performing the fixed point iteration for solving the coupled system in each time step.

Mesh convergence

We take material parameters as follows: $\rho_1 = \rho_2 = 1 kg/m^3$, $\mu_1 = \mu_2 = 1 kg/(m \cdot s)$ and $\frac{\partial \tau}{\partial z} = 25 N/m^2$. The Reynolds number in this case is $Re = 1.3333 \times 10^{-5}$, and the capillary number is $Ca = 6.6667 \times 10^{-3}$. These numbers are comparable with the ones presented in [41] ($Re = Ma = 10^{-4}$, $Ca = 0$) and [53] ($Re = Ma = 2.5 \times 10^{-3}$, $Ca = 0.05$).

We perform numerical experiments to study the dependence of U_{mig}^{num} on grid refinements. The start time is $t_0 = 0$, and the end time is $t_{end} = 0.6 s$. Within this time interval, the droplet moves approximately one diameter length. To compensate the distortion of the level set function, we perform a reparametrization of the level set function every 0.15 s. Next to the interface ($\pm 4 \times 10^{-4} m$) we apply an adaptive mesh refinement. As we refine the grid, the time step sizes are also reduced by $\Delta t_\ell = t_{end}/2^{5+\ell}$ with ℓ the grid refinement level. Time dependent results of the migration velocity are shown in Figure 5.4. In the experiments, we observe that the x/y components of the numerical migration velocity is two orders of magnitudes smaller than the z component for refinement levels above 3.

In Figure 5.4, we observe two time scales: the initial fast acceleration phase and the quasistatic phase. With the current choice of Δt_ℓ , the initial fast acceleration phase is not resolved. Later we will have a closer look at this phase by refining the time step size. We are interested in the quasistatic phase and calculate time averaging results in $[0.03 s, t_{end}]$. The time averaging results are shown in Table 5.1 for different refinement levels. We study the order of convergence of the scalar sequence U_{mig}^{num} , and observe a linear convergence behavior with an approximated reduction factor 0.25 (0.27 on level 3, 0.24 on level 4). Note that after each refinement the grid size h and Δt are both

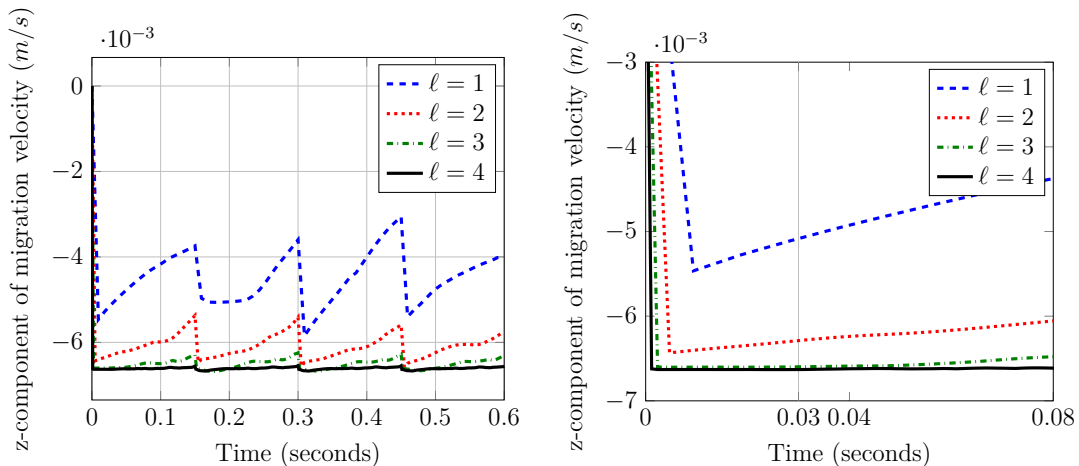


Figure 5.4.: Time dependent numerical migration velocity $U_{mig}^{num}(t)$ for $\frac{\partial\tau}{\partial z} = 25$ on level 1 to level 4 refinement in time interval $[0, 0.6]$ s (left) and a zoom out plot in time interval $[0, 0.08]$ s (right).

halved, hence a reduction factor 0.25 indicates a second order convergence for U_{mig}^{num} . By utilizing the approximated reduction factor 0.25, we obtain a *numerical limiting value* of U_{mig}^{num} , which is -0.006643857 m/s. This numerical limiting value can be considered as the *best possible* value of U_{mig}^{num} . The third and fourth columns in Table 5.1 are absolute and relative errors compared to this numerical limiting value. The theoretical migration velocity for the choice of parameters is $U_{mig}^{theo} = -0.00666667$ m/s. The relative difference between the numerical limiting value -0.006643857 m/s and U_{mig}^{theo} is about 0.3%.

Refinement level (ℓ)	U_{mig}^{num}	abs. error	rel. error
1	-0.00448026	2.164×10^{-3}	33%
2	-0.00608466	5.592×10^{-4}	8.4%
3	-0.00650999	1.339×10^{-4}	2.0%
4	-0.00661039	3.347×10^{-5}	0.50%

Table 5.1.: The numerical migration velocity U_{mig}^{num} on different grid refinements. The unit is m/s. Errors are calculated with respect to the *extrapolated* numerical limiting value -0.006643857 m/s.

By choosing much smaller time steps, we investigate the behavior in the initial fast acceleration phase. In [3], the authors studied a droplet in an instationary Stokes flow with Marangoni effects and derived the initial acceleration of the droplet, which is denoted by $(\mathbf{U}_{mig}^{theo}(0))'$. Without gravity force, the initial acceleration is predicted to be

$$(\mathbf{U}_{mig}^{theo}(0))' = \frac{-3}{(1 + \sqrt{(\mu_1\rho_1)/(\mu_2\rho_2)})} \frac{\sigma_T T_c}{(0.5 + \rho_1/\rho_2) \rho_2 R} \mathbf{e}_z. \quad (5.26)$$

We decrease the time step size Δt to compare numerical results with this prediction. We take $\rho_2 = 1$ and change the value of ρ_1 and keep other parameters the same as in the

5. Simulation of Marangoni effects

previous experiments. As mentioned above, we concentrate on the z -component of the initial acceleration and construct a numerical approximation:

$$(\mathbf{U}_{mig}^{num}(0) \cdot \mathbf{e}_z)' \approx \frac{4\mathbf{U}_{mig}^{num}(\Delta t) - \mathbf{U}_{mig}^{num}(2\Delta t)}{2\Delta t} \cdot \mathbf{e}_z =: (U_z^{num}(0))'. \quad (5.27)$$

Remark 5.3.1. *The quotient in (5.27) is a form of numerical differentiation and derived as follows. For a sufficiently smooth scalar function $f(t)$ at $t = 0$, we express $f(\Delta t)$ and $f(2\Delta t)$ by using Taylor expansions:*

$$f(\Delta t) = f(0) + \Delta t f'(0) + \frac{(\Delta t)^2}{2} f''(0) + \mathcal{O}((\Delta t)^3), \quad (5.28)$$

$$f(2\Delta t) = f(0) + 2\Delta t f'(0) + 2(\Delta t)^2 f''(0) + \mathcal{O}((\Delta t)^3). \quad (5.29)$$

We multiply equation (5.28) by 4 and subtract equation (5.29) from it and obtain:

$$4f(\Delta t) - f(2\Delta t) = 3f(0) + 2\Delta t f'(0) + \mathcal{O}((\Delta t)^3). \quad (5.30)$$

Hence we obtain an approximation of $f'(0)$:

$$f'(0) = \frac{4f(\Delta t) - f(2\Delta t) - 3f(0)}{2\Delta t} + \mathcal{O}((\Delta t)^2). \quad (5.31)$$

At $t = 0$, the droplet is at rest, i.e. $\mathbf{U}_{mig}^{num}(0) = \mathbf{0}$, thus the approximation in equation (5.27) is derived.

We choose different Δt and study the convergence behavior of $(U_z^{num}(0))'$. The density ratios are chosen to be 0.02 and 5. Experiments are performed at level 3 refinement level. The results are presented in Figure 5.5. We observe a second order convergence of the numerical results. For the density ratio $\rho_1/\rho_2 = 0.02$, the numerical limiting value is -62119.10 m/s^2 , and for the density ratio $\rho_1/\rho_2 = 5$, it is -2045.407 m/s^2 . Relative errors of $(U_z^{num}(0))'$ with respect to these numerical limiting values are plotted in Figure 5.5. Compared with the theoretical values from equation (5.26), which are -63180.34 m/s^2 for $\rho_1/\rho_2 = 0.02$ and -2036.72 m/s^2 for $\rho_1/\rho_2 = 5$, the numerical limiting values have 1.7% and 0.43% relative errors correspondingly. Note that the backward Euler scheme also has local truncation error $\mathcal{O}((\Delta t)^2)$, hence the second order convergence observed in Figure 5.5 is in good accordance with the comments we made about approximation errors in Remark 5.3.1, and a good agreement with the theoretical predictions is achieved.

We perform grid refinements and study its effect on the numerical limiting values. The results are shown in Figure 5.6 together with the theoretical prediction. For $\rho_1/\rho_2 = 1$, we list the relative errors in a table. We do not observe a clear convergence behavior of the results. Compared with the results presented in [53], we achieve a much more accurate initial acceleration. In that paper, however, a (much) more complicated problem, in which the fluid dynamics is coupled with the temperature equation, is treated.

Time integration

We discuss now the influence of time integration schemes on the accuracy of numerical results. We compare the Euler scheme, the Crank-Nicolson scheme and a fractional step

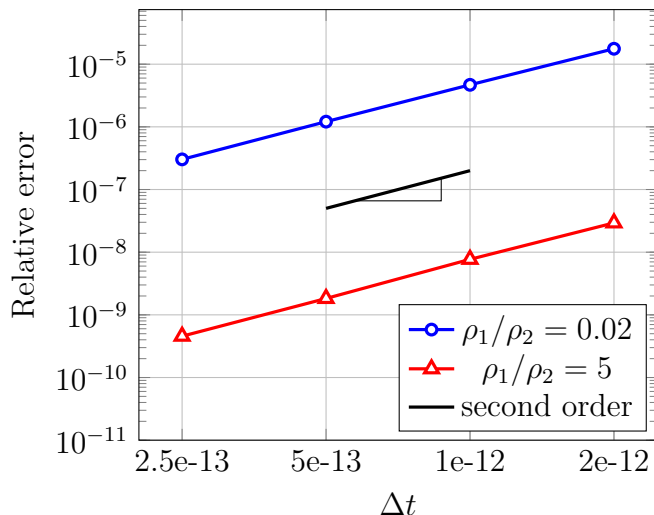


Figure 5.5.: Relative errors in $(U_z^{num}(0))'$ for different Δt and density ratios.

scheme with respect to performance at initial steps and after reparametrization. The Euler scheme has a consistency order of 1, and the Crank-Nicolson and the fractional step scheme both have a consistency order of 2. We refer to [39] for details concerning the Crank-Nicolson and the fractional step scheme.

In Figure 5.7, we present a comparison of initial steps of the aforementioned three time integration schemes. Experiments are performed at level 3 refinement. We observe that the Crank-Nicolson scheme generates the strongest and longest oscillations. This is due to the instantaneous acceleration of the droplet and no smoothing behavior of the Crank-Nicolson scheme. In contrary, the backward Euler scheme has no oscillatory behavior. The performance of the fractional step scheme is somewhere in between.

In the numerical experiments, we need to perform reparametrization once in a while, which facilitates the accurate determination of the zero level of the level set function, i.e. the interface position. We also observe similar oscillations directly after the reparametrization as it is shown in Figure 5.8.

Remark 5.3.2. *Due to the evolution of the level set function, the initial distance function property is lost, which hinders the accurate determination of the zero level. We perform a reparametrization method to restore approximately the distance function property of the level set function. However, a reparametrization method will to some extent alter the position of the zero level. With respect to a time integration scheme, this alternation introduces a perturbation of the initial value for the time step directly after the reparametrization step, which explains the oscillatory behavior seen in Figure 5.8.*

From Figure 5.7 and Figure 5.8, we draw the conclusion that, although the backward Euler scheme has a lower consistency order than the other two, it is significantly more robust with respect to unavoidable perturbations in the simulation. For this reason, we choose the backward Euler scheme for the experiments below.

As described in section 3.5, in each time step we perform a fixed point iteration between the level set function and the fluid dynamics. For solving a strongly nonlinear coupling

5. Simulation of Marangoni effects

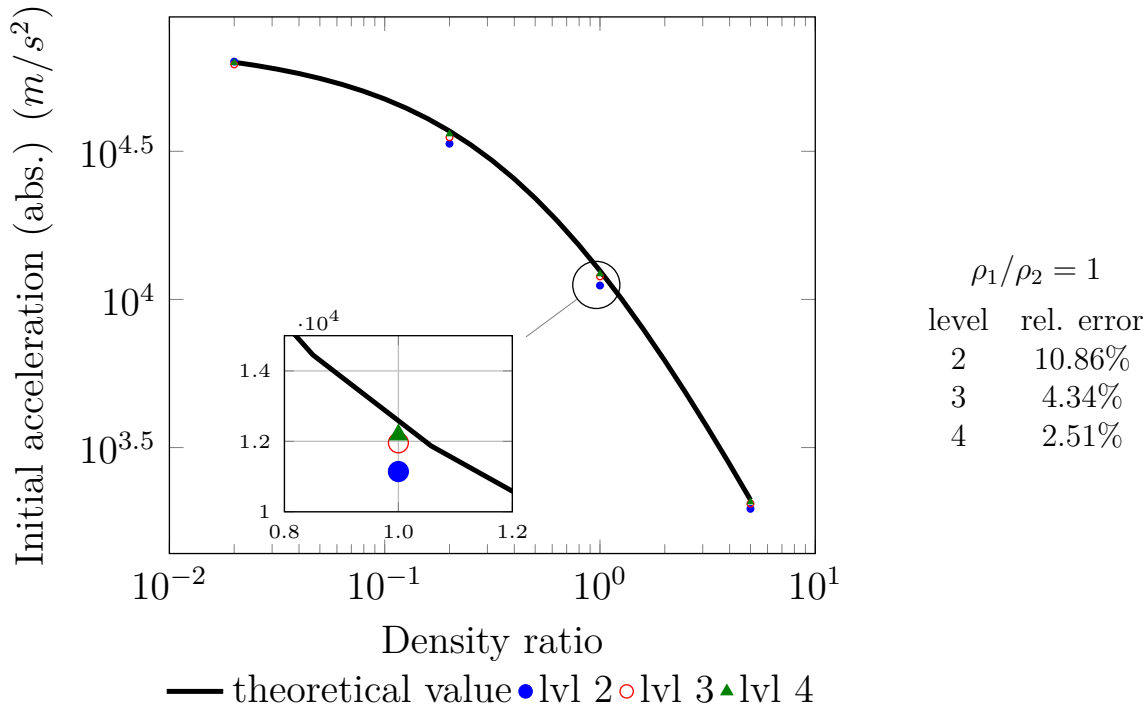


Figure 5.6.: Absolute value of the initial acceleration $\left(U_{mig}^{num}(0)\right)'$ for different density ratios (ρ_1/ρ_2) on refinement levels 2,3 and 4.

between the two sets of equations, it is essential to introduce this iteration. For comparison, we also perform numerical experiments with a time-lagging scheme between the two sets of equations, i.e. in one time step, we only solve Navier-Stokes equation once, and the velocity solutions are used to convect the level set function in the next time step. The results are listed in Table 5.2. Similar to Table 5.1, we observe a second order convergence of U_{mig}^{num} for the decoupling scheme with the fixed point iteration. We do not observe a clear order of convergence for the time-lagging scheme. Regarding the accuracy of the numerical migration velocity, the decoupling scheme with a fixed point iteration outperforms the time-lagging scheme to a large extent. Hence the fixed point iteration between the level set equation and the fluid dynamics is crucial for an accurate numerical result.

Refinement level (l)	FP iteration	time-lagging scheme
1	-0.00448026	-0.00270139
2	-0.00608466	-0.00367348
3	-0.00650999	-0.00468283
4	-0.00661039	-0.00545888

Table 5.2.: Comparison between the decoupling scheme with a fixed point (FP) iteration and a time-lagging scheme. Shown are numerical migration velocity U_{mig}^{num} in time interval $[0.03 \text{ s}, t_{end}]$. The unit is m/s .

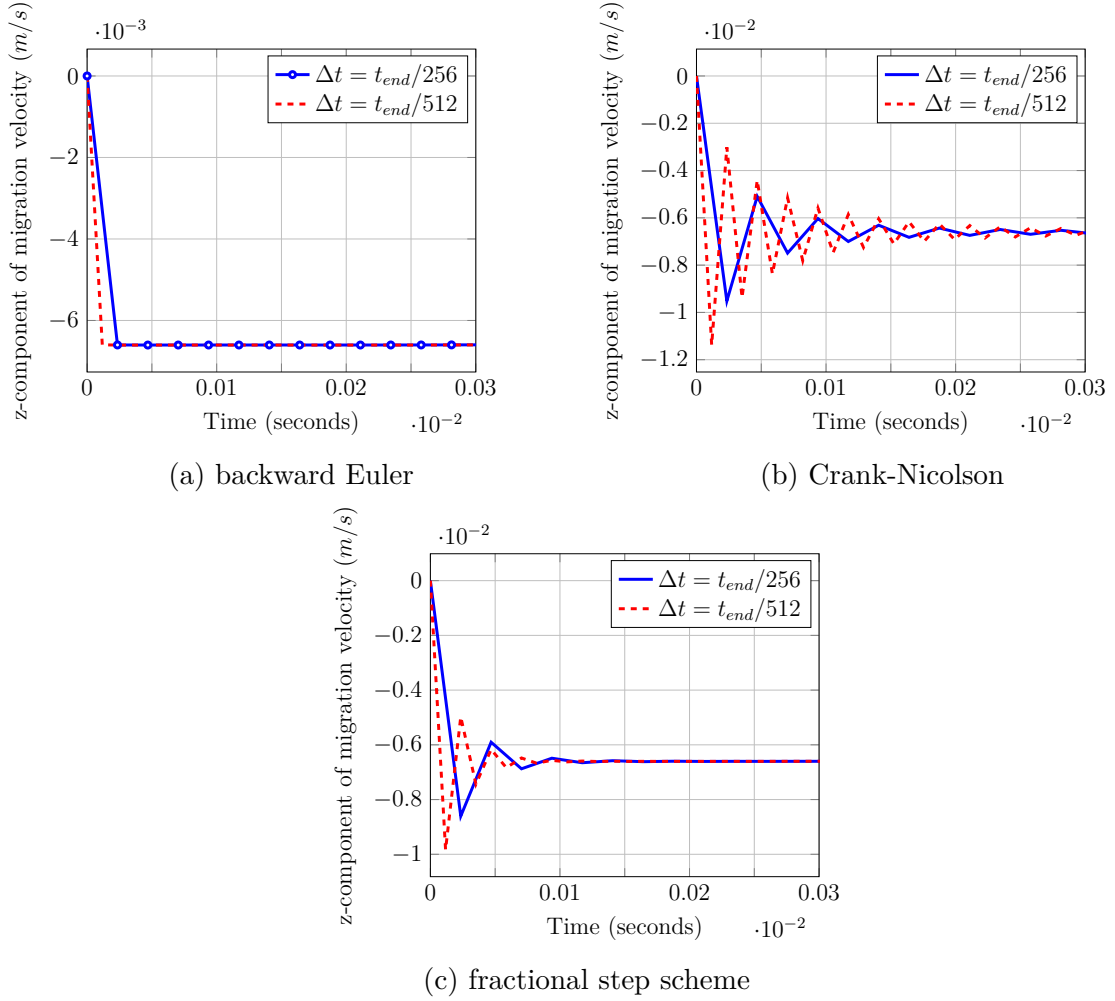


Figure 5.7.: A comparison of the backward Euler, the Crank-Nicolson and a fractional step scheme at initial phase $[0,0.03]$ s. The level set function and the fluid dynamics are decoupled by a fixed point iteration as described in section 3.5.

Robustness with respect to $\frac{\partial \tau}{\partial z}$

$\frac{\partial \tau}{\partial z}$ quantifies the magnitude of the Marangoni effect. A larger magnitude of this quantity increases the numerical complexity. We test our solver by studying the dependence of U_{mig}^{num} on the parameter $\frac{\partial \tau}{\partial z}$. We choose refinement level 3, and let the droplet move a distance of approximately one diameter length. The results are shown in Table 5.3. From the table, we can observe that our solver is able to deliver stable results for larger $\frac{\partial \tau}{\partial z}$, in other words, the solver is robust with respect to the change of $\frac{\partial \tau}{\partial z}$.

5.3.2. Physical effects

In this section, we use our validated numerical solver to study physical effects related to Marangoni forces. In section 5.3.1, our numerical solver is tested with zero velocity boundary condition. Hence, the droplet moves considerably in the domain. In this section, we treat an equivalent problem, in which the droplet remains approximately in the middle

5. Simulation of Marangoni effects

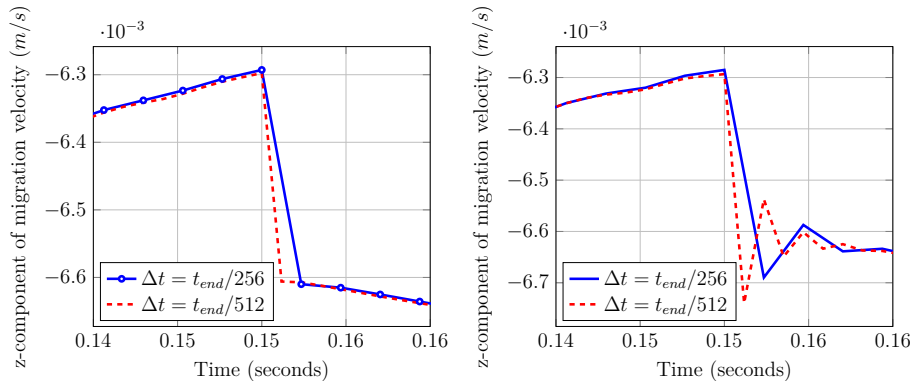


Figure 5.8.: A comparison of the backward Euler (left, with marks) and the fractional step scheme (right) directly after a reparametrization step at $t = 0.15$ s.

$\frac{\partial \tau}{\partial z}$ (N/m^2)	U_{mig}^{num} (m/s)	theoretical value	rel. error	Re
25	-0.00650999	-0.0066667	2.4%	1.3×10^{-5}
50	-0.0131053	-0.013333	1.7%	2.7×10^{-5}
75	-0.0196962	-0.020000	1.5%	4.0×10^{-5}
100	-0.02627621	-0.026667	1.5%	5.3×10^{-5}

Table 5.3.: Numerical migration velocity U_{mig}^{num} with different $\frac{\partial \tau}{\partial z}$ values. The relative errors are calculated with respect to theoretical values.

of the domain. The magnitude of the velocity is smaller than the previous results, thus this is a "simpler" problem with respect to numerical difficulties. More accurate numerical results are expected.

Moving reference frame

We perform an instationary simulation to study the evolving shape of the droplet. The most natural way is to solve the Navier-Stokes equation from section 5.2.1 within a bounded domain with *zero velocity* at all boundaries. The droplet moves within this domain. For some numerical experiments, it is advantageous to let the droplet stay approximately in the center of the domain. We introduce a moving reference frame technique to accomplish this requirement.

We denote the velocity in the Navier-Stokes model with zero velocity at all boundaries as \mathbf{u} . The *theoretical* migration velocity \mathbf{U}_{mig}^{theo} according to (5.21) is subtracted from \mathbf{u} , and a transformed velocity $\tilde{\mathbf{u}} := \mathbf{u} - \mathbf{U}_{mig}^{theo}$ is defined. We consider the Navier-Stokes equations for this transformed velocity. The nonlinear convection term $(\mathbf{u} \cdot \nabla)\mathbf{u}$ has to be transformed to $(\tilde{\mathbf{u}} + \mathbf{U}_{mig}^{theo}) \cdot \nabla \tilde{\mathbf{u}}$ for consistency. Interface conditions remain the same. Boundary conditions for $\tilde{\mathbf{u}}$ are given by

$$\tilde{\mathbf{u}}(\mathbf{x}, t) = -\mathbf{U}_{mig}^{theo}, \quad \mathbf{x} \in \partial\Omega. \quad (5.32)$$

The initial condition is also transformed to $\tilde{\mathbf{u}}(\mathbf{x}, 0) = -\mathbf{U}_{mig}^{theo}$. We perform numerical experiments with this transformed Navier-Stokes equations to study physical effects related

to Marangoni forces.

Relaxation time

In Figure 5.4, we observe that there exist two time scales. Initially at rest, the droplet is almost instantaneously accelerated. After that, the droplet velocity reaches a steady state value. These two time scales have also been noticed by Brady *et al.*[16]. In section 5.3.1, we studied the initial acceleration of the droplet at $t = 0$. In this section, we concentrate on the time needed to reach the steady state value, which is often called the relaxation time.

A much smaller time step $\Delta t = 10^{-7}$ s is chosen, such that the initial acceleration phase can be resolved. Keeping the viscosity ratio μ_1/μ_2 unchanged, we perform numerical experiments with different values of μ_1 and μ_2 . Experiments are performed at the refinement level 3. The results are shown in Figure 5.9. The velocities in the figure are back transformed to the original frame. We observe that the initial accelerations at $t = 0$ are in good agreements with the theoretical prediction (5.26).

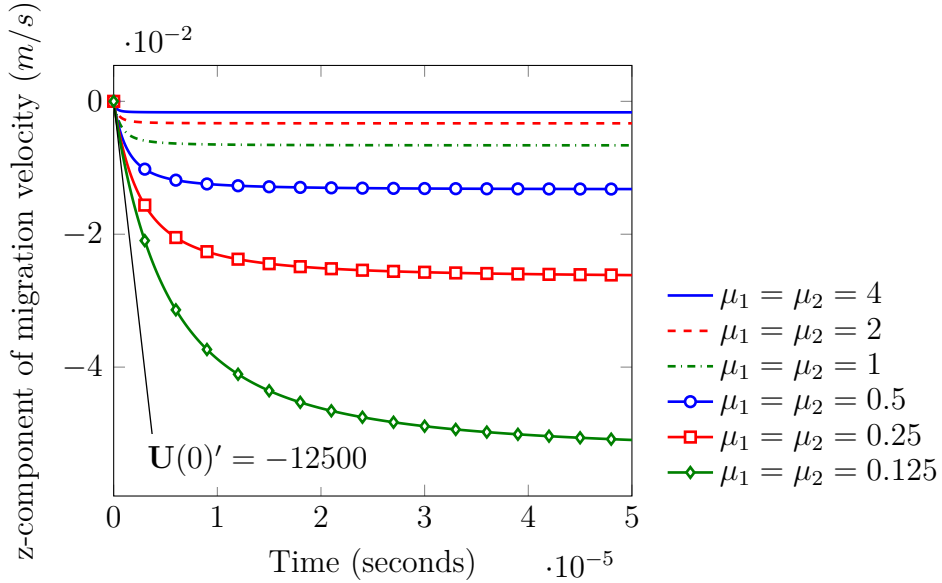


Figure 5.9.: Initial phase of the numerical migration velocity $U_{mig}^{num}(t)$ for $\frac{\partial \tau}{\partial z} = 25$ on level 3 refinement with different viscosities $\mu_1 = \mu_2 = 0.125, \dots, 4$. The theoretical initial acceleration is $(\mathbf{U}_{mig}^{theo}(0))' = -12500$ m/s².

To study the relaxation time, we measure the time needed for the droplet to deaccelerate to a certain value of acceleration, which is chosen as -100 m/s². In this deacceleration process, the viscous forces play an important role. Larger viscous force causes shorter relaxation time, which is observed in Figure 5.9. We list the relaxation times in Table 5.4.

In [83], the authors studied the motion of a droplet driven by a body force through a viscous fluid, they predicted that the time taken to achieve a steady state is proportional to the viscous relaxation time coefficient $\rho R^2/\mu$. In our case, the driving force is the

5. Simulation of Marangoni effects

viscosity ($\mu_1 = \mu_2$)	relaxation time (second)	ratio (t_i/t_{i+1})
0.125	3.94×10^{-5}	2
0.25	1.97×10^{-5}	1.99
0.5	9.9×10^{-6}	1.98
1	5.0×10^{-6}	1.92
2	2.6×10^{-6}	2
4	1.3×10^{-6}	-

Table 5.4.: Relaxation time for different viscosities. The results shown are the time needed for the droplet to deaccelerate from $(\mathbf{U}_{mig}^{num}(0))' \approx -12500 \text{ m/s}^2$ to $(\mathbf{U}_{mig}^{num}(t))' = -100 \text{ m/s}^2$.

interfacial force. From Table 5.4, we observe that the initial relaxation time also satisfies the same relation, i.e. $t \sim \frac{1}{\mu}$.

Shape of the droplet

In the theoretical analysis, the shape of the droplet is assumed to be spherical. We investigate the shape of the droplet in the numerical experiments. We take the example from section 5.3.1, the refinement level is 3, the parameters are $\rho_1 = \rho_2 = 1$, $\mu_1 = \mu_2 = 1$ and $\tau_0 = 1$, $\frac{\partial \tau}{\partial z} = 25$. In Figure 5.10, the evolution of the diameters are presented. We observe that the droplet maintains its spherical shape as it moves through the domain, which can be explained by the relative small capillary number (6.6667×10^{-3}) in the numerical experiments.

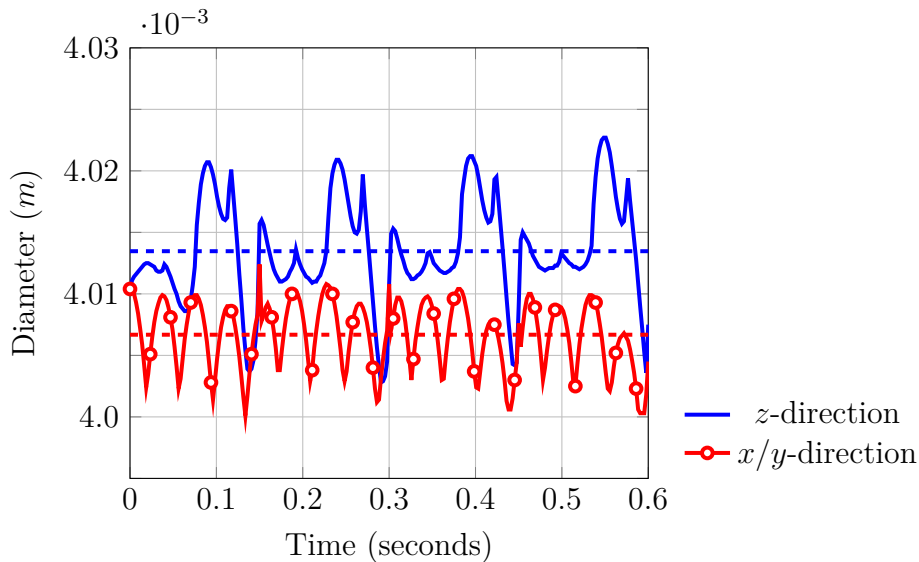


Figure 5.10.: Evolution of diameters in $x/y/z$ -directions for $\tau_0 = 1$ and $\frac{\partial \tau}{\partial z} = 25$. Dashed lines are time averaged values.

5.3.3. Summary

We validated our numerical solvers with respect to mesh convergence. A good agreement between numerical results and the theoretical analysis from [91] is achieved. By comparison with other time integration schemes, we choose the backward Euler scheme for its robustness with respect to perturbations. The importance of the fixed point iteration in the decoupling scheme is presented by comparing with a simple time-lagging method, cf. Table 5.2. We studied the initial relaxation time of the droplet due to the Marangoni forces and the sphericity of the droplet. In both cases, good agreements with theoretical predictions are achieved.

6. Simulation of flows with a viscous interface

6.1. Introduction

Dynamic properties of interfaces, such as interfacial shear and dilatational viscosities, can have a significant effect on the flow behavior. The effects caused by these properties can strongly influence the dynamics of emulsions, of biological fluids, of polymer blends and of many other soft matters. A better understanding of these phenomena is a major topic in the research field of *surface* rheology and in recent years a vast number of papers on dynamic properties of interfaces in soft matters has appeared. We refer to [76] for a recent overview. For the mathematical description of interfacial properties some classical models, like e.g. the Boussinesq-Scriven and the Kelvin Voigt models [80, 26] are known in the literature. These constitutive models were derived on a rather ad hoc basis and are applicable to only few, relatively simple, multiphase systems. In recent years there have been significant developments to systematically derive new (more general) constitutive laws for the stress-deformation behavior of interfaces using methods from nonequilibrium thermodynamics [66, 75]. The resulting models are far more advanced than the classical Boussinesq-Scriven and Kelvin Voigt models. Two-phase incompressible flows with an interfacial stress-deformation (i.e. a surface tension force) are usually modeled by either a diffusive interface or a sharp interface model. We restrict to the numerical simulation of the latter class of models. For numerical simulations based on a diffusive interface model we refer to the literature, e.g. [84, 85, 2]. In systems with incompressible fluids a sharp interface model typically consists of the Navier-Stokes equations for the bulk fluids with a surface tension force term on the right-hand side in the momentum equation, cf. section 6.2 for more details. This surface tension force is based on a certain interfacial stress-deformation constitutive law.

In this chapter we do not treat modeling issues but address certain numerical simulation aspects for a class of two-phase incompressible flow sharp interface models with a *viscous* interface property. The results in this chapter are based on our previous paper [72]. As mentioned in previous chapters, in general two-phase flow problems have a very high numerical complexity. For example, the interface is unknown and due to this the flow problem is strongly nonlinear. Secondly, the surface tension force is localized at the (unknown) interface and often has a strong effect on the fluid dynamics. Thirdly, the pressure has a discontinuity across the interface, and also the viscosity and density coefficients are discontinuous across the interface. Finally, the numerical simulation of such problems requires a suitable coupling of the fluid dynamics (e.g. Navier-Stokes solver) and the evolution of the interface (e.g. level set or VOF technique). There are several important

issues relevant for the simulation of two-phase flows that are non-existent in *one*-phase incompressible flow problems. To handle these issues, special numerical techniques are required. Concerning the development and analysis of such special numerical methods only relatively few (compared to methods for one-phase flows) studies are available in the literature, cf. [39] for an overview.

Only recently there have appeared papers on the numerical simulation of *three-dimensional* two-phase flow problems with a *clean interface* model and either a constant surface tension coefficient or a variable surface tension coefficient (Marangoni effect). We are not aware of any literature in which numerical methods for handling a *viscous sharp interface* constitutive model are treated. In this chapter we study this topic. We use the classical Boussinesq-Scriven constitutive law, cf. (2.37), for describing the response of a viscous interface. The following two topics are addressed. Firstly, we present a method that is based on a variational formulation of the surface tension force and that can be used to discretize viscous interface forces. Secondly, we introduce a benchmark problem that is inspired by the recent paper [77]. In that paper analytical relations for the so-called migration velocity of a spherical droplet in a Stokes-Poiseuille flow with Boussinesq-Scriven viscous interface forces are derived. The benchmark problem that we propose is a sharp interface Navier-Stokes model that in a certain sense is close to the stationary Stokes model studied in [77]. We present results of numerical experiments of our finite element solver applied to this benchmark problem.

6.2. Mathematical models

In this section we introduce the models that we consider. In section 6.2.1 we recall a standard sharp interface model for describing the behavior of two-phase incompressible flows in which a Boussinesq-Scriven viscous interface stress tensor is used. Recently, a much simpler model with the same Boussinesq-Scriven tensor has been analyzed in [77]. This simpler model and results for that are given in section 6.2.2. In section 6.2.3 we discuss conditions under which the simple model is expected to be a reasonable approximation of the standard sharp interface model.

6.2.1. A sharp interface model for flows with a viscous interface

Let $\Omega \subset \mathbb{R}^3$ be a domain containing two different immiscible incompressible phases. The time-dependent subdomains containing the two phases are denoted by $\Omega_1(t)$ and $\Omega_2(t)$ with $\bar{\Omega} = \bar{\Omega}_1 \cup \bar{\Omega}_2$ and $\Omega_1 \cap \Omega_2 = \emptyset$. We assume that Ω_1 and Ω_2 are connected and $\partial\Omega_1 \cap \partial\Omega = \emptyset$ (i. e., Ω_1 is completely contained in Ω). The interface is denoted by $\Gamma(t) = \bar{\Omega}_1(t) \cap \bar{\Omega}_2(t)$. The bulk stress tensor is denoted by

$$\boldsymbol{\sigma} = -p\mathbf{I} + \mu\mathbf{D}(\mathbf{u}), \quad \mathbf{D}(\mathbf{u}) = \nabla\mathbf{u} + (\nabla\mathbf{u})^T,$$

with $p = p(x, t)$ the pressure, $\mathbf{u} = \mathbf{u}(x, t)$ the velocity and μ the bulk viscosity, which is assumed to be constant in each of the two bulk phases. The surface deformation tensor is given by $\mathbf{D}_\Gamma(\mathbf{u}) := \mathbf{P}(\nabla_\Gamma\mathbf{u} + (\nabla_\Gamma\mathbf{u})^T)\mathbf{P}$, with ∇_Γ the surface gradient. Based on

the conservation laws for mass and momentum and using the linear Boussinesq-Scriven constitutive law [80] for describing an interface with a viscous response we obtain the following standard model, cf. for example [39],

$$\begin{cases} \rho_i \left(\frac{\partial \mathbf{u}}{\partial t} + (\mathbf{u} \cdot \nabla) \mathbf{u} \right) = -\nabla p + \rho_i \mathbf{g} + \operatorname{div}(\mu_i \mathbf{D}(\mathbf{u})) & \text{in } \Omega_i \times [0, T] \\ \operatorname{div} \mathbf{u} = 0 & \text{in } \Omega_i \times [0, T] \end{cases} \quad i = 1, 2, \quad (6.1)$$

$$[\mathbf{u}]_\Gamma = 0, \quad [\boldsymbol{\sigma} \mathbf{n}]_\Gamma = \operatorname{div}_\Gamma \boldsymbol{\sigma}_\Gamma, \quad (6.2)$$

$$\boldsymbol{\sigma}_\Gamma := [\tau + (\lambda_\Gamma - \mu_\Gamma) \operatorname{div}_\Gamma \mathbf{u}] \mathbf{P} + \mu_\Gamma \mathbf{D}_\Gamma(\mathbf{u}), \quad (6.3)$$

$$V_\Gamma = \mathbf{u} \cdot \mathbf{n} \quad \text{on } \Gamma. \quad (6.4)$$

The constants μ_i, ρ_i denote viscosity and density of the bulk phases in the subdomains Ω_i , $i = 1, 2$, and \mathbf{g} is an external volume force (gravity). The condition in (6.4), where V_Γ denotes the normal velocity of the interface, follows from immiscibility of the two phases. The first condition in (6.2) results from the viscosity of the phases. From momentum conservation one obtains the second relation in (6.2), cf. section 2.4. The model for the surface stress tensor $\boldsymbol{\sigma}_\Gamma$ in (6.3) is the so-called Boussinesq-Scriven constitutive law, with a surface dilatational viscosity coefficient λ_Γ and a surface shear viscosity coefficient μ_Γ . We assume λ_Γ and μ_Γ to be constants with $\lambda_\Gamma \geq \mu_\Gamma \geq 0$. To make this problem well-posed we need suitable boundary conditions for \mathbf{u} , an initial condition $\mathbf{u}(x, 0)$ and an initial configuration of the interface $\Gamma(0)$. These will be specified at the end of this section.

The location of the interface $\Gamma(t)$ is unknown and is coupled to the fluid dynamics via the condition in (6.4) which determines the transport of the interface. We use a level set method [19, 65, 78] for capturing the interface, cf. section 3.2. Combining the Navier-Stokes equations with the level set method, we obtain the one fluid formulation of the two-phase flow problem (3.4). The surface force functional takes the form

$$\begin{aligned} f_\Gamma(\mathbf{v}) &= - \int_\Gamma \operatorname{tr} \left(\boldsymbol{\sigma}_\Gamma (\nabla_\Gamma \mathbf{v})^T \right) ds \\ &= - \int_\Gamma \operatorname{tr} \left(\tau \mathbf{P} (\nabla_\Gamma \mathbf{v})^T \right) ds - \int_\Gamma \operatorname{tr} \left((\lambda_\Gamma - \mu_\Gamma) \operatorname{div}_\Gamma \mathbf{u} \mathbf{P} (\nabla_\Gamma \mathbf{v})^T \right) ds \\ &\quad - \int_\Gamma \operatorname{tr} \left(\mu_\Gamma \mathbf{D}_\Gamma(\mathbf{u}) (\nabla_\Gamma \mathbf{v})^T \right) ds. \end{aligned} \quad (6.5)$$

The numerical treatment of this $f_\Gamma(\mathbf{v})$ is presented in section 4.3.

We now specify the domain, boundary and initial conditions for the Navier-Stokes two-phase flow problem. For Ω we take a rectangular box with lengths L_x, L_y, L_z in the three coordinate directions. The interface $\Gamma(0)$ is defined as a sphere at the centerline of the box with radius r . The subdomain $\Omega_1(0)$ is the interior of this sphere. The boundary conditions for \mathbf{u} are as follows. On the z -boundaries ($z = \pm \frac{1}{2} L_z$) we use periodic boundary conditions. On the y -boundaries we take Dirichlet no slip conditions ($\mathbf{u} = 0$). On the x -inflow boundary we prescribe a Poiseuille profile that is constant in z -direction and has the form

$$\mathbf{u}^P(y) = U_{center} \left(1 - \left(\frac{2y}{L_y} \right)^2 \right) \vec{\mathbf{e}}_x. \quad (6.6)$$

Here $U_{center} > 0$ denotes the speed of the flow on the centerline. On the x -outflow boundary we impose the zero stress condition $\boldsymbol{\sigma} \mathbf{n} = 0$. A sketch of the cross section of

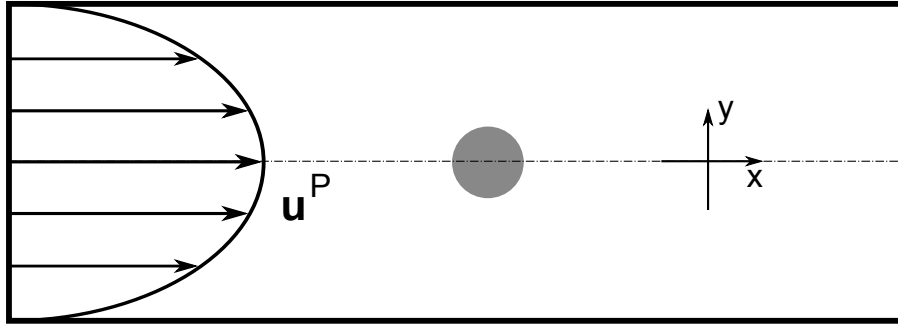


Figure 6.1.: Cross section of the domain, inflow profile and initial droplet position in Navier-Stokes model.

Ω at $z = 0$ is given in Fig. 6.1. The values for the parameters $L_x, L_y, L_z, r, U_{center}$ will be specified further on.

Finally we describe the initial condition $u(\cdot, 0) = u_0(\cdot)$. The function u_0 is taken as the solution of the *stationary Stokes* two-phase problem, obtained by putting the left-hand side in the momentum equation in (6.1) to zero and with interface conditions as in (6.2), (6.3). The boundary conditions and the interface $\Gamma(0)$ for this Stokes problem are the same as the ones specified above.

6.2.2. A stationary Stokes Model

In the recent paper [77], a strongly simplified flow problem with Boussinesq-Scriven interface stresses is studied. In that paper the authors consider an isolated spherical droplet in a Stokes-Poiseuille flow with a jump in the hydrodynamic stress at the interface determined by surface viscous forces according to the Boussinesq-Scriven law. Besides viscous stresses also Marangoni effects, i.e., a variable τ is studied. Here, however, we restrict to the case without Marangoni effects (τ constant). Analytical relations for the so-called *migration velocity* are derived.

We give a more precise definition of the model used in [77]. The stationary droplet Ω_1 is a ball with radius r which has its centre on the x -axis, and $\Omega_2 = \mathbb{R}^3 \setminus \Omega_1$. In both phases creeping flow conditions are assumed, i.e.,

$$\begin{cases} -\mu_i \Delta \mathbf{u} + \nabla p = 0 & \text{in } \Omega_i \\ \operatorname{div} \mathbf{u} = 0 & \text{in } \Omega_i \end{cases} \quad i = 1, 2. \quad (6.7)$$

Instead of a boundary condition the far field condition

$$\mathbf{u}(\mathbf{x}) \rightarrow \mathbf{u}^P(\mathbf{x}) \quad \text{for } \|\mathbf{x}\| \rightarrow \infty \quad (6.8)$$

are used with \mathbf{u}^P given by a Poiseuille flow profile

$$\mathbf{u}^P(y) = U_{center}(1 - \alpha y^2)\vec{e}_x, \quad (6.9)$$

with a given constant $\alpha > 0$, cf. Fig. 6.1. At the interface Γ both kinematic and dynamic boundary conditions are imposed. Define the (droplet) mean velocity $\mathbf{U}_{\Omega_1} := \frac{1}{|\Omega_1|} \int_{\Omega_1} \mathbf{u} \, d\mathbf{x}$. The interface conditions are given by

$$[\mathbf{u}]_{\Gamma} = 0 \text{ on } \Gamma, \quad (6.10a)$$

$$\mathbf{u} \cdot \mathbf{n}_{\Gamma} = \mathbf{U}_{\Omega_1} \cdot \mathbf{n}_{\Gamma} \text{ on } \Gamma, \quad (6.10b)$$

$$[\mathbf{P}\boldsymbol{\sigma}\mathbf{n}]_{\Gamma} = \mathbf{P} \operatorname{div}_{\Gamma} \boldsymbol{\sigma}_{\Gamma} \text{ on } \Gamma. \quad (6.10c)$$

Note that (6.10b) enforces a normal velocity such that the droplet is translating like a rigid body. To obtain a well-posed problem only the *tangential* stress balance condition (6.10c) is imposed.

The model formulated above does not define a unique solution \mathbf{u} due to the unknown mean velocity \mathbf{U}_{Ω_1} . If in (6.10b) the function $\mathbf{U}_{\Omega_1} \cdot \mathbf{n}_{\Gamma}$ is replaced by a *given* scalar function g on Γ , then the model (6.7), (6.8), (6.10), with *data* g in the right-hand side in (6.10b) determines a unique solution, cf. [88]. Hence, for the above model to be well-posed we need an additional condition to determine the mean velocity \mathbf{U}_{Ω_1} . Note that $\int_{\Gamma} \operatorname{div}_{\Gamma} \boldsymbol{\sigma}_{\Gamma} \, ds = 0$. Hence the local force balance $[\boldsymbol{\sigma}\mathbf{n}]_{\Gamma} = \operatorname{div}_{\Gamma} \boldsymbol{\sigma}_{\Gamma}$ in (6.2) implies the global condition $\int_{\Gamma} [\boldsymbol{\sigma}\mathbf{n}]_{\Gamma} \, ds = 0$. This condition is not (necessarily) satisfied in the model above, since only tangential forces are considered in (6.10c). Hence, an additional condition that can be used to determine a unique solution is given by

$$\int_{\Gamma} [\boldsymbol{\sigma}\mathbf{n}]_{\Gamma} \, ds = 0, \quad (6.11)$$

which are three equations that can be used to determine the three unknowns in the mean velocity \mathbf{U}_{Ω_1} .

The Poiseuille flow and spherical droplet are as shown in Fig. 6.1, if we delete the boundaries and extend the Poiseuille profile in y -direction and take it constant in x - and z -direction. Also note that there are no external forces (i.e., a neutrally buoyant droplet), but the interface stress tensor $\boldsymbol{\sigma}_{\Gamma}$ allows surface viscous forces (based on the Boussinesq-Scriven constitutive law).

The difference between the droplet mean velocity \mathbf{U}_{Ω_1} and the unperturbed Poiseuille flow on the x -axis $\mathbf{u}^P(0)$ is called the *migration velocity*:

$$\mathbf{U}_{mig} := \mathbf{U}_{\Omega_1} - \mathbf{u}^P(0). \quad (6.12)$$

In [77] explicit formulas for \mathbf{U}_{mig} are derived. The analysis relies on a representation of \mathbf{u} and \mathbf{u}^P in the basis of spherical harmonics. In the analysis it is essential that the droplet is *spherical*. The following result is from [77], with the dimensionless dilatational Boussinesq number $Bo^d := \frac{\lambda_{\Gamma}}{\mu_2 r}$ and the viscosity ratio $\xi := \frac{\mu_1}{\mu_2}$:

$$\mathbf{U}_{mig} = -\frac{2Bo^d + 3\xi}{3(2 + 2Bo^d + 3\xi)} \alpha r^2 \vec{\mathbf{e}}_x. \quad (6.13)$$

Note that there is a monotonic dependence of \mathbf{U}_{mig} on Bo^d and *no dependence* on the dimensionless shear Boussinesq number $Bo^s := \frac{\mu_{\Gamma}}{\mu_2 r}$.

6.2.3. The stationary Stokes model as approximation for the general two-phase Navier-Stokes model

In the numerical experiments in section 6.3 we use the Navier-Stokes two-phase flow model given in section 6.2.1. Concerning the effect of viscous interface forces on the migration velocity we have the theoretical relation (6.13). The latter is derived for a stationary *Stokes* model on an *unbounded* domain and with *interface conditions that differ* from the ones used in the Navier-Stokes model. We expect, however, that this relation yields a good prediction of what happens in the Navier-Stokes model if the latter is “sufficiently close” to the model discussed in section 6.2.2. In this section we explain what is meant by “sufficiently close”.

We distinguish three steps, treated in the three subsections below. First we discuss the effect of considering the Stokes problem on a *bounded* domain instead of on \mathbb{R}^3 . After that, on the bounded domain, we discuss the validity of using Stokes as an approximation of the non-stationary Navier-Stokes equations. In the third step, for the Navier-Stokes model we introduce a moving reference frame, which reduces the numerical complexity of the model.

The two-phase model is formulated in dimensional physical quantities. Therefore, below we add the units. We always use a fixed Poiseuille profile (6.9) with

$$U_{center} = 0.0125 \text{ m/s}, \quad \alpha = 5 \text{ 1/ms}. \quad (6.14)$$

From the unbounded to a bounded domain

We consider the stationary Stokes model described above, but restrict to the clean interface case, i.e. with $\boldsymbol{\sigma}_\Gamma = \tau \mathbf{P}$. We scale such that $\mu_2 = 1 \text{ kg/ms}$. Instead of an unbounded domain we consider this model on a bounded rectangular box $\Omega = [0, L_x] \times [-\frac{1}{2}L_y, \frac{1}{2}L_y] \times [-\frac{1}{2}L_z, \frac{1}{2}L_z]$. We take the y -boundary such that the Poiseuille profile has zero values on these boundaries, as indicated in Fig. 6.1. Comparing (6.6) with (6.9) leads to $L_y = 0.1 \text{ m}$. In the stationary Stokes model we replace \mathbf{u} by $\mathbf{u} - \mathbf{U}_{\Omega_1}$, resulting in a homogeneous interface condition (6.10b). On the *bounded* domain Ω we consider the homogeneous Stokes equations as in (6.7). The interface conditions are as in (6.10) with $\mathbf{U}_{\Omega_1} = 0$ and $\boldsymbol{\sigma}_\Gamma = \tau \mathbf{P}$. The boundary conditions are given by

$$\mathbf{u}(x, \pm \frac{1}{2}L_y, z) = -\mathbf{U}_{\Omega_1}, \quad (6.15a)$$

$$\mathbf{u}(0, y, z) = \mathbf{u}^P(y) - \mathbf{U}_{\Omega_1}, \quad (6.15b)$$

$$\boldsymbol{\sigma} \mathbf{n} = 0 \text{ at } x = L_x, \quad (6.15c)$$

$$\mathbf{u}(x, y, \pm \frac{1}{2}L_z) \cdot \mathbf{n} = 0. \quad (6.15d)$$

This model is implemented in the flow solver ngsflow [58].

Remark 6.2.1. *We briefly comment on a few aspects related to the implementation of the stationary Stokes model described above. The tetrahedral grids used are aligned to the interface Γ . The interface can be treated as an internal boundary. For the discretization $H(\text{div})$ conforming finite elements are used. The polynomial degree of the elements is varied in the experiments to check the accuracy of the discretization. The shape constraint $\mathbf{u} \cdot \mathbf{n} = 0$ on the interface is easy to implement as a Dirichlet condition on the internal boundary Γ . The tangential interfacial stress condition $[\mathbf{P}\boldsymbol{\sigma}\mathbf{n}]_{\Gamma} = 0$ is treated as a natural “internal boundary” condition. As indicated above, the model is not well-posed due to the fact that the boundary conditions in (6.15a), (6.15b) depend on the unknown average velocity vector \mathbf{U}_{Ω_1} . From symmetry arguments it is clear that \mathbf{U}_{Ω_1} has the direction $\vec{\mathbf{e}}_x$, i.e. $\mathbf{U}_{\Omega_1} = \beta\vec{\mathbf{e}}_x$ with an unknown scalar β . This scalar is determined by using the condition (6.11), but only in the x -direction, i.e. the scalar equation*

$$g(\beta) := \vec{\mathbf{e}}_x \cdot \int_{\Gamma} [\boldsymbol{\sigma}\mathbf{n}]_{\Gamma} ds = 0. \quad (6.16)$$

For a given value the function $g(\beta)$ can be (numerically) evaluated as follows. The given β determines an average velocity $\mathbf{U}_{\Omega_1} = \beta\vec{\mathbf{e}}_x$. Using this the stationary Stokes model on the bounded domain Ω described above can be solved (sufficiently accurate). The resulting velocity field and pressure can be inserted in the stress tensor $\boldsymbol{\sigma}$ and thus the value of $g(\beta)$ can be determined. Using a simple root finding algorithm the zero of g , denoted by β^ , can be determined approximately. This results in the final migration velocity value $\mathbf{U}_{\Omega_1} = \beta^*\vec{\mathbf{e}}_x$.*

Using this implementation we performed experiments for the case $\mu_1 = 2$, $\mu_2 = 1$ kg/ms . Based on these experiments we choose $L_x = L_z = 0.3$ m and a droplet radius $r = 0.0125$ m . For these values the numerically computed migration velocity differs (at most) approximately 1% from the theoretically predicted one in (6.13) (which corresponds to the unbounded domain case). In the remainder we keep these parameter values fixed, i.e., $L_y = 0.1$ m , $L_x = L_z = 0.3$ m and $r = 0.0125$ m and U_{center} , α as in (6.14).

The theoretical migration velocity depends on the viscosity ratio ξ . We performed numerical simulations for the stationary Stokes model on the bounded domain Ω . The results of the experiments and the theoretically predicted correlation are shown in Figure 6.2.

We conclude that on this bounded domain and with boundary conditions as described in (6.15) we obtain a good agreement between theoretical predictions and numerical results.

The stationary Stokes model as approximation for the Navier-Stokes model

In this section we relate the Navier-Stokes model described in section 6.2.1, cf. Fig. 6.1, to the stationary Stokes model on the bounded domain Ω with boundary conditions as in (6.15). From $U_{center} = 0.0125$ m/s and $r = 0.0125$ m we obtain a time scale: per second the droplet moves approximately over a distance comparable to its radius in flow direction. In the experiments we use a time interval $[0, T]$ with $T = 6$ s .

In the Navier-Stokes model we have to specify ρ_i , μ_i and the surface tension coefficient τ . We restrict to systems in which the jumps in density and viscosity are “small”, e.g., both

6. Simulation of flows with a viscous interface

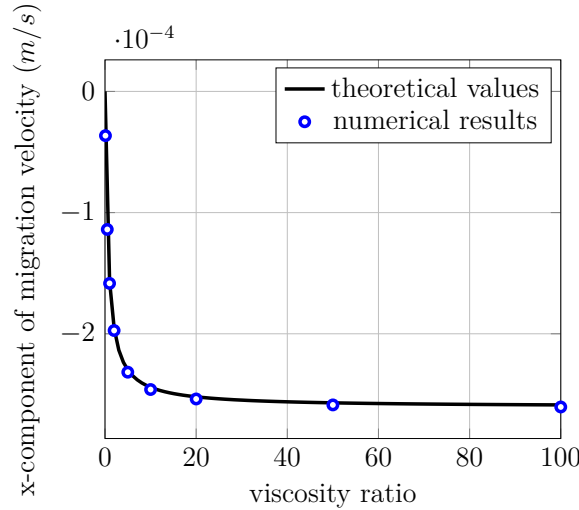


Figure 6.2.: Comparison of theoretical migration velocity and numerical results for various viscosity ratios ξ . Shown is the migration velocity component in the flow direction \vec{e}_x .

phases are liquids. For simplicity we set $\rho_1 = \rho_2$ (unit: kg/m^3) and as an example we take $\mu_1 = 2\mu_2$, i.e., $\xi = 2$. To characterize the fluid behavior the following dimensionless numbers are relevant:

$$Re = \frac{\rho_2 LU}{\mu_2}, \quad We = \frac{\rho_2 LU^2}{\tau}, \quad Ca = \frac{\mu_2 \hat{U}}{\tau}. \quad (6.17)$$

From the units introduced above, it follows that the surface tension coefficient τ has unit kg/s^2 . The Reynolds number relates the size of inertia to that of viscous stresses. The parameters L and U are typical length and velocity scales. In the setting here we can take $L = 0.1 m$, $U = U_{center} = 0.0125 m/s$. For the stationary Stokes model to be a reasonable approximation of the Navier-Stokes model it is necessary that $Re \ll 1$ holds. Hence we obtain the condition $\frac{\rho_2}{\mu_2} \ll 0.8 \cdot 10^3$. The Weber number relates the size of inertia to that of surface tension. For the Stokes model to be a reasonable approximation of the Navier-Stokes model it is necessary that $We \ll 1$ holds. This results in the condition $\frac{\rho_2}{\tau} \ll 0.64 \cdot 10^5$. The capillary number relates the size of the viscous stresses to that of the capillary stresses. For the Stokes model to be a reasonable approximation of the Navier-Stokes model, in the latter *the initial spherical droplet should keep its spherical shape*. This leads to the condition $Ca \ll 1$. For comparing the viscous and capillary stresses one can take a frame of reference with origin moving with speed U_{center} in direction \vec{e}_x . Hence, the size of the migration velocity is a better measure for the typical velocity size \hat{U} (close to the interface) than the inflow velocity size U_{center} . The migration velocity is of the order of magnitude $\alpha r^2 = 5 \cdot 0.0125^2$, cf. (6.13). Hence, $Ca \ll 1$ leads to the condition $\frac{\mu_2}{\tau} \ll 1.3 \cdot 10^3$. We summarize the conditions obtained:

$$\frac{\rho_2}{\mu_2} \ll 0.8 \cdot 10^3, \quad \frac{\rho_2}{\tau} \ll 0.64 \cdot 10^5, \quad \frac{\mu_2}{\tau} \ll 1.3 \cdot 10^3. \quad (6.18)$$

In this parameter range we expect that the flow behavior, modeled by the incompressible two-phase Navier-Stokes equations, is such that the Stokes model yields a reasonable

approximation. In particular the migration velocity behavior in the Navier-Stokes model should be similar to that for the Stokes flow (6.13) (in an unbounded domain). This will be investigated in section 6.3.

Navier-Stokes model in a moving reference frame

Consider the two-phase Navier-Stokes model on a rectangular domain and with a Poiseuille inflow condition as described in section 6.2.1. We use a simple transformation (shift of the frame of reference) such that the resulting transformed quantities are easier to determine numerically. The corresponding transformed Navier-Stokes model is used in the numerical experiments in section 6.3. We change the notation: The velocity occurring in the Navier-Stokes model presented in section 6.2.1 is denoted by \mathbf{u}^* and a transformed velocity $\mathbf{u} := \mathbf{u}^* - U_{center} \vec{\mathbf{e}}_x$ is introduced. We consider the Navier-Stokes model for this transformed velocity. Clearly in the momentum equation the nonlinear convection term changes from $(\mathbf{u}^* \cdot \nabla) \mathbf{u}^*$ to $(\mathbf{u} + U_{center} \vec{\mathbf{e}}_x) \cdot \nabla \mathbf{u}$. In the model for \mathbf{u} the conditions at the interface are the same as in the model for \mathbf{u}^* . The boundary conditions for \mathbf{u} are given by

$$\mathbf{u}(x, \pm \frac{1}{2} L_y, z) = -U_{center} \vec{\mathbf{e}}_x \quad (\text{Dirichlet BC on } y\text{-boundary}) \quad (6.19a)$$

$$\mathbf{u}(0, y, z) = -\left(\frac{2y}{L_y}\right)^2 \vec{\mathbf{e}}_x \quad (\text{shifted Poiseuille on inflow}) \quad (6.19b)$$

$$\boldsymbol{\sigma} \mathbf{n} = 0 \text{ at } x = L_x \quad (\text{zero stress at outflow}) \quad (6.19c)$$

$$\mathbf{u}(x, y, \frac{1}{2} L_z) = \mathbf{u}(x, y, -\frac{1}{2} L_z) \quad (\text{periodic BC on } z\text{-boundary}) \quad (6.19d)$$

The initial conditions are taken the same as described at the end of section 6.2.1 (solution of stationary Stokes problem). Note that

$$\mathbf{U}_{mig}(t) := \frac{1}{|\Omega_1(t)|} \int_{\Omega_1(t)} \mathbf{u}(\mathbf{x}, t) d\mathbf{x} \quad (6.20)$$

quantifies the droplet migration velocity in the Navier-Stokes model. For numerical simulations the transformed model is easier to handle than the original one, due to the fact that close to the droplet the size of \mathbf{u} is much smaller than the size of \mathbf{u}^* . This allows, for example, the use of larger time steps in numerical simulations with the model for \mathbf{u} .

6.3. Benchmark problem and numerical experiments

In this section we present results of our numerical solver applied to the two-phase Navier-Stokes model described in section 6.2.3. Based on the analysis in section 6.2.3 we consider a specific benchmark problem that is “close to” the Stokes model studied in [77]. Hence, it makes sense to determine the droplet migration velocities numerically and compare the dependence of this scalar quantity on other parameters (ξ, Bo^s, Bo^d) to the dependencies

6. Simulation of flows with a viscous interface

derived in [77], e.g. (6.13). We define a scalar numerical migration velocity as follows, cf. (6.12) and (6.20). The x -component of the droplet mean velocity

$$U_{mig}^{num}(t) := \frac{1}{|\Omega_1(t)|} \int_{\Omega_1(t)} \mathbf{u}(\mathbf{x}, t) \cdot \vec{\mathbf{e}}_x \, d\mathbf{x}$$

is determined. A time averaged mean value of $U_{mig}^{num}(t)$, which we call the *numerical migration velocity*, is denoted by U_{mig}^{num} and can be compared to the scalar quantity $U_{mig}^{Stokes} := \mathbf{U}_{mig} \cdot \vec{\mathbf{e}}_x$ from (6.12).

The results that we obtain might be useful for validation of other codes that can handle Boussinesq-Scriven interface forces and therefore we summarize all parameters used. For the Poiseuille inflow profile we take (6.6) with $U_{center} = 0.0125 \, m/s$ and $L_y = 0.1 \, m$. The computational domain is given by $\Omega = [0, 0.3] \times [-0.05, 0.05] \times [-0.15, 0.15] \, m^3$. The boundary conditions on $\partial\Omega$ are given in (6.19). $\Omega_1(0)$ is a sphere with radius $0.0125 \, m$ with center located at the centerline of Ω . The initial velocity $\mathbf{u}(0)$ is described at the end of section 6.2.1. The time interval is $[0, 6] \, s$. In the experiments below we specify the choice of μ_i , ρ_i and τ , λ_Γ , μ_Γ . Based on the discussion in section 6.2.2, we should satisfy the conditions in (6.18). Clearly, a “very large” value for τ is advantageous from a theoretical point of view, in the sense that for a very large surface tension coefficient the moving droplet will remain (almost) spherical. On the other hand, very large τ values are numerically more difficult to handle since larger surface tension forces cause larger spurious velocities close to the interface. Hence, we have the dilemma that *a larger τ value reduces the modeling error but increases the numerical error*.

In our solver we use the numerical methods as presented in Chapter 3. The surface force functional is implemented as described in Chapter 4. In the numerical experiments we perform local refinement close to the interface. Illustrations of typical grids used and of a numerically computed inner circulation pattern are given in Figure 6.3.

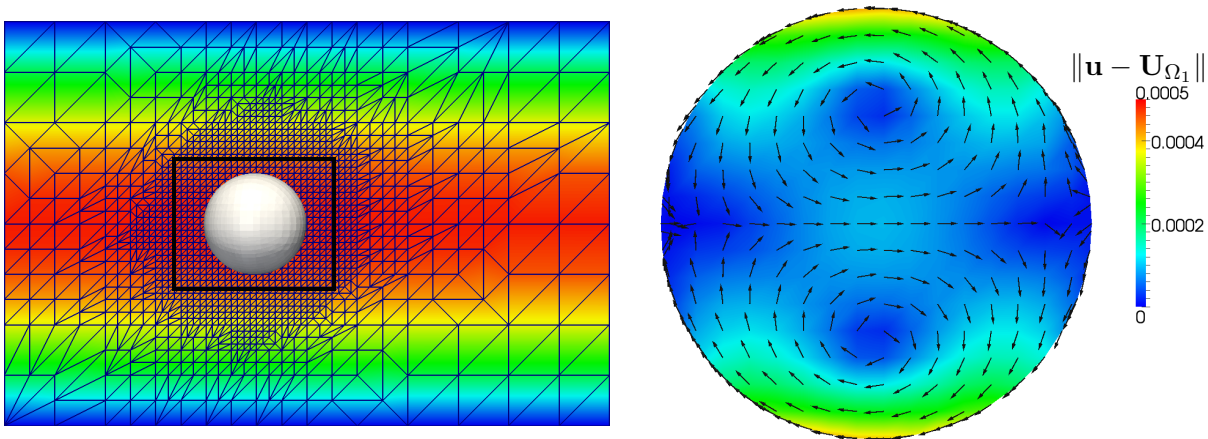


Figure 6.3.: Mesh with level 3 refinement (left) and numerically computed velocities field from a Navier-Stokes simulation at a cut plane. Shown is the computed velocity field minus droplet translation velocity.

In the experiments below we use the following local grid refinement. Within a distance of $0.0125 \, m$ from the interface the grid is locally refined. For the level ℓ refinement the ratio

between droplet diameter and tetrahedron diameter (for the tetrahedra in the refined region) is approximately $2^{\ell+1}$. We use $\ell = 2, 3, 4, 5$. After each timestep, the grid is adaptively refined and coarsened according to the position of the interface. Due to the fully implicit time discretization and the low droplet velocity we can use large time steps in our simulation. On level ℓ the time step is chosen as $\Delta t = 2^{-\ell+2}$. In each timestep, the interface stays in the refined region.

As an illustration we show a result for a clean interface case (no viscous forces) with $\mu_1 = \mu_2 = \rho_1 = \rho_2 = 1$ and $\tau = 0.01, 0.1$ in Figure 6.4. In this figure only a small part of the computational domain is shown, namely that corresponding to the box drawn in Figure 6.3. In this experiment the droplet remains almost spherical for $\tau = 0.1$ and has a visible deformation for $\tau = 0.01$.

We now turn to experiments in which Boussinesq-Scriven surface tension forces are taken into account. In all the experiments we determine the numerical migration velocities U_{mig}^{num} defined above.

Grid convergence. We take parameter values $\rho_1 = \rho_2 = 1$, $\mu_2 = 1$, $\xi = 2$, $\tau = 0.1$, $Bo^d = 10$, $Bo^s = 0$. In this case the dimensionless numbers have the values: $Re = 1.25 \times 10^{-3}$, $We = 1.5625 \times 10^{-4}$ and $Ca = 7.81425 \times 10^{-3}$. We study the dependence of U_{mig}^{num} on grid refinement. Results for $U_{mig}^{num}(t)$ are shown in Fig. 6.5. From these the value for U_{mig}^{num} is calculated by averaging over the time interval $[2, 6]$ s. The results are given in Table 6.1. The results in the second column of this table show a systematic linear convergence behavior with reduction factor 0.5. Based on this the error estimate in the third (absolute error) and fourth column (relative error) are derived.

Refinement	U_{mig}^{num}	absolute error	rel. error
2	-2.623	-	
3	-2.533	0.090	3.6 %
4	-2.487	0.046	1.8 %
5	-2.464	0.023	0.9 %

Table 6.1.: Numerical migration velocity U_{mig}^{num} on different grid refinements. The unit is $10^{-4}m/s$.

In all the following experiments we use the level 4 refinement.

Experiment 1: Dependence on Bo^d . We take parameter values $\rho_1 = \rho_2 = 1$, $\mu_2 = 1$, $\xi = 2$, $\tau = 0.1$, $Bo^s = 0$. These values satisfy the conditions in (6.18). For different Bo^d values we determined the time-dependent migration velocity $U_{mig}^{num}(t)$. Results are shown in Fig. 6.6.

If we take the time average over the time interval $[2, 6]$ s, we obtain the numerical migration velocity U_{mig}^{num} . These are indicated by Δ in Fig. 6.7. In the same figure we show the relation (6.12) for the theoretical Stokes migration velocity U_{mig}^{Stokes} with $\xi = 2$. Note that the numerical migration velocity for the Navier-Stokes model shows a similar dependence on Bo^d as the theoretical Stokes migration velocity. The difference between these two quantities is due to modeling errors (non-stationary Navier-Stokes on bounded domain instead of stationary Stokes on unbounded domain) and numerical errors. For $Bo^d = 10$,

6. Simulation of flows with a viscous interface

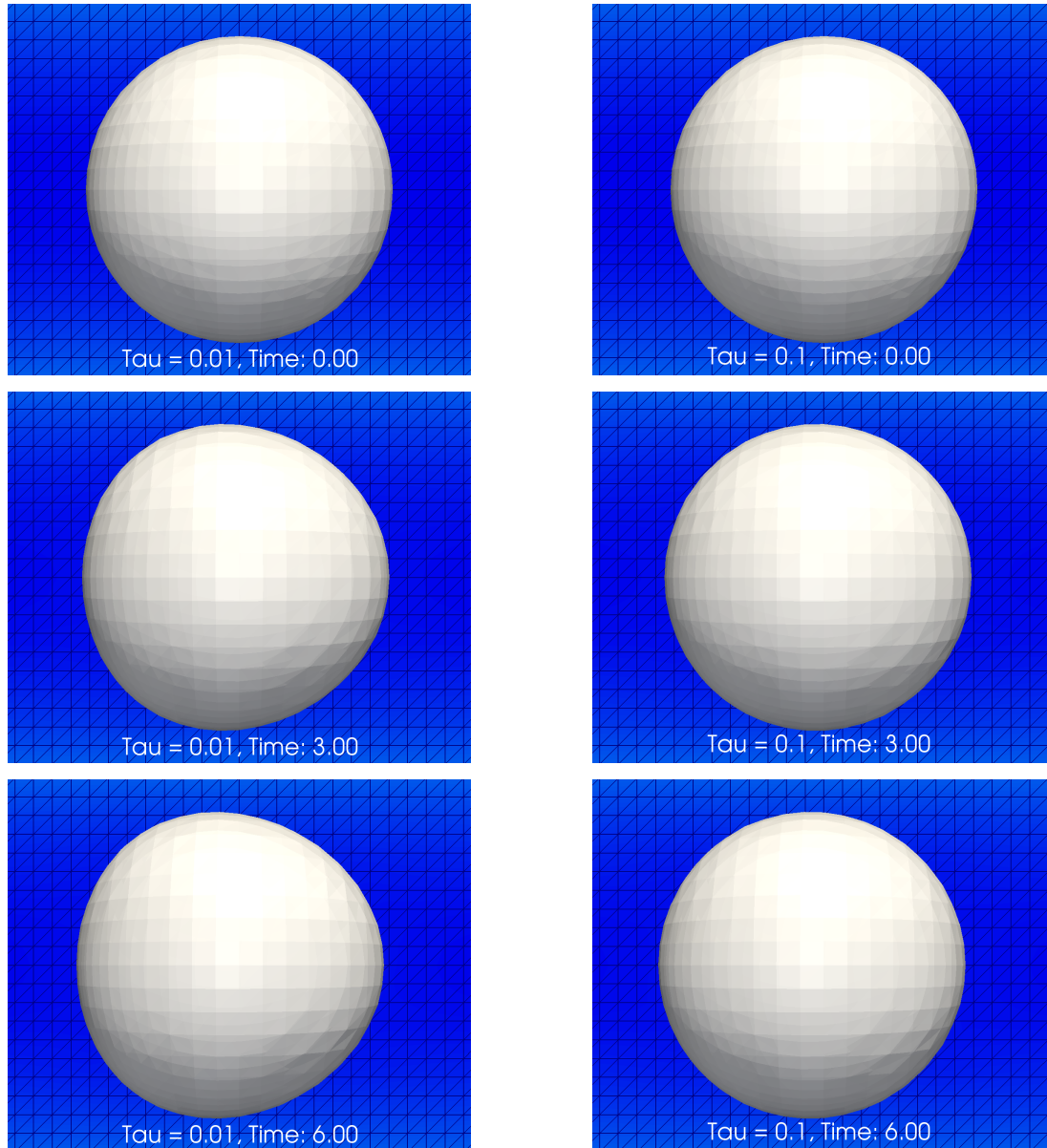


Figure 6.4.: Droplet shapes for $t = 0, 3, 6$ s (from top to bottom). Shown is the interface and the velocity field on a cut plane $z = 0$ m for surface tension coefficient $\tau = 0.01$ (left) and $\tau = 0.1$ (right). Only the solution in the small box drawn in Figure 6.3 is shown.

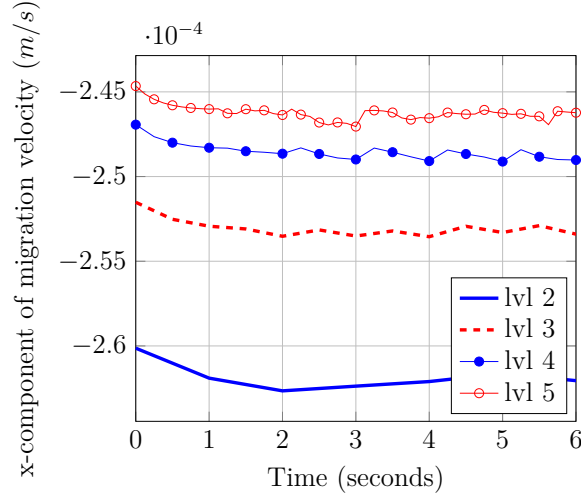


Figure 6.5.: Time-dependent numerical migration velocity $U_{mig}^{num}(t)$ for several refinement levels.

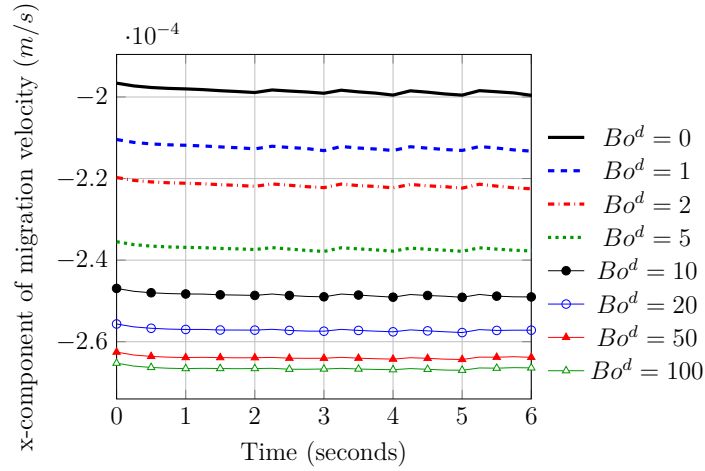


Figure 6.6.: Time-dependent numerical migration velocity $U_{mig}^{num}(t)$ for $Bo^d = 0, 1, 2, 5, 10, 20, 50, 100$ on level 4 refinement.

the theoretical U_{mig}^{Stokes} is $-2.418 \cdot 10^{-4} m/s$. In view of the results in Table 6.1 (about 1.8% numerical error on refinement level 4 and about 2.8% difference between U_{mig}^{Stokes} and U_{mig}^{num}) we expect that the differences between the results of the numerical simulation (\circ in Fig. 6.7) and the theoretical model are not dominated by numerical errors.

Experiment 2: Dependence on ξ . We take $\xi = \frac{1}{3}$. For this case the theoretical relation for the Stokes migration velocity differs significantly from the case $\xi = 2$ (considered in the previous experiment), in particular for small Bo^d values. The two curves for $\xi = 2$ and $\xi = \frac{1}{3}$ are shown in Fig. 6.7. For the Navier-Stokes model the other parameters are taken the same as in the previous experiment, i.e., $\rho_1 = \rho_2 = 1$, $\mu_2 = 1$, $\tau = 0.1$, $Bo^s = 0$. For different Bo^d values we determined, on refinement level 4, the numerical migration velocity U_{mig}^{num} . The results are indicated by \circ in Fig. 6.7. Again the dependence of this numerical migration velocity U_{mig}^{num} on Bo^d is very similar to that of the theoretical Stokes migration velocity.

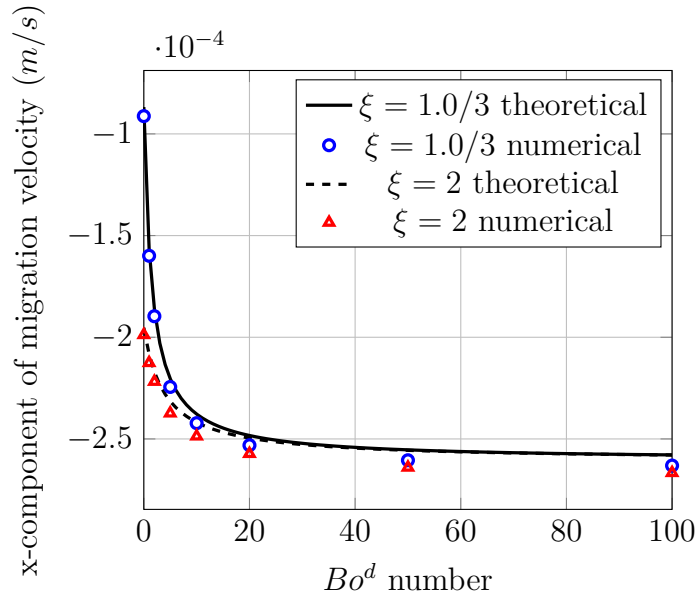


Figure 6.7.: Numerical migration velocity U_{mig}^{num} for $Bo^d = 0, 1, 2, 5, 10, 20, 50, 100$ on level 4 refinement. The cases $\xi = 2$ and $\xi = \frac{1}{3}$ are shown.

Experiment 3: Dependence on ρ_i . The densities ρ_1 and ρ_2 do not influence the theoretical Stokes migration velocity. As long as the conditions in (6.18) are satisfied, we expect the migration velocity obtained from the Navier-Stokes model to be close to that of the Stokes model. Therefore, if we keep all parameters fixed but only increase the ρ_i values, we expect that if the conditions in (6.18) are still satisfied then the numerical migration velocity should be essentially independent of the ρ_i values. In this experiment we verify this claim. We take $\rho_1 = \rho_2 = 100$ and all other parameters the same as in Experiment 1, i.e., $\mu_2 = 1$, $\xi = 2$, $\tau = 0.1$, $Bo^s = 0$. Results for the numerical migration velocity, computed on the level 4 refinement, are given in the fourth column in Table 6.2. Indeed, the results are (almost) the same as the one from Experiment 1 (with $\rho_1 = \rho_2 = 1$). This is also a further indication that the computed numerical migration velocities are accurate, since the results in the third and fourth column are obtained from the numerical simulation of different problems.

Bo^d	Stokes model	Exp. 1	Exp. 3	Exp. 4
0	-1.953	-1.988	-1.989	-
1	-2.083	-2.126	-2.126	-2.126
5	-2.315	-2.374	-2.374	-2.374
10	-2.418	-2.487	-2.487	-2.488
50	-2.556	-2.640	-2.640	-2.644
100	-2.579	-2.667	-2.667	-2.671

Table 6.2.: Numerical migration velocity U_{mig}^{num} in different experiments (unit $10^{-4} m/s$). Simulations are done on level 4 refinement.

Experiment 4: Dependence on Bo^s . The theoretical Stokes migration velocity U_{mig}^{Stokes}

does *not* depend on the shear Boussinesq number, cf. (6.12). Hence, as long as the conditions in (6.18) are satisfied, we expect this to hold for the numerical migration velocity, too. In this experiment we verify this claim. We take the same parameter values as in Experiment 1, but now with varying Bo^s instead of $Bo^s = 0$. We take $Bo^s = Bo^d$, or, equivalently, $\lambda_\Gamma = \mu_\Gamma$. In Experiment 1 we used $Bo^s = 0$ and $Bo^d \neq 0$. In that case, in the surface force functional (6.5) the shear interface viscosity term equals zero and only the dilatational term causes viscous interface effects. If we now take $Bo^s = Bo^d$, then the opposite happens: the dilatational interface viscosity term equals zero and only the shear term causes viscous interface effects. Hence, in Experiment 1 ($Bo^s = 0$) and in this experiment ($Bo^s = Bo^d$) different terms, are used in the simulation of the Navier-Stokes model. Nevertheless we expect similar numerical migration velocities. The results for the case $Bo^s = Bo^d$ are presented in the last column in Table 6.2. Indeed these values are (almost) the same as the one from Experiment 1.

Finally, we present some information on the dimension of the discrete problem and the computing time. On the level 3 refinement we have approximately 116×10^3 velocity unknowns, 5.6×10^3 pressure unknowns and 40×10^3 level set unknowns, hence a total of approximately 162×10^3 unknowns. For the level 4 refinement these numbers are 618×10^3 (velocity), 28×10^3 (pressure), 208×10^3 (level set) and 854×10^3 (total). The time steps are $\Delta t = 0.25$ (level 3) and $\Delta t = 0.125$ (level 4). The total computing times on a workstation with one processor having 4 cores, using an OpenMP parallelization, are approximately 75 minutes (level 3) and 870 minutes (level 4).

7. Simulation of flows with surfactants

7.1. Introduction

Surfactant is an abbreviation for the term “surface active agent”. Surfactants are special molecules which tend to adsorb at fluid interfaces. They have a profound effect on the dynamical properties of droplets in the way that they lower the surface tension [48]. Hence they are often used as emulsifiers and foaming agents [90]. Surfactants also exist in the form of contaminants. Even if the concentration of contaminants is relatively low in the bulk phases, due to the surface active property, there might still be a considerable amount of contaminants on the fluid interfaces. The existence of surfactants also changes the rheological properties of the interfaces, e.g. increasing surface viscosity and changing surface elasticity. There exists a large number of publications on this topic, we refer to a recent review paper [48]. Due to environmental concerns, surfactant-free systems have drawn increasing interests, e.g. particles instead of surfactants [13].

Stone and Leal [82] first performed theoretical studies on finite deformation and breakup of droplets with the existence of interfacial surface tension gradients generated by non-uniformly distributed surfactants. A review paper [81] provides an overview of the topic. Other authors extend the analysis to include soluble surfactant [55], nonlinear surface tension models [27], etc. Numerical simulations have been used to study the dynamics of droplet with surfactants when it is hard to perform theoretical analysis. Different numerical methods have been applied, e.g. the boundary integral method [82, 67, 10], the VOF method [42], the front tracking/finite difference scheme [57] and the diffuse-interface method [85].

In this chapter, we apply the numerical methods introduced previously to simulate the dynamics of droplets with surfactant. We do not treat modeling issues but concentrate on certain aspects of numerical simulations of coupled fluid dynamics and surfactant transport systems. As mentioned in previous chapters, the complexity of a two-phase problem is generally high due to the unknown interface, the (local) surface tension force, the discontinuity in pressure and the nonlinear couplings. To properly account for the effect of surfactants, we also need to treat the coupling problem between fluid dynamics and the surfactant transport equation, which further increases the overall complexity of the problem.

We only consider *insoluble* surfactants, which exist on fluid interfaces and stay there. We do not consider ad/desorption of surfactants from bulk phases to fluid interfaces, or reactions of surfactants on the interfaces. We use the transport equation (2.42) to describe the conservation of surfactants on the interface, and the constitutive relation (2.38) to describe the effect of surfactants on the surface tension. We introduce a benchmark

problem which is inspired by the paper [82]. In that paper theoretical predictions for the shape of the droplet and the distribution of the surfactant on the droplet in an extensional flow are derived. The benchmark problem we propose is a sharp interface Navier-Stokes problem coupled with surfactant which is close to the stationary Stokes model studied in [82]. We present results of numerical experiments of our solver applied to this benchmark problem. Another test problem is considered in section 7.4, namely the breakup of droplets with surfactants. It is a much more complex problem due to the topological changes of the droplets.

7.2. Mathematical models

7.2.1. A sharp interface model for a droplet with insoluble surfactants

We consider a droplet inside a continuous phase. The two fluids are immiscible and incompressible. Let $\Omega \subset \mathbb{R}^3$ be a domain containing the two different phases. The time-dependent sub-domains containing the two phases are denoted by $\Omega_1(t)$ and $\Omega_2(t)$ with $\bar{\Omega} = \bar{\Omega}_1 \cup \bar{\Omega}_2$ and $\Omega_1 \cap \Omega_2 = \emptyset$. We assume that Ω_1 and Ω_2 are connected and $\partial\Omega_1 \cap \partial\Omega = \emptyset$ (i. e., Ω_1 is completely contained in Ω). We use Ω_1 to denote the droplet phase, and Ω_2 to denote the continuous phase. The (sharp) interface is denoted by $\Gamma(t) = \bar{\Omega}_1(t) \cap \bar{\Omega}_2(t)$, cf. section 2.3. The unknown pressure is denoted by $p = p(x, t)$, and the velocity as $\mathbf{u} = \mathbf{u}(x, t)$.

Surface tension force acts at the fluid-fluid interface, as the result of different intermolecular forces in both phases. For a fluid interface with only surface tension effects, the interfacial momentum balance condition is given by (2.28)

$$[\boldsymbol{\sigma}\mathbf{n}]_{\Gamma} = \text{div}_{\Gamma}(\boldsymbol{\tau}\mathbf{P}),$$

where τ is the surface tension coefficient. When τ is constant on the whole interface, this fluid interface is called a clean interface. When temperature variations or surfactants exist, τ is a function of the local temperature field or the concentration of the surfactant. The interface condition becomes $[\boldsymbol{\sigma}\mathbf{n}]_{\Gamma} = \text{div}_{\Gamma}(\boldsymbol{\tau}\mathbf{P}) = -\tau\kappa\mathbf{n}_{\Gamma} + \nabla_{\Gamma}\boldsymbol{\tau}$, with κ the mean curvature and ∇_{Γ} the surface gradient, cf. (A.4).

We use $S(x, t)$ to denote the surfactant concentration for $x \in \Gamma(t)$. τ and S are related by a equation of state. We consider here the simple linear equation of state in the form

$$\tau = \tau(S) = \tau_0 - SRT, \tag{7.1}$$

where τ_0 is the surface tension coefficient for a clean interface, R is the gas constant, and T is the absolute temperature, cf. section 2.6.3. For dilute surfactant concentrations and small perturbations around equilibrium, such linear equation of state is a good approximation and often used in theoretical analysis due to its simplicity [82], [89].

Based on the conservation of mass and momentum, we obtain the following standard

sharp interface two-phase fluid dynamics model, cf. section 2.7

$$\begin{cases} \rho_i \left(\frac{\partial \mathbf{u}}{\partial t} + (\mathbf{u} \cdot \nabla) \mathbf{u} \right) = -\nabla p + \rho_i \mathbf{g} + \operatorname{div}(\mu_i \mathbf{D}(\mathbf{u})) & \text{in } \Omega_i \times [t_0, T] \\ \operatorname{div} \mathbf{u} = 0 & \text{in } \Omega_i \times [t_0, T] \end{cases}, \quad (7.2)$$

$$[\mathbf{u}]_\Gamma = 0, \quad [\boldsymbol{\sigma} \mathbf{n}]_\Gamma = \operatorname{div}_\Gamma(\tau \mathbf{P}), \quad (7.3)$$

$$V_\Gamma = \mathbf{u} \cdot \mathbf{n} \quad \text{on } \Gamma, \quad (7.4)$$

where $i = 1, 2$ and the surface tension coefficient τ is a function on Γ . We use the constants μ_i, ρ_i to denote the viscosity and density of the bulk phases in the sub-domains Ω_i , and \mathbf{g} is an external volume force (gravity). The condition in (7.4), where we use V_Γ to denote the normal velocity of the interface, follows from immiscibility of the two phases, cf. section 2.3.2. The first condition in (7.3) results from the viscosity of the phases. From momentum conservation one obtains the second relation in (7.3), cf. section 2.4. To make this problem (equation (7.1) to (7.4)) well-posed we need suitable boundary conditions for \mathbf{u} , an initial condition $\mathbf{u}(x, t_0)$ and an initial configuration of the interface $\Gamma(t_0)$. Considering the constitutive relation (7.1), we also need a description of the surfactant concentration field $S(t)$ for $t \in [t_0, T]$.

The change of surfactant concentration S on $\Gamma(t)$ is governed by a time-dependent convection-diffusion equation that can be written in the form (2.42)

$$\frac{\partial S}{\partial t} + (\mathbf{u} \cdot \nabla) S + S \operatorname{div}_\Gamma \mathbf{u} = D_\Gamma \Delta_\Gamma S \quad \text{on } \Gamma(t), \quad (7.5)$$

with a constant diffusion constant D_Γ , cf. section 2.5. The initial condition is considered to a uniform distribution $S(t_0) = S^*$. We only consider the case when $\Gamma(t)$ is completely contained in $\Omega(t)$ and has no boundary (no contact line problem). We do not consider the surfactant adsorption and desorption processes between the interface and the bulk fluids, i.e. the total concentration of surfactant is constant on the interface.

The unknown location of the interface $\Gamma(t)$ is coupled to the fluid dynamics via the condition in (7.4). We use a level set method for capturing the interface, cf. section 3.2. A level set function $\phi(x, t)$ is transported by the velocity \mathbf{u} ,

$$\frac{\partial \phi}{\partial t} + \mathbf{u} \cdot \nabla \phi = 0.$$

The coupling between fluid dynamics and the surfactant equation is through the velocity \mathbf{u} and the surface tension $\tau(S)$.

7.2.2. A stationary Stokes model

In this section, we consider an initially spherical droplet with radius r and viscosity μ_1 occupying the domain Ω_1 . The fluid outside with viscosity μ_2 occupies $\Omega_2 = \mathbb{R}^3 \setminus \Omega_1$. The viscosity ratio is defined as $\lambda := \mu_1/\mu_2$. Both fluids are Newtonian and have the same density $\rho_1 = \rho_2$. Far from the droplet, the second fluid undergoes a prescribed axisymmetric extensional flow with a constant shear rate $\dot{\gamma}$. A typical length scale is chosen

7. Simulation of flows with surfactants

as r , and a typical velocity size is $|\dot{\gamma}|r$. The Reynolds number for this simple problem is defined by

$$Re = \frac{\rho_2 |\dot{\gamma}| r^2}{\mu_2}. \quad (7.6)$$

In the models we introduced below, the Reynolds number is assumed to be small, i.e. $Re \ll 1$, such that inertial effects can be neglected. The coordinate system is fixed to the center of mass of the droplet. We illustrate this model problem in Figure 7.1.

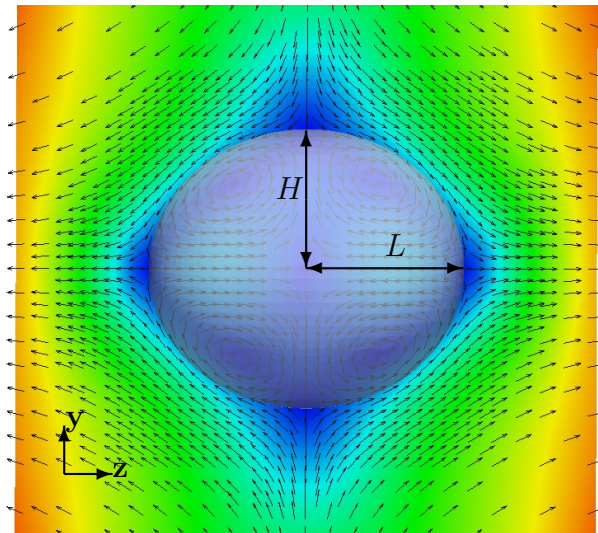


Figure 7.1.: Visualization of numerical results for a droplet in an axi-symmetric extensional flow. Shown is the yz -plane.

Clean interface case

A clean interface case has already been mentioned in section 6.2.3, cf. Figure 6.2. The difference is that in section 6.2.3 a Poiseuille velocity profile is considered, and in this section an axi-symmetric extensional flow is considered.

We introduce the model studied in Barthès-Biesel and Acrivos [7]. We neglect the gravity force and assume that the droplet and the bulk fluid have the same density $\rho_1 = \rho_2$. If we assume the Reynolds number is small, i.e. viscous effects are dominating the fluid dynamics, it is well accepted ([7],[69]) that the change of velocity \mathbf{u} is instantaneously and uniquely determined by the position of $\Gamma(t)$ and the background flow. Hence the quasi-static Stokes equations are used to describe the flow:

$$\begin{cases} \mu_i \Delta \mathbf{u} = \nabla p & \text{in } \Omega_i(t) \\ \operatorname{div} \mathbf{u} = 0 & \text{in } \Omega_i(t) \end{cases} \quad i = 1, 2. \quad (7.7)$$

On the time-dependent interface $\Gamma(t)$, interfacial conditions are assigned. The continuity of velocity and stress balance conditions are the same as in (7.3). The surface tension coefficient τ takes a constant value.

$$[\mathbf{u}]_{\Gamma} = 0, \quad [\boldsymbol{\sigma} \mathbf{n}]_{\Gamma} = \operatorname{div}_{\Gamma}(\tau \mathbf{P}) = -\tau \kappa \mathbf{n}_{\Gamma}. \quad (7.8)$$

The dynamics of the fluid interface is described by an evolution equation:

$$\frac{d\mathbf{x}}{dt} = (\mathbf{u} \cdot \mathbf{n})\mathbf{n} \quad \text{for } \mathbf{x} \in \Gamma(t). \quad (7.9)$$

The initial condition $\Gamma(t_0)$ is a spherical shape with radius r . Far from the droplet, the incident flow is given by

$$\mathbf{u} \rightarrow \dot{\gamma}(\mathbf{E} + \omega)\mathbf{x}, \quad \text{for } \|\mathbf{x}\| \rightarrow \infty, \quad (7.10)$$

with the strain rate tensor \mathbf{E} and the vorticity ω . An axi-symmetric extensional flow is characterized by $\mathbf{E} = \text{diag}(-1/2, -1/2, 1)$ and $\omega = 0$. The capillary number of this problem is defined by

$$Ca = \frac{\mu_2 |\dot{\gamma}| r}{\tau}. \quad (7.11)$$

If the surface tension force is strong enough, the droplet will keep a stationary shape without break-up. If the capillary number is small, this stationary shape can be assumed to be nearly spherical, i.e. with small deformations. Barthès-Biesel and Acrivos [7] analyzed the shape of the droplet by using small deformation theory. They predicted the deformation of the droplet for different types of linear shear flows. We also refer to the review paper [69]. The deformation parameter D is defined by $D := (L - H)/(L + H)$, where L and H represent the longer and shorter semi principal-axes lengths of the deformed droplet, cf. Figure 7.1. For $Ca \ll 1$, the prediction of D is given by [69]:

$$D \approx \frac{3}{2} \frac{19\lambda + 16}{16\lambda + 16} Ca. \quad (7.12)$$

Remark 7.2.1. *The prediction in (7.12) is an $\mathcal{O}(Ca)$ approximation of the result from [7]. The authors in [7] perform small deformation analysis and express the shape function ("radius") of the deformed droplet with different order terms of Ca . The $\mathcal{O}(Ca)$ approximation keeps only the first order term in Ca and neglects higher order terms. The deformed interface Γ^∞ is predicted to be*

$$r^\infty(\mathbf{x}) = r - \frac{3r}{4} Ca F(1 + 3 \cos(2\phi)) + \mathcal{O}(Ca^2), \quad \mathbf{x} \in \Gamma^\infty, \quad (7.13)$$

where $r^\infty(\mathbf{x}) := (\mathbf{x} - \mathbf{x}_c)^T (\mathbf{x} - \mathbf{x}_c)$ with \mathbf{x}_c the center of the droplet, ϕ is the angle between z -axis and y -axis in the yz -plane (i.e. $z = r \cos \phi$, $y = r \sin \phi$) and $F = F(Ca, \lambda)$ is a known function. Barthès-Biesel and Acrivos [7] have also provided $\mathcal{O}(Ca^2)$ prediction of D , which takes the form:

$$D = \left| \frac{Ca \left[-\frac{9}{2}F - \frac{399}{2b_0} Ca F(-b_1 + b_2 F) \right]}{1 - \frac{3Ca}{2}(F + \frac{24}{5} Ca F^2) - \frac{891}{2b_0} Ca^2 F(-b_1 + b_2 F)} \right|, \quad (7.14)$$

where $b_i = b_i(\lambda)$ and F are known functions. Expressions for F and b_i can be found in [7] (we have a different notation for shear rate: $\dot{\gamma} = \frac{1}{2}G$, where G is the shear rate defined in [7]). For larger values of Ca , equation (7.14) provides a good correction to the linear prediction (7.12), which we will show in our numerical experiments.

Interface with an insoluble surfactant

Stone and Leal [82] extended the small deformation analysis in [7] to include a surfactant on the fluid interface. The surfactant is assumed to be insoluble in the bulk phases. We describe the model used in their paper. Reynolds number is assumed to be small, and the quasi-static Stokes equation (7.7) is used to describe the bulk fluid dynamics. On $\Gamma(t)$, the continuity of velocity condition is the same as in (7.8), but the stress balance condition is modified due to a variable τ (2.36):

$$[\mathbf{u}]_{\Gamma} = 0, \quad [\boldsymbol{\sigma}\mathbf{n}]_{\Gamma} = \operatorname{div}_{\Gamma}(\tau\mathbf{P}) = -\tau\kappa\mathbf{n}_{\Gamma} + \nabla_{\Gamma}\tau, \quad (7.15)$$

where $\tau = \tau(S)$ is a function of the surfactant concentration S . The linear equation of state (2.38) is used. Equation (7.9) describes the dynamics of the interface. An axisymmetric extensional flow is prescribed far from the droplet as in equation (7.10) with a strain rate tensor $\mathbf{E} = \operatorname{diag}(-1/2, -1/2, 1)$ and vorticity $\boldsymbol{\omega} = 0$.

The droplet is assumed to be initially spherical with a uniform concentration S^* of surfactant on $\Gamma(t_0)$. The effective surface tension coefficient of the uniformly contaminated droplet is denoted by τ^* . From the equation of state (2.38), we obtain $\tau^* = \tau_0 - S^*RT$. We introduce a dimensionless constant ξ in the form $\xi := \frac{\tau^*}{\tau_0} = 1 - \frac{S^*RT}{\tau_0}$. The constant ξ satisfies $0 \leq \xi \leq 1$. The effective capillary number is defined by

$$Ca^* := \frac{\mu_2|\dot{\gamma}|r}{\tau^*}. \quad (7.16)$$

On Γ , the concentration S of surfactant is governed by the time-dependent convection-diffusion equation (7.5):

$$\frac{\partial S}{\partial t} + \mathbf{u} \cdot \nabla S + S \operatorname{div}_{\Gamma} \mathbf{u} = D_{\Gamma} \Delta_{\Gamma} S \quad \text{on } \Gamma(t).$$

The initial condition is $S(0) = S^*$. The dimensionless surface Péclet number measures the relative effect of convection to diffusion on Γ and is defined by

$$Pe := \frac{|\dot{\gamma}|r^2}{D_{\Gamma}}. \quad (7.17)$$

We introduce a dimensionless number α to denote the ratio between Pe and Ca^* :

$$\alpha := \frac{Pe}{Ca^*} = \frac{\tau^* r}{\mu_2 D_{\Gamma}}. \quad (7.18)$$

In [82], the authors assumed that the droplet radius and the surfactant concentration to be slightly perturbed from their equilibrium values, they did a small deformation analysis of the problem (7.7), (7.15), (7.9), (7.10) coupled with (7.5). They derived predictions of the steady state deformed droplet Γ^{∞} :

$$r^{\infty}(\mathbf{x}) \approx r + rCa^*b_r \frac{(\mathbf{x} - \mathbf{x}_c)^T \mathbf{E}(\mathbf{x} - \mathbf{x}_c)}{(\mathbf{x} - \mathbf{x}_c)^T (\mathbf{x} - \mathbf{x}_c)}, \quad \mathbf{x} \in \Gamma^{\infty}, \quad (7.19)$$

where $r^{\infty}(\mathbf{x}) := (\mathbf{x} - \mathbf{x}_c)^T (\mathbf{x} - \mathbf{x}_c)$ with \mathbf{x}_c the center of the droplet. The deformation parameter D is predicted to be

$$D \approx \frac{3Ca^*b_r}{4 + Ca^*b_r}, \quad (7.20)$$

In the predictions (7.19) and (7.20), b_r is a constant, which depends on the parameters $\lambda := \mu_1/\mu_2$, α and ξ :

$$b_r = \frac{5}{4} \frac{(16 + 19\lambda) + 4\alpha(1 - \xi)/\xi}{10(1 + \lambda) + 2\alpha(1 - \xi)/\xi}. \quad (7.21)$$

Remark 7.2.2. Consider the case $\xi = 1$, which corresponds to the clean interface case, i.e. $S^* = 0$, $\tau^* = \tau_0$ and $Ca^* = Ca$. From (7.21), we obtain

$$b_r = \frac{5}{4} \frac{(16 + 19\lambda)}{10(1 + \lambda)}.$$

and from (7.20), we obtain

$$D = \frac{3Ca^*b_r}{4 + Ca^*b_r} = \frac{3(19\lambda + 16)Ca}{2(16\lambda + 16) + (19\lambda + 16)Ca} \stackrel{Ca \ll 1}{\approx} \frac{3(19\lambda + 16)Ca}{2(16\lambda + 16)},$$

which is the prediction of D for a clean interface in (7.12). Hence the prediction (7.20) is consistent with the prediction (7.12) for a clean interface.

The authors have also predicted the concentration $S^\infty(\mathbf{x})$ on Γ^∞ :

$$S^\infty(\mathbf{x}) \approx S^* + \alpha S^* Ca^* b_S \frac{(\mathbf{x} - \mathbf{x}_c)^T \mathbf{E}(\mathbf{x} - \mathbf{x}_c)}{(\mathbf{x} - \mathbf{x}_c)^T (\mathbf{x} - \mathbf{x}_c)}, \quad \mathbf{x} \in \Gamma^\infty, \quad (7.22)$$

where the parameter b_S is given by

$$b_S = \frac{5}{10(1 + \lambda) + 2\alpha(1 - \xi)/\xi}. \quad (7.23)$$

7.2.3. A quasi-static Stokes approximation

In the numerical experiments in section 7.3 we solve the sharp interface Navier-Stokes two-phase flow model coupled with the surfactant convection-diffusion equation, cf. section 7.2.1. Concerning the effect of surfactant on the deformation of the droplet we have the theoretical predictions (7.20) and (7.22). These relations are derived for a quasi-static *Stokes* model coupled with equation (7.5) on an *unbounded* domain and with *interface conditions that differ* from the ones used in the Navier-Stokes model. There are three aspects where these two models differ from each other: a) the boundedness of the domain, b) the approximation of the Navier-Stokes equation by the Stokes equation, and c) the small deformation assumption. We show in this section that under certain conditions the theoretical relations yield good predictions of numerical results from the Navier-Stokes model if the model discussed in section 7.2.2 is a good approximation of the Navier-Stokes model in section 7.2.1.

The same surfactant convection-diffusion equation (7.5) is used in both models, thus the focus is on the fluid dynamics. We distinguish two steps, treated in the two subsections below. First we discuss the validity of using the quasi-static *Stokes* model coupled with an evolution equation of the interface as an approximation of the time-dependent *Navier-Stokes* two-phase flow model on an *unbounded* domain. After that, we discuss the effect of considering the Navier-Stokes problem on a *bounded* domain instead of on \mathbb{R}^3 .

The quasi-static Stokes model as approximation for the Navier-Stokes model

In this section we relate the Navier-Stokes model described in section 7.2.1 to the quasi-static Stokes model on an *unbounded domain* with interface conditions as in (7.9). On an *unbounded domain*, both models are used to describe the dynamics of the droplet with insoluble surfactant on the interface under the incident far-field flow condition (7.10). We start the discussion with the comparison of interface conditions between the two models. The interfacial conditions (7.3) and (7.15) are the same. The only difference is the kinematic conditions, which are (7.4) for the Navier-Stokes model and (7.9) for the quasi-static Stokes model. We can decompose the velocity of a (virtual) particle at position \mathbf{x} on $\Gamma(t)$ by

$$\frac{d\mathbf{x}}{dt} = V_\Gamma(\mathbf{x})\mathbf{n}(\mathbf{x}) + \mathbf{P}\left(\frac{d\mathbf{x}}{dt}\right), \quad \mathbf{x} \in \Gamma(t), \quad (7.24)$$

where $V_\Gamma(\mathbf{x})\mathbf{n}(\mathbf{x})$ is the normal velocity of the particle, and we use $\mathbf{P}\left(\frac{d\mathbf{x}}{dt}\right)$ to denote the tangential velocity. The kinematic condition (7.4): $V_\Gamma = \mathbf{u} \cdot \mathbf{n}$ in the Navier-Stokes model originates from the immiscibility condition of the two fluids, and constrains only the normal velocity of the interface (particle). The condition (7.9) in the quasi-static Stokes model: $\frac{d\mathbf{x}}{dt} = (\mathbf{u} \cdot \mathbf{n})\mathbf{n}$ implies that the tangential velocity $\mathbf{P}\left(\frac{d\mathbf{x}}{dt}\right)$ equals *zero*. For a droplet in the aforementioned axi-symmetric flow and a coordinate system fixed to the center mass of the droplet, the motion of the droplet is pure extension or compression in the radial direction without translational or rotational movement. Hence, the tangential velocity is actually *zero*. In this sense the kinematic conditions (7.4) and (7.9) are consistent.

The next topic is the approximation of Navier-Stokes equations by the quasi-static Stokes equation. To this end, we express the Navier-Stokes equation (7.2) without gravity force in a dimensionless form with a typical length scale $L_R := r$ and a typical velocity size $U_R := |\dot{\gamma}|r$. We define the dimensionless variables as:

$$\tilde{x} := \frac{x}{L_R}, \quad \tilde{t} := \frac{t}{L_R/U_R}, \quad \tilde{\mathbf{u}}(\tilde{x}, \tilde{t}) := \frac{\mathbf{u}(x, t)}{U_R}, \quad \tilde{p}_i(\tilde{x}, \tilde{t}) := \frac{p(x, t)}{\rho_i U_R^2}, \quad i = 1, 2. \quad (7.25)$$

The domains are also scaled, $\tilde{\Omega}_i := \frac{1}{L_R}\Omega := \{\tilde{x} \in \mathbb{R}^3 : L_R\tilde{x} \in \Omega_i\}$. The Reynolds number is defined as in (7.6): $Re = \frac{\rho_2 L_R U_R}{\mu_2}$. Outside the droplet in Ω_2 , the dimensionless Navier-Stokes equations without gravity force take the form (we drop the tilde notation):

$$\begin{cases} \frac{\partial \mathbf{u}}{\partial t} - \frac{1}{Re} \Delta \mathbf{u} + (\mathbf{u} \cdot \nabla) \mathbf{u} + \nabla p = 0 & \text{in } \Omega_2 \times [0, T] \\ \operatorname{div} \mathbf{u} = 0 & \text{in } \Omega_2 \times [0, T] \end{cases} \quad (7.26)$$

Inside the droplet in Ω_1 , the equations are slightly different:

$$\begin{cases} \frac{\partial \mathbf{u}}{\partial t} - \frac{1}{\frac{\rho_1/\rho_2}{\lambda} Re} \Delta \mathbf{u} + (\mathbf{u} \cdot \nabla) \mathbf{u} + \nabla p = 0 & \text{in } \Omega_1 \times [0, T] \\ \operatorname{div} \mathbf{u} = 0 & \text{in } \Omega_1 \times [0, T] \end{cases} \quad (7.27)$$

where $\lambda := \mu_1/\mu_2$ is the viscosity ratio. When the two fluids have the same density, the ratio ρ_1/ρ_2 equals 1. For the quasi-static Stokes model to be a reasonable approximation

of the Navier-Stokes model, we require that $Re \ll 1$ and $Re/\lambda \ll 1$, such that the inertial term can be neglected. With the definition of Re , we obtain

$$\frac{\rho_2|\dot{\gamma}|r^2}{\mu_2} \ll 1, \quad \frac{\rho_2|\dot{\gamma}|r^2}{\lambda\mu_2} \ll 1. \quad (7.28)$$

In this parameter range we expect that the fluid dynamics modeled by the Navier-Stokes equations (7.2) can be accurately approximated by the Stokes equations (7.7).

Next we turn to another important assumption used in the theoretical model, namely the "sufficiently small deformation" assumption. In general this assumption is not satisfied in the sharp interface two-phase flow model. We now derive sufficient conditions for this assumption to hold. For clarification, we summarize some parameters in Table 7.1.

notation	definition
τ_0, Ca	quantities assigned to a clean interface
τ^*, S^*, Ca^*, Ma^*	quantities assigned to an interface $\Gamma(t_0)$ uniformly covered by surfactants
D_Γ	surface diffusion coefficient
ξ	τ^*/τ_0
α	$Pe/Ca^* = \tau^*r/(\mu_2D_\Gamma)$
\hat{S}	S/S^*
$\Delta\hat{S}$	$(S - S^*)/S^* = \hat{S} - 1$
R	gas constant

Table 7.1.: Definitions of parameters.

We study the stress balance condition in (7.15). We introduce a second set of scaling factors to study the influence of the dimensionless capillary number and Marangoni number on the droplet deformation as it was done in [89]. The typical length scale $L_R = r$ and the typical velocity size $U_R = |\dot{\gamma}|r$ remain the same. We define the dimensionless variables by (with a hat notation):

$$\begin{aligned} \hat{x} &:= \frac{x}{L_R}, \quad \hat{\mathbf{u}}(\hat{x}, \hat{t}) := \frac{\mathbf{u}(x, t)}{U_R}, \quad \hat{\mu}_i = \frac{\mu_i}{\mu_2}, \quad \hat{p}_i(\hat{x}, \hat{t}) := \frac{p(x, t)}{\mu_2 U_R / L_R}, \\ \hat{\boldsymbol{\sigma}}_i &:= \frac{\boldsymbol{\sigma}_i}{\mu_2 U_R / L_R}, \quad \hat{\tau} = \frac{\tau}{\tau^*}, \quad \hat{S} = \frac{S}{S^*}, \quad i = 1, 2. \end{aligned} \quad (7.29)$$

We consider $\tau = \tau(S)$ as in (2.38). Hence the tangential derivative $\nabla_\Gamma \tau$ equals

$$\nabla_\Gamma \tau(S(\mathbf{x}, t)) = \frac{d\tau}{dS} \nabla_\Gamma S.$$

The dimensionless stress balance condition takes the form:

$$[\hat{\boldsymbol{\sigma}}\mathbf{n}]_\Gamma = \frac{-1}{Ca^*} \hat{\tau} \hat{\kappa} \mathbf{n} + \frac{d\tau}{dS} \frac{S^*}{\mu_2 U_R} \hat{\nabla}_\Gamma \hat{S},$$

7. Simulation of flows with surfactants

where $\frac{d\tau}{dS}S^* = -(\tau_0 - \tau^*) =: -\Delta\tau$ quantifies the change of surface tension coefficient due to the equilibrium surfactant concentration S^* , $\hat{\nabla}_\Gamma$ is the surface gradient with respect to \hat{x} , and $\hat{\kappa} = \hat{\nabla}_\Gamma \cdot \mathbf{n}$. We define the Marangoni number as

$$Ma^* := \frac{\Delta\tau}{\mu_2 U_R} = \frac{\Delta\tau}{\mu_2 |\dot{\gamma}| r}. \quad (7.30)$$

Hence we obtain

$$[\hat{\boldsymbol{\sigma}}\mathbf{n}]_\Gamma = \frac{-1}{Ca^*} \hat{\tau} \hat{\kappa} \mathbf{n} - Ma^* \hat{\nabla}_\Gamma \hat{S}. \quad (7.31)$$

We define $\Delta\hat{S} = \hat{S} - 1$. From the equation of state (2.38), we obtain

$$\hat{\tau} = \frac{\tau}{\tau^*} = \frac{\tau_0 - SRT}{\tau_0 - S^*RT} = 1 - \frac{(S - S^*)RT}{\tau_0 - S^*RT}.$$

From the definition of ξ , we obtain

$$\xi = \tau^*/\tau_0 = (\tau_0 - S^*RT)/\tau_0 = 1 - S^*RT/\tau_0.$$

Hence the equation (7.31) takes the form [82]:

$$[\hat{\boldsymbol{\sigma}}\mathbf{n}]_\Gamma = \frac{-1}{Ca^*} \hat{\kappa} \mathbf{n} \left(1 - \frac{(1 - \xi)\Delta\hat{S}}{\xi} \right) - Ma^* \hat{\nabla}_\Gamma(\Delta\hat{S}). \quad (7.32)$$

The Marangoni number (7.30) can be reformulated as

$$Ma^* = \frac{1 - \xi}{\xi Ca^*}.$$

In equation (7.32) on the right hand side, the first term is the normal component of the surface stress, which is responsible for the evolution of the droplet shape, and the second term is the tangential component. We can observe that the local concentration of surfactant influences both the normal and the tangential surface stress. The infinitesimal deformation assumption of the droplet leads to the following restrictions:

$$Ca^* \ll 1, \quad \frac{(1 - \xi)|\Delta\hat{S}|}{\xi} \ll 1, \quad (7.33)$$

such that the droplet is nearly spherical. The surface Péclet number is also required to be small, i.e. $Pe \ll 1$, such that the transport equation (7.5) is diffusion dominated and the local variation of surfactant concentration $|\Delta\hat{S}|$ is small.

Remark 7.2.3. We recall that $\xi := 1 - \frac{S^*RT}{\tau_0}$. We assume that $Pe \ll 1$, i.e. $|\Delta\hat{S}|$ is small. The effective surface tension coefficient τ^* should not be negative. Hence the uniform surfactant concentration S^* is bounded by $\frac{\tau_0}{RT}$, which results from

$$\tau^* = \tau_0 - S^*RT \geq 0 \Rightarrow S^* \leq \frac{\tau_0}{RT}.$$

We use $S^{max} = \frac{\tau_0}{RT}$ to denote the maximum value of S . In order to satisfy the second condition in (7.33), we require

$$\frac{S^*}{S^{max} - S^*} |\Delta\hat{S}| \ll 1. \quad (7.34)$$

In the numerical experiments, we take $T = 300 \text{ K}$. The gas constant is $R = 8.3144621 \text{ JK}^{-1}\text{mol}^{-1}$. From the condition $Ca^* \ll 1$, we then obtain

$$\frac{\mu_2|\dot{\gamma}|r}{\tau_0 - 300RS^*} \ll 1. \quad (7.35)$$

From the condition $Pe \ll 1$, we obtain

$$\frac{|\dot{\gamma}|r^2}{D_\Gamma} \ll 1. \quad (7.36)$$

We summarize the conditions we derived above in (7.28), (7.34), (7.35), (7.36)

$$\begin{aligned} \frac{\rho_2|\dot{\gamma}|r^2}{\mu_2} \ll 1, \quad \frac{\rho_2|\dot{\gamma}|r^2}{\lambda\mu_2} \ll 1, \quad \frac{S^*}{S^{max} - S^*}|\Delta\hat{S}| \ll 1 \\ \frac{\mu_2|\dot{\gamma}|r}{\tau_0 - 300RS^*} \ll 1, \quad \frac{|\dot{\gamma}|r^2}{D_\Gamma} \ll 1. \end{aligned} \quad (7.37)$$

From the unbounded to a bounded domain

In the numerical experiments, we consider the Navier-Stokes model described in section 7.2.1 on a *bounded* domain $\Omega = [-\frac{1}{2}L_x, \frac{1}{2}L_x] \times [-\frac{1}{2}L_y, \frac{1}{2}L_y] \times [-\frac{1}{2}L_z, \frac{1}{2}L_z]$. Due to the axi-symmetry of the far field condition (7.10), we take $L_x = L_y$. The boundary conditions are given by

$$\mathbf{u}(x, y, z) = \dot{\gamma}\left(-\frac{1}{2}x, -\frac{1}{2}y, z\right)^T, \quad (x, y, z)^T \in \partial\Omega. \quad (7.38)$$

The initial condition of the fluid dynamics is the undisturbed velocity profile $\mathbf{u}(\mathbf{x}) = \dot{\gamma}\mathbf{E}\mathbf{x}$. The initial shape of the droplet is a sphere located at the origin with a radius $r = 0.25 \text{ m}$. The initial surfactant concentration is $S(0) = S^*$ with a uniform concentration S^* .

Remark 7.2.4. *As we solve the Navier-Stokes equations in a bounded domain, the boundary effect will occur, which is neglected in the theoretical analysis, i.e. the unbounded domain assumption. If we choose a large enough domain, this boundary effect will decrease to a certain level, such that the resulting error in the solutions will have the same order of magnitude as the numerical errors.*

To choose proper values for L_x , L_y and L_z , we perform numerical experiments for a series of domains and compare the results. Details can be found in section 7.3.

7.3. Numerical experiments

In this section we present results of our numerical solver applied to the two-phase Navier-Stokes model described in section 7.2.1. Based on the analysis in section 7.2.2 we consider a specific benchmark problem that is close to the Stokes model studied in [82]. Hence, it makes sense to determine the droplet deformation and surfactant concentration numerically and compare the dependence of these quantities on parameters (λ, α, ξ) to the

7. Simulation of flows with surfactants

dependencies derived in [82] cf. (7.19), (7.20) and (7.22). The domain and boundary conditions are described in section 7.2.3. We define a numerical droplet deformation parameter as follows. We use $d_x(t)$, $d_y(t)$ and $d_z(t)$ to denote the side lengths of the bounding box of the droplet, which are obtained from the numerical solutions. In the experiments, we observe that $d_x(t)$ and $d_y(t)$ have the same values, which reflects the symmetric nature of the model problem. We determine a numerical deformation parameter

$$D^{num}(t) = \frac{d_z(t) - d_y(t)}{d_z(t) + d_y(t)}. \quad (7.39)$$

We summarize all parameters that are fixed in the experiment. We take $r = 0.25 \text{ m}$, $\rho_1 = \rho_2 = 1 \text{ kg/m}^3$, $\mu_2 = 1 \text{ Pa} \cdot \text{s}$, $\tau_0 = 1 \text{ N/m}$. From the conditions we listed in (7.37), we obtain restrictions on other parameters

$$|\dot{\gamma}| \ll 16, \quad \frac{|\dot{\gamma}|}{\lambda} \ll 16, \quad \frac{|\dot{\gamma}|}{1 - 300RS^*} \ll 4, \quad \frac{|\dot{\gamma}|}{D_\Gamma} \ll 16. \quad (7.40)$$

Clearly $|\dot{\gamma}|$, λ , S^* and D_Γ are independent parameters that are to be chosen for numerical experiments. As the local variation of surfactant concentration $|\Delta \hat{S}|$ is not known a-priori, we require that S^* is not *too close* to $S^{max} = \frac{1}{300R} \approx 4.01 \times 10^{-4} \text{ mol/m}^2$.

In the experiments below we use the following local grid refinement. Within a distance of 0.25 m from the interface the grid is locally refined. For the level ℓ refinement the ratio between droplet diameter and tetrahedron diameter is approximately $3 \cdot 2^\ell$. We use $\ell = 1, 2, 3, 4$. After each time step, the grid is adaptively refined and coarsened according to the position of the interface. On level ℓ the time step is chosen as $\Delta t = 2^{3-\ell} \times 10^{-1} \text{ s}$. In each time step, the interface stays in the refined region.

7.3.1. Clean interface

We first show numerical results for a clean interface case. The theoretical approximation of D is given in (7.12). For this approximation to be valid, we require that $Re \ll 1$ and $Re/\lambda \ll 1$ as given in (7.28) and $Ca \ll 1$ from the small deformation assumption. With $\mu_2 = 1$, $\rho_1 = \rho_2 = 1$ and $\tau_0 = 1$, we obtain the following conditions

$$|\dot{\gamma}| \ll 16, \quad \frac{|\dot{\gamma}|}{\lambda} \ll 16.$$

First we choose the shear rate $\dot{\gamma} = 0.01 \text{ s}^{-1}$ and obtain the condition for λ :

$$\lambda \gg 6.25 \times 10^{-4}. \quad (7.41)$$

We calculate the capillary number: $Ca = 2.5 \times 10^{-3}$, and the Reynolds number: $Re = 6.25 \times 10^{-4}$. The theoretical prediction in (7.12), i.e. $D \approx \frac{3}{2} \frac{19\lambda+16}{16\lambda+16} Ca$, is a monotonically increasing function for $\lambda > 0$ with an asymptotic value $D^\infty = 4.453 \times 10^{-3}$. Hence we expect a small deformation of the droplet with the choice of parameters, and choose the domain size ratio $\frac{L_z}{L_{x(y)}} = 1$, and use L_d to denote the side length.

Domain size. We choose $\lambda = 1$, which satisfies (7.41), and perform numerical experiments on different sizes of domain on level 3 refinement. We expect that if the domain

is too small, the boundary effect will be observed in the results, which is not taken into account in the theoretical analysis. The numerical results $D^{num}(t)$ are shown in Figure 7.2 for different domain sizes ranging from $L_d = 2/3 m$ to $L_d = 4 m$ (the ratio of L_d to the droplet diameter is $4/3, 2, 4$ and 8). In Figure 7.2 we observe a converging behavior of $D^{num}(t)$ when the size of the domain increases, which implies the decreasing of boundary effects as we discussed in Remark 7.2.4.

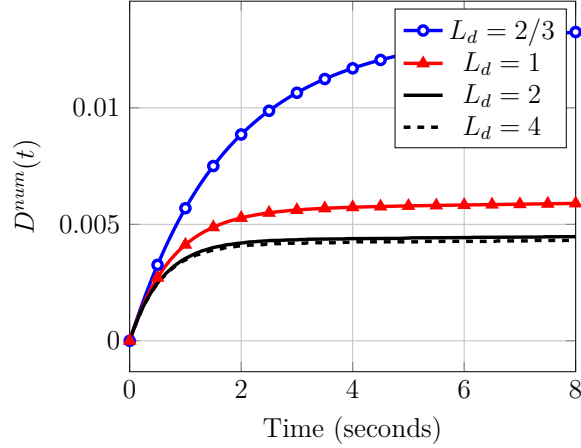


Figure 7.2.: Numerical deformation parameter $D^{num}(t)$ for different domain sizes on level 3 refinement.

We calculate the time averaging results of $D^{num}(t)$ for $t \in [6, 8]$ s with $L_d = 2, 4, 8 m$, and use \bar{D}^{num} to denote the averaging value. The results are shown in Table 7.2. Based on these results, we choose $L_d = 4 m$ for all subsequent experiments.

L_d	\bar{D}^{num}
2	4.45×10^{-3}
4	4.29×10^{-3}
8	4.27×10^{-3}

Table 7.2.: Time averaged results \bar{D}^{num} for $L_d = 2, 4, 8 m$ on level 3 refinement for $t \in [6, 8]$ s.

Grid convergence. We choose $\lambda = 1$ and other parameters unchanged. In calculating the numerical deformation parameter $D^{num}(t)$ in equation (7.39), if $d_z(t) \approx d_y(t)$ and both quantities contain (discretization) errors, the operation $d_z(t) - d_y(t)$ will lead to numerical cancellation effect. Hence we first study the dependence of $d_z(t)$ and $d_y(t)$ on grid refinements separately. Results for $d_z(t)$ and $d_y(t)$ are shown in Figure 7.3. We calculate the time averaging results \bar{d}_z and \bar{d}_y for $t \in [6, 10]$ s. The results are shown in Table 7.3. One may check that these values indicate a linear convergence behavior with a reduction factor 0.25 for both \bar{d}_z and \bar{d}_y . Hence we calculate the numerical limiting values, which are $0.50282 m$ for \bar{d}_z and $0.49864 m$ for \bar{d}_y , and achieve the error estimates in the third (absolute error) and fourth columns (relative error). These results indicate a second order of convergence of the numerical results with respect to grid refinements.

From equation (7.13), we calculate the theoretical values d_z^{theo} and d_y^{theo} , which are 0.50275

7. Simulation of flows with surfactants

m and $0.49863 m$ correspondingly. On refinement level 3, the relative error between \bar{d}_z and d_z^{theo} is 0.15%, the relative error between \bar{d}_y and d_y^{theo} is 0.09%. On refinement level 4, the relative errors decrease to 0.05% and 0.03% correspondingly. We also calculate the theoretical deformation parameter from equation (7.12), which is 4.102×10^{-3} for the choice of parameters given above. On refinement level 3, we calculate the time averaging result of $D^{num}(t)$, and obtain 4.27×10^{-3} , which has a relative error of 4% compared to the theoretical prediction. On refinement level 4, the relative error decreases to 2.3%. Note that $\bar{d}_z \approx \bar{d}_y$ (cf. Table 7.3) and thus we have to expect a strong error amplification in the quantity \bar{D}^{num} , cf. (7.39). Nevertheless, a good agreement with the theoretical prediction is achieved.

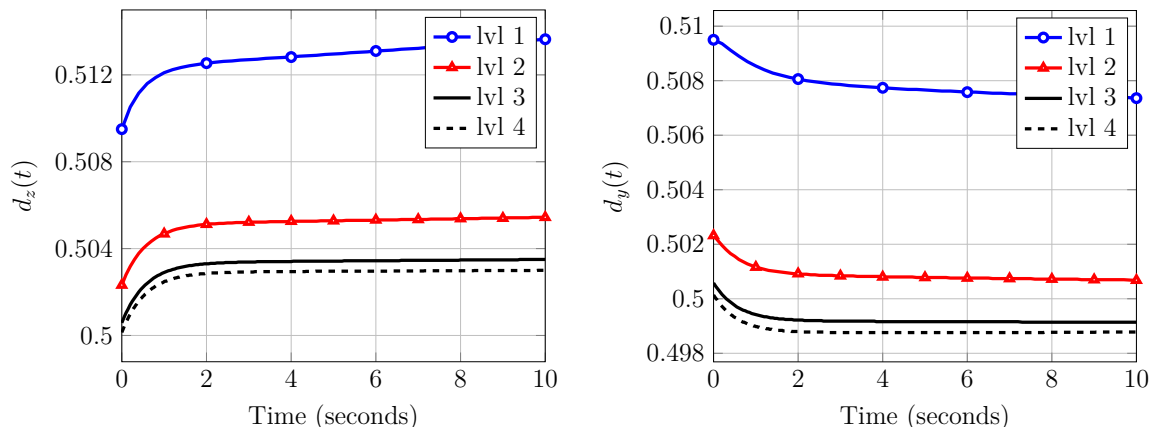


Figure 7.3.: Numerical results $d_z(t)$ and $d_y(t)$ on different refinement levels for a clean droplet in a domain with length $L_d = 4 m$. The shear rate $\dot{\gamma}$ is $0.01 s^{-1}$.

refinement	\bar{d}_z	abs. error	rel. error
1	0.5134	1.05×10^{-2}	2.1%
2	0.5054	2.56×10^{-3}	0.51%
3	0.5035	6.52×10^{-4}	0.13%
4	0.5030	1.63×10^{-4}	0.03%

refinement	\bar{d}_y	abs. error	rel. error
1	0.5075	8.83×10^{-3}	1.8%
2	0.5007	2.08×10^{-3}	0.42%
3	0.4991	5.04×10^{-4}	0.10%
4	0.4988	1.26×10^{-4}	0.03%

Table 7.3.: Time averaged results \bar{d}_z and \bar{d}_y on refinement levels 1, 2, 3, 4 for $t \in [6, 10] s$. Theoretical values are $0.50275 m$ (d_z) and $0.49863 m$ (d_y).

Dependence on Ca . From the theoretical analysis [69], the prediction of D in (7.12) is valid for a small Ca number. For a larger Ca number, the prediction has to be modified with higher terms of Ca (see Remark 7.2.1). From the definition of Ca in (7.11), we vary the value of $|\dot{\gamma}|$ to study the dependence of D on Ca . The experiments are performed at level 3 refinement. Time averaging results of $D^{num}(t)$ are shown in Figure 7.4 together

with theoretical predictions from [7]. From Figure 7.4, we can conclude that numerical results are in very good accordance with $\mathcal{O}(Ca^2)$ predictions, and for larger Ca numbers the $\mathcal{O}(Ca^2)$ corrections are necessary to predict the deformation of droplets.

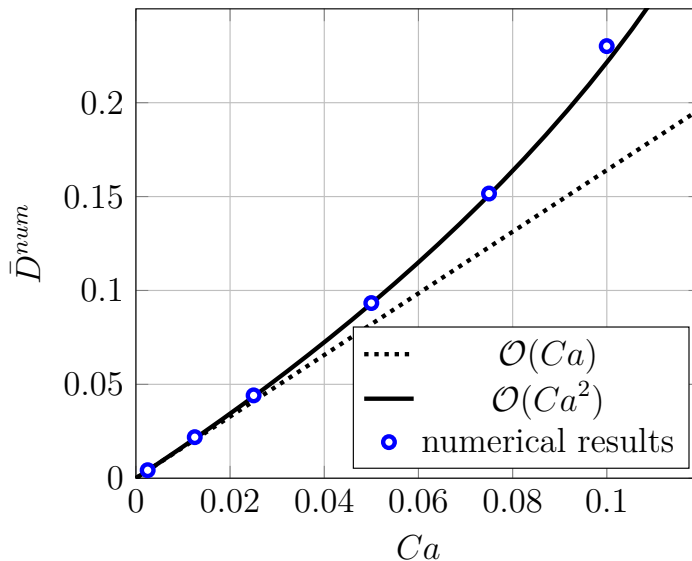


Figure 7.4.: Numerical deformation parameter \bar{D}^{num} on refinement level 3 for a clean droplet with various capillary numbers. The dashed line is the prediction (7.12) according to $\mathcal{O}(Ca)$ approximation, the solid line is the $\mathcal{O}(Ca^2)$ prediction (7.14) from [7].

7.3.2. Interface with an insoluble surfactant

We now consider the fluid dynamics coupled with surfactant transport on the interface. We will show the effects of surfactant transport on the deformation parameter $D^{num}(t)$. We compare numerical results with theoretical predictions given for D in (7.20) and for S in (7.22). We take parameters $\mu_2 = 1$, $\rho_1 = \rho_2 = 1$ and $\tau_0 = 1$. The restrictions on $|\dot{\gamma}|$, λ , S^* and D_Γ are given in (7.40) with the maximum allowed surfactant concentration $S^{max} \approx 4.01 \times 10^{-4} \text{ mol/m}^2$. The initial surfactant concentration S^* should not be too close to S^{max} .

In this section, our focus is on the coupling effect of surfactant transport and fluid dynamics. We choose $\lambda = 1$ and vary the values of $|\dot{\gamma}|$, S^* and D_Γ (ξ and α).

Properties of numerical methods

Grid convergence. Now we are dealing with a significantly more complex problem. We try to perform the same kind of experiment as in the clean interface case. We use the decoupling scheme introduced in section 4.4. We choose $S^* = \frac{1}{2}S^{max}$ and $D_\Gamma = 0.01 \text{ m}^2/\text{s}$, i.e. $\xi = 0.5$ and $\alpha = 12.5$, and study the dependence of $d_z(t)$ and $d_y(t)$ on grid refinements. $\dot{\gamma}$ is chosen to be 0.01 s^{-1} , which leads to $Ca^* = 0.005$ and $Pe = 0.0625$. Results are presented in Figure 7.5. The time averaging result of $d_z(t)$ for $t \in [12, 20] \text{ s}$ is given in

7. Simulation of flows with surfactants

Table 7.4. These values show a converging behavior, but we do not observe a regular linear convergence behavior. To test the robustness of our solver, we also perform numerical experiments with $\dot{\gamma} = 0.1 \text{ s}^{-1}$ ($Ca^* = 0.05$, $Pe = 0.625$). With this choice of $\dot{\gamma}$, the Pe number does not satisfy the condition $Pe \ll 1$. Hence we expect a large deviation from the theoretical prediction in equation (7.20). Results are shown in Figure 7.6 and Table 7.4. The oscillations in Figure 7.6 are caused by reparametrizations of the level-set function, which is performed if the norm of the gradient of the level-set function next to the interface is larger than 5 or smaller than 0.5. These oscillations are getting smaller for finer grids. The results also show a converging behavior, but a regular linear convergence behavior is not observed.

From equation (7.19), we calculate the theoretical values d_z^{theo} and d_y^{theo} for $\dot{\gamma} = 0.01$, which are 0.50590 m and 0.49705 m correspondingly. On refinement level 3, the relative error between \bar{d}_z and d_z^{theo} is 0.24%, the relative error between \bar{d}_y and d_y^{theo} is 0.09%. On refinement level 4, the relative errors decrease to 0.09% and 0.01% correspondingly. We also calculate the theoretical deformation parameter from equation (7.20), which is 8.828×10^{-3} . On refinement level 3, we calculate the time averaging result of $D^{num}(t)$, and obtain 9.57×10^{-3} , which has a relative error of 8% compared to D^{theo} . On refinement level 4, the relative error decrease to 5%. Note that $\bar{d}_z \approx \bar{d}_y$ (cf. Table 7.4), the numerical cancellation effect causes the error amplification in the quantity \bar{D}^{num} , cf. the discussion in the clean interface case. When $\dot{\gamma} = 0.1$, the relative error between \bar{D}^{num} and D^{theo} is about 20% on level 3 refinement. On level 4 refinement, this relative error decreases not so much. Note that this relative error is calculated between numerical results and the $\mathcal{O}(Ca)$ theoretical prediction. We suspect that the relatively high capillary number ($Ca^* = 0.05$) contributes a major part in this 20% relative error by introducing a large model error, which is similar to the clean interface case, cf. Figure 7.4. A higher order theoretical prediction for the surfactants covered droplet is to our knowledge not available yet. The dependency of \bar{D}^{num} on Ca^* is investigated in the next section.

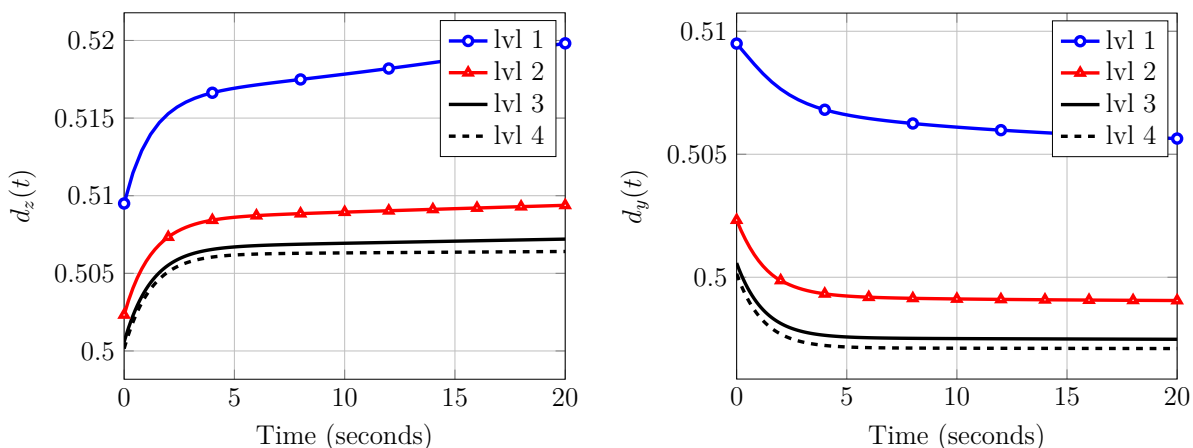


Figure 7.5.: Numerical results $d_z(t)$ and $d_y(t)$ on different refinement levels for a droplet with surfactant. The shear rate $\dot{\gamma}$ is 0.01 s^{-1} . $\xi = 0.5$ and $\alpha = 12.5$.

In Figure 7.8 and Figure 7.9, we show the shapes of the deformed droplet in a yz -cutting plane at the end time $t = 20 \text{ s}$ and the distance r between surface points and the center of the droplet. In Figure 7.10, normalized surface concentrations S/S^* on deformed droplets

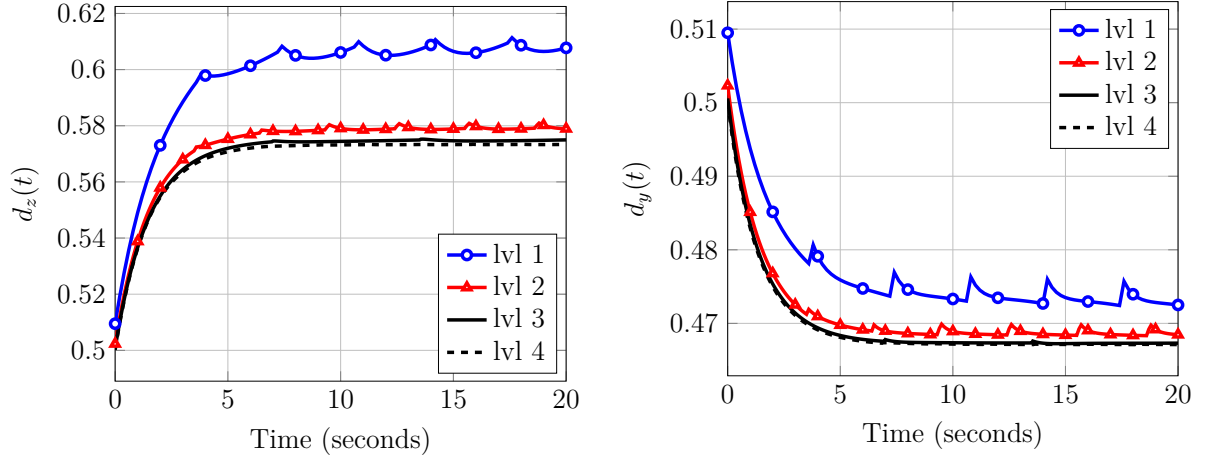


Figure 7.6.: Numerical results $d_z(t)$ and $d_y(t)$ on different refinement levels for a droplet with surfactant. The shear rate $\dot{\gamma}$ is 0.1 s^{-1} . $\xi = 0.5$ and $\alpha = 12.5$.

refinement	\bar{d}_z	\bar{d}_y
1	0.5190	0.5058
2	0.5092	0.4991
3	0.5071	0.4975
4	0.5064	0.4971

(a) $\dot{\gamma} = 0.01 \text{ s}^{-1}$

refinement	\bar{d}_z	\bar{d}_y
1	0.6072	0.4733
2	0.5792	0.4687
3	0.5748	0.4673
4	0.5733	0.4671

(b) $\dot{\gamma} = 0.1 \text{ s}^{-1}$

Table 7.4.: Time averaged results of $d_z(t)$ and $d_y(t)$ for $t \in [12, 20] \text{ s}$ on refinement levels 1, 2, 3, 4 for (a) $\dot{\gamma} = 0.01 \text{ s}^{-1}$ and (b) $\dot{\gamma} = 0.1 \text{ s}^{-1}$.

7. Simulation of flows with surfactants

are shown. Schematics of the definition of r and how we plot these two surface quantities are shown in Figure 7.7. Convergence of the numerical results are observed for both quantities for $\dot{\gamma} = 0.01$ and $\dot{\gamma} = 0.1$. Theoretical predictions for r^∞ from equations (7.19) and S^∞ from (7.22) are compared with the numerical results. From the figures, we observe that when $\dot{\gamma}$ equals 0.01, numerical results r and S are in very good accordance with theoretical predictions; when $\dot{\gamma}$ equals 0.1, the results are less good, but it is expected due to the larger values $Ca^* = 0.05$ and $Pe = 0.625$.

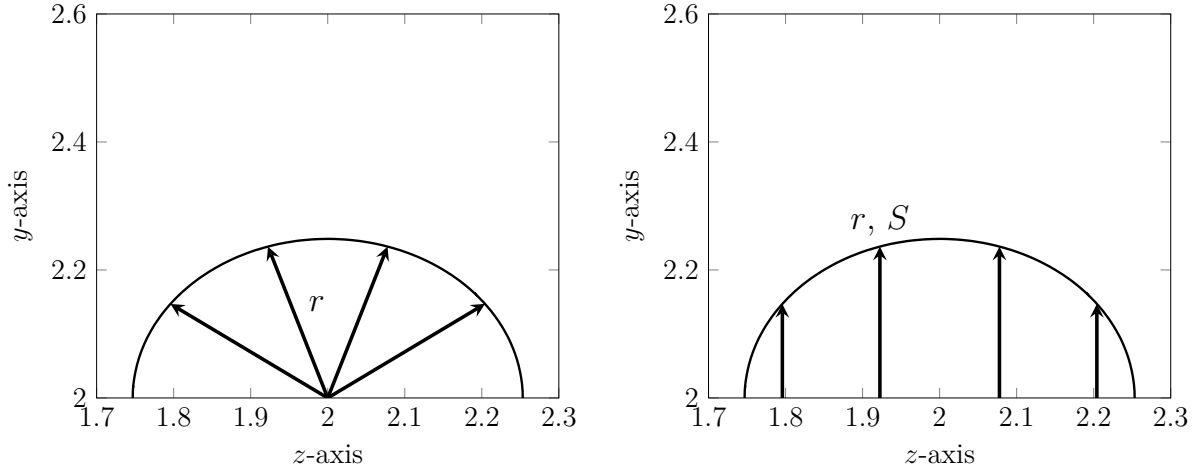


Figure 7.7.: Schematics of the definition of r (left) and how the surface quantities r and S/S^* are plotted on yz cutting planes with respect to z -axis in Figure 7.8, 7.9 and 7.10 (right).

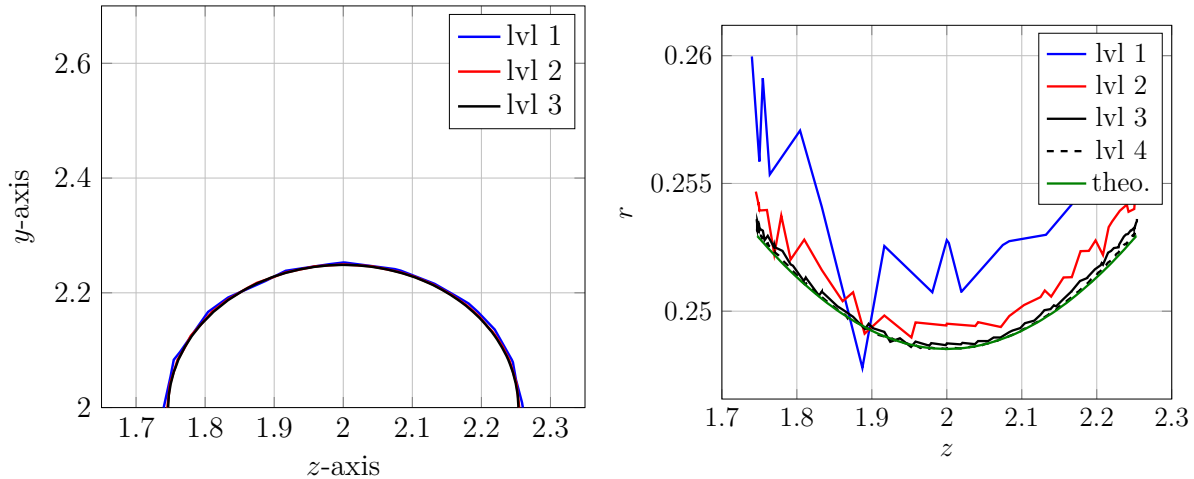


Figure 7.8.: The shape of droplets at $t = 20$ s on different refinement levels. Shown are yz -cutting plane (left) and the distance r between surface points and the center of the droplet (right). $\xi = 0.5$, $\alpha = 12.5$ and $\dot{\gamma} = 0.01$.

Nonlinear coupling and linear algebra. We apply the Gauss-Seidel iterative method introduced in section 4.4 to decouple the bulk fluid dynamics with the interfacial surfactant transport. In each Gauss-Seidel iteration of the decoupling scheme, cf. Figure 4.2 and Figure 4.7, we solve the level set equation, the Navier-Stokes equation and the surfactant equation in the space-time finite element formulation (3.31) in steps. The linear system of

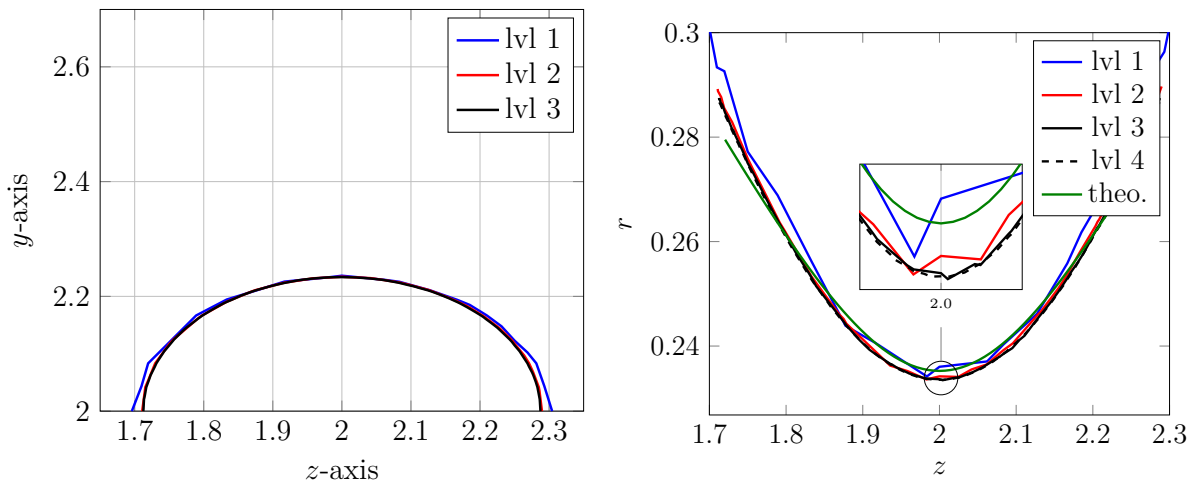


Figure 7.9.: The shape of droplets at $t = 20$ s on different refinement levels. Shown are yz -cutting plane (left) and radius of the droplet (right). $\xi = 0.5$, $\alpha = 12.5$ and $\dot{\gamma} = 0.1$.

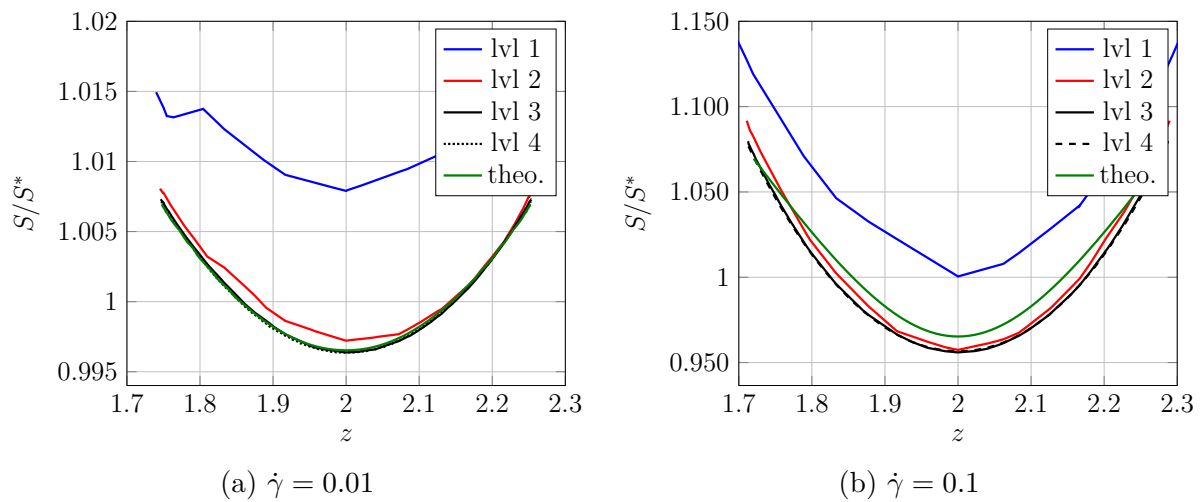


Figure 7.10.: Normalized surfactant concentration S/S^* on the deformed droplet at $t = 20$ s. $\xi = 0.5$, $\alpha = 12.5$. The shear rates are (a) $\dot{\gamma} = 0.01$ and (b) $\dot{\gamma} = 0.1$.

7. Simulation of flows with surfactants

the surfactant equation is solved by the generalized minimal residual method (GMRES) with a Gauss-Seidel preconditioning. To study the convergence behavior of the decoupling scheme and the GMRES solver, we solve one time step at $t = 2$ s and compare the number of iterations. The stopping criteria are chosen as follows: for the decoupling scheme, the residual of \mathbf{u} is required to be smaller than 10^{-8} , and for the GMRES solver, the residual is required to be smaller than 10^{-10} . The shear rate chosen is $\dot{\gamma} = 0.01$. We obtain similar results for $\dot{\gamma} = 0.1$. The results are listed in Table 7.5 for different refinement levels. Noting that the time steps are chosen as $\Delta t = 2^{3-l} \times 10^{-1}$ s. We take the level 3 refinement and perform one time step at $t = 2$ s with different time step sizes. The results are listed in Table 7.6.

refinement	number of unknowns			GS iteration	GMRES
	S	pressure	velocity		
1	87	2321	38205	9	44
2	276	3033	51465	10	69
3	1068	5423	92259	5	146
4	4244	16183	279999	4	250

Table 7.5.: Number of unknowns, Gauss Seidel iterations and GMRES iterations. The last column are the GMRES iteration numbers needed for solving the surfactant equation once, i.e. in one iteration of the Gauss-Seidel scheme.

Δt	GS iteration	GMRES
1×10^{-3}	2	724
2×10^{-3}	2	624
5×10^{-3}	3	380
1×10^{-2}	3	226
2×10^{-2}	3	201
5×10^{-2}	4	162
1×10^{-1}	5	146
2×10^{-1}	5	127
5×10^{-1}	12	152

Table 7.6.: Gauss-Seidel iterations and GMRES iterations for different time step sizes on level 3 refinement. The last column are the GMRES iteration numbers needed for solving the surfactant equation once, i.e. in one iteration of the Gauss-Seidel scheme.

Dependence on Ca^* . For a droplet with a clean interface, we have shown in Figure 7.4 that for a larger value of Ca the $\mathcal{O}(Ca)$ approximation of the deformation parameter D leads to a large discrepancy in the results. Theoretical predictions (7.19), (7.20) and (7.22) are also $\mathcal{O}(Ca)$ approximation for a droplet with surfactant. Hence we expect larger discrepancies if we choose Ca^* too big. The experiment results in Figure 7.8 ($\dot{\gamma} = 0.01$), Figure 7.9 ($\dot{\gamma} = 0.1$) and Figure 7.10 give evidence of this claim. In this section, we perform numerical experiments with the same parameters as in the previous section except that we choose a series of $\dot{\gamma}$ and compare the numerical result with the prediction (7.20) as

shown in Figure 7.11. The experiments are performed on level 3 refinement. From the figure, we observe a similar behavior as in Figure 7.4. As it is mentioned in [82], the prediction (7.20) is only valid for small capillary number. For a droplet with surfactant, a higher order approximation of D , which is similar to the $\mathcal{O}(Ca^2)$ result for a clean interface, has not been found yet.

In the subsequent section 7.3.2, we keep $Ca^* = 5 \times 10^{-3}$ and perform experiments with fixed values of ξ .

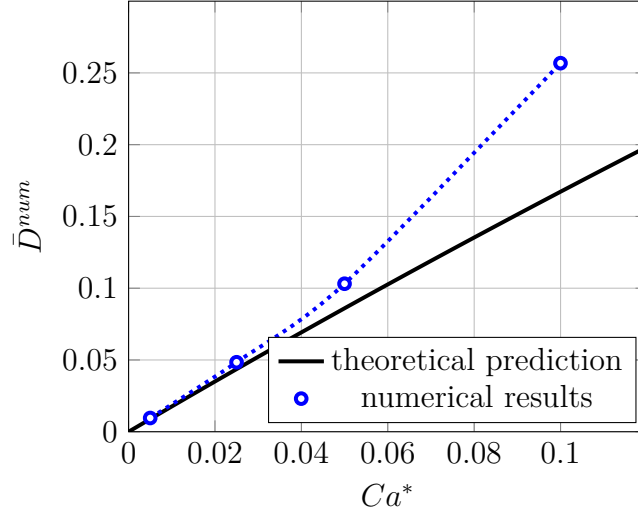


Figure 7.11.: Numerical deformation parameter \bar{D}^{num} on refinement level 3 for a droplet with surfactant. The parameters are $\xi = 0.5$, $\alpha = 12.5$ and $D_\Gamma = 0.01$.

Experiments with fixed ξ and varying α

We choose $\xi = 0.5$ and $\dot{\gamma} = 0.01$. We perform experiments with varying α (D_Γ) values. Note that $\alpha := \frac{Pe}{Ca^*}$ and $Pe := \frac{|\dot{\gamma}|r^2}{D_\Gamma}$. With fixed values of Ca^* , $|\dot{\gamma}|$ and r , a lower surface diffusivity D_Γ leads to a larger value of α . From (7.40), we obtain restrictions on D_Γ ($\dot{\gamma} = 0.01$ and $\lambda = 1$): $D_\Gamma \gg 6.25 \times 10^{-4}$ ($\alpha \ll 200$). This condition requires that the surface diffusion should not be too small compared with surface convection.

With the given values of λ and ξ , we can calculate b_r from (7.21):

$$b_r = \frac{5}{4} \frac{35 + 4\alpha}{20 + 2\alpha}.$$

From (7.20), we obtain the prediction of D for given λ , ξ and Ca^* :

$$D = \frac{0.075(35 + 4\alpha)}{32.1\alpha + 320.875}, \quad (7.42)$$

which is a monotonically increasing function for $\alpha > 0$. From $\alpha \ll 200$, we obtain $D < 9.3 \times 10^{-3}$. We perform numerical experiments with varying α on level 3 refinement. Results are shown in Figure 7.12. We have reproduced a similar behavior of the dependency of \bar{D}^{num} on α as the theoretical result. Relative errors between \bar{D}^{num} and

7. Simulation of flows with surfactants

theoretical prediction from equation (7.42) are about 8% to 10% (left). For comparison, we have performed the same test for $\dot{\gamma} = 0.001$ ($Ca^* = 5 \times 10^{-4}$). Again we have reproduced a similar result. The smaller relative errors for $\dot{\gamma} = 0.001$ (approx. 3.5%) confirms that the theoretical formula in (7.42) gives a more accurate prediction of the deformation parameter for smaller Ca^* .

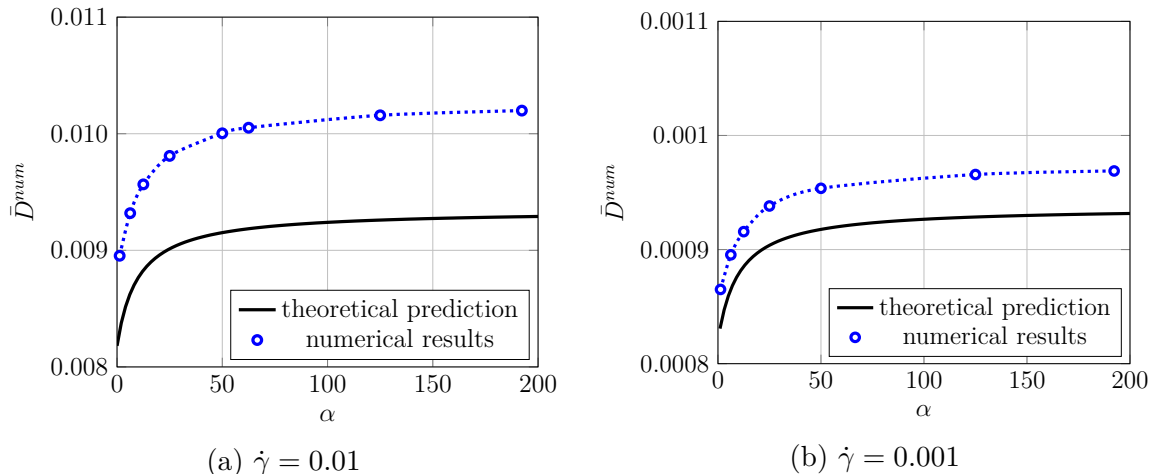


Figure 7.12.: Numerical deformation parameter \bar{D}^{num} with varying α (D_Γ) on refinement level 3 for a droplet with surfactant. The fixed parameters are $\xi = 0.5$ and $Ca^* = 5 \times 10^{-3}$ (left), $\xi = 0.5$ and $Ca^* = 5 \times 10^{-4}$ (right).

7.4. Droplet breakup in shear flow

In this section we apply the validated numerical methods to study the breakup of an initially spherical droplet in a simple shear flow. Recall the stationary Stokes model introduced in section 7.2.2, when the capillary number is small, i.e. a small shear rate $|\dot{\gamma}|$ and a big surface tension coefficient τ , cf. (7.11) or (7.16), the droplet keeps a steady form in the shear flow. There exists a critical capillary number, above which the droplet will no longer maintain a steady form, and it keeps deforming until it breaks up [51, 68]. For a two-phase system with equal viscosities, i.e. $\lambda := \mu_1/\mu_2 = 1$, the critical capillary number is predicted to be 0.41 [68]. In [51], the authors studied this problem for a clean droplet by using a volume-of-fluid method. Three dimensional results are presented for $\lambda = 1$, $Ca = 0.42$ and $Re = 0$. The critical capillary number is determined to be between 0.4 and 0.42. In [85], the authors applied a diffuse-interface method and included the influence of soluble and insoluble surfactants on the deformation of the droplet. The dimensionless numbers are chosen as $\lambda = 1$, $Ca = 0.42$ and $Re = 0.4$. The authors compared the breakup process of a droplet with and without insoluble surfactants. We study the influence of insoluble surfactants on the droplet breakup behavior by performing a similar experiment as in [85]. The difference with [85] is that we utilize a sharp interface model. By performing simulations of this relatively complex problem, we show that our numerical solver is able to handle topological changes.

We briefly describe the model problem presented in [85]. A spherical droplet with a radius r is placed in the center of a rectangular box with a dimension $[-L_x/2, L_x/2] \times$

$[-L_y/2, L_y/2] \times [-L_z/2, L_z/2]$. The rest of the domain is occupied by a surrounding fluid. Dirichlet boundary conditions $\mathbf{u} = \pm \frac{L_z}{2} \mathbf{e}_x$ are imposed on the upper and lower boundaries. Hence the unperturbed flow, i.e. without the droplet, has a shear rate $\dot{\gamma} = 1$. Periodic boundary conditions are imposed on other boundaries. The densities and the viscosities are denoted by ρ_i and μ_i , where $i = 1$ represents the droplet, and $i = 2$ represents the surrounding fluid. The two fluids have equal densities, i.e. $\rho_1 = \rho_2$. The viscosity ratio $\lambda = \mu_1/\mu_2$ equals 1. The surface tension coefficient is denoted by τ_0 for a clean interface. No gravity force is considered. The dimensionless numbers are defined by: the Reynolds number $Re = \rho_2 |\dot{\gamma}| r^2 / \mu_2$, the capillary number for a clean droplet $Ca = \mu_2 |\dot{\gamma}| r / \tau_0$.

7.4.1. Critical capillary number

First we consider the critical capillary number of a clean droplet. As described above, this number is predicted to be around 0.41. We perform a similar experiment as in [51] to determine the numerical critical capillary number. We choose $r = 1.0$. The domain size is $L_x = L_z = 8$, $L_y = 4$. Densities are $\rho_1 = \rho_2 = 0.0625$. The Reynolds number is then $Re = 0.0625$. Numerical simulations are performed for $Ca = 0.40$ ($\tau_0 = 2.5$) and $Ca = 0.42$ ($\tau_0 = 2.3810$). The domain is divided into $8 \times 4 \times 8$ equal-sized cubes, and each cube is divided into 6 tetrahedra. Next to the interface, the mesh is adaptively refined three times. The time step size is 0.05.

In Figure 7.13, we present the evolutions of the droplets for $Ca = 0.40$ ($\tau_0 = 2.5$) and $Ca = 0.42$ ($\tau_0 = 2.3810$). When $Ca = 0.4$, i.e. the left columns of Figure 7.13, the droplet maintains a steady shape in the shear flow. Oppositely, when $Ca = 0.42$, the droplet does not keep a steady shape and breaks up. Hence we predict the numerical critical capillary number to be between 0.40 and 0.42, which is in accordance with the theoretical prediction and the results in [51]. Hence our numerical solver is capable of accurately simulating droplet breakup processes.

7.4.2. Influence of surfactants

We choose $r = 1.0$, $L_x = 12$, $L_y = L_z = 4$, $Re = 0.4$ and $Ca = 0.42$ as in [85]. From the definition of Re , we obtain the values of the densities $\rho_1 = \rho_2 = Re \mu_2 / (|\dot{\gamma}| r^2) = 0.4$. From the definition of Ca , we obtain $\tau_0 = \mu_2 |\dot{\gamma}| r / Ca = 2.3810$. The Langmuir model (2.39) is used to describe the effect of the surfactants on the surface tension coefficient. We scale the Langmuir model as follows

$$\frac{\tau(S)}{\tau_0} = 1 + \frac{RTS_\infty}{\tau_0} \ln\left(1 - \frac{S^* S}{S_\infty S^*}\right) =: 1 + \beta \ln\left(1 - \chi \frac{S}{S^*}\right),$$

where $\beta := RTS_\infty/\tau_0$, $\chi := S^*/S_\infty$, and S^* is the initial uniform surfactant concentration. In [85], the authors chose $\beta = 0.2$ and $\chi = 0.1$. With $T = 300$ and $\tau_0 = 2.3810$, we obtain $S_\infty = 1.9091 \times 10^{-4}$ and $S^* = 0.1S_\infty = 1.9091 \times 10^{-5}$. The surface Péclet number $Pe := |\dot{\gamma}| r^2 / D_\Gamma$ is chosen to be 10. Hence we obtain $D_\Gamma = 0.1$. We solve the two-phase Navier-Stokes equations (7.2) with interface conditions (7.3),(7.4). On $\Gamma(t)$, the convection-diffusion equation (7.5) is solved with the space-time trace finite element

7. Simulation of flows with surfactants

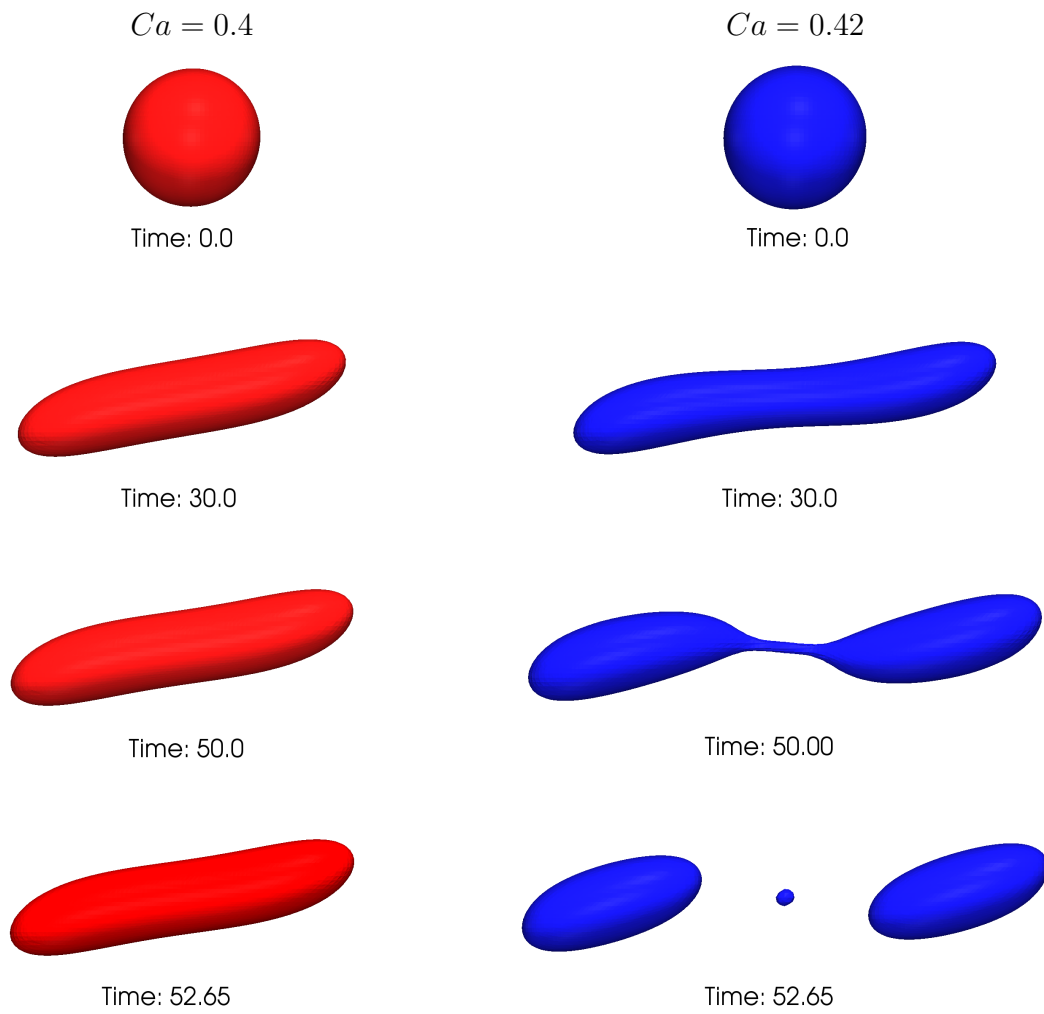


Figure 7.13.: Evolution of a clean droplet for $Ca = 0.4$ (left) and $Ca = 0.42$ (right). The corresponding surface tension coefficients are $\tau_0 = 2.5$ (left) and $\tau_0 = 2.3810$ (right).

method. The coupling between the fluid dynamics and the surfactant transport is treated with the Gauss-Seidel type of method, cf. section 4.4.

The mesh is constructed as follows: the rectangular box is first divided into $12 \times 4 \times 4$ equal-sized cubes, each cube is then divided into 6 tetrahedra. Next to the interface, the mesh is adaptively refined three times. We choose the time step size to be 0.05.

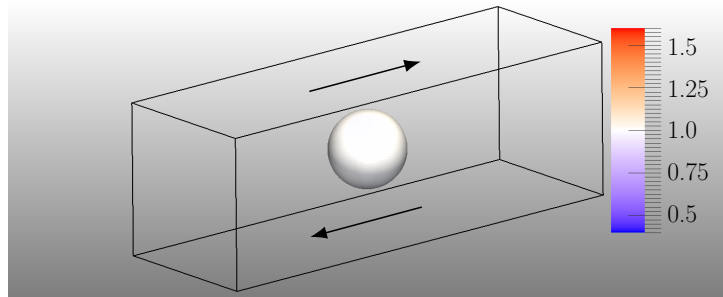
In Figure 7.14, the evolution of the droplet shape and the surfactant concentration are presented. We achieve a very similar result as Figure 7.13 in [85]. From $t = 0$ to $t = 20$ s, we can observe an initial stretching phase. After that, necks are formed near the two ends of the droplet, cf. $t = 30$ s. The necks are getting thinner, cf. $t = 37$ s, and the droplet finally breaks up at $t = 37.5$ s. We observe three satellite droplets on each side after the breakup. The surfactant concentration is also very similar to the result in [85], e.g. the high concentrations on both ends of the three big droplets after the breakup, cf. $t = 38.5$ s and $t = 40$ s. We also compare the breakup behavior of the surfactant covered droplet to the clean droplet, which is illustrated in Figure 7.16. We observe that the surfactant covered droplet deforms more than the clean droplet and breaks up earlier. At $t = 37.5$ s, the surfactant covered droplet (the red filled droplet in Figure 7.16) has already broken up, and the clean droplet (the droplet with blue line) is still connected. The reason for the early breakup is the reduced surface tension coefficient $\tau(S)$ compared to τ_0 , cf. the right columns of Figure 7.16. The surfactant gathers at the necks before the breakup, cf. $t = 37$ s in Figure 7.14, which results in a smaller surface tension coefficient, cf. $t = 37$ s in the right columns of Figure 7.16. It has also been reported in [85] that the surfactant covered droplet breaks up earlier than the clean droplet. We summarize the breakup time in Table 7.7. In conclusion, we achieve a good agreement with the results presented in [85].

Cases	breakup time
clean	37.8 s
with surfactant	37.5 s

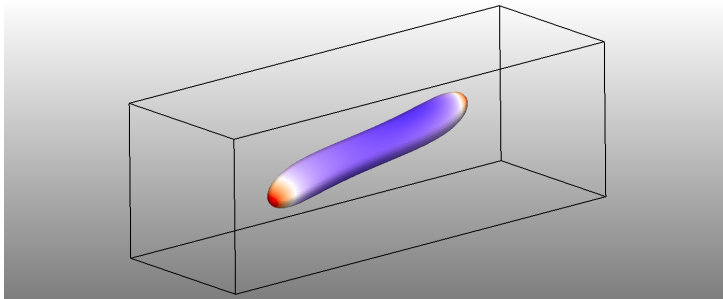
Table 7.7.: Breakup time of a clean droplet and the surfactant contaminated droplet.

7. Simulation of flows with surfactants

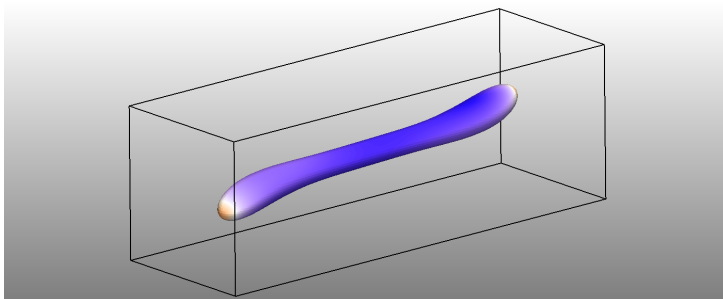
Figure 7.14.: Evolution of a droplet with surfactants for $Ca = 0.42$ and $Re = 0.4$. The droplet is uniformly covered with surfactant at the initial time. Shown is the scaled surfactant concentration S/S^* with $S^* := S(0)$.



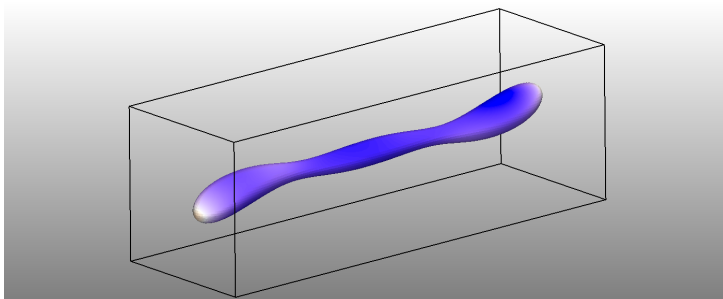
(a) $t = 0$



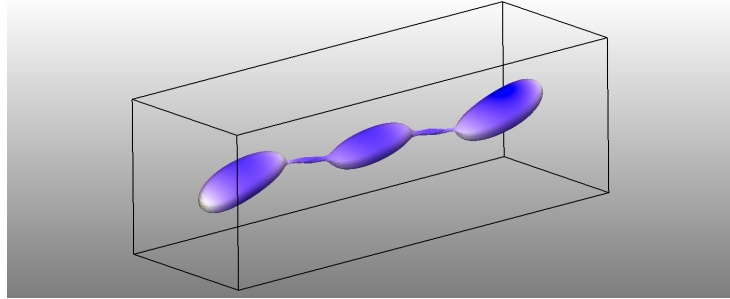
(b) $t = 10$ s



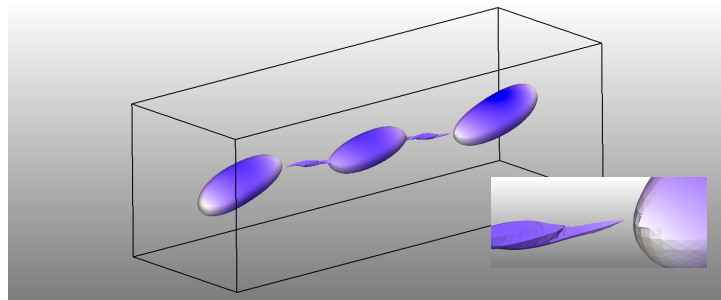
(c) $t = 20$ s



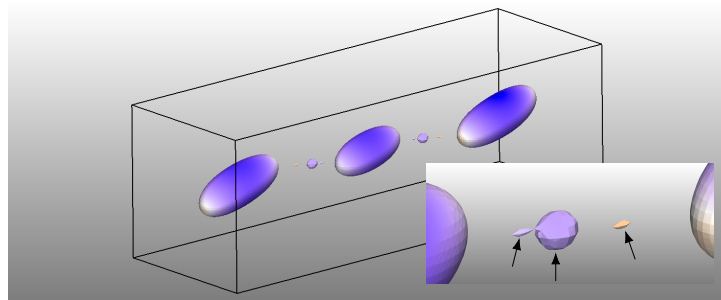
(d) $t = 30$ s



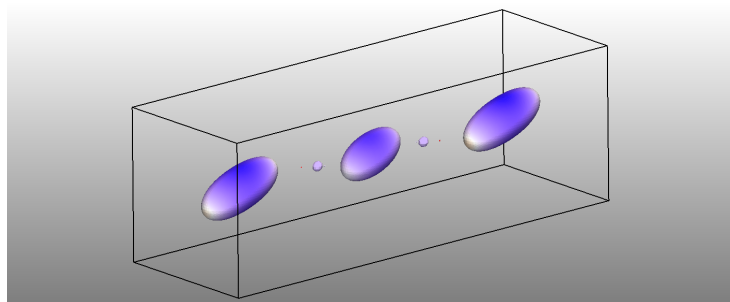
(e) $t = 37 \text{ s}$



(f) $t = 37.5 \text{ s}$



(g) $t = 38.5 \text{ s}$



(h) $t = 40 \text{ s}$

7. Simulation of flows with surfactants

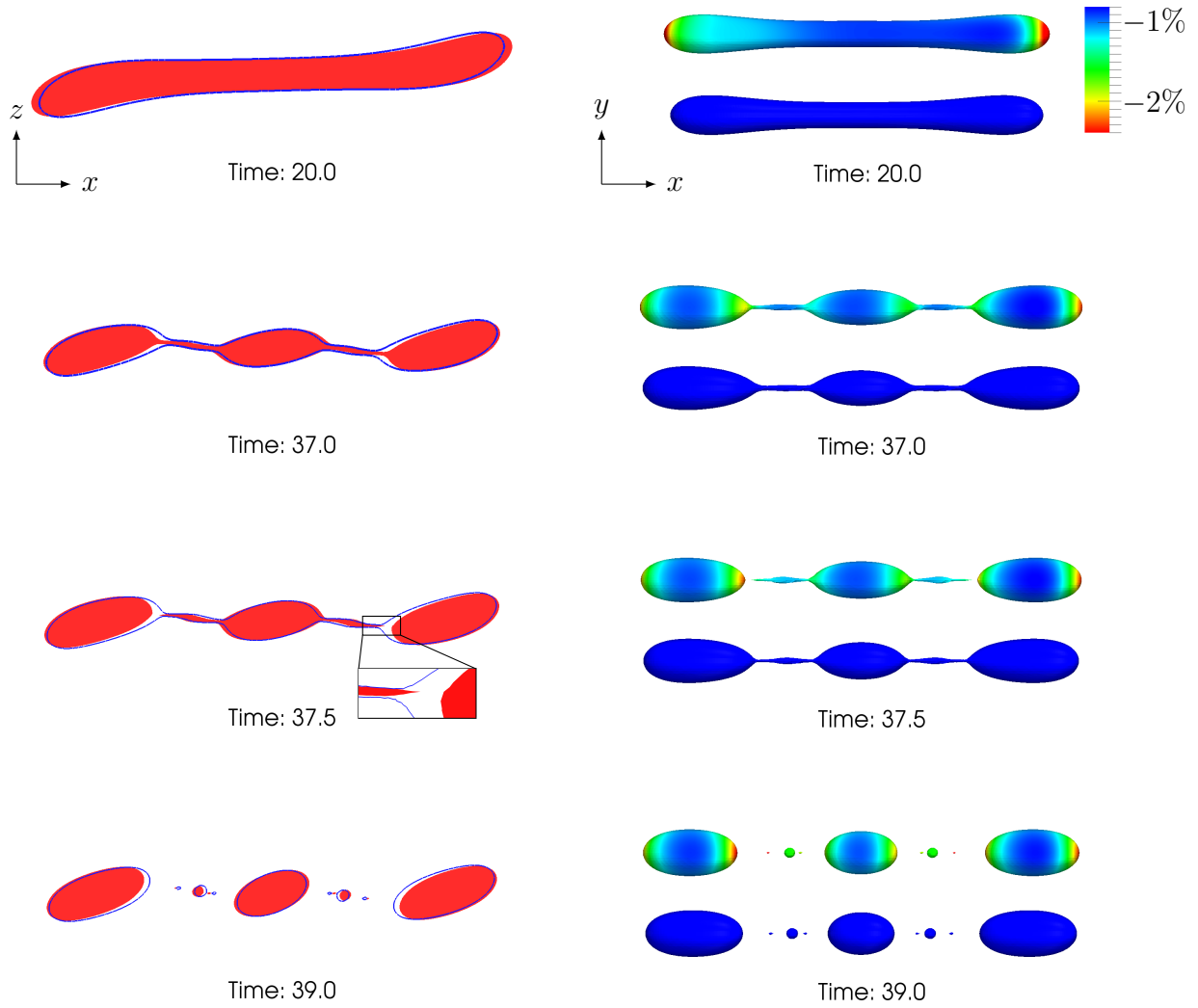


Figure 7.16.: Comparison between a surfactant covered droplet and a clean droplet. The left column shows the droplets in x/z cutting plane. The red filled shape is the surfactant covered droplet, and the blue line represents the clean droplet. The right column shows the droplets in x/y plane (looking from above). On the surfactant covered droplet, the relative difference between $\tau(S)$ and τ_0 is presented, i.e. $(\tau(S) - \tau_0)/\tau_0$. The blue one is the clean droplet.

8. Discussion and outlook

In this thesis, we perform numerical simulations of two-phase flows with complex interfaces. We develop and implement numerical methods for three specific classes of flows with complex interfaces: interfaces with surface tension gradients (Marangoni effects), viscous interfaces according to the Boussinesq-Scriven law and interfaces with insoluble surfactants. We focus on the influence of complex interfaces on fluid dynamics by investigating the motion of a droplet with the aforementioned complex interfaces in a surrounding fluid. A systematic validation methodology is adopted to study the accuracy of the numerical solver.

We use a sharp interface model for two-phase flows. The derivation of this model is based on mass and momentum conservation of a two-phase body containing an interface. At the interface, the jump of bulk phase Cauchy stresses is balanced by interfacial forces. The most important interfacial force is the surface tension force, which accounts for the spherical shape of an undisturbed droplet in a surrounding fluid. Other phenomena occur at the interface and change the dynamic properties of droplets. In this thesis, we adopt a unified approach to model these complex interfaces, i.e. via proper modeling of the surface stress tensor $\boldsymbol{\sigma}_\Gamma$. $\boldsymbol{\sigma}_\Gamma$ is the two dimensional analogon of the Cauchy stress tensor. The advantage of this approach is the straightforward extension to another type of interfacial forces. The surfactant transport on the interface is modeled by a convection-diffusion equation.

We use the DROPS package to simulate two-phase flows with complex interfaces. A level set method is used to capture the position of the interface. Quadratic finite elements combined with a streamline diffusion stabilization are used to discretize the level set function. The level set method is not volume preserving. We preserve the volume of the droplet by a level set function shifting technique. In numerical simulations, the level set function needs to be reinitialized from time to time, such that the (approximate) distance function property is maintained. The discrete interface is constructed by linear interpolation of the quadratic level set function on a once refined grid. Hence the interface is cutting through the tetrahedral mesh, i.e. the mesh is not aligned with the interface. We use continuous quadratic finite elements to discretize the velocity unknowns and an extended finite element method (XFEM) to discretize the discontinuous pressure. The XFEM method increases the approximation accuracy (in L^2 -norm) of the linear continuous finite element method from $\mathcal{O}(\sqrt{h})$ to $\mathcal{O}(h^2)$ for the discontinuous pressure. The surface force functional is integrated at the discrete interface. By deriving the surface normals from the discrete level set function, we increase the approximation quality of the discrete surface force functional. Implicit time discretization schemes are needed due to the strongly non-linear surface force term and the stiffness of the Navier-Stokes equations. We treat the following coupling issues: the coupling between Navier-Stokes equations and the level set function, the coupling between two-phase flows and the surfactant transport. We apply

a Gauss-Seidel type iterative method to decouple the two-phase Navier-Stokes equations and the level set equation. A convergence acceleration technique based on extrapolation of the surface force functional greatly increases the efficiency of the decoupling scheme. The surfactant transport on the interface is treated with a space-time trace finite element method. In this method, the surface quantities are represented by traces of finite elements on the volumetric mesh. The advantage of this method is that we can solve (bulk) fluid dynamics and the surface transport equation with the same finite elements, and it is relatively simple to couple the two sets of equations. This method can also handle topological changes, e.g. the droplets break up or collide.

We apply a systematic validation method to test the accuracy of the numerical methods. We consider the classical theoretical analysis of the motion of a droplet with complex interfaces, which rely on perturbation analysis and certain assumptions, e.g. *infinite domain, spherical shape, small deformation and creeping flow conditions*. By constructing benchmark problems, in which theoretical analysis can be considered valid, we compare numerical results with theoretical predictions.

We obtain the following main conclusions and results:

- By numerical treatment of the surface stress tensor, we achieve an efficient and unified approach to handle the above mentioned three classes of flows with complex interfaces. When handling interfaces with variable surface tension force, which characterizes Marangoni effects and the influence of surfactants, the standard approach is to consider the surface force functional

$$f_{\Gamma}^{var}(\mathbf{v}) = \int_{\Gamma} -\tau\kappa\mathbf{n} \cdot \mathbf{v} + \nabla_{\Gamma}\tau \cdot \mathbf{v} ds,$$

which requires the numerical treatment of the mean curvature κ , e.g. through the Laplace-Beltrami characterization, and the surface tension gradient $\nabla_{\Gamma}\tau$. By introducing the surface stress tensor $\boldsymbol{\sigma}_{\Gamma} = \tau\mathbf{P}$, the surface force functional is represented as

$$f_{\Gamma}(\mathbf{v}) = \int_{\Gamma} \operatorname{div}_{\Gamma} \boldsymbol{\sigma}_{\Gamma} \cdot \mathbf{v} ds = - \int_{\Gamma} \operatorname{tr} (\tau\mathbf{P}(\nabla_{\Gamma}\mathbf{v})^T) ds.$$

The task is now the numerical treatment of the projection operator \mathbf{P} . In chapter 4, we showed that by using information from the discrete level set function a better approximation of the projection operator \mathbf{P} is obtained, and thus a higher order approximation of the surface force functional is achieved.

- In all three classes of interfaces, we achieve very good agreements with theoretical predictions.
 - In the case of flows with Marangoni effects, we investigate the motion of an initially spherical droplet with constant Marangoni forces, i.e. constant surface tension gradients on the interface. The droplet and the surrounding flow is initially at rest. No volume force, e.g. gravity, is present. Zero velocity conditions are applied at all boundaries. The motion of the droplet is induced purely by Marangoni forces. Two stages of the droplet motion are observed in the simulations, namely an initial fast acceleration stage and a quasistatic stage, cf. Figure 5.4. In the fast acceleration stage, we compare numerical accelerations of the droplet with theoretical predictions, cf. (5.26). The relative errors between these are less than 5% above level 3 refinement, and good

agreements are achieved for a large range of density ratios, cf. Figure 5.6. In the quasistatic stage, the numerical migration velocity of the droplet oscillates around a constant value, cf. Figure 5.4. We calculate a time averaged migration velocity and compare this quantity with theoretical migration velocity, cf. (5.21). For the choice of parameters, the relative errors between these are less than 2.5% above level 3 refinement for a range of magnitudes of Marangoni forces, cf. Table 5.3. The spherical shape of the droplet is maintained in the simulations, cf. Figure 5.10, which is in good agreement with the normal stress balance condition, cf. Remark 5.2.1.

- In the case of flows with viscous interfaces, we investigate the motion of an initially spherical droplet with surface viscous forces in a Poiseuille flow. Due to the surface viscous forces, the droplet moves at a speed, which is slower than the speed of a clean droplet. In numerical simulations, we observe that the migration velocity of the droplet oscillates around a constant value after an initial relaxation time, cf. Figure 6.5. We calculate a time averaged numerical migration velocity and compare this quantity with theoretical predictions (6.13). The relative errors between these are less than 3% above refinement level 4. Concerning the parameter dependence of the migration velocity on the Bo^d number, we test droplets with two different viscosity ratios over a range of Bo^d numbers and achieve good agreements in both cases, cf. Figure 6.7. We also validated the theoretical prediction that the migration velocity is indifferent to changes in the surface shear viscous force, cf. Table 6.2.
- In the case of flows with insoluble surfactants, we consider the deformation and breakup of droplets in shear flows. There exists a critical capillary number, above which the droplet in a shear flow can not maintain a static (elliptic) shape and breaks up. We study the static shape of a droplet with insoluble surfactants in an axi-symmetric extensional flow, i.e. the capillary number is *below* the critical number. We compare the lengths of the two axes of the droplet with theoretical predictions, cf. (7.19). The relative errors between these are very small for $Ca^* = 0.005$, namely less than 0.1% above level 4 refinements. The relative errors are larger for $Ca^* = 0.05$, cf. Table 7.4. This difference is getting larger for increasing Ca^* , cf. Figure 7.11. The reason is that the theoretical prediction is a first order approximation in Ca^* , and only valid for small values of the capillary number. A higher order theoretical prediction, as in the clean interface case (7.14) and Figure 7.4, is not known in the literature. We also compare the surfactant concentration on the deformed droplet with theoretical predictions. Very good agreements have been achieved, cf. Figure 7.10. To study the breakup behavior of a droplet with insoluble surfactants, we investigate the deformation of a droplet in a simple shear flow with capillary numbers which are *above* the critical number. Due to the existence of the surfactants, the droplet breaks up earlier than a clean droplet, cf. Figure 7.16. The evolution of the droplet and the surfactant concentration are presented in Figure 7.14. Qualitative agreements have been achieved with another recent numerical simulation study [85].

- With respect to the iterative solvers, we mention the following results and conclu-

sions. The combination of the Broyden method and the prediction of surface forces greatly accelerates the convergence behavior of the Gauss-Seidel type decoupling scheme between Navier-Stokes equations and the level set equation, cf. Table 4.1. The magnitude of the surface shear viscous force has a very significant influence on the convergence behavior of the aforementioned decoupling scheme, cf. Table 4.2 and Figure 4.6. The Gauss-Seidel type of decoupling scheme is crucial for obtaining accurate numerical results, cf. Table 5.2. The reparametrization of the level set function is needed for the accurate approximation of the zero level, but it also introduces perturbations to the system. Concerning the quantity of interest, e.g. the migration velocity or the length of the axes of the droplet, the magnitude of perturbations induced by the reparametrization method decreases for finer grids, cf. Figure 5.4 and Figure 7.6. The problem size of the surfactant equation with the trace finite element method is much smaller than the (bulk) fluid dynamics, cf. Table 7.5, which reflects the two-dimensional nature of the method. The calculation of the surfactant equation takes a small portion (less than 10%) of the overall simulation time.

- For two-phase flows with complex interfaces, experimental techniques are limited to the measurement of average quantities [48], e.g. the average surface tension coefficient with the existence of surfactants. Numerical simulations provide detailed insights in the dynamic processes of such problems. The DROPS package has been validated with experimental studies with realistic parameters [12, 54].

We list a few problems that are of interest for future research.

- Treatment of viscoelastic interface. In [76], the author applied the extended irreversible thermodynamics approach to derive a model for a viscoelastic interface. The model is a tangential differential equation of the surface stress tensor posed on the interface. We define a surface extra stress tensor $\boldsymbol{\sigma}_\Gamma^s := \boldsymbol{\sigma}_\Gamma - \tau \mathbf{P} \in \mathbb{R}^{3 \times 3}$, and define the symmetric traceless part of $\boldsymbol{\sigma}_\Gamma^s$ by $\overline{\boldsymbol{\sigma}_\Gamma^s} = \boldsymbol{\sigma}_\Gamma^s - \frac{1}{2} \text{tr}(\boldsymbol{\sigma}_\Gamma^s) \mathbf{P}$. The model is a Maxwell type of material model: on $\Gamma(t)$ the following holds

$$\begin{aligned} \overline{\boldsymbol{\sigma}_\Gamma^s} &= \mu_\Gamma \overline{\mathbf{D}_\Gamma} - \tau_s \frac{d_s}{dt} \overline{\boldsymbol{\sigma}_\Gamma^s} \\ \text{tr}(\boldsymbol{\sigma}_\Gamma^s) &= \lambda_\Gamma \text{tr}(\mathbf{D}_\Gamma) - \tau_d \frac{d_s}{dt} \text{tr}(\boldsymbol{\sigma}_\Gamma^s) \\ \boldsymbol{\sigma}_\Gamma^s \cdot \mathbf{n} &= 0 \end{aligned}$$

where $\overline{\mathbf{D}_\Gamma} := \mathbf{D}_\Gamma - \frac{1}{2} \text{tr}(\mathbf{D}_\Gamma) \mathbf{P}$ is the symmetric traceless part of the surface rate of deformation tensor $\mathbf{D}_\Gamma(\mathbf{u})$, μ_Γ and λ_Γ are the surface shear and dilatational viscosity, τ_s and τ_d are the surface shear and dilatational relaxation time, $\frac{d_s}{dt}$ is the surface material derivative. As mentioned in section 2.4, the rank of $\boldsymbol{\sigma}_\Gamma$ is less than or equals to 2. It is not clear how to solve such a tangential differential equation on a manifold.

- Ad/de-sorption processes of surfactants on the interface. In order to treat such processes, the bulk phase mass transport has to be coupled with the surfactant equation on the interface through special flux conditions.
- Currently the grid is refined/coarsened according to the position of the interface. This is sufficient if we consider primarily spherical droplets. For a complex problem,

e.g. the break up of droplets in section 7.4, a more advanced refinement strategy is desirable, e.g. a curvature based refinement strategy. Error estimators with respect to the surface force functional can also be applied to mark refinement regions.

- An open problem related to the space-time trace FEM for the surfactant equation is the efficient iterative solution of the resulting linear system.
- An adaptive time stepping method may be considered. Two factors need to be taken into account: errors in time discretization and the convergence behavior of the Gauss-Seidel type decoupling scheme, i.e. a larger time step leads to a slower convergence of the decoupling scheme.
- The linear system resulting from the two-phase Navier-Stokes equations (3.25) is solved with a preconditioned Generalized Conjugate Residual (GCR) method with block conditioners. The linear system has the following structure

$$\begin{pmatrix} \mathbf{A} & \mathbf{B}^T \\ \mathbf{B} & 0 \end{pmatrix} \begin{pmatrix} \mathbf{v} \\ \mathbf{q} \end{pmatrix} = \begin{pmatrix} \mathbf{b}_1 \\ \mathbf{b}_2 \end{pmatrix},$$

where \mathbf{A} corresponds to the combination of the mass matrix, the stiffness matrix and the convection term, \mathbf{B} corresponds to the discretized divergence operator, \mathbf{v} and \mathbf{q} are the velocity and the pressure unknowns. The block conditioner can be written by

$$\mathbf{P} = \begin{pmatrix} \mathbf{Q}_A & 0 \\ \mathbf{B} & -\mathbf{Q}_S \end{pmatrix},$$

where \mathbf{Q}_A is the preconditioner of the \mathbf{A} block and \mathbf{Q}_S is the preconditioner of the Schur complement $\mathbf{S} := \mathbf{B}\mathbf{A}^{-1}\mathbf{B}^T$. We generally use one multigrid V-cycle for \mathbf{Q}_A . The task of choosing an optimal \mathbf{Q}_S turns out to be a very difficult one. In the numerical experiments, we usually choose between two types of preconditioners: the so-called BFB^T -preconditioner [29] and the SIMPLER [87]. We observe that SIMPLER often results in a faster convergence of the GCR iteration, but it is not robust. Improved preconditioners should be developed.

Appendices

A. Appendix

A.1. Partial integration rules for a surface

We assume the surface $\Gamma \subset \mathbb{R}^d$ is an oriented C^2 -hypersurface. We use W to denote an open neighbourhood of Γ , i.e. $\Gamma \subset W$. There exists a C^1 -vector field $\mathbf{n} : W \rightarrow \mathbb{R}^d$ with the property that $\mathbf{n}(\mathbf{x}) \perp T_{\mathbf{x}}\Gamma$ and $\|\mathbf{n}(\mathbf{x})\|_2 = 1$ for $\mathbf{x} \in \Gamma$. The tangential gradient of a C^1 -function $f : W \rightarrow \mathbb{R}$ is defined by

$$\nabla_{\Gamma} f(\mathbf{x}) := \left(\mathbf{I} - \mathbf{n}(\mathbf{x})\mathbf{n}(\mathbf{x})^T \right) \nabla f(\mathbf{x}) =: \mathbf{P}(\mathbf{x})\nabla f(\mathbf{x}), \quad \mathbf{x} \in \Gamma,$$

where $\mathbf{P}(\mathbf{x}) := \mathbf{I} - \mathbf{n}(\mathbf{x})\mathbf{n}(\mathbf{x})^T$ is the orthogonal projection from \mathbb{R}^d onto $T_{\mathbf{x}}\Gamma$.

We consider an open bounded domain $\Omega \in \mathbb{R}^d$, which contains two subdomains denoted by Ω_1 and Ω_2 with $\bar{\Omega} = \bar{\Omega}_1 \cup \bar{\Omega}_2$ and $\Omega_1 \cap \Omega_2 = \emptyset$. The interface is denoted by $\Gamma = \bar{\Omega}_1 \cap \bar{\Omega}_2$. Both of the two subdomains are connected, and Ω_1 will not touch the outer boundary, i.e. $\partial\Omega_1 \cap \partial\Omega = \emptyset$. The orientation of the normal field $\mathbf{n}(\mathbf{x})$ for $\mathbf{x} \in \Gamma$ is pointing from Ω_1 to Ω_2 . The mean curvature of Γ is given by

$$\kappa = \operatorname{div}_{\Gamma} \mathbf{n}.$$

If Ω_1 is a sphere with a radius R , then the mean curvature of Γ is given by $\kappa = 2/R$.

The following identities hold for $c \in C^1(W)$ and $\mathbf{b} \in C^1(W)^d$:

$$\nabla(c\mathbf{b}) = c\nabla\mathbf{b} + \mathbf{b}(\nabla c)^T, \tag{A.1}$$

$$\operatorname{div}_{\Gamma}(c\mathbf{b}) = c\operatorname{div}_{\Gamma}\mathbf{b} + \operatorname{tr}\left(\mathbf{P}\mathbf{b}(\nabla c)^T\right). \tag{A.2}$$

The proof of the first identity (A.1) is trivial. The second identity (A.2) is easily shown as follows

$$\begin{aligned} \operatorname{div}_{\Gamma}(c\mathbf{b}) &= \operatorname{tr}(\nabla_{\Gamma}(c\mathbf{b})) = \operatorname{tr}(\mathbf{P}\nabla(c\mathbf{b})) \stackrel{(A.1)}{=} \operatorname{tr}\left(c\mathbf{P}\nabla\mathbf{b} + \mathbf{P}\mathbf{b}(\nabla c)^T\right) \\ &= c\operatorname{div}_{\Gamma}\mathbf{b} + \operatorname{tr}\left(\mathbf{P}\mathbf{b}(\nabla c)^T\right), \end{aligned}$$

which is the identity (A.2).

Applying (A.2) and noting $\mathbf{P}\mathbf{n} = 0$, we obtain

$$\operatorname{div}_{\Gamma}(c\mathbf{n}) = c\operatorname{div}_{\Gamma}\mathbf{n} + \operatorname{tr}\left(\mathbf{P}\mathbf{n}(\nabla c)^T\right) = c\operatorname{div}_{\Gamma}\mathbf{n} = c\kappa. \tag{A.3}$$

A. Appendix

Noting that $\mathbf{P} = \mathbf{I} - \mathbf{n}\mathbf{n}^T$, we obtain

$$\operatorname{div}_\Gamma(c\mathbf{P}) = \operatorname{div}_\Gamma(c\mathbf{I} - c\mathbf{n}\mathbf{n}^T) = \operatorname{div}_\Gamma(c\mathbf{I}) - \begin{pmatrix} \operatorname{div}_\Gamma(c n_1 \mathbf{n}^T) \\ \dots \\ \operatorname{div}_\Gamma(c n_d \mathbf{n}^T) \end{pmatrix}.$$

It is simple to show that $\operatorname{div}_\Gamma(c\mathbf{I}) = \nabla_\Gamma c$. Applying (A.3), we obtain

$$\operatorname{div}_\Gamma(c\mathbf{P}) = \nabla_\Gamma c - c\kappa\mathbf{n}. \quad (\text{A.4})$$

If c is a constant, then $\operatorname{div}_\Gamma(c\mathbf{P}) = c \operatorname{div}_\Gamma \mathbf{P} = -c\kappa\mathbf{n}$.

We consider an open subset $\gamma \subset \Gamma$ with boundary $\partial\gamma$. The normal to $\partial\gamma$ in the tangent plane $T_x\gamma$ is denoted by $\boldsymbol{\xi}$. The partial integration rule holds for $f \in C^1(U)$ with $i \in \{1, 2, \dots, d\}$ [25, 39]:

$$\int_\gamma (\nabla_\Gamma)_i f \, ds = \int_\gamma f \kappa n_i \, ds + \int_{\partial\gamma} f \xi_i \, dl, \quad (\text{A.5})$$

where n_i and ξ_i are the i -th component of \mathbf{n} and $\boldsymbol{\xi}$ respectively.

From (A.5), we obtain the following rules:

$$\int_\gamma \nabla_\Gamma f \, ds = \int_\gamma f \kappa \mathbf{n} \, ds + \int_{\partial\gamma} f \boldsymbol{\xi} \, dl. \quad (\text{A.6})$$

For a second order tensor \mathbf{M} , each element of which belongs to $C^1(U)$, we write it as a matrix, then the following rule holds

$$\int_\gamma \operatorname{div}_\Gamma \mathbf{M} \, ds = \int_\gamma \kappa \mathbf{M}\mathbf{n} \, ds + \int_{\partial\gamma} \mathbf{M}\boldsymbol{\xi} \, dl. \quad (\text{A.7})$$

If Γ is the boundary of an open bounded set $\Omega \subset \mathbb{R}^d$, i.e. Γ has no boundary. The partial integration rule (A.5) becomes

$$\int_\Gamma (\nabla_\Gamma)_i f \, ds = \int_\Gamma f \kappa n_i \, ds. \quad (\text{A.8})$$

For a vector function $\mathbf{g} \in H^1(U)^d$, we obtain the following property by inserting $f g_i$ into (A.8):

$$\int_\Gamma f \operatorname{div}_\Gamma \mathbf{g} + \mathbf{g} \cdot \nabla_\Gamma f \, ds = \int_\Gamma f \kappa \mathbf{g} \cdot \mathbf{n} \, ds. \quad (\text{A.9})$$

Now we consider a matrix \mathbf{G} , and each row of \mathbf{G} belongs to $H^1(U)^d$, then the following rule holds

$$\int_\Gamma \mathbf{f} \cdot \operatorname{div}_\Gamma \mathbf{G} \, ds = - \int_\Gamma \operatorname{tr}(\mathbf{G}(\nabla_\Gamma \mathbf{f})^T) \, ds + \int_\Gamma \kappa \mathbf{G}\mathbf{n} \cdot \mathbf{f} \, ds, \quad \mathbf{f} \in H^1(U)^d. \quad (\text{A.10})$$

If we further assume that $\mathbf{G}\mathbf{P} = \mathbf{G}$, then equation (A.10) can be simplified by utilizing $\mathbf{P}\mathbf{n} = 0$:

$$\int_\Gamma \mathbf{f} \cdot \operatorname{div}_\Gamma(\mathbf{G}\mathbf{P}) \, ds = - \int_\Gamma \operatorname{tr}(\mathbf{G}\mathbf{P}(\nabla_\Gamma \mathbf{f})^T) \, ds, \quad \mathbf{f} \in H^1(U)^d. \quad (\text{A.11})$$

In component-wise form the right hand side of (A.11) is given by

$$\int_\Gamma \operatorname{tr}(\mathbf{G}\mathbf{P}(\nabla_\Gamma \mathbf{f})^T) \, ds = \int_\Gamma \operatorname{tr}(\mathbf{G}(\nabla_\Gamma \mathbf{f})^T) \, ds = \sum_{i=1}^d \int_\Gamma (\mathbf{e}_i^T \mathbf{G}) \cdot \nabla_\Gamma f_i \, ds, \quad (\text{A.12})$$

where \mathbf{e}_i is the standard basis.

Bibliography

- [1] Drops package for simulation of two-phase flows.
<http://www.igpm.rwth-aachen.de/DROPS/>.
- [2] S. Aland, J. Lowengrub, and A. Voigt. A continuum model of colloid stabilized interfaces. *Physics of Fluids*, 23:062103, 2011.
- [3] L. Antanovskii and B. Kopbosynov. Nonstationary thermocapillary drift of a drop of viscous liquid. *Journal of Applied Mechanics and Technical Physics*, 27(2):208–213, 1986.
- [4] R. Balasubramaniam and A. Chai. Thermocapillary migration of droplets: An exact solution for small marangoni numbers. *Journal of Colloid and Interface Science*, 119(2):531 – 538, 1987.
- [5] R. Balasubramaniam and R. Subramanian. The migration of a drop in a uniform temperature gradient at large marangoni numbers. *Physics of Fluids*, 12(4):733–743, 2000.
- [6] E. Bänsch. Finite element discretization of the Navier-Stokes equations with a free capillary surface. *Numerische Mathematik*, 88:203–235, 2001.
- [7] D. Barthès-Biesel and A. Acrivos. Deformation and burst of a liquid droplet freely suspended in a linear shear field. *Journal of Fluid Mechanics*, 61:1–22, 1973.
- [8] G. K. Batchelor. *An Introduction to Fluid Dynamics*. Cambridge University Press, 2000.
- [9] I. B. Bazhlekov. *Non-singular boundary-integral method for deformable drops in viscous flow*. PhD thesis, Technical University Eindhoven, 2003.
- [10] I. B. Bazhlekov, P. D. Anderson, and H. E. Meijer. Numerical investigation of the effect of insoluble surfactants on drop deformation and breakup in simple shear flow. *Journal of Colloid and Interface Science*, 298(1):369 – 394, 2006.
- [11] T. Belytschko, N. Moës, S. Usui, and C. Parimi. Arbitrary discontinuities in finite elements. *International Journal for Numerical Methods in Engineering*, 50(4):993–1013, 2001.
- [12] E. Bertakis, S. Groß, J. Grande, O. Fortmeier, A. Reusken, and A. Pfennig. Validated simulation of droplet sedimentation with finite-element and level-set methods. *Chemical Eng. Science*, 65:2037–2051, 2010.
- [13] B. Binks and T. Horozov. *Colloidal Particles at Liquid Interfaces*. Cambridge University Press, Cambridge, 2006.

Bibliography

- [14] D. Bothe, J. Prüss, and G. Simonett. Well-posedness of a two-phase flow with soluble surfactant. In H. Brezis, M. Chipot, and J. Escher, editors, *Nonlinear Elliptic and Parabolic Problems*, volume 64 of *Progress in Nonlinear Differential Equations and Their Applications*, pages 37–61. Birkhäuser, Basel, 2005.
- [15] J. Brackbill, D. Kothe, and C. Zemach. A continuum method for modeling surface tension. *Journal of Computational Physics*, 100:335–354, 1992.
- [16] P. T. Brady, M. Herrmann, and J. M. Lopez. Confined thermocapillary motion of a three-dimensional deformable drop. *Physics of Fluids*, 23(2), 2011.
- [17] D. Braess. *Finite elements-Theory, fast solvers, and applications in solid mechanics*. Cambridge University Press, Cambridge, third edition, 2007.
- [18] J. Cahn and J. Hilliard. Free energy of a nonuniform system. I. interfacial free energy. *J. Chem. Phys.*, 28:688–699, 1958.
- [19] Y. Chang, T. Hou, B. Merriman, and S. Osher. A level set formulation of Eulerian interface capturing methods for incompressible fluid flows. *Journal of Computational Physics*, 124(2):449 – 464, 1996.
- [20] J. Chen and K. Stebe. Surfactant-induced retardation of the thermocapillary migration of a droplet. *Journal of Fluid Mechanics*, 340:35–59, June 1997.
- [21] A. J. Chorin and J. E. Marsden. *A Mathematical Introduction to Fluid Mechanics, Third Edition*, volume 4 of *Texts in Applied Mathematics*. Springer-Verlag New York, 1993.
- [22] R. Clift, J. Grace, and M. Weber. *Bubbles, Drops and Particles*. Academic Press, New York, London, 1978.
- [23] J. Donea and A. Huerta. *Finite Element Methods for Flow Problems*. Finite Element Methods for Flow Problems. John Wiley & Sons, 2003.
- [24] G. Dziuk. An algorithm for evolutionary surfaces. *Numerische Mathematik*, 58:603–611, 1991.
- [25] G. Dziuk and C. M. Elliott. Finite elements on evolving surfaces. *IMA Journal of Numerical Analysis*, 27(2):262–292, 2007.
- [26] D. Edwards, H. Brenner, and D. Wasan. *Interfacial Transport Phenomena and Rheology*. Butterworth-Heinemann, Boston, 1991.
- [27] C. D. Eggleton, Y. P. Pawar, and K. J. Stebe. Insoluble surfactants on a drop in an extensional flow: a generalization of the stagnated surface limit to deforming interfaces. *J. Fluid Mech.*, 385:79–99, 1999.
- [28] M. Ehmann, G. Wozniak, and J. Siekmann. Numerical analysis of the thermocapillary migration of a fluid particle under zero-gravity. *ZAMM - Journal of Applied Mathematics and Mechanics / Zeitschrift für Angewandte Mathematik und Mechanik*, 72(8):347–358, 1992.
- [29] H. Elman, V. Howle, J. Shadid, R. Shuttleworth, and R. Tuminaro. Block precon-

- ditioners based on approximate commutators. *SIAM J. on Scientific Computing*, 27:1651–1668, 2006.
- [30] G. Fix. Phase field methods for free boundary problems. In A. Fasano and M. Primicerio, editors, *Free boundary problems: theory and applications*, Research notes in mathematics, pages 580–589. Pitman Advanced Pub. Program, Boston, 1983.
- [31] J. Gibbs. *The collected works of J.W. Gibbs*. Longmans, Green and Co., New York, 1928.
- [32] J. Grande. Eulerian finite element methods for parabolic equations on moving surfaces. *SIAM J. on Scientific Computing*, 36(2):B248–B271, 2014.
- [33] J. Grande. Finite element discretization error analysis of a general interfacial stress functional. *SIAM J. on Numerical Analysis*, 53(3):1236–1255, 2015.
- [34] J. Grande and A. Reusken. A higher order finite element method for partial differential equations on surfaces. IGPM report 403, RWTH-Aachen University, 2014.
- [35] S. Groß. *Numerical methods for three-dimensional incompressible two-phase flows*. Phd thesis, RWTH Aachen University, 2008.
- [36] S. Gross, M. A. Olshanskii, and A. Reusken. A trace finite element method for a class of coupled bulk-interface transport problems. IGPM report 398, RWTH-Aachen University, 2014.
- [37] S. Groß, V. Reichelt, and A. Reusken. A finite element based level set method for two-phase incompressible flows. *Computing and Visualization in Science*, 9(4):239–257, 2006.
- [38] S. Groß and A. Reusken. An extended pressure finite element space for two-phase incompressible flows with surface tension. *Journal of Computational Physics*, 224:40–58, 2007.
- [39] S. Groß and A. Reusken. *Numerical Methods for Two-phase Incompressible Flows*, volume 40 of *Springer series in computational mathematics*. Springer, Heidelberg, 2011.
- [40] H. Haj-Hariri, A. Nadim, and A. Borhan. Effect of inertia on the thermocapillary velocity of a drop. *Journal of Colloid and Interface Science*, 140(1):277 – 286, 1990.
- [41] H. Haj-Hariri, Q. Shi, and A. Borhan. Thermocapillary motion of deformable drops at finite Reynolds and Marangoni numbers. *Physics of Fluids*, 9(4):845–855, 1997.
- [42] A. J. James and J. Lowengrub. A surfactant-conserving volume-of-fluid method for interfacial flows with insoluble surfactant. *Journal of Computational Physics*, 201(2):685–722, 2004.
- [43] H. Kim and R. Subramanian. Thermocapillary migration of a droplet with insoluble surfactant: I. surfactant cap. *Journal of Colloid and Interface Science*, 127(2):417 – 428, 1989.
- [44] H. Kim and R. Subramanian. The thermocapillary migration of a droplet with insol-

Bibliography

- uble surfactant: II. general case. *Journal of Colloid and Interface Science*, 130(1):112 – 129, 1989.
- [45] D. Korteweg. Sur la forme que prennent les équations du mouvements des fluides si l'on tient compte des forces capillaires causées par des variations de densité considérables mais continues et sur la théorie de la capillarité dans l'hypothèse d'une variation continue de la densité. *Arch. Neerl. Sci. Exactes Nat.*, 6:1, 1901.
- [46] H. Lamb. *Hydrodynamics*. Dover Publications, New York, 6 edition, 1945.
- [47] J. Langer. Models of pattern formation in first-order phase transitions. In G. Grinstein and G. Mazenko, editors, *Directions In Condensed Matter Physics*, volume 1 of *Series on Directions in Condensed Matter Physics*, pages 165–186. World Scientific, Singapore, 1986.
- [48] D. Langevin. Rheology of adsorbed surfactant monolayers at fluid surfaces. *Annual Review of Fluid Mechanics*, 46:47–65, 2014.
- [49] L. Leal. *Advanced Transport Phenomena: fluid mechanics and convective transport processes*. Cambridge Series in Chemical Engineering. Cambridge University Press, Cambridge, 2007.
- [50] C. Lehrenfeld. Hybrid discontinuous Galerkin methods for incompressible flow problems. Diploma thesis, RWTH Aachen, 2010.
- [51] J. Li, Y. Y. Renardy, and M. Renardy. Numerical simulation of breakup of a viscous drop in simple shear flow through a volume-of-fluid method. *Physics of Fluids*, 12(2):269–282, 2000.
- [52] E. Loch. *The level set method for capturing interfaces with applications in two-phase flow problems*. PhD thesis, RWTH Aachen University, 2013.
- [53] C. Ma and D. Bothe. Direct numerical simulation of thermocapillary flow based on the volume of fluid method. *International Journal of Multiphase Flow*, 37(9):1045 – 1058, 2011.
- [54] H. Marschall, S. Boden, C. Lehrenfeld, et al. Validation of interface capturing and tracking techniques with different surface tension treatments against a Taylor bubble benchmark problem. *Computers & Fluids*, 102:336 – 352, 2014.
- [55] W. J. Milliken and L. Leal. The influence of surfactant on the deformation and breakup of a viscous drop: The effect of surfactant solubility. *Journal of Colloid and Interface Science*, 166(2):275–285, 1994.
- [56] N. Mos, J. Dolbow, and T. Belytschko. A finite element method for crack growth without remeshing. *International Journal for Numerical Methods in Engineering*, 46(1):131–150, 1999.
- [57] M. Muradoglu and G. Tryggvason. A front-tracking method for computation of interfacial flows with soluble surfactants. *Journal of Computational Physics*, 227:2238–2262, 2008.
- [58] ngsflow flow solver package with different applications in 3D and 2D for Net-

- gen/NGSolve.
<http://sourceforge.net/projects/ngsflow/>.
- [59] M. A. Olshanskii and A. Reusken. A finite element method for surface PDEs: matrix properties. *Numerische Mathematik*, 114(3):491–520, 2010.
 - [60] M. A. Olshanskii and A. Reusken. Error analysis of a space-time finite element method for solving PDEs on evolving surfaces. *SIAM J. on Numerical Analysis*, 52(4):2092–2120, 2014.
 - [61] M. A. Olshanskii, A. Reusken, and J. Grande. A finite element method for elliptic equations on surfaces. *SIAM J. on Numerical Analysis*, 47(5):3339–3358, 2009.
 - [62] M. A. Olshanskii, A. Reusken, and X. Xu. On surface meshes induced by level set functions. *Computing and Visualization in Science*, 15(2):53–60, 2012.
 - [63] M. A. Olshanskii, A. Reusken, and X. Xu. An Eulerian space-time finite element method for diffusion problems on evolving surfaces. *SIAM J. on Numerical Analysis*, 52(3):1354–1377, 2014.
 - [64] M. A. Olshanskii, A. Reusken, and X. Xu. A stabilized finite element method for advection-diffusion equations on surfaces. *IMA Journal of Numerical Analysis*, 34:732–758, 2014.
 - [65] S. Osher and R. Fedkiw. Level set methods: An overview and some recent results. *Journal of Computational Physics*, 169(2):463 – 502, 2001.
 - [66] H. Öttinger, D. Bedeaux, and D. Venerus. Nonequilibrium thermodynamics of transport through moving interfaces with application to bubble growth and collapse. *Physical Review E*, 80:021606, 2009.
 - [67] C. Pozrikidis. Interfacial dynamics for Stokes flow. *Journal of Computational Physics*, 169(2):250–301, 2001.
 - [68] J. M. Rallison. A numerical study of the deformation and burst of a viscous drop in general shear flows. *Journal of Fluid Mechanics*, 109:465–482, 1981.
 - [69] J. M. Rallison. The deformation of small viscous drops and bubbles in shear flows. *Annual Review of Fluid Mechanics*, 16(1):45–66, 1984.
 - [70] A. Reusken. Analysis of an extended pressure finite element space for two-phase incompressible flows. *Computing and Visualization in Science*, 11:293–305, 2008.
 - [71] A. Reusken. Analysis of trace finite element methods for surface partial differential equations. *IMA Journal of Numerical Analysis*, doi:10.1093/imanum/dru047, 2014.
 - [72] A. Reusken and Y. Zhang. Numerical simulation of incompressible two-phase flows with a Boussinesq-Scriven interface stress tensor. *Int. J. Numer. Meth. Fluids*, 73(12):1042–1058, 2013.
 - [73] O. Reynolds. *Papers on Mechanical and Physical Subjects*, volume III. Cambridge: at the university press, 1903.
 - [74] M. J. Rosen and J. T. Kunjappu. *Surfactants and Interfacial Phenomena*. Wiley, New Jersey, 4th edition, 2012.

Bibliography

- [75] L. Sagis. Dynamics of encapsulation and controlled release systems based on water-in-water emulsions: Liposomes and polymersomes. *Physica A*, 388:2579–2587, 2009.
- [76] L. Sagis. Dynamic properties of interfaces in soft matter: experiments and theory. *Rev. Mod. Phys.*, 83(4):1367, 2011.
- [77] J. T. Schwalbe, F. R. Phelan, Jr., P. M. Vlahovska, and S. D. Hudson. Interfacial effects on droplet dynamics in Poiseuille flow. *Soft Matter*, 7:7797–7804, 2011.
- [78] J. A. Sethian. *Level set methods and fast marching methods*. Cambridge University Press, 1999.
- [79] J. C. Slattery. *Advanced Transport Phenomena*. Cambridge Series in Chemical Engineering. Cambridge University Press, 1999.
- [80] J. C. Slattery, L. Sagis, and E. Oh. *Interfacial Transport Phenomena*. Springer, New York, second edition, 2007.
- [81] H. Stone. Dynamics of drop deformation and breakup in viscous fluids. *Annual Review of Fluid Mechanics*, 26(1):65–102, 1994.
- [82] H. A. Stone and L. G. Leal. The effects of surfactants on drop deformation and breakup. *Journal of Fluid Mechanics*, 220:161–186, 1990.
- [83] R. S. Subramanian and R. Balasubramaniam. *The motion of bubbles and drops in reduced gravity*. Cambridge University Press, 2001.
- [84] K. Teigen, X. Li, J. Lowengrub, F. Wang, and A. Voigt. A diffuse-interface approach for modeling transport, diffusion and adsorption/desorption of material quantities on a deformable interface. *Comm. Math. Sci.*, 7:1009–1037, 2009.
- [85] K. Teigen, P. Song, J. Lowengrub, and A. Voigt. A diffuse-interface method for two-phase flows with soluble surfactants. *Journal of Computational Physics*, 230(2):375–393, Jan. 2011.
- [86] R. Thompson, K. Dewitt, and T. Labus. Marangoni bubble motion phenomenon in zero gravity. *Chemical Engineering Communications*, 5(5-6):299–314, 1980.
- [87] M. ur Rehman, C. Vuik, and G. Segal. Block preconditioners for the incompressible Stokes problem. In I. Lirkov, S. Margenov, and J. Waśniewski, editors, *Large-Scale Scientific Computing*, volume 5910 of *Lecture Notes in Computer Science*, pages 829–836. Springer Berlin Heidelberg, 2010.
- [88] R. Verfürth. Finite element approximation of incompressible Navier-Stokes equations with slip boundary condition. *Numerische Mathematik*, 50:697–721, 1987.
- [89] P. M. Vlahovska, J. Bławzdziwicz, and M. Loewenberg. Small-deformation theory for a surfactant-covered drop in linear flows. *Journal of Fluid Mechanics*, 624:293–337, 2009.
- [90] P. Walstra. Principles of emulsion formation. *Chemical Engineering Science*, 48(2):333–349, 1993.
- [91] N. O. Young, J. S. Goldstein, and M. J. Block. The motion of bubbles in a vertical temperature gradient. *Journal of Fluid Mechanics*, 6:350–356, 1959.